



DISSERTATION

Simulation of condensed matter dynamics in strong femtosecond laser pulses

ausgeführt zum Zwecke der Erlangung des akademischen Grades eines
Doktors der technischen Wissenschaften unter der Leitung von

O.Univ.-Prof. Dipl.-Phys. Dr.rer.nat. Joachim Burgdörfer
Institut für Theoretische Physik, e136

eingereicht an der Technischen Universität Wien
Fakultät für Physik

von

Georg Wachter

Matrikelnummer 0326872
Neulerchenfelderstraße 50/12
1160 Wien, Österreich, EU
georg.wachter@tuwien.ac.at

Wien, am

Ultrakurze Laserpulse mit hoher Intensität erlauben es, die Bewegung von Elektronen in Atomen, Molekülen und Festkörpern auf einer Zeitskala von (sub-) Femtosekunden zu steuern. Dieser Monograph erörtert Elektronenkontrolle durch Licht in drei paradigmatischen Festkörper-Systemen: einer Metall-Nanostruktur (nanometrische Spitze), einem Isolator (Quarzglas), und dem Buckminsterfulleren-Molekül (C_{60}).

Wir diskutieren sowohl quantenmechanische Simulationen mit zeitabhängiger Dichtefunktionaltheorie zur Beschreibung der mikroskopische Elektronenbewegung auf der atomaren Längenskala, als auch einfache klassische und semi-klassische Modelle zum Verständnis der zugrundeliegenden Mechanismen. Wo bereits vorhanden, vergleichen wir unsere Ergebnisse mit experimentellen Daten und finden gute Übereinstimmung. Mit steigender Laser-Intensität finden wir einen Übergang von vertikaler zu hochgradig nicht-linearer tunnel-artiger Photoanregung. Bei Nanostrukturen führt diese zu zeitlich lokalisierter Tunnelemission und zu Quanten-Interferenzen in den Energiespektren der Elektronen. Ähnliche Tunnelprozesse finden zwischen benachbarten Atomen in einem Isolator unter Einwirkung starker Laserfelder statt. Dadurch werden ultraschnelle Ströme angeregt und die Materialeigenschaften ändern sich binnen Femtosekunden. Elektron-Elektron-Wechselwirkung führt zu Feldverstärkung und Lokalisierung der nicht-linearen Antwort und wird sowohl klassisch durch Lösen der Maxwellgleichungen in der Nähe einer Nanostruktur als auch quantenmechanisch durch ab-initio Simulation des Fulleren-Moleküls untersucht.

Unsere Ergebnisse zeigen, dass ultrakurze Laserpulse Elektronenkontrolle in Festkörpern ermöglichen und dass zeitabhängige Dichtefunktionaltheorie die Beschreibung der hoch nichtlinearen Antwort erlaubt.

Ultrashort custom-tailored laser pulses can be employed to observe and control the motion of electrons in atoms and small molecules on the (sub-) femtosecond time scale. Very recently, efforts are underway to extend these concepts to solid matter. This monograph theoretically explores first applications of electron control by ultrashort laser pulses in three paradigmatic systems of solid-state density: a metal nano-structure (nanometric metal tip), a bulk dielectric (quartz glass), and the buckminsterfullerene molecule (C_{60}) as arguably the smallest possible nano-particle.

The electron motion is resolved on the atomic length and time scale by ab-initio simulations based on time-dependent density functional theory. Our quantum simulations are complemented by classical and semi-classical models elucidating the underlying mechanisms. We compare our results to experiments where already available and find good agreement. With increasing laser intensity, we find a transition from vertical photoexcitation to tunneling-like excitation. For nanostructures, that leads to temporally confined electron photoemission and thereby to quantum interferences in the energy spectra of emitted electrons. Similarly, tunneling can be induced between neighboring atoms inside an insulator. This provides a mechanism for ultrafast light-field controlled currents and modification of the optical properties of the solid, promising to eventually realize light-field electronic devices operating on the femtosecond time scale and nanometer length scale. Electron-electron interaction leads to near field enhancement and spatial localization of the non-linear response and is investigated both classically by solving the Maxwell equations near a nanostructure as well as quantum mechanically for the fullerene molecule. For the latter, we discuss scrutiny of the molecular near-field by the attosecond streaking technique.

Our results demonstrate that ultrashort laser pulses can be employed to steer the motion of electrons in solid matter, and that the latter can be accurately described by time-dependent density functional theory.

To Leopold, Gerhild, Leonhard, and Dani

Kurzfassung	iii
Abstract	v
1 Introduction	1
Publications	4
2 Near-field response of nano-tips	7
2.1 Introduction	7
2.2 Field enhancement	8
2.3 Numerical solution of Maxwell's equations by the boundary element method	11
2.4 Near-field around nano-tips	14
2.5 Wavelength dependence of field enhancement and distortion of an ul- trashort pulse	15
2.6 Dependence of field enhancement on tip geometry	17
2.7 Near-field around a pair of nano-tips	18
2.8 Conclusions and outlook	21
3 Electron emission and rescattering from metal nano-tips by intense few- cycle laser pulses	23
3.1 Introduction	23
3.2 Simple man's model for nanostructures	27
3.3 Microscopic model of electron emission with time-dependent density functional theory (TD-DFT)	35
3.3.1 Pedestrian approach to TD-DFT	35
3.3.2 Simulation of electron dynamics of a nano-tip	38

3.4	Simulation of electron emission and rescattering	42
3.5	Appearance of plateau with increasing laser intensity	44
3.6	Carrier-envelope phase dependence of rescattering	45
3.7	Electric field distribution during the laser pulse	48
3.8	From the multiphoton to the tunneling regime: wavelength dependence	50
3.9	Sensitivity to the surface potential	52
3.10	Emission of high harmonic radiation from nano-tips	55
3.11	Conclusions and outlook	61
4	Strong-field induced electron dynamics in bulk insulators	65
4.1	Introduction	65
4.2	Time-dependent density functional theory for a bulk solid	67
4.3	Ground state properties	70
4.4	Optical properties	71
4.5	Optical-field induced currents in insulators	74
4.6	Influence of the macroscopic shape of the sample	81
4.7	Number of excited electrons and petahertz electronics	82
4.8	Non-linear ultrafast bulk photogalvanic effect	85
4.9	Optical signal of ionization and non-linear polarization	91
4.10	Conclusions and outlook	94
5	Molecular near fields and streaking of endohedral fullerenes	99
5.1	Introduction	99
5.2	TD-DFT simulation of fullerenes and endohedral fullerenes	100
5.3	Geometry and ground-state properties	101
5.4	Absorption and polarizability	102
5.5	Density change and near field induced by few-cycle laser pulses	103
5.6	Dependence on the orientation of the molecule	105
5.7	Dependence on the laser intensity	106
5.8	Streaking of endohedral fullerenes in few-cycle optical laser pulses	108
5.9	Streaking of dipole excitations	111
5.10	Conclusions and outlook	115
6	Conclusions and outlook	119
	Appendix	125
A	Simulation of plasmonic tips with BEM	127
B	Scientific environment	131
	List of Figures	135
	Symbols	137

Acronyms	139
Bibliography	141
Acknowledgments	155
Curriculum vitae	158

When someone asked me during my Ph.D. what topic could divert me for so long from the pleasures of a normal life, I would answer: “It is about how solid state matter interacts with intense optical few-cycle laser pulses.” People were usually shocked and felt slightly sorry for me, and answered “What? Who could possibly be interested in that?”

As it turns out, a great many scientists from a variety of disciplines are interested in such topics. From the foundations of the interaction of radiation with matter by Einstein [1917] and the inception of the laser [Gould, 1959; Maiman, 1960; Kastler, 1967], the laser has become an indispensable tool in everyday applications from data storage to eye surgery. In parallel to the development of industry-grade laser technology, fundamental research on ever improved control of laser output radiation has led to the development of the Ti:sapphire laser [Moulton, 1986] characterized by a broadband output spectrum that together with advanced pulse shaping by chirped mirrors [Szipöcs et al., 1994] allows the generation of well controlled, intense, ultrashort pulses. Here, “ultrashort” means that only few optical cycles are below the laser envelope (occur during the laser pulse length). For example, commercial applications routinely operate with pulse durations of 10 - 100 femtoseconds (fs, $1 \text{ fs} = 10^{-15} \text{ s}$), and in laser science laboratories pulse durations below 4 fs are state of the art. For comparison, the duration of the laser period at 800 nm wavelength is 2.67 fs. This compression of the laser pulse energy in time allows extremely high peak field strengths of the electric field. In fact, the electric field can be even larger than the electric field that a bound electron feels in an atom. As matter on earth is essentially governed by the electromagnetic interaction between its constituent parts, the strong time-dependent electric field of a laser is an ideal tool to control and probe the

motion of electrons in atoms, molecules, and solid matter. Going from a fundamental interest in building better and bigger lasers to applications in atomic and molecular physics and physical chemistry, the technological development of such intense, well-controllable laser sources has led to unprecedented insights into the dynamics of electron motion. These are often summarized by the buzzword of “attosecond science” referring to the natural time scale of electron motion in atoms, molecules, and solids (the classical orbital period of an electron in a hydrogen atom is about 150 attoseconds or 0.15 fs). Attosecond science has succeeded to directly demonstrate a number of abstract concepts that have been part of elementary textbooks on physics and chemistry for a long time but the observability of which was unthinkable just a few years ago. Examples include a direct measurement of the oscillations of the electric field vector in real time [Goulielmakis et al., 2004], “tomographic” measurements of molecular orbitals [Itatani et al., 2004], ballistic motion of electrons in solids [Cavaliere et al., 2007], the time dependence of electron tunneling ionization [Uiberacker et al., 2007] and the time dependence of the phase of the wave function at the tunnel exit [Xie et al., 2012], and the time-dependent dipole induced in molecules by the electric field of the laser [Neidel et al., 2013]. These advances have all been achieved within the last decade. In addition to the optical physicists, atomic physicists, and physical chemists fascinated by these milestones marking truly a new era of understanding and control of the microscopic properties of matter, solid state and surface physicists are becoming increasingly aware of the promise that attosecond science holds also for their field. Employing ultrashort laser pulses together with state-of-the-art control of sample quality, surface structure, and possibly surface modifications by modern nanotechnology will open the door to exciting possibilities. On one hand, fundamental questions about the properties of interacting quantum many body systems subject to a strong time-dependent perturbation can be answered. Currently, the theoretical description of such systems is less developed compared to smaller atomic or molecular targets, and experiments will soon reach parameter regimes where the validity of presently tractable theory is questionable. On the other hand, a wealth of possible applications has been envisioned for solid-state systems illuminated by ultrashort laser pulses. To name but two that will play a major role in the pages ahead, metal nano-tips have been suggested as ultrafast, nanometric, coherent sources for femtosecond electron pulses [Hoffrogge et al., 2014; Gulde et al., 2014] that may in the long term be employed to visualize electron motion inside solids [Baum et al., 2007]. Secondly, employing ultrashort laser pulses to change the properties of bulk dielectrics on the femtosecond time scale has been suggested as a way to realize ultrafast switching devices that will be, in principle, capable of operating at clock speeds surpassing those of semiconductor technology operating today’s computers by several orders of magnitude [Krausz and Stockman, 2014].

In the course of this monograph, we will visit three systems of current interest where laser induced non-linear response plays a crucial role, and we will describe the response mainly by an ab-initio framework named time-dependent density func-

tional theory (TD-DFT). Wherever possible, we will supplement our calculations by direct comparison with experiment and with simpler classical or semi-classical models that capture only the essential physical mechanism.

The first part of the thesis is devoted to investigating the strong field response of paradigmatic nano-structures, a nanometric metal tip, and the control of electron motion near the surface of the nanostructure by ultrashort laser pulses. We begin by investigating the near-field response of a nano-tip, at first on a classical level described by the Maxwell equations (chapter 2) which also serves to introduce the concept of field enhancement. The near field at the tip apex is enhanced due to the dynamic lightning-rod effect and subsequently enters into a quantum simulation of surface dynamics and electron photoemission around the nanometric apex of the tip (chapter 3). Comparing our simulation to recent experiments, we demonstrate that electrons are first photoemitted from the nanotip and then driven back towards the surface by the laser field where they can scatter from the first layer of surface atoms. These quantum surface dynamics leave distinctive marks on the electron spectra that are intimately related to the exquisite control over the motion of the electron outside the nano-structure by the shape of the laser field. Due to the mesoscopic size of the nano-structure, far larger than what can be modeled by present-day quantum simulations, the quantum dynamics in chapters 2 and 3 are treated separately from the dynamics of the incoming laser field, and the quantum dynamics is restricted to the reaction coordinate along the surface normal. In the remainder of the monograph, we investigate two other systems where this restriction is lifted and fully three-dimensional microscopic quantum simulations are employed to describe the interaction of matter with laser pulses. First, in chapter 4, we investigate an idea complementary to controlling electron motion with strong laser fields *outside* a metal nanostructure, namely controlling electron motion *within* a transparent dielectric. We investigate the charge that is transferred within a dielectric only by virtue of a strong femtosecond laser field and compare our findings to very recent experiments. The steep rise in the charge transfer signal as a function of laser intensity is linked to the emergence of electron tunneling between neighboring atoms inside the solid for high laser intensity that can lead to quasi-free currents in the dielectric and changes the material properties on the ultrafast time scale. Secondly, in chapter 5, we investigate a system that is on the one hand large enough to show field enhancement, but on the other hand small enough that an ab-initio description is still tractable. We investigate the time-dependent near-field of arguably the smallest possible nano-particle, a single C₆₀ molecule, by three-dimensional ab-initio simulations and find surprising analogies to the textbook model of a dielectric sphere in a laser field. We suggest how a sophisticated pump-probe scheme called attosecond streaking can be employed to probe the time-dependent molecular near-fields, excitation, and decay ensuing laser irradiation.

Atomic units are used unless stated otherwise.

Publications

The results discussed in this work have in part been published as indicated by footnotes throughout the text. A list of publications with references to the respective parts of this thesis is given below. Publications without peer-review are marked with a star *.

Interaction of few-cycle laser pulses with nano-tips (chapters 2 and 3)

- G Wachter, C Lemell, J Burgdörfer, M Schenk, M Krüger, P Hommelhoff
Electron rescattering at metal nanotips induced by ultrashort laser pulses
Physical Review B, 86, 035402 (2012)
- M Krüger, M Schenk, P Hommelhoff, G Wachter, C Lemell, J Burgdörfer
Interaction of ultrashort laser pulses with metal nanotips: a model system for strong-field phenomena
New Journal of Physics, 14, 085019 (2012)
- G Wachter, C Lemell, J Burgdörfer
Electron rescattering at metal nanotips induced by ultrashort laser pulses
J. Phys.: Conf. Ser., 488, 012005 (2014)
- M Krüger, S Thomas, M Förster, L Maisenbacher, G Wachter, C Lemell, J Burgdörfer, P Hommelhoff
*Attosecond physics at a nanoscale metal tip: strong field physics meets near-field optics**
SPIE OPTO, 862313-862313-6 (2013)
- G Wachter, C Lemell, J Burgdörfer
Electron emission from a metal nano-tip by ultrashort laser pulses
J. Phys.: Conf. Ser., 399, 012010 (2012)

Strong-field induced electron dynamics in insulators (chapter 4)

- G Wachter, C Lemell, J Burgdörfer, SA Sato, XM Tong, K Yabana
Ab initio simulation of electrical currents induced by ultrafast laser excitation of dielectric materials
Physical Review Letters 113, 087401 (2014)

Molecular near-fields and streaking of endohedral fullerenes (chapter 5)

- S Nagele, R Pazourek, M Wais, G Wachter, J Burgdörfer
Time-resolved photoemission using attosecond streaking
J. Phys.: Conf. Ser., 488, 012004 (2014)

Other topics

- H Li, B Mignolet, G Wachter, S Skruszewicz, S Zharebtsov, F Süßmann, A Kessel, S A Trushin, Nora G Kling, M Kübel, B Ahn, D Kim, I Ben-Itzhak, C L Cocke, T Fennel, J Tiggesbäumker, K-H Meiwes-Broer, C Lemell, J Burgdörfer, R D Levine, F Remacle, M F Kling
Coherent electronic wave packet motion in C_{60} controlled by the waveform and polarization of few-cycle laser fields
submitted to Physical Review (2014)

- S Neopl, R Ernstorfer, A L Cavaliere, C Lemell, G Wachter, E Magerl, E Bothschafter, M Hofstetter, J V Barth, D Menzel, J Burgdörfer, P Feulner, F Krausz, R Kienberger
Real-time observation of electron propagation and dielectric screening on the atomic length scale
submitted to Nature publishing group (2014)
- A S El-Said, R A Wilhelm, R Heller, R Ritter, G Wachter, S Facsko, C Lemell, J Burgdörfer, F Aumayr
Nanostructuring CaF₂ surfaces with slow highly charged ions
J. Phys.: Conf. Ser., 488, 012002 (2014)
- G Wachter, K Tókési, G Betz, C Lemell, J Burgdörfer
Modelling surface restructuring by slow highly charged ions
Nucl. Instrum. Methods Phys. Res. Sect. B, 317, 149 (2013)
- A S El-Said, R A Wilhelm, R Heller, S Facsko, C Lemell, G Wachter, J Burgdörfer, R Ritter, F Aumayr
Phase diagram for nanostructuring CaF₂ surfaces by slow highly charged ions
Physical Review Letters 109, 117602 (2012)
- G Wachter, E Persson, M Pichler, T Hisch, J Burgdörfer, S Gräfe
Quantum control of electron wavepacket dynamics in molecules by trains of half-cycle pulses
J. Phys.: Conf. Ser., 388, 132018 (2012)
- D Klotz, S Sacuto, C Paladini, J Hron, G Wachter
*Geometrical model fitting for interferometric data: GEM-FIND**
SPIE Astronomical Telescopes and Instrumentation, SPIE Conference Series 8445, 84451A (2012)
- E Persson, M Pichler, G Wachter, T Hisch, W Jakubetz, J Burgdörfer, S Gräfe
Quantum control of electron wave packets in bound molecules by trains of half-cycle pulses
Physical Review A, 84, 043421 (2011)
- P Tiwald, C Lemell, G Wachter, J Burgdörfer
Theory of below-threshold kinetic electron emission
J. Phys.: Conf. Ser., 257, 012012 (2010)
- A Golczewski, K Dobes, G Wachter, M Schmid, F Aumayr
A quartz-crystal-microbalance technique to investigate ion-induced erosion of fusion relevant surfaces
Nuclear Instruments and Methods in Physics Research B, 267, 695 (2009)

2.1 Introduction

Nano-technological advances combined with the advent of modern computing power have given rise to a renewed interest in the electrodynamics of continuous media. Many concepts that were originally developed for radio-wavelengths and macroscopic length dimensions like the classic directional Yagi-Uda antenna [Uda, 1927] have been taken to the nanometric length scale and optical frequencies [Maksymov et al., 2012; Novotny and van Hulst, 2011]. Employing field enhancement at sub-wavelength structures to concentrate energy below what is attainable by conventional optical elements like lenses and mirrors holds the promise to enhance the performance and efficiency of photodetection, light emission, and sensing. The ever-growing field of “plasmonics” investigates the properties of such localized or propagating excitations at surfaces, nano-particles, arrays of nano-particles, or custom-made structures with the goal to use surface plasmons to confine energy or transfer information on the nanometer length scale [Maier and Atwater, 2005; Stockman and Hewageegana, 2007; Brongersma and Kik, 2007]. Recently, advances into the non-linear regime have also been attempted [Kauranen and Zayats, 2012].

In this chapter, we study the electrodynamic response of nano-tips, a paradigmatic nano-structure where field enhancement takes place. Nanometric tips or wires (tips with small opening angle) where the electric near-field is concentrated near the apex serve to enhance non-linear processes in a wide range of applications from scanning near-field optical microscopy (SNOM) [Martin et al., 2001; Hartschuh, 2008], tip-enhanced Raman scattering (TERS) [Kawata et al., 2009; Sonntag et al., 2014], as sources of second-harmonic generation [Bouhelier et al., 2003], as sources of ultrafast photoemitted electrons [Hommelhoff et al., 2006b,a; Ropers et al., 2007; Barwick et al.,

2007], as possible directional light emitters [Grzela et al., 2012] or as semi-conductor nano-antennas for improved absorption of light in novel photodetectors and photo-voltaic devices [Grzela et al., 2014]. An important conceptual difference to plasmonics is, however, that the open geometry of a nano-tip does not permit sharp localized resonances, which are usually exploited in plasmonics to attain the strongest energy concentration. On the other hand, this lack of sharp resonances provides field enhancement over a wide frequency range so that the pulse shape of an incoming few-cycle laser pulse is conserved. We treat the dielectric properties of the tip in linear response by the macroscopic Maxwell equations and neglect the back-action of possible non-linear contributions on the near field. Our main quantity of interest is the enhanced time-dependent electric field at the apex of the nano-tip, which we will use as input for the subsequent quantum mechanical simulation of electron emission and rescattering in the next chapter.

We start by discussing the lightning-rod effect leading to field enhancement for the most simple case, a nano-sphere in a quasi-static laser electric field, and extensions to field enhancement at ellipsoids. After exhausting the analytical options, we turn to a brief survey of available numerical methods for the solution of Maxwell's equations and describe our choice, the boundary element method as implemented in the public domain SCUFF-EM package. We then present simulations for experimentally relevant tungsten nanotips investigating the near-field around a metal nanotip and the magnitude and phase shift of the field enhancement at the tip apex as a function of laser wavelength and tip geometry. Towards the end of the section, we present simulation results for a pair of nano-tips.

2.2 Field enhancement

In this section, we discuss the mechanism leading to field enhancement at sharp geometrical features, which is also called the "lightning-rod" effect. The mechanism of field enhancement is not due to retardation effects of a propagating electromagnetic field and can be discussed in the quasi-static approximation¹ (see Sarid and Challener [2010]; Jackson [1998]; Purcell and Morin [2013]; Bohren and Huffman [1998]).

We briefly recollect the textbook problem of a dielectric sphere of radius R_{sphere} and dielectric constant $\epsilon(\omega)$ in a quasi-static electric field $F_0 e^{-i\omega t}$ in z direction, which is a good approximation for nanospheres irradiated by a laser if their radius is much smaller than the laser wavelength $\lambda = 2\pi c/\omega$ with c the velocity of light in vacuum. The solution of the Laplace equation with the appropriate electrostatic boundary conditions at the surface of the sphere yields for the electrostatic potential

$$\phi_{\text{sphere}}(\mathbf{r}) = \begin{cases} F_0 A z & \text{for } r < R_{\text{sphere}} \\ -F_0 z + F_0 B z / r^3 & \text{for } r \geq R_{\text{sphere}} \end{cases} \quad (2.1)$$

¹ In the literature, some authors distinguish between the (electrostatic) lightning-rod effect in DC fields and the "dynamic" lightning-rod effect induced by oscillating light fields. As we are concerned with field enhancement at optical frequencies, we consider only this "dynamic" lightning-rod effect.

where the field inside the sphere is reduced by $A = -3/(\epsilon + 2)$ compared to the external field, and the potential outside the sphere is that of a dipole. The amplitude of the dipole is $B = R_{\text{sphere}}^3(\epsilon - 1)/(\epsilon + 2) = \alpha_{\text{sphere}}$, the so-called polarizability of a sphere, and the total induced dipole moment is $\mathbf{p}_{\text{sphere}} = \alpha_{\text{sphere}}\mathbf{F}_0$. The electric field is given by $\mathbf{F}_{\text{sphere}}(\mathbf{r}) = -\nabla\phi_{\text{sphere}}(\mathbf{r})$,

$$\mathbf{F}_{\text{sphere}}(\mathbf{r}) = \begin{cases} -AF_0\hat{\mathbf{z}} & \text{for } r < R_{\text{sphere}} \\ F_0\hat{\mathbf{z}} - \mathbf{p}_{\text{sphere}}/r^3 + 3\frac{\mathbf{p}_{\text{sphere}}\cdot\mathbf{r}}{r^5}\mathbf{r} & \text{for } r \geq R_{\text{sphere}} \end{cases} \quad (2.2)$$

and the maximum value of the electric field is attained on the surface of the sphere in the direction of the external field giving a field enhancement factor

$$\zeta_{\text{FE}}^{\text{sphere}} = F_{\text{sphere}}(0, 0, R_{\text{sphere}})/F_0 = \frac{3\epsilon}{\epsilon + 2}. \quad (2.3)$$

Fig. 2.1 shows the potential and near-field of a nano-sphere. For a dielectric like glass, the potential and field are real, that is, in phase with the external field. However, if the dielectric constant has a non-negligible imaginary part, the induced field has an imaginary component, meaning that it is phase shifted with respect to the incoming field. This is the case for typical tip materials at optical frequencies. For most metals at optical wavelengths, $|\epsilon| \gg 1$ so that the field enhancement of a spherical nanoparticle is $\zeta_{\text{FE}}^{\text{sphere}} \approx 3$. The dipole resonance of a nanosphere is at $\epsilon \sim -2$ (Eq. 2.3).

The field inside the dielectric is reduced compared to the field outside (Fig. 2.1 b), and the reduction is roughly proportional to $|\epsilon|$ (Eq. 2.2). In the special case of spheres, the field inside the dielectric is also constant. This screening inside the dielectric leads to a reduced slope of the potential inside the dielectric (Fig. 2.1 a). Far away from the dielectric, however, the potential must approach the correct asymptotic potential $-F_0z$. Therefore, the total potential which is continuous across the interface must have a curvature to join the potential inside the sphere with the potential far away from the sphere. This curvature leads to an increase in the gradient $F = -\nabla\phi$, which is the origin of the enhanced field at the surface.

An alternative interpretation for field enhancement can be given in terms of the induced surface charge density. As the sphere is exposed to the external electric field, the ‘‘bound’’ charges in the dielectric are moved in the direction of the incoming field. We can imagine this polarization as the displacement of a uniform positively charged sphere against a sphere of equal uniform negative charge (Fig. 2.1c). This movement of bound charge leads to a layer of surface charge on the dielectric, which induces an additional electric field, which in turn acts back self-consistently on the movement of the charge. The solution of the Laplace equation with the electrostatic boundary conditions gives, by design, the self-consistent solution to this problem. The field enhancement can be interpreted as the Coulomb force $\int d^3r' n_{\text{bound}}(\mathbf{r}') \cdot (\mathbf{r} - \mathbf{r}')/|\mathbf{r} - \mathbf{r}'|^3$ exerted by the surface charge on a test charge in the vicinity of the nanosphere.

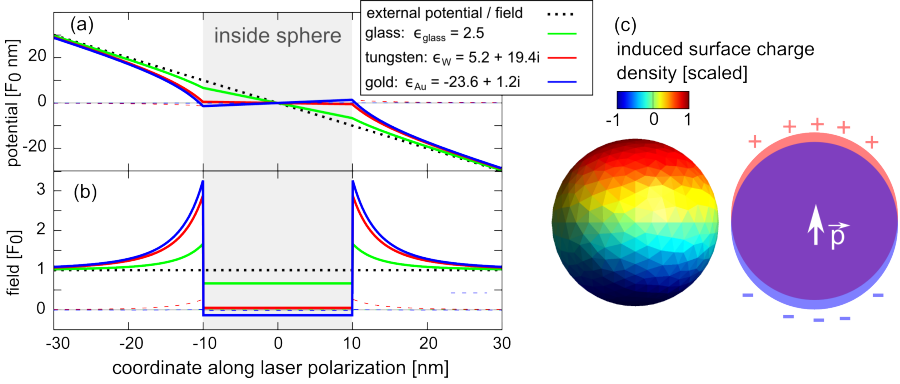


Figure 2.1: Field enhancement of a nano-sphere. (a) Quasi-static electric potential. Dotted line: external potential $-F_0 z$. Potentials are calculated for dielectrics with different dielectric constants: green (glass), $\epsilon_{\text{glass}} = 2.5$; red (tungsten), $\epsilon_{\text{W}} = 5.2 + 19.4i$; blue (gold), $\epsilon_{\text{Au}} = -23.6 + 1.2i$. Real parts are solid lines and imaginary parts are dashed lines. (b) Electric field. (c) Induced surface charge density on a nano-sphere (for $\epsilon_{\text{glass}} = 2.5$). Left: calculated distribution of surface charge. Right: model system consisting of two displaced charged spheres showing the origin of the surface charge distribution.

We further analyze the geometry dependence of near-field enhancement by discussing a sub-wavelength ellipsoid with two equal axes with the field direction taken along the third axis. The analytical solution for the field enhancement at the apex in the quasi-static approximation is [Sarid and Challener, 2010; Bohren and Huffman, 1998]

$$\zeta_{FE}^{\text{ellipsoid}} = \frac{\epsilon}{1 + A_s(\epsilon - 1)} \quad (2.4)$$

with the so-called shape factor $A_s = (1 - s^2)^{-1} - s(1 - s^2)^{-3/2} \sin^{-1}(\sqrt{1 - s^2})$ for aspect ratio s taken to be the length of the ellipsoid along the field direction divided by its width. A_s varies smoothly over the range of possible geometries, from pancake-shaped ellipsoids ($A_s \rightarrow 1$) to spheres ($A_s \rightarrow 1/3$) to needle-like ellipsoids ($A_s \rightarrow 0$). For a sphere ($A_s = 1/3$), we recover Eq. 2.3, and for a flat surface ($A_s = 1$), $\zeta_{FE}^{\text{ellipsoid}} = 1$, i.e., the field enhancement vanishes as expected. Going from a sphere to a needle-like ellipsoid ($1/3 \geq A_s \geq 0$), the qualitative behavior of $\zeta_{FE}^{\text{ellipsoid}}$ depends on the dielectric function. For dielectrics ($\text{Re } \epsilon > 1$), the field enhancement increases monotonically as the needle becomes more and more sharp, while for good conductors at optical frequencies ($\text{Re } \epsilon < -1$), there is an optimal aspect ratio where the field enhancement is maximal at the dipole resonance. In the quasi-static approximation for a needle-like ellipsoid ($A_s \rightarrow 0$), the field enhancement becomes

$$\zeta_{FE}^{\text{needle}} = \epsilon \quad (2.5)$$

This result can be compared to the quasi-static field enhancement obtained for a paraboloid [Chang et al., 2007, 2009], which is also $\zeta_{FE}^{\text{paraboloid}} = \epsilon$ independent of

its curvature. While modeling an infinitely extended needle or paraboloid within the quasi-static approximation is questionable, these estimates lead us to suspect that a variation of the dielectric function will also lead to a similar proportional variation in the field enhancement for other nano-structures.

Analytical models of field enhancement that include retardation and a finite illumination spot, a focus, have so far not been achieved. We therefore turn to a numerical solution of Maxwell's equations in the following section.

2.3 Numerical solution of Maxwell's equations by the boundary element method

In this section, we discuss the numerical solution of the Maxwell equations for a nanotip in a laser focus. After discussing advantages and disadvantages of the available methods, we describe our choice, the boundary element method, in more detail.

Over the past 20 years, an enormous increase in electromagnetic ab-initio simulation has taken place. Electromagnetism is especially favorable for ab-initio computation because the Maxwell equations are exact (in the macroscopic limit) and the relevant material properties such as the frequency-dependent bulk dielectric function can be experimentally determined to a high degree of accuracy. Results derived from the macroscopic Maxwell equations have consistently agreed with experiments for structures down to the nm length scale, allowing for the computer to become a pre-laboratory for the investigation and optimization of photonic devices before they are fabricated. An added complication for simulations of a nano-tip is the disparity in length scales. On one hand, field enhancement takes place on the length scale of the nanometric apex of the tip and requires a resolution on the sub-nanometer length scale, but on the other hand, the extended geometry of the nanotip must be modeled to account for the full distribution of polarization inside the material and its retarded contributions to the field at the apex on the micrometer scale.

Computational electromagnetism problems fall into two main categories [Joannopoulos et al., 2011; Gray, 2012]. The first is *time-domain calculations*, where the electric and magnetic fields are evolved in time according to the Maxwell equations (SI units are used in this section),

$$\begin{aligned}\nabla \cdot \mathbf{D} &= \rho \quad , \quad \nabla \cdot \mathbf{B} = 0 \\ \nabla \times \mathbf{F} &= -\partial_t \mathbf{B} \quad , \quad \nabla \times \mathbf{H} = \mathbf{J} + \partial_t \mathbf{D}\end{aligned}\quad (2.6)$$

where \mathbf{F} and \mathbf{B} are the electric and magnetic fields, ρ and \mathbf{J} are the (free) charge and current density, the derived fields in linear materials read $\mathbf{D} = \epsilon_0 \epsilon \mathbf{F}$ and $\mathbf{H} = \mathbf{B} / (\mu_0 \mu)$, and $\mathbf{J} = \sigma \mathbf{F}$. The material constants ϵ , μ and σ are called dielectric function, relative magnetic permeability, and specific conductivity and can be, in general, tensor valued and dependent on space (and time if we extend the equations to non-linear materials). The Maxwell equations are linear in the fields, which has the prac-

tical consequence that the solutions of the Maxwell equations presented below are normalized to an arbitrary field amplitude F_0 (e.g., 1 V/m). At boundaries between two homogeneous media the continuity conditions for the fields in medium (1) and medium (2) read

$$\begin{aligned} \mathbf{n}_{12} \cdot (\mathbf{D}_2 - \mathbf{D}_1) &= \sigma_{\text{surf}}, & \mathbf{n}_{12} \cdot (\mathbf{B}_2 - \mathbf{B}_1) &= 0 \\ \mathbf{n}_{12} \times (\mathbf{F}_2 - \mathbf{F}_1) &= 0, & \mathbf{n}_{12} \times (\mathbf{H}_2 - \mathbf{H}_1) &= \mathbf{K}_{\text{surf}} \end{aligned} \quad (2.7)$$

where \mathbf{n}_{12} is the surface normal vector pointing from material (1) to (2). The discontinuity of the normal component of \mathbf{D} is due to the surface charge density σ_{surf} and of the tangential component of \mathbf{H} is due to the surface current \mathbf{K}_{surf} . The Maxwell equations (2.6) are integrated in real space and real time to find the response of a system defined by space-dependent material constants $\epsilon(\mathbf{r})$, $\mu(\mathbf{r})$ and $\sigma(\mathbf{r})$ due to some external excitation which can consist of incoming electromagnetic fields or time-dependent source currents.

Alternatively, the linear Maxwell equations can be solved in a *frequency-domain calculation* yielding the complex field amplitudes $\mathbf{F}(\mathbf{r}, \omega)$ and $\mathbf{H}(\mathbf{r}, \omega)$ at point \mathbf{r} and frequency ω . The time domain fields can be recovered from a superposition of calculations for different frequencies,

$$\mathbf{F}(\mathbf{r}, t) = \frac{1}{2\pi} \int d\omega e^{-i\omega t} \mathbf{F}(\mathbf{r}, \omega) \quad . \quad (2.8)$$

The main factor that decides the computational cost of calculations both in time domain and in frequency domain is the choice of discretization for the partial differential equations. The most often employed integrator for Maxwell's equations is the finite-differences time domain (FDTD) method (Kunz and Luebbers [1993], Taflove and Hagness [2005], Oskooi et al. [2010]). Integration is performed on a Cartesian grid in time and space, which makes it difficult to resolve field enhancement at sharp structures much below the wavelength of the incoming light. Adaptive grids are at present not available in public domain implementations, but are in principle straightforward to implement [Taflove and Hagness, 2005] and are available in some commercial implementations like *Lumerical*. Alternatively, discontinuous Galerkin time domain methods allow flexible grids and are gaining popularity [Descombes et al., 2013; Swanwick et al., 2014]. Another popular discretization method is finite elements (FEM), which is most effectively employed in frequency-domain. Calculations can be performed with most modern public domain or proprietary finite element solvers, for example *COMSOL*. While FEM is well suited for efficient discretization of the three-dimensional space in the vicinity of sharp structures, fully three-dimensional finite element simulations of a mesoscopic nanotip in a laser focus are challenging even for modern computers. We instead employed a boundary element method (BEM, also called "surface integral equations formulation" or "method of moments"). In contrast to FDTD and FEM methods, which discretize three-dimensional space and solve a spatially local form of Maxwell's equations, the BEM takes advantage of the

analytically known solutions of Maxwell's equations in homogeneous media, so that only the boundary of a region of homogeneous dielectric properties has to be discretized. The numerical complexity thus scales with the *surface* of the structure that is modeled instead of its *volume* and allows an accurate treatment of nanotips with mesoscopic sizes up to the micron range with moderate memory requirements. On the other hand, while FDTD and FEM can handle arbitrary spatial variations of dielectric properties, BEM is restricted to piecewise homogeneous material configurations.

We used the public domain implementation of the boundary element method SCUFF-EM by M. T. Homer Reid (see Reid and Johnson [2013]; Reid et al. [2013] and homerreid.com/scuff-em). Similar capabilities, with the exception of a focused laser beam as excitation, are present in the *MNPBEM* package [Hohenester and Trügler, 2011]. A typical simulation run proceeds as follows. First, the tip geometry is defined as a combination of primitive geometrical shapes depending on the geometrical parameters like tip radius and tip opening angle. The surface of the tip is then discretized into flat triangles (“meshing”) employing the public domain meshing software *gmsh* [Geuzaine and Remacle, 2009]. Our adaptive mesh can resolve the fine features of the near field around the apex of the tip with discretization steps of the order of 0.2 nm near the apex. The rest of the tip is discretized in steps of about 1–20 nm that resolve the curvature of the geometry and are much smaller than the wavelength of surface plasmons, which can be excited at the sharp tip apex. The total length of a simulated tip is between 1.7 micron to 6 micron for a focus size of ~ 2 micron. The inside of the nanotip is designated the experimental dielectric bulk constant of the material at the working frequency [Palik, 1991].

The boundary element method solver SCUFF-EM is then employed to solve for the scattered electromagnetic fields for a given incoming laser beam. This is done in two steps. First, the so-called “equivalent surface currents” on the surface of the tip are computed. They are defined so as to satisfy the boundary conditions of Maxwell's equations (2.7) on the surface of the nano-tip. This prescription is cast into an integral equation which, upon discretization, yields a matrix equation for the equivalent surface currents. The latter is solved with standard linear algebra methods. The size of the BEM matrix scales as N_{panels}^2 where N_{panels} is the number of panels used for the discretization of the nano-tip (in the calculations presented below, $N_{\text{panels}} \sim 10000$ which needs on the order of 15 GB of memory). After the equivalent surface currents have been computed, the electric and magnetic fields at any point in space can be evaluated with the same numerical effort per point. If the evaluation point is chosen closer to the nanotip boundary than the local surface discretization step, discretization errors can lead to local fluctuations in the calculated electric field. These can be circumvented by either smoothing out the fluctuations, extrapolating the field towards the surface, or improving the resolution of the discretization. For the evaluation of field enhancement at the apex of the tip, we found that for a typical discretization of the region near the apex of 0.2 nm, evaluation points at a distance of only 0.01

nm from the apex are still reliable and do not show numerical instabilities. To evaluate the field exactly at the position of the apex, we extrapolate the near field towards the tip apex on a length scale of ~ 0.05 nm. The difference to the field evaluated at 0.01 nm in front of the apex is typically in the range of 1 %.

2.4 Near-field around nano-tips

We investigate the time and space dependent near field distribution around nano-tips. While there have been a number of other studies on field enhancement near nano-tips, a detailed study of the dependence of the near fields on the tip design parameters (material, radius, opening angle) and including the distortion of few-cycle laser pulses is still lacking. Notable earlier works include Martin et al. [2001] who employed early three-dimensional finite-element time domain simulations for selected geometries and Zhang et al. [2009] who performed frequency domain finite element calculations within cylindrical symmetry. Recently, the influence of surface roughness and of non-local corrections on the propagation of surface plasmons on a tip has been studied [Wiener et al., 2012; Esteban et al., 2012]. One time-domain study employing the Green dyadic method has been presented by Arbouet et al. [2012], which however might be considered unreliable due to the relatively small tip length employed. A very recent study on silicon tips was performed by Swanwick et al. [2014].

A typical near-field distribution around a nano-tip is shown in Fig. 2.2a. While the electric field far away from the tip is almost unchanged (Fig. 2.2a inset top left), the field is strongly enhanced in a nanometric region around the apex and decays on the length scale of the tip radius. Correspondingly, strongly non-linear processes will be confined to the nanometric area around the tip apex. Inside the nano-tip, the polarization charge layer screens the inside of the tip from the external electric field (Fig. 2.2 b). For tip radii much smaller than the laser wavelength, the largest electric field is reached on the surface along the tip axis at the apex of the tip and points along the tip axis $\mathbf{F}(\mathbf{r}_{\text{apex}}) \approx F_{\parallel}(\mathbf{r}_{\text{apex}}) \cdot \hat{\mathbf{r}}_{\text{tipaxis}}$. The phase shift with respect to the incoming field can be visualized by the contour line where the electric field along the tip axis is zero (the incoming field is zero at $x = 0$ at the time shown in Fig. 2.2a) or equivalently by the argument of the complex electric field component along the tip direction (Fig. 2.2c). The phase shift extends somewhat further away from the tip apex than the near-field enhancement. The total electric field vector around the nanotip is oriented approximately perpendicular to the surface of the apex, leading to a total field that is more spread out over the apex than the field component along the tip axis.

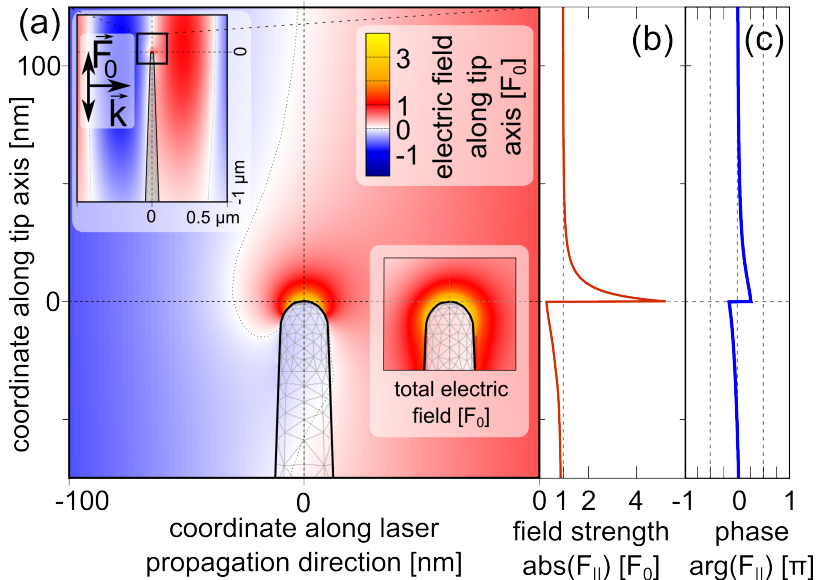


Figure 2.2: Near-field distribution around nano-tips. (a) Snapshot of near-field enhancement around a tungsten nano-tip of radius 10 nm and half opening angle 2 deg at laser wavelength 800 nm. Field component along the tip axis $\text{Re}(F_{||}(r))$ as color contours. The mesh used for discretization of the tip geometry is superimposed (thin grey lines). **Inset top left:** Zoomed-out view on the micrometer scale. The laser impinges from the left and is polarized along the tip axis. **Inset bottom right:** Total instantaneous field strength $|\text{Re}(F(r))|$ on the same color scale. (b) Field enhancement $\text{abs}(F_{||}(r))$ along the tip axis. (c) Phase shift $\text{arg}(F_{||}(r))$ along the tip axis.

2.5 Wavelength dependence of field enhancement and distortion of an ultrashort pulse

We now discuss the wavelength dependence of the electric near-field enhancement at the tip apex. The complex field enhancement factor [Bouhelier et al., 2003; Brongersma and Kik, 2007] at the tip apex is the ratio of the total field perpendicular to the tip surface to the incoming field along the tip axis (Fig. 2.3 b,c). The typical magnitude of the field enhancement factor for slim tungsten nanotips currently used in experiment is between 3–6 and neither field enhancement nor phase shift show a strong dependence on the laser wavelength in the experimentally relevant region between 200 nm and 2000 nm wavelength. The slight local maxima and minima in the field enhancement and phase shift can be traced back to the frequency dependence of the dielectric function (Fig. 2.3 a). The frequency-dependent field enhancement is Fourier transformed to give the time-dependent near field due to excitation by a few-cycle laser pulse (Fig. 2.3 d-h). As the response varies only little over the spectral width of a few-cycle pulse at typical experimental near-infrared (Fig. 2.3 e) or infrared (Fig. 2.3 g) wavelengths or even over the extended spectrum of a light “transient” [Wirth et al.,

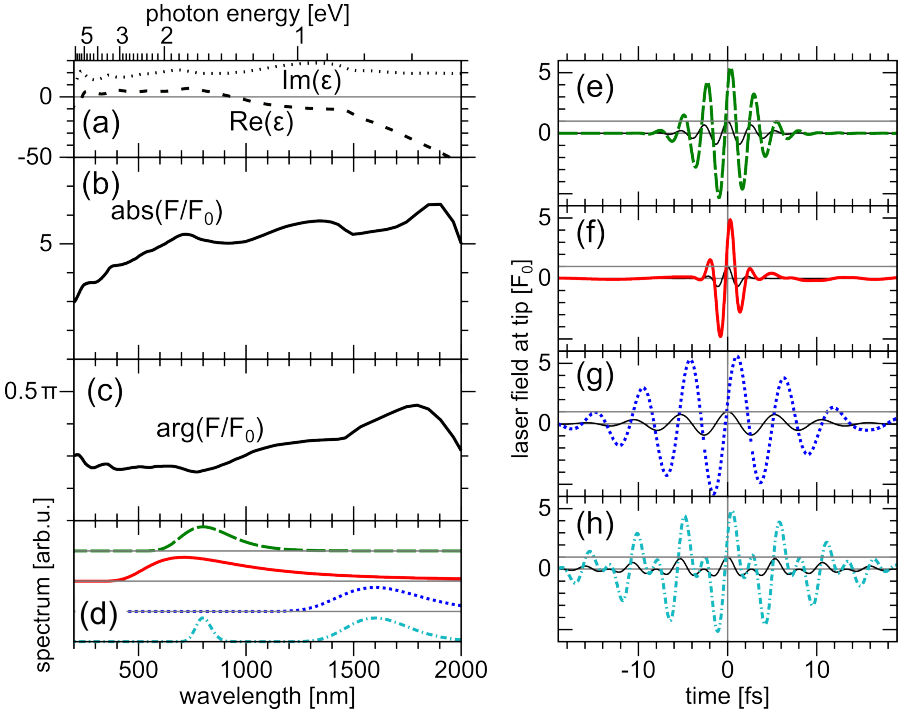


Figure 2.3: Near-field response in time and frequency domain for a tungsten nano tip of tip radius 10 nm and half opening angle 2 deg. (a) Real and imaginary part of the dielectric function (b) Field enhancement factor $|F(\lambda)|/F_0$ at wavelength λ . (c) Phase shift $\text{arg}(F(\lambda))$. (d) Spectra of typical experimental laser pulses (offset for clarity). Green dashed: 800 nm, 6 fs; red solid: light “transient” (710 nm, 2.1 fs [Wirth et al., 2011; Hassan et al., 2012]); blue dotted: 1600 nm 12 fs infrared few-cycle pulse; turquoise dash-dotted: two-color pulse at 800 nm + 1600 nm with unity mixing ratio. (e-h) Time-domain electric field at tip surface corresponding to the spectra in (d) (colored lines) and incoming electric field (black solid line).

2011; Hassan et al., 2012], the electric field at the tip apex is still an ultrashort pulse with, however, an offset in the carrier-envelope phase that is identified with the argument of the complex field enhancement factor (Fig. 2.3 c). While the average response over the frequency spectrum of a broadband pulse is described well by a carrier-envelope offset, details of the relative phase of the frequency response can be probed by an incoming spectrum containing more than one maximum, as is the case for a two-color pulse (Fig. 2.3 d,h). The difference in frequency response between the first harmonic (1600 nm, $\text{arg}(F/F_0) \sim 0.4\pi$) and the second harmonic (800 nm, $\text{arg}(F/F_0) \sim 0.25\pi$) leads to qualitatively different temporal pulse shape compared to the incoming pulse.

2.6 Dependence of field enhancement on tip geometry

We investigate the dependence of the field enhancement and phase shift at the apex of a tungsten nano-tip at optical frequencies on the geometry of the tip near the apex. The two main parameters are the tip radius R_{tip} and the tip half opening angle α_{tip} (inset of Fig. 2.4 c). For typical experimental tip parameters $R_{\text{tip}} \sim 10$ nm and $\alpha_{\text{tip}} = 0 - 5$ deg, the complex field enhancement factor is about $5 \cdot \exp(i0.25\pi)$. While the field enhancement does not depend strongly on the tip geometry for small opening angles (Fig. 2.4), we find somewhat surprisingly that both field enhancement and phase shift change strongly if the tip opening angle is substantially increased to 20 deg or larger. For all radii, the field enhancement increases with increasing opening angle and has a broad maximum around 35-45 deg for sharp and blunt tips respectively. The increase in field enhancement is not specific to tungsten and qualitatively similar results can be obtained for gold nanotips (see appendix A).

Investigating the mechanism for this increase of field enhancement, we first rule out the influence of propagation effects on the micrometer scale. Within the BEM, we resolve the contributions from the various surface elements along the tip shank towards the field enhancement at the apex. Furthermore, we compare the fully retarded sum including propagation effects to the Hartree approximation, i.e. the electrostatic field due to the induced surface charge. We find that only the surface charge near the tip apex on a length scale of up to $\lambda/4$ contributes appreciably to the field enhancement, and that the Hartree approximation gives field enhancement values similar to the fully retarded field enhancement including the dependence on the tip opening angle. From these observations we infer that the mechanism of field enhancement does not rely on retardation of the electric field and is localized at the tip apex. This is corroborated by calculations with a different incoming field, a point dipole located at some distance in front of the tip axis oriented along the tip axis, that yields a similar dependence of field enhancement on the tip opening angle as our calculations for a tip in a Gaussian beam. Our results are in agreement with the work of Bladel [1996] and Goncharenko et al. [2006] who studied the Laplace equation near a conical singularity and who also found that maximum field enhancement is attained for cones with non-zero opening angles. In our simulations, we find that the charge density distribution along the tip shaft is similar for all opening angles, extending about $\lambda/4$ along the tip shaft. We investigate the effect of this induced surface charge on the enhanced near-field at the apex within a simple quasi-static model taking into account the geometric parameters of the tip. We assume that the induced surface charge along the tip shaft is constant and extends up to a distance of about $\lambda/4$ from the apex. The surface charge σ_0 is set to the surface charge induced on an infinitely extended surface in an electric field $E_0 \sin(\alpha)$ perpendicular to the surface where α is the tip semi-angle given by $\sigma_0 = E_0 \sin(\alpha)(1 - 1/\epsilon)$. The resulting field at the apex is given by (see

Fig. 2.4d inset)

$$\begin{aligned}
 E^{\text{apex}} &= \int_S d^2S \sigma_0 \frac{\mathbf{r}}{|\mathbf{r}|^3} = \\
 &= E_0 \hat{z} (1 - 1/\epsilon) (\pi/2) \ln \left(\frac{z_2}{z_1} \right) \sin^2(2\alpha) \quad (2.9)
 \end{aligned}$$

where S denotes the surface of the tip shank between $z_1 \sim R_{\text{tip}}$ and $z_2 \sim \lambda/4$ and \hat{z} is the unit vector along the tip axis. This model predicts an increase in field enhancement up to an angle of 45 deg in good qualitative agreement to the full calculations. We thus interpret the field enhancement for tungsten as a geometrical effect that relies on the interplay between magnitude of induced surface charge σ_0 and the distance of the induced surface charge to the apex (second factor in the integrand). The amplitude of the angle-dependent field enhancement is estimated as $(1 - 1/\epsilon)(\pi/2) \ln(z_2/z_1) \sim 6$ for $z_1 = 5$ nm and $z_2 = 200$ nm, in reasonable agreement to the calculated value of ~ 8 for W tips with $R_{\text{tip}} = 5$ nm and decaying for smaller tip radii. The dielectric function of the material enters only into the factor $(1 - 1/\epsilon) \sim 1$ for $|\epsilon| \gg 1$, indicating that this mechanism is nearly independent of the dielectric function. The CEP shift does not depend strongly on the tip opening angle except for very sharp tips.

2.7 Near-field around a pair of nano-tips

While a single nano-tip is a prototypical system for investigating field enhancement at nano-structures, a pair of tips can serve as a test system for a well-controlled nano-junction [Savage et al., 2012] or can be investigated as a prototype system for tip-based sensing applications. In this section, we investigate how the electromagnetic near field around a nano-tip changes due to the presence of a second nano-tip entering the laser focus (Fig. 2.5a).

The near field enhancement is localized around the tip apex and decays on the length scale of the tip radius (Fig. 2.5a) in qualitative agreement to the field enhancement around a single nanotip (Fig. 2.2). We investigate the dependence of field enhancement and phase shift on the distance d_{tip} between the apexes (Fig. 2.5 c,d). For tip distances much larger than the tip radius, field enhancement and phase shift of a single tip are recovered at the tip apex while the field enhancement and phase shift vanish in the center of the gap that coincides with the laser focus.² As the distance between the tips is decreased and enters the order of magnitude of the tip radius, the field between the tips becomes more homogeneous until the values for the field at the tip and in the gap coincide below $d_{\text{tip}} \lesssim 5$ nm. The entrance of a second tip induces an additional field enhancement and phase shift on the surface of the first tip that become apparent at $d_{\text{tip}} \lesssim 50$ nm and $d_{\text{tip}} \lesssim 200$ nm respectively for $R_{\text{tip}} = 20$ nm.

²The drop of the field enhancement for $d_{\text{tip}} > 2$ micron comes about as the tips move out of the laser focus.

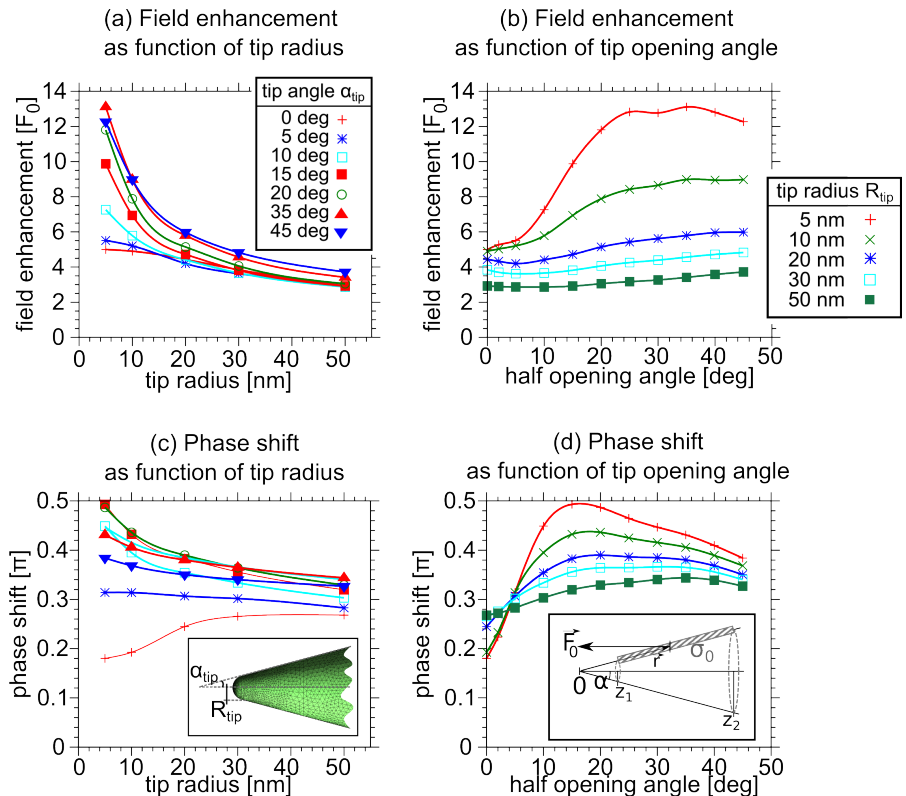


Figure 2.4: Geometry dependence of near-field response of tungsten nanotips. (a) Field enhancement as function of tip radius. All data presented refer to a tungsten nanotip illuminated by a 800 nm laser. (b) Field enhancement as function of tip half opening angle. (c) Phase shift as function of tip radius. **Inset:** Typical tip geometry with tip half opening angle α_{tip} and tip radius R_{tip} . (d) Phase shift as function of tip half opening angle. **Inset:** Geometry for the electrostatic model of field enhancement. The electric field F_0 polarized along the tip axis \hat{z} induces a surface charge σ_0 along the tip shank (gray hatched area) between z_1 and z_2 .

Therefore, a second tip can be used to control the carrier-envelope phase of the local electric field on the surface of a nanotip even when the tips are still hundreds of nm apart. At closer distances, a second tip can provide additional field enhancement when it is closer than $\sim R_{\text{tip}}$. At very close tip distances on the nm scale, we numerically find that the field enhancement increases as $\sim d_{\text{tip}}^{-3/4}$. Microscopic calculations including smearing out of the polarization charge on the quantum mechanical length scale based on time-dependent density functional theory [Zuloaga et al., 2009, 2010; Stella et al., 2013; Zhang et al., 2014] suggest a saturation of field enhancement and the onset of chemical bonding on the length scale of 0.5 nm. Both field enhancement and phase shift change only slowly as a function of tip distance, indicating the absence of resonances for the “open” tip-tip geometry.

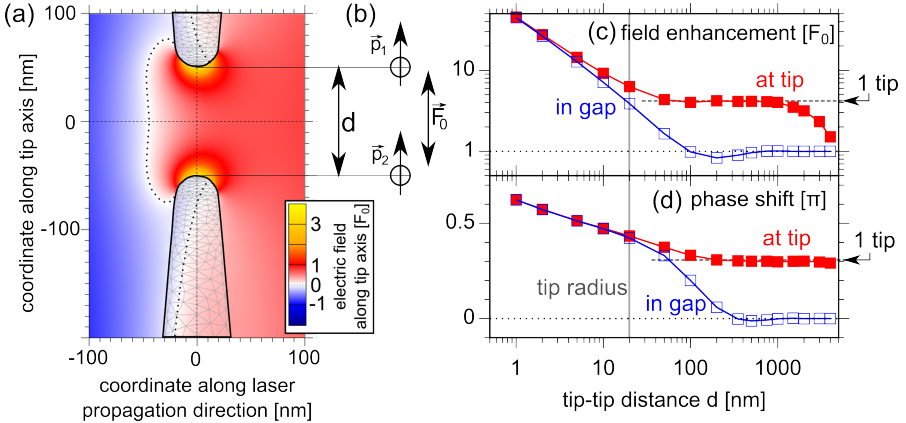


Figure 2.5: Near field around a pair of nano-tips. (a) Snapshot of near-field enhancement around a pair of tungsten nano-tips of radius 20 nm and opening angle 5 deg at laser wavelength 800 nm with a gap $d = 100$ nm. Field component along the tip axis $\text{Re}(F_{\parallel}(\mathbf{r}))$ as color contours. The mesh used for discretization of the tip surface is superimposed (thin grey lines). (b) Sketch of simplified model consisting of two dipoles in an electric field (details see text). (c) Field enhancement as function of tip distance d . Red full squares: field enhancement at tip surface (the drop for $d_{\text{tip}} \gtrsim 2$ micron comes about as the tips move out of the laser focus). Blue open squares: field enhancement in center of gap. Grey line: tip radius ($R_{\text{tip}} = 20$ nm). (d) Phase shift as function of tip distance d . Red full squares: phase shift at tip surface; blue open squares: phase shift in center of gap.

To understand how a second tip causes a shift in the carrier-envelope phase depending on the distance d_{tip} between the tips, we consider a simplified system that can be interpreted as the most basic discrete dipole approximation [Gullans et al., 2012; Sheikholeslami et al., 2010; Draine and Flatau, 2012]. The tips are replaced by point dipoles \mathbf{p}_1 and \mathbf{p}_2 to model the far field of a nano-tip for $d_{\text{tip}} \gg R_{\text{tip}}$ and we consider a homogenous quasi-static incoming field \mathbf{F}_0 where a time dependence $\exp(i\omega t)$ is implied in the following (Fig. 2.5b). We neglect retardation effects, which is valid for $d_{\text{tip}} \ll \lambda \sim 800$ nm. The strength of dipole \mathbf{p}_1 is proportional to the total electric field at its position, which is the sum of the external field plus the field from the other dipole \mathbf{p}_2 . The proportionality constant is the effective polarizability α of the nano-tip [Bouhelier et al., 2003] which is proportional to the near field enhancement and can be complex:

$$\mathbf{p}_1 = \alpha \mathbf{F}_{\text{tot}} = \alpha (\mathbf{F}_0 + \mathbf{F}(\mathbf{p}_2)) , \quad (2.10)$$

and likewise for \mathbf{p}_2 . The dipole field due to \mathbf{p}_1 at position \mathbf{r} is

$$\mathbf{F}_{\text{dip}}(\mathbf{r}; \mathbf{p}_1) = -\frac{\mathbf{p}_1}{r^3} + 3\frac{\mathbf{p}_1 \cdot \mathbf{r}}{r^5} \mathbf{r} \quad (2.11)$$

so that the self-consistent equations for the dipoles \mathbf{p}_1 and \mathbf{p}_2 on the tip-tip axis read

$$p_1 = \alpha \left(F_0 + 2p_2/d^3 \right) = p_2 \quad (2.12)$$

where the second equality follows from symmetry and thus

$$p_2 = F_0 \cdot \alpha \frac{1}{1 - 2\alpha/d^3} . \quad (2.13)$$

The effective polarizability or field enhancement factor (factors after the dot in Eq. 2.13) is thus changed by the self-consistent near field of both tips (fraction in Eq. 2.13). We investigate Eq. 2.13 in the far field region where $d \gg R_{\text{tip}}$. The polarizability of a sphere of radius R_{sphere} is given by $\alpha = R_{\text{sphere}}^3 \cdot \tilde{\alpha}$ where the reduced polarizability $\tilde{\alpha} = (\epsilon - 1)/(\epsilon + 2)$. For typical experimental values of ϵ of tungsten or gold, $|\epsilon| \gg 1$ and $\tilde{\alpha} \sim 1 + 1/\epsilon$ is a complex number of magnitude ~ 1 and thus $2\alpha/d^3 \ll 1$ for tip distances much larger than the sphere radius so that we expand

$$p_2 \sim F_0 \alpha \left(1 + 2\alpha/d^3 + \dots \right) . \quad (2.14)$$

Eq. 2.14 shows that for a complex field enhancement factor for a single nanotip α , we can expect an increased field enhancement and an additional retarding phase shift as a consequence of the second tip that sets in as the separation d between the tips becomes a few times the tip radius in agreement to the full calculation (in Fig. 2.5, $R_{\text{tip}} = 20 \text{ nm}$).

2.8 Conclusions and outlook

In this chapter, we have discussed the mechanism for field enhancement at nano-structures and have presented simulation results for field enhancement at nano-tips. In all cases, the region where the electric field is enhanced is restricted to a nanometric region around the apex of the tip, where strongly non-linear processes may occur for sufficiently high laser intensities. We found that the tip enhances the incoming laser field by approximately a factor of 5 and that this enhancement does not vary strongly with geometrical parameters and laser wavelength for slim tips that are employed in present experiments. However, we found that field enhancement increases strongly with increased tip opening angle, which has so far not been explored experimentally. Additionally, we found a phase shift in the response of the near field at the tip apex, which has the effect of a carrier-envelope-phase shift for few-cycle laser pulses, and is typically of the order of 0.25π . We also investigated the near-field distribution around a pair of nano-tips and found that the interaction between the induced dipoles at the tip apexes leads to an additional field enhancement and phase shift as the distance between the tips is reduced below a few times the tip radius.

Future work on the electromagnetic near-fields of nano-tips will extend the above analysis to other laser polarizations. For linear laser polarization perpendicular to the tip axis, a much larger part of the nano-tip will experience field enhancement, and due to the confined geometry perpendicular to the tip axis resonances can be expected possibly leading to high field enhancements. Such resonances somewhere

along the tip shaft can lead to excitations that propagate towards the tip apex, leading to new spatio-temporal near field shapes. Notably, while a laser polarization along the tip axis leads to surface plasmon excitations which are symmetric with respect to the tip axis, excitations created by a linearly polarized laser pulse perpendicular to the tip axis are antisymmetric with respect to the tip axis. Employing circular or elliptical polarization can mix both symmetries and could lead to new and unexpected effects. A grating at the tip shaft can be added such that plasmons are excited that propagate towards the apex [Giugni et al., 2013], possibly leading to constructive interference at the apex and even higher field enhancements.

Electron emission and rescattering from metal nano-tips by intense few-cycle laser pulses

3.1 Introduction

In this chapter, we turn from the study of time and space dependent electric fields near a metal nanostructure to the effect that this field has on the electronic system of the nanostructure. At low laser intensity, the response is linear and macroscopically described by the Maxwell equations. As the laser intensity is increased, nonlinearities in the response appear. At high laser intensity, the time-dependent electric field at the tip can lead to photoemission of electrons from the apex of the tip. This strong-field photoemission will be the main topic of this chapter.

Since the early days of quantum physics, the study of electron emission from solids by static or time-dependent electric fields has been a cornerstone for understanding the electronic structure and dynamics of matter and the interaction of electric fields with matter. Electron emission from surfaces by static fields (Fowler–Nordheim tunneling) is governed by the strength of the electric field at the surface [Fowler and Nordheim, 1928]. The number of emitted electrons per unit time increases exponentially with increasing field strength. The underlying idea is an electron tunneling through a barrier where the tunneling rate decreases with increasing barrier width. This picture is fundamentally different to the picture put forward by Einstein [1905] in his landmark paper on the photoelectric effect. There, electron emission had been found to be governed by the photon energy and the light intensity at the surface, proportional to the second power of the electric field, as explained by first-order time-dependent perturbation theory (Fermi’s golden rule). Higher order transitions, that correspond to the absorption of more than one photon by the electron and scale more

non-linearly with the intensity to the power of the number of photons absorbed, were first observed by Agostini et al. [1979] and have been called “above-threshold ionization”. The analogous process in solids, called “above-threshold photoemission”, was first reported by Luan et al. [1989]. The first theory that could explain the transition between these different regimes from a power law to exponential dependence on the amplitude of the applied electric field was put forward by Keldysh [1965] who combined the photon energy ω , the binding energy (work function) W of the electron, and the field strength F_0 of the applied electric field into the dimensionless Keldysh parameter,

$$\gamma = \frac{\omega\sqrt{2W}}{F_0} = \sqrt{\frac{W}{2U_p}} \sim \frac{T_{\text{tunnel}}}{T_{\text{field}}}, \quad (3.1)$$

where the ponderomotive energy $U_p = (F_0/2\omega)^2$ is the average kinetic energy of a free singly-charged test particle initially at rest in an oscillating field $F_0 \sin(\omega t)$. The Keldysh parameter was originally motivated by a semi-classical picture of tunneling, where γ was interpreted as the ratio between the laser period and the semi-classical time scale of the tunneling process, the “tunneling time” it would take an electron of (Kepler) velocity $\sim \sqrt{W}$ to pass the tunneling barrier of length W/F_0 . To this date and especially in the light of recent experiments that have striven to make the “tunneling time” experimentally accessible [Eckle et al., 2008b; Pfeiffer et al., 2012; Shafir et al., 2012], the notion of a “tunneling time” is a subject of controversy. It has, however, been experimentally assessed that the Keldysh parameter governs the transition from a tunneling-like ionization process [Uiberacker et al., 2007] at $\gamma \ll 1$ dominated by ionization bursts around the field maxima towards the multi-photon regime at $\gamma \gg 1$ where the sub-cycle ionization dynamics eventually level out [Yudin and Ivanov, 2001].

Direct observation of the predicted dynamics within the time scale of a laser period became possible with the advent of modern laser technology around the turn of the millennium. Nowadays, advanced laser sources provide intense few-cycle laser pulses with a reproducible electric field $F(t)$ under the envelope. Fine-tuning of the pulse shape enables steering the electron motion on the atomic length and time scale and elicits highly non-linear response like above-threshold photoionization, high-harmonic generation, rescattering, and non-sequential double ionization [Mulser and Bauer, 2010; de Morisson Faria and Liu, 2011; Becker et al., 2012]. Often, this highly non-linear response can be understood with the semi-classical “three-step” or “simple man’s” model of strong-field physics pioneered by Corkum [1993] and Schafer et al. [1993] and developed further by Lewenstein et al. [1994, 1995]. First, the electron is ionized around the maxima of the electric field by a tunneling-like process that leaves the electron with zero velocity in the continuum. Secondly, the motion of the electron after ionization is governed by the laser field and can be understood through classical trajectories. Depending on the pulse shape and time of ionization, the electron can be driven back towards the parent matter, where the recolliding (rescattering) electron in a third step undergoes highly non-linear pro-

cesses leading to the emission of high-energy electrons, high-energy photons (high harmonic generation) or multiple ionization of the parent matter by electron-electron scattering (non-sequential double ionization). It is the delicate interplay of the ionization dynamics concentrated around the maximum of the laser field together with the trajectory of the electron in the continuum that provide the mechanism leading to a timing structure shorter than the time scale of the driving laser field.

Although Einstein's photoeffect, Fowler-Nordheim tunneling, and in part Keldysh's theory had originally been formulated for solid-state systems, studies of electron motion driven by intense few-cycle laser pulses and the ensuing highly non-linear response have been performed mostly on gas-phase targets of atoms and molecules with a focus on rare-gas atoms [Paulus et al., 1994]. Recently, pioneering studies on solid-state density targets have been performed on dielectric nanospheres [Zherebtsov et al., 2011, 2012], bulk semiconductors [Ghimire et al., 2011a; Zaks et al., 2012], and bulk insulators [Gertsvolf et al., 2008, 2010; Mitrofanov et al., 2011; Schiffrin et al., 2013; Schultze et al., 2013]. High-order non-linear surface response has been predicted to occur [Faisal et al., 2005]. So far, the exploration of strong-field physics at solid metal surfaces has remained elusive mainly due to two reasons. Firstly, the range of usable intensities is restricted due to the surface damage threshold which is determined, on one hand, by the lower work function of metals compared with the ionization potential of atoms and, on the other hand, by the efficiency of heat transport away from the surface that inhibits destruction of the surface by ablation. Secondly, the spatial area where non-linear processes occur is determined by the spot size of the laser on the surface which is at least of the order of μm for visible radiation, and for grazing incidence where the polarization vector can be oriented along the surface normal the spot size is much larger. Even if the incoming laser pulse shape is well-defined, the reflection of the light wave on the surface in a complicated interference pattern leads to intensity and carrier-envelope phase averaging over the mesoscopic spot size. Most likely this is the main reason why predicted carrier-envelope phase sensitivity [Lemell et al., 2003] has been observed only at a very low contrast level [Apolonski et al., 2004; Dombi et al., 2004].

Both problems can be avoided when employing a nano-tip instead of a flat surface as a target for few-cycle laser pulses. The sub-wavelength apex of a nano-tip leads to field enhancement triggering non-linear processes on a surface area of nanometric dimensions, overcoming focal averaging. Importantly, we have shown in chapter 2 that the shape of an ultrashort pulse at the apex is conserved up to an enhancement factor and a carrier-envelope phase shift, so that the electrons at the surface of the tip are exposed to a well-controlled laser field. Since only a very small area at the apex of the tip is exposed to high field strengths, the nano-metric hot-spot is efficiently cooled by the tip shank and thermal electron emission is suppressed. Moreover, the enhancement of the laser intensity by up to two orders of magnitude allows to employ a low-power laser oscillator instead of an amplified laser system, yielding repetition rates in the 100 MHz range that allow for good statistics and a high dynamical range

in the recorded electron spectra. The combination of these properties makes nano-tips an ideal test bed for studying strong field physics at metal surfaces. Starting with the discovery that high-order multi-photon electron emission from a metal nano-tip could be observed [Schenk et al., 2010], a flurry of research activity revolving around the strong-field emission and steering of electrons near metal nano-tips has emerged [Bormann et al., 2010; Krüger et al., 2011; Park et al., 2012; Krüger et al., 2012; Herink et al., 2012; Wachter et al., 2012, 2013, 2014a; Thomas et al., 2013; Wimmer et al., 2014; Piglosiewicz et al., 2014]. A representative electron spectrum measured by Krüger et al. [2012] is shown in Fig. 3.1. Two very interesting and at first sight unexpected features are apparent. Firstly, the exponentially decaying energy spectrum is modulated by equi-spaced peaks at multiples of the photon energy, the signature of coherent quantum surface dynamics leading to multi-photon electron emission in the strong-field regime. Secondly, the spectra show a large-scale modulation at intermediate to high electron energies where the decay is substantially slower than at low electron energies up to a certain cut-off value.

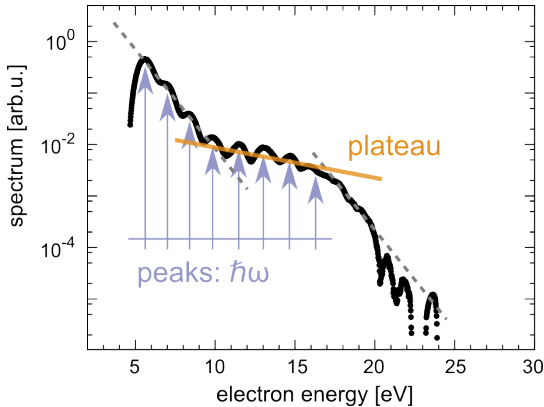


Figure 3.1: Experimental electron spectrum [Krüger et al., 2012]. Exponential decay (dashed lines) at low and high electron energies. Superimposed are multi-photon peaks (arrows) and a plateau at intermediate to high electron energies (full line).

We begin this chapter with an intuitive semi-analytical model based on the simple man’s model that can account for the qualitative features of the electron spectra observed in experiment (section 3.2). The multi-photon peaks are traced back to periodic bursts of electron emission around the maxima of the laser field, and the plateau is traced back to the elastic backscattering of electrons from the topmost layer of surface atoms that are driven back towards the surface as the laser field changes its sign. We then present our microscopic simulation of the quantum surface dynamics driven by intense few-cycle laser pulses with time-dependent density functional theory in section 3.3. In the remainder of the chapter, we present results obtained by the semi-analytical model and the quantum simulations and compare them to exper-

imental results where available. We first introduce the physics at play discussing a sample simulation run in detail (section 3.4) and discuss the appearance of the plateau with increasing laser intensity (section 3.5). The sensitivity to the details of the laser pulse shape and the accuracy of our theory is demonstrated by a comparison with carrier-envelope phase resolved experimental data in section 3.6. Our quantum mechanical simulation of surface dynamics resolves the microscopic electric field near a metal surface including the self-consistent screening of the incoming light field, an observable that has only recently become accessible to experiment with the advent of attosecond surface streaking (section 3.9). After verifying the accuracy of our simulation by comparison with experimental results, we explore in the remainder of the chapter parameter regimes where no experimental data is available yet. We discuss the transition from the multiphoton to the tunneling regime by varying the laser wavelength (section 3.8), possible traces of the surface potential in the spectra of the photoemitted electrons (section 3.9), and we critically discuss possible high harmonic emission (section 3.10).

3.2 Simple man's model for nanostructures

In this section³, we discuss the quantum surface dynamics leading to the observed features in the electron spectra, that is to the equispaced interference peaks across the whole spectral range and the plateau at intermediate to high energies. This phenomenological description can be viewed as an extension of the simple man's model [Corkum, 1993; Schafer et al., 1993; Lewenstein et al., 1994, 1995] to metal nanotips and, possibly, other nanostructures. Despite the increased complexity of a metal nanostructure compared to an atomic gas target, several geometrical and dynamical properties allow simplifications that result in a model that is even simpler than its atomic analogue. This remarkable simplicity underscores that metal nanotips may serve as a favorable testing ground for strong field processes.

A key ingredient is the local field at the surface of the nano-tip. The enhanced near field is confined to the apex of the tip and varies on the length scale of the tip radius $R_{\text{tip}} \sim 10$ nm, much smaller than the laser wavelength $\lambda \sim 800$ nm. Strongly non-linear electron emission is thus also confined to a spot of size $\sim R_{\text{tip}}$, which is, however, still much larger than the characteristic length of the electron wave functions (Fermi wavelength $\lambda_{\text{F}} \sim 0.1$ nm). The translational symmetry of the electron subsystem in the surface plane is approximately conserved, allowing for a quasi one dimensional treatment with the surface normal as reaction coordinate. For typical experimental parameters, a wavelength of $\lambda = 800$ nm and an effective intensity $I_{\text{eff}} = 2 \times 10^{13}$ W/cm², the quiver radius of a classical point charge in a harmonic laser field of frequency ω is $\alpha_{\text{quiver}} = F_{\text{eff}}/\omega^2 \sim 0.4$ nm $\ll R_{\text{tip}}$ where the effective field strength at the surface includes field enhancement and throughout this

³This section is an adapted and expanded version of the original description given by the author and co-workers in section 3 of Krüger et al. [2012].

monograph we convert between the peak electric field and the peak laser intensity $I_{\text{eff}} = (c/8\pi)F_{\text{eff}}^2$ of a linearly polarized laser pulse as

$$F_{\text{eff}} [\text{a.u.}] = 5.338 \times 10^{-9} \sqrt{I_{\text{eff}} [\text{W}/\text{cm}^2]} \quad (3.2)$$

As the quiver radius is much smaller than the length scale where the local field varies, we treat the laser field as homogeneous. Since the quiver radius scales as $\alpha_{\text{quiver}} \propto \lambda^2$, this simplification would no longer be valid for wavelengths in the far IR where the electrons can escape the near field even during one optical cycle [Herink et al., 2012].

The second key ingredient is the screening of the electric field inside the solid (compare Fig. 2.1 and Fig. 2.2 for the near-field distribution calculated by the Maxwell equations; the quantum-mechanical screening of the electric field on the atomic length scale will be discussed in section 3.7). The key result entering the model presented in the following is that the electric field component along the surface normal is screened within only a few a.u., leading to a drastic reduction of possible pathways for emitted electrons to reach the detector compared to atomic gas targets.

The simple man's model for nanostructures (SMMN, Fig. 3.2) assumes that electrons are photo-emitted around the maximum of the laser force and are subsequently driven away from the tip. A fraction of them is driven back towards the surface as the laser field changes sign and can be rescattered from the topmost layer of atoms. Thereby, they receive an additional momentum kick propelling them to higher final energies after the laser pulse. These rescattered electrons lead to the plateau and cut-off structures at high electron energies. Interferences in the energy spectra develop as the process is quasi-periodically repeated after multiples of the optical cycle $T = 2\pi/\omega$. These processes can be conveniently parameterized in a single-active electron model by a linear combination of Gaussian wave packets for the direct and rescattered wave packets and the classical trajectories followed by their expectation values according to Ehrenfest's theorem, permitting an analytical description of the shape of the experimentally observed spectra.

The time-dependent Schrödinger equation for an electron described by the wave function $\psi(p, t)$ in momentum space for a laser pulse in dipole approximation in velocity gauge with a time-dependent vector potential $A(t) = -\int_{-\infty}^t F_{\text{eff}}(t') dt'$ reads

$$i \frac{d}{dt} \psi(p, t) = \frac{(p + A(t))^2}{2} \psi(p, t) \quad (3.3)$$

where the instantaneous velocity (kinetic momentum) v is related to the (canonical) momentum p as $v = p + A(t)$. The time evolution of a wave function from time t_1 to t_2 is given by the Volkov propagator [Volkov, 1935]

$$\psi(p, t_2) = \exp(-iS_p(t_2, t_1)) \psi(p, t_1) \quad (3.4)$$

where the phase

$$S_p(t_2, t_1) = \int_{t_1}^{t_2} dt \frac{1}{2} (p + A(t))^2 \quad (3.5)$$

is the integral of the classical action. Quantum-classical correspondence is invoked here on two different levels. First, according to Ehrenfest's theorem the time evolution of the expectation values of velocity and position

$$\langle v(t_2) \rangle = \langle v(t_1) \rangle - A(t_1) + A(t_2) \quad (3.6)$$

$$\langle x(t_2) \rangle = \int_{t_1}^{t_2} \langle v(t') \rangle dt' + \langle x(t_1) \rangle \quad (3.7)$$

follow Newton's equations of motion for a point charge in a laser field. Secondly, according to (3.4), the *individual momentum components* p of a wave function acquire a phase according to their time-dependent kinetic energy $v^2/2 = (p + A(t))^2/2$, which in turn is that for a classical point charge following Newton's equations of motion (3.6).

It is instructive to analyze the terms contributing to the phase according to the action integral (3.5) for a monochromatic vector potential, $A(t) = -(F_{\text{eff}}/\omega) \sin(\omega t)$,

$$S_p(t_2, t_1) = \left\{ \frac{p^2}{2} t + \alpha_{\text{quiver}} p \cos(\omega t) + U_p \left[t - \frac{1}{2\omega} \sin(2\omega t) \right] \right\} \Big|_{t_1}^{t_2}. \quad (3.8)$$

In addition to the first term associated with the kinetic energy, the momentum components acquire phases associated with the quiver motion of amplitude $\alpha_{\text{quiver}} = F_{\text{eff}}/\omega^2$ in the laser field. By virtue of the last term they experience an additional constant and a time-dependent energy shift proportional to the ponderomotive energy, $U_p = (F_{\text{eff}}/2\omega)^2$.

We now turn to modeling electron emission and rescattering according to the simple man's model. We consider the time evolution of a Gaussian wavepacket (ignoring normalization) launched at time t_1 with expectation value p_1 and momentum width σ_p ,

$$\psi_G(p, t, t_1) = e^{-(p-p_1)^2/4\sigma_p^2} e^{-iS_p(t, t_1)} e^{+i|W|t_1}, \quad (3.9)$$

with a Gaussian momentum spectrum centered at the initial velocity $v_1 = p_1 + A(t_1)$. Prior to the emission at t_1 , the evolution of a bound state at the Fermi energy E_F is determined by the initial energy $-W$ with respect to vacuum (work function $W > 0$), while the subsequent time evolution is given by Eq. 3.4.

The probability for electron emission is highest around the maximum of the electric field ("direct part"). For electrons emitted by tunneling, we expect zero velocity at the tunnel exit, and vanishing vector potential since the force has an extremum, so that in Eq. 3.9 $p_1 = 0$,

$$\psi_d(p, t, t_1) = e^{-p^2/4\sigma_p^2} e^{-iS_p(t, t_1)} e^{+i|W|t_1} \quad (3.10)$$

and the associated momentum spectrum after the end of the pulse is

$$|\psi_d(p)|^2 = e^{-p^2/2\sigma_p^2} \quad , \quad (3.11)$$

i.e., an exponentially decaying spectrum as function of the energy $E = p^2/2$ with decay constant $1/\sigma_p^2$. An estimate for the longitudinal momentum distribution σ_p of emitted electrons for a given Keldysh parameter $\gamma = \sqrt{2W}\omega/F_{\text{eff}}$ has been given by Popov [1999]. It reduces to the ADK formula [Ammosov et al., 1986] in the tunneling regime $\gamma \ll 1$:

$$P(p) = P_0 \exp\left(-p^2 c_1(\gamma)/\omega\right) \quad (3.12)$$

with

$$c_1(\gamma) = \text{ArcSinh}(\gamma) - \gamma(1 + \gamma^2)^{-1/2}. \quad (3.13)$$

Consequently, $\sigma_p^2 = \omega/2c_1(\gamma)$. Inserting the experimental values for the work function ($W \simeq 4.5 - 6$ eV) and the effective electric field ($F_{\text{eff}} \simeq 0.02$ a.u. from the position of the cut-off, see below) we obtain for the width $\sigma_p \simeq 0.26 - 0.23$ a.u. in good agreement with the experimental spectrum of low-energy electrons of $\sigma_p = 0.225$ (Fig. 3.2b).

Subsequently, part of the emitted electron wave packet is driven back towards the surface as the laser field changes its sign. We incorporate elastic scattering from the first layer of surface atoms (“rescattering”) by making the approximation that all components of the wave packet emitted at t_1 and returning to the surface are elastically scattered at the same time t_2 , reversing the velocity (or kinetic momentum $p + A(t_2)$) $v(t_2) \rightarrow -v(t_2)$. This gives rise to a displacement of the wave function in momentum space

$$p(t \rightarrow t_2^+) = -p(t \rightarrow t_2^-) - 2A(t_2). \quad (3.14)$$

The reflected Gaussian wave packet ψ_r tunneled at t_1 and reflected at t_2 accordingly reads

$$\psi_r(p, t, t_2, t_1) = e^{-[p+2A(t_2)-A(t_1)]^2/4\sigma_p^2} e^{+iW|t_1} e^{-iS_{-p-A(t_2)}(t_2, t_1)} e^{-iS_p(t, t_2)}. \quad (3.15)$$

Its momentum spectrum after the conclusion of the laser pulse is then

$$|\psi_r(p)|^2 = \exp\left(- (p + 2A(t_2) - A(t_1))^2 / 2\sigma_p^2\right) \quad , \quad (3.16)$$

a Gaussian with displaced average momentum

$$p_r = \langle \hat{p} \rangle = 2A(t_2) - A(t_1) \quad (3.17)$$

depending on the moment of emission and rescattering according to Newton’s equation of motion (3.6). The classical cut-off energy derived in the simple man’s model for atoms follows from maximizing (3.17) while constraining the rescattering time t_2 to times where the wavepacket emitted at t_1 is in the vicinity of the surface $\langle x(t_2) \rangle =$

0, yielding for a harmonic vector potential $p_r = \max(2A(t_2) - A(t_1))$

$$p_r^2/2 = 10.0 \cdot U_p \quad (3.18)$$

with optimal emission time $t_1 = 0.0415 \cdot T$ and rescattering time $t_2 = 0.727 \cdot T$. These electrons rescatter with an energy of $E_{\text{scat}} \approx 3.1U_p$, while the electrons that rescatter with the highest velocity ($E_{\text{max}} = 3.17U_p$), which are responsible for the classical cut-off energy for high harmonic radiation, have a slightly smaller final energy after the pulse.

Since the direct (d) and rescattered (r) portions of the wave function are well separated in momentum space, they can be added incoherently

$$|\psi(p)|^2 = |\psi_d(p)|^2 + |\psi_r(p)|^2 \quad (3.19)$$

without introducing a significant error. The relative weight between $|\psi_d(p)|^2$ and $|\psi_r(p)|^2$ can be used as a fit parameter. For suitable pulse shapes the overlap in momentum space between direct and rescattered parts could be increased, giving rise to additional interference effects. The plateau structure is associated with the rescattered electrons (Fig. 3.2). Our model predicts the momentum width σ_p of the direct and rescattered wave packets to be the same as there is no broadening process included. For the description of the experimental spectra, however, we find that the momentum width of the rescattered part is roughly twice as large as that of the direct part. Broadening could be accounted for by allowing for a distribution of rescattering times t_2 as different momentum components follow classical trajectories back to the surface, or by considering an ensemble of rescattering trajectories with emission times throughout the laser cycle. Another broadening mechanism would be the energy dependence of the backscattering amplitude, which could be included into the model by multiplying (3.15) by a reflection amplitude $R(p) \exp(i\delta(p))$ with scattering phase $\delta(p)$. Experimentally, the broadening of the emitted wave packet could be investigated by comparing the slope of the direct part (at low to intermediate electron energies) to the asymptotic slope of the rescattered part (at high electron energies), which will however require a substantial increase of the experimental dynamic range.

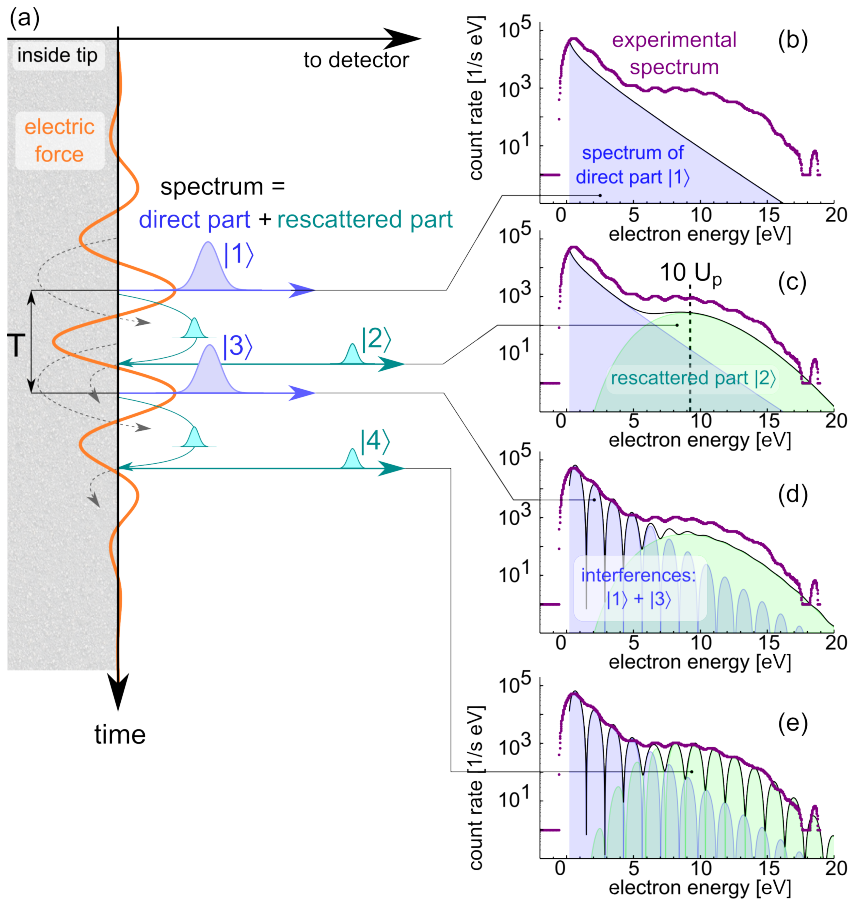


Figure 3.2: Simple man's model for nanostructures. (a) Sketch of the dynamics leading to the observed plateau and interference structures as described in the simple man's model for nanostructures. Orange line: laser electric force, blue: direct wave packets, green: rescattered wave packets, dashed lines: trajectories which are suppressed due to screening of the electric field at the surface of the tip. (b) Exponentially decreasing spectrum due to the first direct wave packet |1> (blue filled curves). (c) The plateau forms due to rescattering of the wave packet |2> (green filled curves). (d) The repetition of the electron emission after one optical cycle $T = 2\pi/\omega$ gives rise to interference fringes in the energy spectra between wave packets |1> and |3>. (e) The full spectrum also includes interferences between rescattered wave packets |2> and |4> and closely resembles the experimental spectrum (pink).

Having explained the formation of a plateau in the electron spectra by the rescattering of electrons from the top layer of surface atoms, we now turn our attention to the modulation by equidistant peaks spaced by the photon energy ω . Within our model, these peaks follow from a coherent superposition of otherwise identical wavepackets launched at times t_j delayed relative to each other by multiples of the laser period T

$$\psi_d^{\text{ATP}}(p, t) = \sum_j c_{d;j} \psi_d(p, t, t_j) . \quad (3.20)$$

For simplicity we restrict the sum in (3.20) to two terms (packets |1⟩ and |3⟩ in Fig. 3.2a). The total wave function for the direct part then reads (assuming a maximum of the electric field at $t = 0$)

$$\begin{aligned} \psi_d^{\text{ATP}}(p, t) &= c_{d;1} \psi_d(p, t, 0) + c_{d;2} \psi_d(p, t, T) \\ &= e^{-p^2/4\sigma_p^2} \left(c_{d;1} e^{-iS_p(T,0)} + c_{d;2} e^{+i|W|T} \right) e^{-iS_p(t,T)} . \end{aligned} \quad (3.21)$$

The propagation after the ejection of the second wavepacket ($t > T$) yields a global phase that drops out upon taking the absolute value (last term). The momentum spectrum is, upon evaluating $S_p(T, 0)$ for the vector potential (3.8),

$$|\psi_d^{\text{ATP}}(p)|^2 = e^{-p^2/2\sigma_p^2} \left\{ c_{d;1}^2 + c_{d;2}^2 + 2c_{d;1}c_{d;2} \cos \left[\left(\frac{p^2}{2} + U_p + W \right) T \right] \right\} \quad (3.22)$$

giving rise to ATP peaks of multiphoton order n (Fig. 3.2d)

$$E_{\text{kin}} + U_p + W = n\omega . \quad (3.23)$$

Analogously, the train of rescattered wavepackets yields a momentum spectrum

$$|\psi_r^{\text{ATP}}(p)|^2 = e^{-(p-p_r)^2/2\sigma_p^2} \left\{ c_{r;1}^2 + c_{r;2}^2 + 2c_{r;1}c_{r;2} \cos \left[\left(\frac{p^2}{2} + U_p + W \right) T \right] \right\} \quad (3.24)$$

with the same interference phase (term in square brackets). We note that the precise value of the interference phase depends sensitively on the pulse shape (Eq. 3.8). For short pulses the shape of the electric field can change from one optical cycle to the next, influencing the timing between emission and rescattering and thus leading to an additional phase shift and a slightly different repetition time T in (3.24). In Fig. 3.2e, the phase shift is $\sim \pi/6$ and the repetition time is $\sim 0.93T$.

The resulting spectrum (Fig. 3.2e)

$$|\psi^{\text{ATP}}(p)|^2 = |\psi_d^{\text{ATP}}(p)|^2 + |\psi_r^{\text{ATP}}(p)|^2 \quad (3.25)$$

resembles the experimental data amazingly well. It should be noted that the SMMN can be used to investigate laser nanotip interaction along two different lines. Firstly, one can fit the experimental spectrum to Eq. 3.25 and deduce from the extracted value for p_r the effective field enhancement and, thereby, possibly even the tip geometry.

Here, the fit gives $p_r \approx 0.8$ and thus $F_{\text{eff}} = 0.021$ a.u. Conversely, one can use the field enhancement derived from the solution of Maxwell's equations near the tip, and predict the spectrum via Eqs. 3.18 and 3.25, thereby testing the ingredients of this elementary strong-field model. Its success hinges, in part, on the fact that, in contrast to above-threshold ionization spectra from single atoms, fewer classes of trajectories contribute to the total spectrum due to broken symmetry at the metal surface as the laser field is strongly screened inside the solid (Fig. 3.2a). On the one hand, electrons that return to the surface and enter into the bulk experience no further significant interaction with the laser field and do not contribute to the total spectrum. On the other hand, there are no trajectories launched towards the inside of the solid. In laser-atom interaction, trajectories taking off during the same cycle in opposite directions give rise to intra-cycle interferences [Arbó et al., 2006]. The reduction to only two types of trajectories for nanotip targets greatly simplifies the interpretation of electron spectra.

We briefly discuss how the SMMN maps the main physical parameters of the experiment, the strength and temporal shape of the laser electric field, onto properties of the electron spectra. The laser intensity or electric field strength F_{eff} affects the slope (width) σ_p of the direct and rescattered wave packets (Eq. 3.12) as well as the extension of the plateau up to $10 \cdot U_p = 10 \cdot F_{\text{eff}}^2 / 4\omega^2$. Accordingly, we expect that for low laser intensities the center of the plateau will move to lower electron energies until the plateau is submerged below the exponential slope of the direct part [Wachter et al., 2012; Krüger et al., 2012]. As the intensity increases and the ponderomotive energy U_p reaches the same order of magnitude as the photon energy ω , the effect of the laser intensity also becomes appreciable in the interference phase and the positions of the interference peaks (Eq. 3.23). This change of peak position with increasing laser intensity has been experimentally observed in Schenk et al. [2010] and has an intuitive interpretation in terms of channel closing. In addition to the energy W required for ionization, the laser electric field must also provide the wiggle energy U_p of a free electron in the laser field. The cut-off of the plateau around $10 \cdot U_p \propto \lambda^2$ can alternatively be increased by increasing the laser wavelength. While up to now no experimental data for larger wavelengths have become available, our quantum simulations display this behavior (section 3.8). The SMMN as presented here only includes two separate trajectories, one which starts at the field maximum and one which acquires the maximal rescattering momentum, so that the final spectrum consists of the linear combination of only two sets of Gaussian wave packets centered around 0 and $10U_p$ respectively. However, trajectories starting at other times can also contribute to the intermediate region that comprises the plateau extending from low electron energies up to $10U_p$. These additional trajectories can be incorporated into the SMMN by extending Eq. 3.20 into an integral over all possible emission times during the laser cycle.

Another parameter that can be fine-tuned in experiment is the carrier-envelope phase (CEP) of a few-cycle pulse. It changes the effective field during ionization

$F_{\text{eff}}(t_1)$ entering in Eq. 3.12 as well as the energy at rescattering. The final energy is large if the acceleration back to the surface is strong. Accordingly, we can expect that the energy spectra in the cutoff region show a strong modulation with the CEP, and that the largest number of high-energy electrons will be measured for $-\cos$ -pulses. This strong modulation with the CEP has been measured by Krüger et al. [2011].

In experiment, an additional weak static (dc) electric field is used to accelerate the electrons from the nano-tip into the electron detector. We inquire into the effect of an additional static field F_{dc} predicted by the SMMN. To leading order the static field will decrease the surface barrier height

$$W \rightarrow W(F_{\text{dc}}) = W - \sqrt{|F_{\text{dc}}|} \quad . \quad (3.26)$$

This leads to a lowering of the threshold for photoemission (Eq. 3.23) and to the appearance of an additional multi-photon peak below the zero-field threshold. In addition, through the dependence of the width of the longitudinal momentum distribution on W (Eq. 3.12), the presence of a static field F_{dc} broadens the tunneling momentum distribution and to a reduces the slope of the direct part of the spectrum. Finally, the SMMN predicts a (slight) decrease of the cut-off energy $E_{\text{cut}} \approx 10 \cdot (F_{\text{eff}} - |F_{\text{dc}}|)^2 / 4\omega^2$ since the presence of the dc field effectively reduces the kinetic energy and momentum of the returning electron at the moment of rescattering. All the predicted trends are in agreement with the experimental data and with quantum simulations [Krüger et al., 2012].

3.3 Microscopic model of electron emission with time-dependent density functional theory (TD-DFT)

After having put forward a semi-analytical model that accounts for the qualitative features observed in experiment, we present a quantitative model for the quantum surface dynamics including electron-electron interaction on the mean-field level based on time-dependent density functional theory (TD-DFT). We briefly review the theory (section 3.3.1) before we describe the implementation employed in the remainder of this chapter (section 3.3.2).

3.3.1 Pedestrian approach to TD-DFT

In the following we give a very brief introduction to TD-DFT. Further information is available from a wealth of textbooks [Parr, 1994; Fiolhais et al., 2003; Giuliani and Vignale, 2005; Marques et al., 2006; Ullrich, 2011; Marques et al., 2012] and review articles [Maitra et al., 2002; Onida et al., 2002; Parr and Sen, 2002; Chelikowsky et al., 2003; Marques, 2003; Marques and Gross, 2004; Castro et al., 2006; Yabana et al., 2006; Botti et al., 2007; Casida and Huix-Rotllant, 2012; Andrade et al., 2012; K. Yabana et al., 2013].

Time-dependent density functional theory [Runge and Gross, 1984] is a reformulation of non-relativistic quantum mechanics of time-dependent interacting many body systems. Its central quantity is the time-dependent electron density $n(\mathbf{r}, t)$, that is the probability of finding an electron at position \mathbf{r}

$$n(\mathbf{r}, t) = N \int d^3\mathbf{r}_2 \dots \int d^3\mathbf{r}_N |\Psi(\mathbf{r}, \dots, \mathbf{r}_N)|^2 \quad . \quad (3.27)$$

The integral over the density is the number of particles, $\int d^3\mathbf{r} n(\mathbf{r}, t) = N$, and the generalized space coordinate \mathbf{r} includes the spin degree of freedom. While the full wave function $\Psi(\mathbf{r}, \dots, \mathbf{r}_N)$ depends on $N \times 3$ coordinates in 3D space, the time-dependent density $n(\mathbf{r}, t)$ depends only on 3 coordinates, a tremendous simplification for systems with more than a few particles N . The central theorem of TD-DFT, the Runge-Gross theorem, states that despite this drastic simplification there is a one-to-one mapping between the time-dependent electron density $n(\mathbf{r}, t)$ and the time-dependent potential, i.e., the time-dependent Hamiltonian and thereby the solution of the full Schrödinger equation. Specifically, we consider the time-dependent Schrödinger equation (TDSE)

$$i\partial_t \Psi(\mathbf{r}_1 \dots \mathbf{r}_N, t) = H\Psi(\mathbf{r}_1 \dots \mathbf{r}_N, t) \quad (3.28)$$

with the Hamiltonian

$$H(t) = \sum_{j=1}^N \left\{ \frac{1}{2} \left[\frac{\nabla_j}{i} + \mathbf{A}_{\text{ext}}(\mathbf{r}_j, t) \right]^2 + V_{\text{ext}}(\mathbf{r}_j, t) \right\} + \frac{1}{2} \sum_{k,j \neq k}^N V_{\text{ee}}(\mathbf{r}_i - \mathbf{r}_k) \quad . \quad (3.29)$$

Here, $V_{\text{ext}}(\mathbf{r}_j, t)$ is the external scalar potential (typically the potential of the ionic cores and external electric fields) and $\mathbf{A}_{\text{ext}}(\mathbf{r}, t)$ is the external vector potential (typically representing external electric or magnetic fields). The electron-electron interaction is $V_{\text{ee}}(\mathbf{r}_i - \mathbf{r}_k) = 1/|\mathbf{r}_i - \mathbf{r}_k|$. For a given initial state, the TDSE maps the external potentials \mathbf{A}_{ext} and V_{ext} to the time-dependent wave function $\Psi(\mathbf{r}_1 \dots \mathbf{r}_N)$ and from there to the density $n(\mathbf{r}, t)$. The Runge-Gross theorem [Runge and Gross, 1984] and its extensions [van Leeuwen, 1999; Vignale, 2004] state that this map is invertible. Therefore, at least in principle, the external potential, the Hamiltonian, the many-body wave function, and all observables are functionals of the density (and the initial state). The analogous central theorem of static density functional theory is the Hohenberg-Kohn theorem [Hohenberg and Kohn, 1964] linking the static density to the static potential. The success of static and time-dependent DFT now hinges on finding a suitable way to (approximately) calculate the density without having to solve the full interacting TDSE. In static DFT, this is achieved by mapping the interacting system to an auxiliary noninteracting system [Kohn and Sham, 1965] for which $V_{\text{ee}} = 0$. For this auxiliary reference system the many-body wave function reduces to a single Slater determinant and the N -body Schrödinger equation reduces to N one-body equations. In TD-DFT, this map between the interacting system and an auxiliary non-interacting system is provided by the van Leeuwen theorem [van Leeuwen,

1999]. Accordingly, a non-interacting ($V_{ee} = 0$) initial state with the correct initial density and time derivative of the density is evolved to the correct time-dependent density by the potentials $V_{KS}(\mathbf{r}, t)$ and $\mathbf{A}_{KS}(\mathbf{r}, t)$ which are *unique* for a given density evolution. In general, the potentials are functionals of the time-dependent density including the density in the past, the initial many-body state, and the initial noninteracting state. The effective potentials are given as

$$V_{KS}[n](\mathbf{r}, t) = V_{\text{ext}}(\mathbf{r}, t) + V_H[n](\mathbf{r}, t) + V_{xc}[n](\mathbf{r}, t) \quad (3.30)$$

with the Hartree potential

$$V_H[n](\mathbf{r}, t) = \int d^3\mathbf{r}' \frac{n(\mathbf{r}', t)}{|\mathbf{r} - \mathbf{r}'|} \quad (3.31)$$

and similarly

$$\mathbf{A}_{KS}[n](\mathbf{r}, t) = \mathbf{A}_{\text{ext}}(\mathbf{r}, t) + \mathbf{A}_H[n](\mathbf{r}, t) + \mathbf{A}_{xc}[n](\mathbf{r}, t) \quad . \quad (3.32)$$

These equations define the so-called exchange-correlation (XC) potentials $V_{XC}[n](\mathbf{r}, t)$ and $\mathbf{A}_{XC}[n](\mathbf{r}, t)$. The non-interacting system evolves according to the time-dependent Kohn-Sham (TDKS) equations

$$i\partial_t \psi_j(\mathbf{r}, t) = H_{KS}(t) \psi_j(\mathbf{r}, t) \quad (3.33)$$

for occupied orbitals ψ_j , $j = 1 \dots N$, with the non-interacting Kohn-Sham Hamiltonian

$$H_{KS}(t) = \frac{1}{2} \left[\frac{\nabla}{i} + \mathbf{A}_{KS}(\mathbf{r}, t) \right]^2 + V_{KS}(\mathbf{r}, t) \quad . \quad (3.34)$$

The above choice of XC potentials guarantees that both systems give the same density $n(\mathbf{r}, t) = \sum_{j=1}^N |\psi_j(\mathbf{r}, t)|^2$. In practice, tractable approximations to the XC potentials must be found. Practical calculations mostly employ the *adiabatic* approximation, i.e., they only take into account the density at time t to generate the XC potential at time t and neglect the dependence on the history of the system. The XC scalar potential can then be derived from an XC functional of static DFT, for example the XC potential in a homogenous electron gas, the local density approximation (LDA) [Perdew and Zunger, 1981]. The XC vector potential plays a key role in describing dissipation and relaxation in time-dependent *current* functional theory (TD-CDFT) [Vignale and Kohn, 1996], an extension of TD-DFT with the time dependent current as basic quantity. In analogy to the LDA, the Vignale-Kohn functional is derived from the homogeneous electron gas [Vignale and Kohn, 1996; Vignale et al., 1997; Ullrich and Vignale, 2002]. However, in many applications, the external vector potential \mathbf{A}_{ext} is removed by a gauge transform, and the XC vector potential is neglected ($\mathbf{A}_{KS} = 0$).

3.3.2 Simulation of electron dynamics of a nano-tip

We now describe the application of TD-DFT to the interaction of intense few-cycle laser pulses with a metal nano tip. As the size of the tip ($R_{\text{tip}} \sim 10$ nm) is much larger than the characteristic length scale of the electron system (Fermi wavelength ~ 0.1 nm), translational invariance in the surface plane is approximately conserved. Since a full-dimensional calculation is presently out of reach, we treat the surface normal at the tip apex as the reaction coordinate. The time and space dependent electron density $n(z, t)$ is expanded into a sum of n_{occ} Kohn-Sham pseudo wave functions

$$n(z, t) = \sum_{k=1}^{n_{\text{occ}}} a_k |\psi_k(z, t)|^2 \quad . \quad (3.35)$$

The a_k are weight coefficients due to the projection of the three-dimensional Fermi sphere on the one-dimensional reaction coordinate [Eguiluz et al., 1984; Liebsch, 1997; Pitarke and Eguiluz, 2001],

$$a_k = |E_k - E_F| / \pi \quad (3.36)$$

with E_k is the Kohn-Sham energy of the wave function in the ground state and E_F is the Fermi energy. We assume that the coefficients a_k are independent of time, corresponding to a decoupling of degrees of freedom along the surface normal and perpendicular to the surface normal. In principle, another density of states could be used, for example derived from three-dimensional ab-initio calculations. The initial density $n_0(z) = n(z, t = 0)$ is determined by the ground state potential $V_{\text{GS}}(z)$ of which the ground state orbitals $\phi_k(z) = \psi_k(z, t = 0)$ are eigenfunctions,

$$\left[-\frac{1}{2} \frac{d^2}{dz^2} + V_{\text{GS}}(z) \right] \phi_k(z) = E_k \phi_k(z) \quad , \quad (3.37)$$

and $n_0(z) = \sum_k a_k |\phi_k(z)|^2$. The ground state potential contains the contributions from the atomic cores, the electrostatic (Hartree) term, and the exchange-correlation term, $V_{\text{GS}} = V_{\text{cores}} + V_{\text{es}} + V_{\text{xc}}$. In many three-dimensional static and time-dependent DFT codes, V_{cores} is fixed (e.g. by pseudopotentials) and the other summands are computed self-consistently. We instead choose to fix $V_{\text{GS}}(z)$ since it gives more flexibility. For example, high-quality fitted potentials for various surfaces that reproduce the surface state structure and image states are available as parameterizations of $V_{\text{GS}}(z)$ [Chulkov et al., 1999]. Alternatively, $V_{\text{GS}}(z)$ can be computed as average of a three-dimensional DFT calculation parallel to the surface plane (although the resulting electron density $n_0(z)$ is then not guaranteed to coincide with the average of the three-dimensional electron density). In most variants of the jellium model for surfaces, the homogeneous positive background charge vanishes abruptly at the surface, thereby determining V_{cores} by the Poisson equation. The one-dimensional ground state potential $V_{\text{GS}}(z)$ for a jellium slab can be obtained by various public-domain DFT codes,

for example GPAW⁴ [Chen et al., 2012]. For the simulations presented below, we instead employ a parameterization of the jellium potential that agrees closely to DFT calculations inside the slab [Lang and Kohn, 1970] but has the correct $1/(4z)$ tail of the image potential outside [Jennings et al., 1988; Burgdörfer, 1994]:

$$V_{\text{jellium}}(z) = \begin{cases} -\frac{V_0}{A \exp(Bz)+1} & \text{for } z < z_{\text{im}} \\ \frac{1-\exp(-bz)}{4z} & \text{for } z \geq z_{\text{im}} \end{cases} \quad (3.38)$$

where the total depth of the potential is $V_0 = E_F + W$ for work function W and Fermi energy $E_F = k_F^2/2$. The Fermi energy is related to the bulk electron number density n_{bulk} as

$$n_{\text{bulk}} = \frac{1}{3\pi^2} (2E_F)^2 \quad (3.39)$$

and n_{bulk} is related to the so-called Wigner-Seitz radius r_s , the radius of a sphere containing on average one electron, as $n_{\text{bulk}} = 3/(4\pi r_s^3)$. The position of the image plane relative to the jellium edge is $z_{\text{im}} = -0.2r_s + 1.25$, and the transition to the asymptotic $1/(4z)$ image potential is chosen as $b = k_F$ such that $A = 4V_0/b - 1$ and $B = V_0/(4V_0/b - 1)$. We thus neglect the influence of the d-electrons which are difficult to incorporate into a one-dimensional model. d-electrons can heuristically be accounted for by adding a polarizable dielectric inside the slab [Liesch, 1997] at the expense of additional free parameters and it has been found that they are necessary in some cases to account for details of the response such as the negative slope of the surface plasmon polariton dispersion relation in silver. To account for rescattering at the first surface layer, a localized potential that mimics the atomic cores of the first atomic layer is added to the jellium potential, which we parameterize by a screened soft-core Coulomb potential

$$V_{\text{atom}}(z) = -\frac{1}{1+|z|} e^{-|z|/\lambda_{\text{TF}}} \quad (3.40)$$

where the Thomas-Fermi screening length $\lambda_{\text{TF}} = 2\pi/k_{\text{TF}} \approx 1$ a.u. is given through $k_{\text{TF}} = 6\pi n_{\text{bulk}}/E_F$. We find the parameterization of the first layer potential V_{atom} to be of small importance as long as the correct reflection coefficient is obtained (see section 3.9 for details).

For comparison with the experiments on tungsten nanotips in the remainder of this chapter, we use $E_F = 9.2$ eV ($r_s = 2.334$) according to the s-electron density of tungsten. The work function for a clean tungsten (310) surface is reported as $W_{\text{W}(310)} = 4.35$ eV [Yamamoto et al., 1978] which is, however, sensitive to adsorbates on the surface. In experiment, the effective work function was found to be $W_{\text{eff}} \approx 6$ eV [Krüger et al., 2012] and W was found to vary as a function of time after cleaning the surface. A work function of $W_{\text{eff}} \approx 6$ eV is consistent with an oxygenated tungsten surface [Kawano, 2008]. The simulations below are performed with a work

⁴See <https://wiki.fysik.dtu.dk/gpaw/tutorials/jellium/jellium.html> for technical instructions.

function of $W = 6.2$ eV for which we find best agreement with experiment. The slab width was typically 150 a.u. ($n_{\text{occ}} \sim 50$ orbitals).

The evolution of the electron density is governed by the time-dependent Kohn-Sham (TDKS) equations

$$i\partial_t\psi_k(z, t) = \left\{ -\partial_z^2 + V[n(z, t)] + V_{\text{ext}}(z, t) \right\} \psi_k(z, t) \quad (3.41)$$

for the orbitals $\psi_k(z, t)$, starting from the initial values $\psi_k(z, t = 0) = \phi_k(z)$, $V[n_0(z)] = V_{\text{GS}}(z)$, and the external potential $V_{\text{ext}}(z, t = 0) = 0$.

The external potential of the electric field in dipole approximation is $V_{\text{ext}}(z, t) = zF_{\text{eff}}(t) + zF_{\text{dc}}$ where the laser field is

$$F_{\text{eff}}(t) = F_{\text{eff},0} \cos(\omega t + \phi_{\text{CE}}) e^{-t^2/(2\tau_{\text{field}}^2)} \quad (3.42)$$

with amplitude $F_{\text{eff},0}$, photon energy ω , carrier-envelope phase ϕ_{CE} and duration τ_{field} (FWHM field; the duration of the FWHM in intensity is $\tau = \tau_{\text{field}}/\sqrt{2}$). $F_{\text{eff}}(t)$ is the local field at the surface of the tip that already includes the near-field enhancement and phase shift and is typically of amplitude $F_{\text{eff},0} \sim 0.005 - 0.025$ a.u.. The dipole approximation of homogeneous external electric fields is justified as the typical propagation distances of the electrons in the laser field ($\alpha_{\text{quiver}} = (F_{\text{eff},0}^2/2\omega)^2$) are of sub-nanometric dimension so that the free electron motion does not sample the inhomogeneity of the local electromagnetic field for the wavelengths employed [Herink et al., 2012]. Extension to nonuniform fields is possible along the lines of [Iwasa and Nobusada, 2009, 2010]. $F_{\text{dc}} \approx -0.4$ GV/m = -0.00078 a.u. is a small static extraction field (also including possible field enhancement) that is used in both experiment and simulation to accelerate the emitted electrons away from the tip, but that does not lead to appreciable electron emission on its own. In the simulation, we also treat it as a time-dependent electric field that is switched on very slowly at the beginning of the simulation before the laser field. In order to detect the final energy of the electrons (see below), the static potential is smoothly converted to a constant potential near the border of the box.

The time-dependent potential

$$V[n(z, t)] = V_{\text{cores}} + V_{\text{es}}[n(z, t)] + V_{\text{xc}}[n(z, t)] = V_{\text{GS}} + \Delta V[n(z, t); n_0(z)] \quad (3.43)$$

includes the ground state potential and the induced potential $\Delta V[n(z, t); n_0(z)]$ due to the change in electron density in terms of the change in electrostatic (Hartree) and exchange-correlation (XC) potentials. The electrostatic potential is given as solution of the Poisson equation

$$\partial_z^2 V_{\text{es}}(z, t) = -4\pi n(z, t) \quad (3.44)$$

with Neumann boundary conditions outside the simulation box,

$$\partial_z V_{\text{es}}(z \rightarrow \infty, t) \rightarrow 2\pi \int_{\text{box}} n(z, t) dz, \quad (3.45)$$

where the electric field (gradient of the potential) outside a charged slab is obtained by Gauß' law. The Poisson equation can equivalently be solved as

$$V_{\text{es}}(z) = -2\pi \int_{-\infty}^{\infty} (z - z')n(z')dz' \quad . \quad (3.46)$$

This latter form of the Poisson equation requires a double loop over all points z and therefore scales with N_{points}^2 for a simulation box discretized into N_{points} intervals. It is numerically advantageous to solve Eq. 3.44 directly. This is efficiently accomplished by a high-order spatial difference forward integration and scales only as N_{points} . While the Poisson equation (Eq. 3.44) describes a flat surface (infinite extension in x and y directions), in principle Eq. 3.44 can easily be substituted by an effective Poisson equation along the reaction coordinate z for a fixed *finite* transverse extension of the system ("quantum wire"). This restricted geometry then gives rise to field enhancement and an inhomogeneous near-field on the length scale of the assumed transverse extension. For the exchange-correlation potential, we employ the adiabatic local density approximation in the parameterization of Perdew and Zunger [1981]. We have numerically demonstrated that the choice of XC potential does not affect the electron spectra from metal nano-tips presented in the remainder of this chapter [Wachter et al., 2012]. The change of the electrostatic and XC potentials with respect to the ground state potential, $\Delta V[n(z, t); n_0(z, t)]$, is a measure for the local microscopic electric field induced by the laser pulse in the material. It is given by evaluating the above equations for both the ground state density $n_0(z)$ and the time-dependent density $n(z, t)$ and subtracting the results (Eq. 3.43).

We integrate the TDKS equations (Eq. 3.41) by the Crank-Nicolson method employing a space discretization of $\Delta z = 0.15$ a.u. and time step $\Delta t = 0.05$ a.u., extrapolating the time-dependent Hamiltonian at $t + \Delta t/2$ to second order in time. The simulation time of typically 120 fs is chosen such that the energy spectra are converged with respect to the low energy electrons. The size of the simulation box is typically ~ 1500 a.u. ($N_{\text{points}} = 10^5$) including imaginary absorbing potentials near the borders of the simulation box to avoid unphysical reflections of electrons at the box border. As the laser pulse excites the electrons in the slab, density waves move from the surface towards the inside of the slab, which can lead to unphysical reflections at the back side of the slab. To minimize the influence of these reflections, we firstly increased the slab size so as to increase the round-trip time of the density waves that are reflected from the back side, and we secondly added an imaginary potential inside the slab that is proportional to the difference density $n(z, t) - n(z, 0)$. Recent efforts in modeling "quantum friction" within TD-DFT might provide a more efficient solution to this problem [Neuhauser and Lopata, 2008].

The observable of interest for comparison with the experimental data is the energy spectrum of the photoemitted electrons. We employ the so-called sampling-point method [Pohl et al., 2000, 2001, 2003, 2004; Dinh et al., 2013]. It postulates that the photoelectron spectrum is, to a good degree of approximation, given by

the sum of the spectra of the Kohn-Sham orbitals ψ_k . This is corroborated by the agreement of photoelectron spectra derived by the sampling point method with a recently proposed alternative method for the extraction of photo-electron spectra from single-particle theories like TD-DFT motivated by a phase-space interpretation of the single-determinant Wigner function [De Giovannini et al., 2012]. In the sampling point method, the probability to measure an electron with a definite energy E is calculated by recording the Kohn-Sham orbitals in time $\psi_k(z_D, t)$ at a fixed detection point z_D near the border of the simulation box where only outgoing waves are found. The wave function is expanded into plane waves of energy $E = k^2/2$ with Fourier coefficients $\tilde{p}_k(E)$,

$$\psi_k(z_D, t) = \int dE \tilde{p}_k(E) e^{ik(E)z} e^{-iEt}. \quad (3.47)$$

The electron spectrum $S(E)$ at total electron energy E is then given by the sum of the inverse Fourier transforms of the recorded orbitals,

$$S(E) = \sum_{k=1}^{n_{\text{occ}}} a_k \left| \int_{-\infty}^{\infty} dt e^{iEt} \psi_k(z_D, t) \right|^2. \quad (3.48)$$

We numerically confirmed that the electron spectra (Eq. 3.48) give the same results as projecting on plane waves in space and on box energy eigenstates of the unperturbed system. In practice, z_D must be chosen such that appreciable electron density arrives at z_D only after the laser pulse is over and the simulation must be continued until the lowest energy electrons of interest have passed the detection point z_D . For the simulations below, this amounts to a total simulation time of about 100 fs. While not numerically challenging in one dimension, calculating electron spectra in more dimensions is performed more efficiently by the implementation described by De Giovannini et al. [2012]. For comparison with experiment, the electron spectra are broadened by 0.5 eV, corresponding to the typical experimental spectrometer resolution.

3.4 Simulation of electron emission and rescattering

In this section, we discuss a representative sample simulation of electron emission and rescattering with time-dependent density functional theory. Fig. 3.3a displays the time-dependent induced density response $\delta n(z, t) = n(z, t) - n(z, -\infty)$ for laser field amplitude $F_{\text{eff}} = 0.02$ a.u. corresponding to an intensity $I_{\text{eff}} = 1.4 \times 10^{13}$ W/cm², central wavelength $\lambda = 800$ nm, pulse length 6.4 fs (FWHM intensity), and static field $F_{\text{dc}} = -1.9 \times 10^{-4}$ a.u.. Taking into account the field enhancement factor for tungsten calculated in chapter 2 of about ~ 5 , this field strength can be reached with a nominal laser intensity of only $I_0 = 5.6 \times 10^{11}$ W/cm².

We start with the region inside the tip ($z \leq 0$). The external laser field induces density fluctuations at the surface that screen the external field. As the time scale of the laser period $T = 800 \text{ nm}/c = 2.67 \text{ fs} = 110 \text{ a.u.}$ is very large compared to

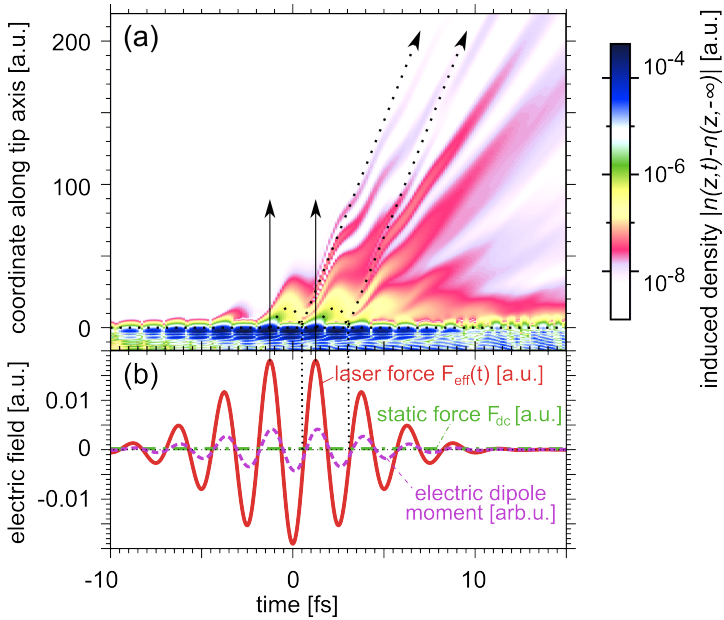


Figure 3.3: Time-dependent density functional theory simulation of electron emission and rescattering. (a) Contour plot of the absolute value of the induced density, $|n(z,t) - n(z,-\infty)|$ where $z \leq 0$ refers to the inside of the nano-tip. Full horizontal arrows mark the maximum of the electric force when most charge is ionized; dashed lines mark typical trajectories of rescattered electrons (slope corresponds to $10U_p$). Interferences in position space with increasing slopes (velocities) are the signature of the equi-spaced multi-photon peaks in the electron energy spectra. (b) Full red line: laser electric force $F_{\text{eff}}(t)$; dashed pink line: time-dependent dipole moment (arb.u.); dash-dotted green line: static field F_{dc} .

the time scale of electronic motion in the solid $\lambda_F/v_F \sim 5$ a.u., the electrons are fast enough to adiabatically adjust to the external field and form a dipole layer on the surface that screens the external field. The amount of electron charge necessary for screening ($\sim 10^{-4}$ a.u. from Fig. 3.3) is, at this laser intensity, still only a small fraction of the total valence electron density $n_0 = 1.88 \times 10^{-2}$ a.u.. This near-instantaneous following of the driving force is reflected in a dipole moment that is almost in phase with the driving field (Fig. 3.3 b).

Turning now to the region outside the tip ($z > 0$) where the charge is emitted towards the detector, we observe electron emission into the continuum that is localized in time around the maxima of the electric force (black arrows in Fig. 3.3a). The effective Keldysh parameter is $\gamma_{\text{eff}} = \omega\sqrt{2W}/F_{\text{eff}} \sim 1.9$, in the transition between the multi-photon regime ($\gamma_{\text{eff}} \gg 1$) and the tunneling regime ($\gamma_{\text{eff}} \ll 1$). The density of emitted charge is several orders of magnitudes lower than the charge density change that is induced at the surface of the solid and decreases with increasing distance from the surface as the electron wave packets spread longitudinally. After the laser pulse, interferences form along approximately straight lines of constant slope (constant ve-

locity), which are directly associated with multi-photon peaks in the energy spectra. The electrons of largest energy thus correspond to the density structures with the steepest slope. According to the simple man’s model for nanostructures (section 3.2), these fastest electrons should be generated by the rescattering mechanism. The electrons are first emitted near the maxima of the electric field (solid arrows). As the laser field changes its sign, they are driven back towards the surface and can rescatter from the first layer of atoms. In the semi-classical model, the optimal timing for rescattering leading to the highest final energies of $10U_p$ is slightly before the zero crossing of the electric field. Indeed, we observe interferences starting from the surface at times when the electric field is zero (dotted lines in Fig. 3.3b). The interferences proceed along the dotted arrows in Fig. 3.3 whose slope corresponds to a kinetic energy of $10U_p$, a direct indication of the rescattering mechanism in the real space density.

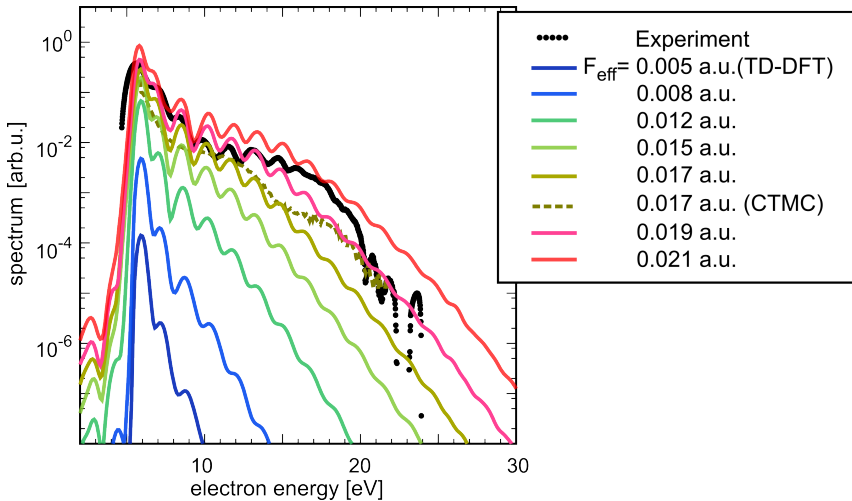


Figure 3.4: Intensity dependence of simulated electron spectra. Electron energy spectra for increasing intensities (full lines), classical trajectory Monte Carlo results (dashed line, for $F_{\text{eff}} = 0.017$ only), experiment (black line/points, nominal intensity $I_0 = 1.1 \times 10^{11} \text{ W/cm}^2$ [Krüger et al., 2012]).

3.5 Appearance of plateau with increasing laser intensity

We investigate the dependence of the electron spectra on the laser intensity (Fig. 3.4, for pulse parameters as in the preceding section, averaged over the carrier-envelope phase). For low laser intensities ($F_{\text{eff}} = 0.005 \text{ a.u.} \rightarrow I_{\text{eff}} = 8.8 \times 10^{11} \text{ W/cm}^2$) we do not observe a plateau but an exponential decay modulated by equi-spaced multi-photon peaks in agreement to experiments for lower intensity [Schenk et al., 2010]. In terms of the simple man’s model, the classical cut-off energy is here only $10U_p(F_{\text{eff}}) = 0.5 \text{ eV}$ indicating that the plateau is completely overshadowed by the “direct” elec-

trons. The multi-photon peaks, however, reflect the periodic repetition of electron emission at each optical period and persist for the direct electrons even at comparatively low laser intensities. With increasing laser intensity plateau and cut-off emerge in the electron spectra. The simulations describe the experimental data for the highest intensities very well including the position of the multi-photon peaks. We estimate the enhanced experimental field strength as $F_{\text{eff}} = 0.020$ a.u.. This is corroborated by the experimental estimate of the laser intensity $I_0 = 1.1 \times 10^{11}$ W/cm² $\rightarrow F_0 = 0.0018$ and Maxwell simulations that yield field enhancement factors of order of magnitude 5-10. A dedicated measurement of electric near-fields employing the cut-off of the electron spectra and a comparison with calculated field enhancement factors for the measured tip geometries shows similarly good agreement [Thomas et al., 2013].

Fig. 3.4 also shows the result of a complementary classical-trajectory Monte Carlo (CTMC) simulation on the single active electron level in three dimensions including realistic cross sections for atom-surface scattering derived from partial-wave calculations [Wachter et al., 2012; Salvat et al., 2005]. The CTMC simulation reproduces the ratio of direct electrons to plateau electrons. Unlike for single atoms, the electrons do not have to return to their parent atomic core but may also rescatter from neighboring atoms ensuing the transverse spread of the electron wave packet. The enhanced density of scattering centers on the metal surface thus enhances the intensity of the plateau compared to gas targets.

3.6 Carrier-envelope phase dependence of rescattering

The delicate steering of the electron wave packet in the vicinity of the metal nanostructure can be probed by recording electron spectra while varying the shape of the laser pulse. Experimentally, the laser pulse shape can be fine-tuned by allowing the laser to propagate through an adjustable length of fused silica, which changes the carrier-envelope phase (CEP) ϕ_{CE} proportional to the optical path length in the dielectric. Comparing our theory to the ϕ_{CE} -resolved experimental data (Fig. 3.5 a,b) provides a stringent test of the accuracy of our simulation. Comparison to experiments [Krüger et al., 2011] reveals excellent agreement between theory and experiment over the full spectral range (Fig. 3.5 c,d) including the position of the multi-photon peaks and some of the fine structure. The dominant feature in the data is a large-scale structure of bent stripes that converge towards a maximum at $\phi_{\text{CE}} = \pi$ ($-\cos$ pulse) for large electron energies. This asymptotic behavior can be understood from the rescattering process that yields the highest energies when the force driving the electron back towards the surface is largest. This “bent stripes” structure has also been observed in electron spectra from atoms [Paulus et al., 2003; Milošević et al., 2006] and dielectric nano-spheres [Zherebtsov et al., 2011, 2012] and is used for carrier-envelope phase single shot measurements by the “stereo-ATI” technique [Wittmann et al., 2009].

In the following, we present a minimal model based on the simple man’s model

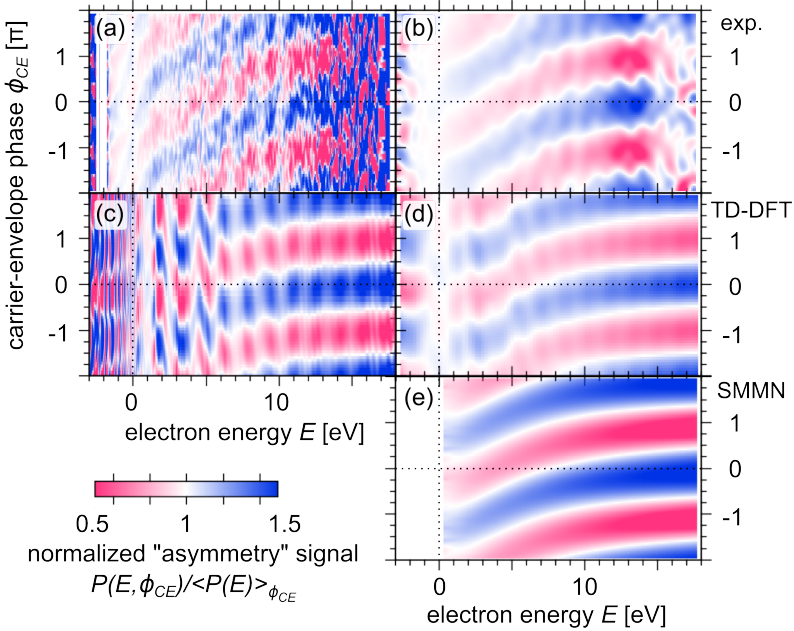


Figure 3.5: Carrier-envelope phase (ϕ_{CE}) dependence of electrons spectra. (a-b) ϕ_{CE} -dependence of experimental data [Krüger et al., 2011] shown as normalized “asymmetry” signal, i.e., divided by the ϕ_{CE} -averaged signal, $P(E, \phi_{CE}) / \int_0^{2\pi} d\phi_{CE} P(E, \phi_{CE})$. (a) Raw data, (b) smoothed over 1.5 eV and 0.5 π . Since in experiment only a relative phase was measured, the absolute phase has been adjusted to match the TD-DFT simulation (c-d). (c-d) ϕ_{CE} -dependence of TD-DFT simulation (field amplitude 0.019 a.u., 760 nm, 4.8 fs, static field 0.4 GV/m). (c) raw data, (d) smoothing as for experiment. (e) CE-phase dependent spectrum modeled by the SMMN (Eq. 3.50), color scale for this plot goes from 0.2 to 1.8. Parameters as for the TD-DFT calculation and $\sigma_p = 0.12$ a.u. (details see text).

for nanotips (SMMN, see section 3.2) that gives an intuitive interpretation of the carrier-envelope phase dependence. We integrate over all possible birth times t_b during the laser pulse, weighing the classically possible rescattering trajectories with an ADK tunneling rate [Ammosov et al., 1986] that depends on the moment of ionization during the laser pulse as

$$\Gamma^{\text{ADK}}(F_{\text{eff}}(t)) \propto \exp \left[-\frac{2(2W)^{3/2}}{3F_{\text{eff}}(t)} \right]. \quad (3.49)$$

We then incoherently add the electron spectra of all rescattering trajectories, assuming that each trajectory gives a spectrum centered around the classical momentum p_{resc} reached by an electron along its classical rescattering trajectory. We assume that the width of the spectra σ_p is constant and adjust σ_p such that the CEP-averaged experimental spectrum is well reproduced. Our model then gives a prediction of the

carrier-envelope phase dependence of the spectrum as

$$P(p) = \int_{-\infty}^{\infty} dt_b \Gamma^{\text{ADK}}(F_{\text{eff}}(t_b)) e^{-(p-p_{\text{resc}}(t_b))^2/2\sigma_p} . \quad (3.50)$$

The dependence on ϕ_{CE} enters both in the ionization rate as well as in $p_{\text{resc}}(t_b)$, the final momentum of the electron that has been ionized at t_b and undergone a rescattering event along its classical trajectory in the laser field. Both Γ^{ADK} and $p_{\text{resc}}(t_b)$ depend sensitively on the pulse shape $F_{\text{eff}}(t)$. The CE-phase dependence agrees very well to both TD-DFT simulation and experiment and reproduces the bent stripes structure including the curvature and the slope of the low-energy part. We infer that the bent stripes structure is due to the interplay of the strongly non-linear tunneling rate and the rescattering process. For $\phi_{\text{CE}} = \pi$ ($-\cos$ pulse), the rescattering is strongest leading to the largest number of electrons at high energies. The tilt in the spectra at lower electron energies is due to the interplay of the ionization rate at birth time t_b with the rescattering momentum $p_{\text{resc}}(t_b)$. For a $-\cos$ pulse ($\phi_{\text{CE}} = \pi$) the rescattering is strongest and p_{resc} is highest. However, the tunneling probability at the maximum preceding the $-\cos$ peak is lower compared to, e.g., a $+\sin$ -pulse, where the rescattering energy is lower but the tunneling probability is higher, leading to different relative weights of these contributions and in total to the bent stripe pattern in the CEP dependence. Notably, the convergence of the spectra with electron energy to the maximum near $\phi_{\text{CE}} = \pi$ is very slow. In Fig. 3.5, the maximal attainable classical electron energy is $10U_p = 6.8\text{ eV}$, but due to the contributions of wavepackets from lower final energies which are weighed by larger ionization probabilities the convergence happens only around $\sim 20U_p$. While the high energy part scales with U_p , the slope and curvature of the stripes in the low energy part reflect the field strength dependence of the ionization rate during the laser cycle and thus depend on the absolute value of the field strength and Keldysh parameter.

In the experiment [Krüger et al., 2011], the absolute value of the CE-phase could not be determined due to the low nominal laser intensity much below the intensity needed for absolute characterization of the CE-phase. However, the excellent agreement with the theory data shown in Fig. 3.5 strongly suggests that the absolute phase of the experiment can be reconstructed by comparison with TD-DFT calculations. We note that even an absolute CE-phase measurement of the laser pulse $F(t)$ in vacuum would not be sufficient to know the CE-phase of the enhanced laser field $F_{\text{eff}}(t)$ on the surface of the tip since the CE-phase of the near-field can be shifted with respect to the incoming field depending on the material and geometry of the nano-tip near the apex. A dedicated measurement for the absolute value of the CE-phase to verify the agreement of the carrier-envelope phase resolved electron spectra with respect to the SMMN and TD-DFT simulations will have to take into account the nanoscopic shape of the tip and the incurred Maxwell CE-phase shift.

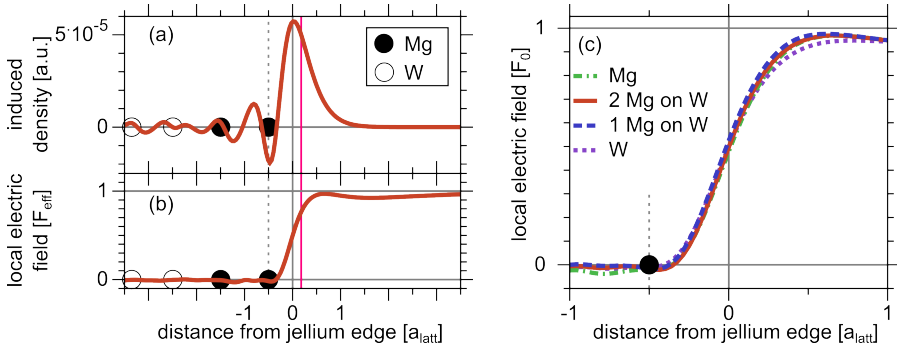


Figure 3.6: Microscopic electric field at the surface. (a) Snapshot of the induced charge density on the surface at the electric field maximum (intensity 2×10^{11} W/cm², pulse duration 4 fs (FWHM intensity), cosine-pulse) for 2 monolayers Mg on W(110). Dashed line: position of the first atomic layer (Mg, full circle; W, open circles). Pink vertical full line: centroid of induced charge density (dynamic image plane). $a_{\text{latt}}^{\text{Mg}} = 4.9$ a.u.. (b) Microscopic electric field calculated from the induced charge density. The electric field is screened on the atomic length scale before it reaches the surface. (c) Comparison of microscopic electric field for varying number of Mg adlayers: Green dash-dotted line: pure Mg; full red line: 2 ML Mg on W; dashed blue line: 1 ML Mg on W; dotted purple line: pure W ($a_{\text{latt}}^{\text{W}(110)} = 4.2$ a.u.).

3.7 Electric field distribution during the laser pulse

We now analyze the screening of the electric field near the surface in more detail. We depart for this section from the simulation of nano-tips and use the same methods to calculate the response of a flat metal *surface* to few-cycle laser pulses of lower intensity in the linear response regime [Lemell et al., 2003; Apolonski et al., 2004]. Operationally, the only difference to the above simulations is that the field enhancement factor for a surface is unity and thus $F_{\text{eff}} = F_0$. Here, we are not interested in the electrons that are emitted from the surface, but stay in the linear response regime where no electrons are emitted and investigate the local accumulation of screening charge $\delta n(z, t)$ and the corresponding local electric field $F_{\text{local}}(z, t)$ along the surface normal.

Our investigations are motivated by recent *attosecond surface streaking* experiments [Cavalieri et al., 2007; Neppel and et al., 2014]⁵ which we describe briefly in the following. Attosecond surface streaking is a pump-probe scheme where the probe is a few-cycle NIR pulse with a component along the surface normal (similar to the laser pulses employed in the preceding chapters), and the pump is a XUV laser pulse ($\omega_{\text{XUV}} \sim 100$ eV) with a duration in the 0.1 fs range that is used to excite electrons in the first few surface layers to the conduction band with a well-defined kinetic energy at a well-defined time. On their way out towards the detector, the electrons experience the local electric field $F_{\text{local}}(z, t)$, the sum of the NIR few-cycle pulse plus the dynamical screening of the laser field by the electrons near the surface. The origin of the excited electrons along the surface normal coordinate can be chosen by using

⁵The results presented in this section have been discussed in Neppel and et al. [2014].

atomically flat surfaces with adlayers of different atomic species, so that the XUV photoelectrons from the different atomic species are well-separated in energy, giving a space resolution of a fraction of the interlayer spacing $a_{\text{latt}} \sim 5$ a.u.. By varying the time delay between pump and probe pulses, the time at which electrons originating from different layers feel the field of the laser pulse can be pinpointed to a relative precision of about 0.01 fs. Attosecond streaking has therefore been interpreted as a direct measurement of electron transport in the time domain [Lemell et al., 2009; Neppl and et al., 2014] and of the position of the electronic surface with respect to the first layer of atoms. The most recent experiments use a W(110)/Mg hetero-structure with a tunable number of Mg layers on W.

The perpendicular component of the incident NIR streaking field induces a polarization charge layer on the metal surface which screens the inside of the conductor. The position and width of this screening charge layer determine the position and width of the screening of the electric field at the surface. The (full) width w of the surface charge layer is given by the period of the Friedel oscillations, half the Fermi wavelength $w \approx \lambda_F/2 = 3.8$ a.u. for W and 4.4 a.u. for Mg. The position z_0 of the centroid of the induced surface charge (“image plane”) with respect to the first layer has been calculated within the jellium approximation for a static external field ($\omega \sim 0$) as $z_0^{\text{el}} \approx a_{\text{latt}}/2 + \delta_0$ a.u. [Serena et al., 1988; Liebsch, 1997], where a_{latt} is the lattice constant (layer spacing) and the value of δ_0 ranges from 1 a.u. to 1.5 a.u. depending on the value of the electron density. For $a_{\text{latt}}^{\text{Mg}} = 4.9$ a.u., we estimate $z_{0,\text{Mg}}^{\text{el}} \approx 3.6$ a.u. and for $a_{\text{latt}}^{\text{W}(110)} = 4.2$ a.u., $z_{0,\text{W}(110)}^{\text{el}} \approx 3.2$ a.u.. These estimates put the screening charge layer more than half its width outside the surface, suggesting that the electric field is screened by the electron density spill-out before it reaches the first atomic layer.

We expect that the position and width of the induced charge density and the dynamical image plane depend on the strength, direction, and frequency of the applied field as well as on the lattice structure of the target. The importance of these corrections is assessed within a TD-DFT calculation (Fig. 3.6). The density and resulting mean-field potential of a static three-dimensional DFT calculation for a W slab with Mg overlayers is averaged perpendicular to the surface normal, providing the starting point for one-dimensional TD-DFT calculations with the surface normal as reaction coordinate.

We find, indeed, that the induced screening charge layer is located well outside the first atomic layer (Fig. 3.6 a). We calculate the local electric field $F_{\text{local}}(z, t) = -\frac{d}{dz}[V_{\text{ext}} + \Delta V[n(z, t), n(z, -\infty)]]$ as a superposition of the external potential from the laser field V_{ext} and the response of the system in terms of the induced density $\delta n(z, t) = n(z, t) - n(z, -\infty)$ (Fig. 3.6 b). The electric field is screened by the induced charge density in front of the surface on a length scale of a few atomic units and is virtually zero at the position of the first atomic layer. This result is in excellent agreement with the most recent experimental data, indicating that the attosecond surface streaking technique can be used to probe the local electric field within solids and at interfaces on the atomic length and femtosecond time scale.

Within our model, we find that the local screening is almost identical for pure W, pure Mg, and a varying number of Mg adlayers on W. We have also performed a calculation for a pure Mg slab based on the one-dimensional potential prescribed by Chulkov et al. [1999] which is fitted to reproduce the correct surface electronic structure of Mg(0001) (projected energy gap, surface state binding energy, and energy of the first image state) with similar results.

The rapid screening of the electric field inside the metal is also important for electron emission and rescattering from nano-tips. There, the rapid screening leads to the reduction of classes of classical trajectories that contribute to the electron spectra compared to atomic or molecular targets. In atoms and molecules, trajectories that take off in the direction opposite to the detector, are then turned around by the laser field, and are subsequently re-scattered with small scattering angle in forward direction so that they reach the detector, also contribute to the spectra. Such trajectories lead to intermediate energies between the “direct” ($\lesssim 2U_p$) and “rescattered” electrons ($\sim 10U_p$) that lead to the formation of the plateau. These additional contributions can thus cloud the plateau that is typical for rescattering but are absent for nanotips because of this screening effect.

3.8 From the multiphoton to the tunneling regime: wavelength dependence

We now turn to parameter combinations and observables for which no experimental data are available yet but should become so in the near future. We first explore the influence of the driving laser wavelength on the quantum surface dynamics⁶, keeping all other parameters of the effective pulse shape of the electric field at the tip apex fixed (carrier-envelope phase, field envelope, and pulse duration).

We calculate electron spectra for central laser wavelengths in the range of $\lambda = 500 - 2000$ nm (Fig. 3.7a). In this wavelength range, the effective Keldysh parameter $\gamma_{\text{eff}} = \omega\sqrt{2W}/F_{\text{eff}} \propto 1/\lambda$ varies between 4 and 1 so that we expect a transition from the multiphoton regime at small wavelengths to the non-adiabatic tunneling regime at larger wavelengths. On the other hand, the maximal attainable electron energy for rescattering $10 \cdot U_p \propto \lambda^2$ varies from 2 eV to 30 eV over this wavelength range. Indeed, we observe a transition from the multiphoton regime with peaks approximately given by $E_n = n\omega - U_p - W$ with n integer (cf. Eq. 3.23) to spectra dominated by the rescattering plateau up to a cut-off energy of $10 \cdot U_p$. The absolute intensity is reduced by several orders of magnitude from 500 nm to 2000 nm (Fig. 3.7c). This decrease is partly attributed to the reduced field strength at tunneling for longer wavelengths. However, the increase in signal between 800 nm and 500 nm is attributed to more efficient multi-photon ionization as the integer number of photons N_{phot} needed to overcome the excitation gap of $W = 6.2$ eV is reduced from $N_{\text{phot}}^{800\text{nm}} = 4$ to $N_{\text{phot}}^{500\text{nm}} = 3$. The intensity of the rescattering plateau relative to

⁶The results in this section have also been presented in Wachter et al. [2014a].

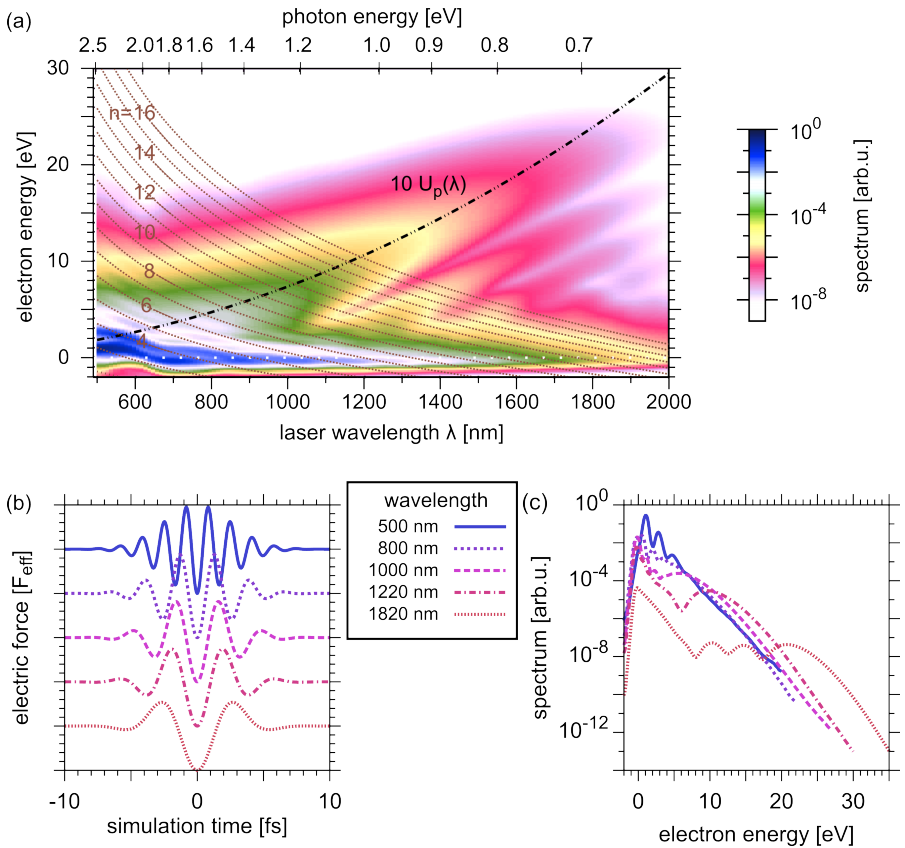


Figure 3.7: Wavelength dependence of simulated electron spectra. (a) Wavelength dependence of electron emission spectra for the pulse shapes shown in (b). The dash-dotted line marks the classical rescattering cut-off at $10 \cdot U_p \propto \lambda^2$. Dotted lines give estimates for the position of the multi-photon peaks, $E_n = n\omega - U_p - W$ with n is shown in the insets. (c) Line-out of (a) at various wavelengths.

the direct part strongly decreases with increasing wavelength by about two orders of magnitude between 1000 nm and 2000 nm. A minor part of this decrease is due to the energy dependence of the over-barrier reflection coefficient of the one-dimensional first layer potential. The reflection coefficient decreases by about a factor of 4 as the kinetic energy of the fastest electrons at rescattering varies between $E_{\text{scat}} \sim 3 \cdot U_p \sim 2$ eV and 10 eV. This decrease is also reproduced in three-dimensional partial wave calculations for an atomic tungsten potential [Salvat et al., 2005], where, however, the decrease is only a factor of two over the same energy range. We speculate that a major part of the decrease in plateau intensity is due to the sub-cycle dependence of the ionization rate, which is sensitively probed by the rescattering process. While the intensity of the direct part mostly comes from electrons that tunnel around the

maximum of the electric field, the intensity of the rescattering plateau comes from those electrons that start about $0.05T$ after the maximum of the electric field. For longer wavelengths (deeper in the tunneling regime), the tunneling rate varies more strongly with instantaneous field strength. Such a frequency dependence of the tunneling probability has been predicted by non-adiabatic tunneling theory [Yudin and Ivanov, 2001]. Another prominent feature of the calculated spectra is the build-up of additional large-scale structures in the spectra. We observe pronounced modulations of one order of magnitude or more spaced by several eV at large wavelengths, by far exceeding the photon energy. The large energy spacing points to a process happening on a short time scale within one laser cycle. We conjecture that these structures can be associated with the interferences between short and long rescattering trajectories (“intracycle interferences”) in analogy to the structures found in the spectra for gas targets [Paulus et al., 2002; Arbó et al., 2010b,a; Xie et al., 2012].

3.9 Sensitivity to the surface potential

Here, we investigate the sensitivity of rescattering on the surface potential⁷. We first show that a strong potential gradient in addition to a smooth jellium potential is necessary to provide a realistic backscattering coefficient to mimic the first layer of surface atoms. However, details of the rescattering potential are not of importance for the electron spectra at 800 nm laser wavelength. We then investigate along the same lines if the rescattering process can, in principle, be used to probe the atomic structure of the surface in terms of the lattice structure of the target or adsorbates on the surface. For this, we employ larger laser wavelengths or, equivalently, higher electron rescattering energies so that the electron de Broglie wavelength resolves interatomic distances. We demonstrate that a minimum in the surface reflection coefficient is mapped onto a minimum in the electron spectra.

Backscattering happens with a high probability when the impinging electron wave function experiences a steep potential gradient. In strong field experiments for atoms or molecules, the potential gradient is provided by the Coulomb potential of the atomic cores. Our jellium description of the surface, on the other hand, smears out these potentials to a smooth background charge. The resulting smooth single-particle ground state potential has a small reflection coefficient. Therefore, elastic scattering of accelerated electrons from the atomic cores of the surface is not contained in the jellium ground state potential and is achieved by an additional potential mimicking the surface layer. It is therefore of interest to compare simulated spectra with and without this additional potential and for different parameterizations of the core potential (Eq. 3.40).

Fig. 3.8 shows a comparison of calculated spectra for different choices of the surface potential, a jellium potential (Eq. 3.38) without an additional atomic potential at the surface and two approximate choices for the atomic potential at the surface, a 1D

⁷Parts of the results presented here were originally published in Wachter et al. [2012].

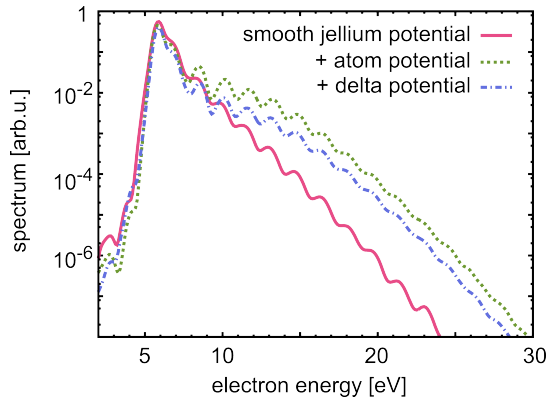


Figure 3.8: Sensitivity of rescattering to the empirical surface potential. Electron spectra for $F_{\text{eff}} = 0.021$ a.u., $\omega = 0.06$ a.u. ($\lambda = 760$ nm) for a pulse length of 6.4 fs (FWHM intensity). Solid red line: jellium potential; dashed green line: jellium potential plus 1D-atomic potential; dash-dotted blue line: jellium potential plus delta potential.

screened Coulomb potential (Eq. 3.40) and a delta potential. The low-energy parts of the spectra look very similar whereas the high-energy parts show striking differences. While the calculations including a surface potential show the formation of a rescattering plateau, the over-barrier reflection coefficient of the jellium potential is so low that rescattering is overshadowed by the exponentially decaying direct part modulated by multi-photon peaks.

Comparing the two different choices for the atom potential at the surface, we observe that the relative magnitude of the rescattering plateau is somewhat different due to the different over-barrier reflection coefficient of the atom potential that can be adjusted to give values in agreement with experiment. However, the shape of the plateau and cut-off as well as the position and visibility of the interference fringes (multi-photon peaks) are essentially the same for both potentials. This indicates that the details of the shape of the surface potential are not important in this range of laser parameters. There are two separate aspects to this independence of the electron spectra from the detailed shape of the surface potential. Firstly, details of the scattering potential are encoded in the energy dependence of the scattering phase (phase of the reflection coefficient). The electron spectra in the plateau region, however, only contain electrons that have undergone scattering events with similar energies, and thus the contributions from the scattering phase to the observed interference patterns cancel out. Only in the overlap region between the direct part and the rescattered part could we hope to detect interferences that are related to the energy dependence of the scattering phase similar to “photoelectron holography” techniques employed for atoms and molecules [Huisman et al., 2011; Bian et al., 2011; Bian and Bandrauk, 2012]. Exquisite control of the laser pulse shape, for example employing two-color laser pulses, may help in selecting rescattering trajectories such that this overlap re-

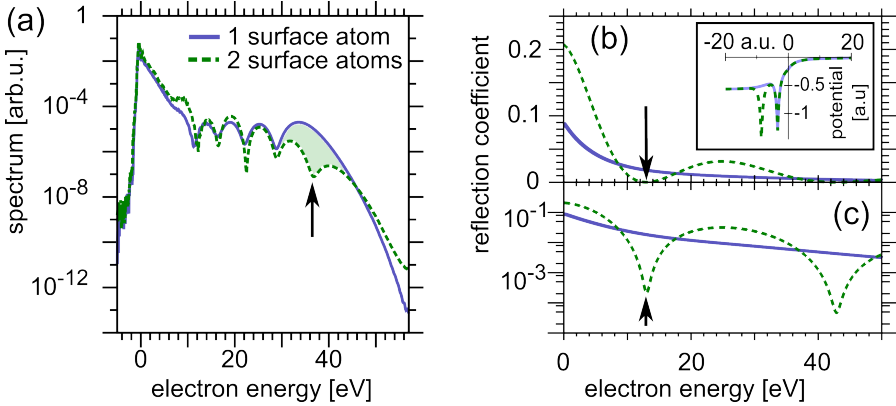


Figure 3.9: Sensitivity of rescattering to the surface structure. (a) Electron spectra for $F_{\text{eff}} = 0.022$ a.u., $\omega = 0.03$ a.u. ($\lambda = 1519$ nm) for a very short pulse (3.8 fs FWHM intensity). Solid blue line: one atom potential at the surface; dashed green line: additional second atom potential at distance $a_{\text{latt}} = 5.2$ a.u. from the first, see inset in (b). Arrow indicates additional minimum for the two-Coulomb potentials. (b) Reflection coefficient of the one-atom (blue solid line) and two-atoms potentials (green dashed line) on linear scale and log scale (c). Arrows indicate minimum of the reflection coefficient for the two-atom potential. **Inset:** One-atom (blue solid line) and two-atom potential (green dashed line) $V(z)$ along the surface normal z .

gion is magnified [Xie et al., 2012].

Secondly, the length scale of structures of the surface potential that can be resolved by the rescattering electron is related to the electron energy at rescattering, $E_{\text{scat}} = p_{\text{scat}}^2/2 \sim 3U_p = 3(F_{\text{eff}}/2\omega)^2$ via its de Broglie wavelength $\lambda_{\text{dB}} = h/p_{\text{scat}}$. For these laser parameters, $U_p \sim 0.8$ eV and $\lambda_{\text{dB}} \sim 15$ a.u., much larger than the typical extension of an atomic core potential (typical Thomas-Fermi screening length $\lambda_{\text{TF}} \sim 1$ a.u.). In this low-energy limit the rescattering coefficient varies slowly over the energy range in Fig. 3.8 and only its average magnitude is important for the spectra.

In a solid, besides the typical extension of the potential of a single atom, a second length scale is of importance: The average distance between two atoms sets the basic parameters for the Brillouin zone and band structure. At the parameters discussed above, the de Broglie wavelength $\lambda_{\text{dB}} \sim 15$ a.u. is several times the typical layer spacing of $a_{\text{latt}} \sim 5$ a.u.. We can, however, expect that for increased scattering energy $E_{\text{scat}} \sim 3 \cdot U_p = 3(F_{\text{eff}}/2\omega)^2 \propto 1/\lambda$, λ_{dB} will come into the range of the lattice constant. While the laser field strength is already near the destruction threshold at 800 nm, we may employ the laser wavelength to increase the rescattering energy. We performed proof-of-principle calculations for $\omega = 0.03$ a.u. ($\lambda = 1519$ nm) at field strength $F_0 = 0.022$ a.u. such that $U_p \sim 3.7$ eV and $\lambda_{\text{dB}} \sim 7$ a.u.. In one calculation, we kept the atomic potential as described above, while in the second calculation, we added a second layer of atoms at a distance of 5.25 a.u. from the first (inset in Fig. 3.9 b). The second atomic layer leads to additional minima in the reflection coefficient (arrow in Fig. 3.9 b,c; the reflection coefficient is calculated from a solution of the static Schrödinger equation for the potentials shown in the inset of (b) by the

Numerov algorithm). The first minimum of the reflection coefficient is at about 13 eV, corresponding to a de Broglie wavelength of the incoming electron of about 6.4 a.u., which is however reduced by the smooth attractive surface potential. According to the simple man's model we expect that electrons that scatter with about $3U_p$ will reach final energies of about $10U_p$, gaining a factor of about 3 between rescattering and the end of the laser pulse. We therefore expect an additional minimum in the electron spectra that corresponds to the minimum in the reflection coefficient at around 40 eV (Fig. 3.9). Indeed, while the electron spectra show good agreement for the low energy parts of the spectra between simulations with a single layer and a double layer, we find an additional pronounced minimum near 40 eV that we trace back to the minimum in the reflection coefficient for the double layer simulation.

The ideas and results presented in this section show that the rescattering process can be sensitive to details of the surface structure on the length scale of a few atomic units if electrons of a de Broglie wavelength that can resolve these structures are used by increasing the laser wavelength. Our findings suggest that the so-called quantitative rescattering theory developed for atoms and molecules for both electron spectra and high harmonic spectra can be extended to surfaces as well [Chen et al., 2009; Le et al., 2009; Lin et al., 2010; Le et al., 2012].

3.10 Emission of high harmonic radiation from nano-tips

Up to now, we have investigated the energy spectra of the electrons which are photoemitted from a metal nanotip by ultrashort laser pulses. In this final section, we discuss (and allow ourselves to speculate on) the feasibility of investigating the spectrum of photons emitted by high-harmonic generation (HHG, see e.g. Corkum and Krausz [2007]; Krausz and Ivanov [2009]; Midorikawa [2011]). In the interaction of intense few-cycle laser pulses with atoms and molecules, HHG has been robustly observed across a range of atomic and molecular targets and laser parameters. It has been used for a variety of applications, from the generation of isolated attosecond pulses in the XUV range [Chini et al., 2014] to the generation of bright coherent X-rays in the keV range [Popmintchev et al., 2012] to the tomographic imaging of molecular orbitals [Itatani et al., 2004; Vozzi et al., 2011]. Analogously to the emission of high-energy electrons, the emission of high harmonic radiation can be understood by the quasi-classical three step model. The electron tunnels out near the maxima of the electric field and is subsequently driven back towards the atomic core as the laser electric field changes its sign. As the electronic wave packet interferes with the remaining ground state portion of the wave function in the steep potential gradient near the atomic core, high harmonic radiation is emitted [Kohler et al., 2010]. The cutoff of the radiation energy corresponds to the energy difference between ground state at $-I_p$ and the maximal return energy of the electron, and is given classically by $E_{\text{cut}} = I_p + 3.17U_p$.

While the generation of high harmonics is relatively well understood for atoms

and molecules, studies for systems with many atoms and the investigation of collective effects have remained elusive. Collective excitation effects in atoms, namely the giant resonance analogous to the plasmon resonance in solid state physics, have only recently been demonstrated to affect HHG [Shiner et al., 2011]. Only few experiments have been carried out for cluster targets (see Fennel et al. [2010] and references therein), all of which show a significant enhancement of HHG compared with atomic spectra but no clear signatures of collective excitations. Another promising candidate system is C_{60} , where an extension of the harmonic cutoff was found experimentally and has been attributed to multi-electron effects [Ganeev et al., 2009]. This interpretation agrees with theoretical predictions that in multi-electron targets an additional reaction pathway for recollisional excitation may open up [Ruggenthaler et al., 2008]: Plasmons, quanta of collective electronic excitations, may be excited by the recolliding electron. While estimates for C_{60} predict that plasmon excitations decay faster than the laser period at optical frequencies [Ruggenthaler et al., 2008], high harmonic emission from a highly correlated one-dimensional model system has shown a qualitatively different behavior [Zanghellini et al., 2006]. Ionization starts from the plasmon state and recolliding electrons can return to the ground state, thereby extending the cutoff by the plasmon energy. For metal nano-tips, second-harmonic generation from the tip apex has been observed [Bouhelier et al., 2003; Neacsu et al., 2005] but observation of higher-order harmonics has so far remained elusive.

In the following, we discuss proof-of-principle simulations that employ the same numerical model that was used to describe electron emission and rescattering and evaluate the spectrum of emitted radiation from the time-dependent dipole moment near the surface. Before presenting the results of our simulation, we halt to discuss the physics of high-harmonic generation in nanostructures and the capability of our simulation to faithfully model this process.

Firstly, high-harmonic generation for atoms relies on the interference of the recolliding wave-packet with the portion of the initial state that has remained at the atomic core. While for an atom, the remaining portion of the wave function necessarily stays localized at the core, the situation is different for a dynamical “hole” in a metal. It is presently not clear in how far hole dynamics including diffusion of the hole away from the surface are correctly reproduced in TD-DFT, or how the effectively one-dimensional treatment impacts the underlying dynamics. Even in view of such uncertainties, our simulation surpasses the present state of the art employing a single active electron approach with a hard wall and an empirical well potential [Ciappina et al., 2014]. Unfortunately, further improvements in the physical description appear difficult to come by, so that the final assessment of the validity of the approximations employed must be deferred until experimental data become available.

As a second caveat, we note that while our model contains the basic mechanisms of screening and tunneling of a metal surface along with a correct description of the local microscopic electric field along the surface, the dielectric behavior of a d-electron metal like tungsten is not correctly reproduced by our free-electron model. Instead,

our model gives a Drude-like dielectric function typical of free electron metals with a single sharp peak at the plasma frequency ($\omega_p = 13.2$ eV). Such a well-defined collective excitation is a prerequisite for the observability of the collective effects discussed in the following. Realistically, it can only be expected in nanostructures made from free-electron metals like Mg or Al. However, since our model correctly reproduces the intensity of the rescattering plateau for electron emission, we can hope that it should also give the right order of magnitude for the generation of high harmonic radiation up to the plasmon energy even for materials that are less free-electron like.

After discussing the validity of our theory, we turn to describe the physics at play in our simulation. We calculate the spectrum of the emitted radiation as the Fourier transform of the acceleration of the surface dipole moment. Only the induced dipole near the surface of the metal is taken into account, as integration over the whole simulation box introduces artifacts associated with the absorbing potentials. We evaluate the time-dependent dipole moment over a region of 50 a.u. (~ 2.5 nm) near the surface, which is much larger than the width of the induced screening charge layer (Friedel oscillation wavelength $\lambda_F/2 \sim 4$ a.u.). While the shape of the spectra changes somewhat with the integration border, the main features and conclusions presented in the following are independent of this parameter.

We simulate high harmonic spectra for laser parameters of present experiments for several laser intensities up to $I_{\text{eff}} = 1.1 \times 10^{13}$ approaching the experimental destruction threshold. All spectra show the characteristic high harmonic peaks at multiples of ω , where, in contrast to atomic targets, both even and odd multiples are observed due to the broken inversion symmetry at the tip surface. A plateau extending over several peaks is followed by a cutoff, and the cutoff energy increases with intensity. In contrast to atomic spectra, strong differences appear: Even at the lowest intensity, an additional peak shows the presence of a collective excitation which is identified with the jellium plasma frequency $\omega_p = \sqrt{3/r_s^3} = 13.2$ eV (Fig. 3.10 a). While the classical cutoff law $E_{\text{cut}} = W + 3.17U_p$ holds for the lowest intensities, the presence of the plasmon peak appears to enhance the spectral intensity up to ω_p for the larger intensities. For the intermediate intensity $F_{\text{eff}} = 0.010$ a.u. an additional large-scale modulation above the cutoff energy is visible, where multiple plateaus and cutoffs can be identified. Zanghellini et al. [2006] proposed the following mechanism for the extension of the cutoff by collective excitations: First, the plasmon state is populated by rescattering. Then, an electron from the plasmon state is ionized and during its motion in the continuum obtains the maximal classical return energy of $3.17 U_p$ from the laser field. Upon returning it interferes with the ground state wave function, extending the cutoff by the plasmon energy. This estimate for the maximum energy of emitted radiation fits our calculations quite well ($E'_{\text{max}} = W + 3.17U_p + \omega_p$). We verified that this extension of the cut-off is linked to plasmon excitation by switching off the electron-electron interaction in the time-dependent Kohn-Sham equations, in which case the extension of the cut-off is not observed.

We further analyze the dynamics of HHG by a time-frequency analysis of the dipole

acceleration for $F_{\text{eff}} = 0.018$ a.u. (Fig. 3.10 b,c). The dynamics of the real-space density are the same as discussed in section 3.4: Around the maxima of the electric field, electrons tunnel out and are subsequently accelerated back towards the surface where they can be backscattered from the first layer of atoms. The induced dipole moment is for the most part due to the screening charge layer that forms near the surface synchronized to the driving field, which is responsible for the strongest peak in the harmonic spectra at $1 \times \omega$. This peak corresponds to the large structure in the time-frequency plot around $1 \times \omega$ that is, notably, symmetric with respect to the center of the laser pulse at $t = 0$ (Fig. 3.10b). The radiation emitted at higher frequencies shows a very different timing behavior. The emission of the highest frequencies approximately coincides with the collision times expected from the simple man's model around the zeros of the laser field. The maximal energy of emitted radiation is increased beyond the maximum classical energy. The emission of high-energy radiation is *not* symmetric with respect to the pulse envelope, but is delayed by about two optical cycles. This behavior is consistent with the scenario suggested by Zanghellini et al. [2006]: the leading edge of the laser pulse serves to sufficiently populate electron states around the plasmon energy ω_p . Only thereafter can electrons released with the plasmon energy obtain additional kinetic energy from the laser field, and recombine to the ground state giving rise to the high-energy radiation.

Up to now, high harmonic generation from nanostructures including from a metal tip has not been observed. We briefly give an order-of-magnitude estimate of the expected photon yield to illustrate why this could be the case. We first estimate the order of magnitude of the linear response in absolute units (peak at 1.55 eV in Fig. 3.10a). For simplicity, we model the nano-tip as a nano-sphere of the same radius of curvature since the enhanced near-field is strongly localized at the apex of the tip. The order of magnitude of the induced dipole moment $d(\omega)$ at the driving wavelength in linear response can be used as a measure of the scattering power of a nanostructure and follows from the polarizability of a sphere of dielectric constant ϵ , $\alpha_{\text{sphere}} = R_{\text{sphere}}(\epsilon - 1)/(\epsilon + 2)$ as $d(\omega) = \alpha_{\text{sphere}}F_0$. Assuming the angle-integrated radiation is detected, the integral of the scattered field of the dipole over the solid angle is given as [Jackson, 1998]

$$\int d\Omega |E_{\text{scat}}|^2 = F_0^2 \frac{4\pi}{3} \left(\frac{2\pi}{\lambda} \right)^4 R_{\text{sphere}}^6 \left| \frac{\epsilon - 1}{\epsilon + 2} \right|^2 \quad (3.51)$$

where the last factor is of the order of 1 for metals at optical frequencies. The incoming pulse, taken to have an intensity of $I_0 = 1.1 \times 10^{11}$ W/cm² (enhanced intensity at the apex $I_{\text{eff}} \sim 6 \times 10^{12}$ W/cm²) focused to 1.6 μm with a pulse length of 6.5 fs and a wavelength of 800 nm, contains about 2.3×10^8 photons. Evaluation of Eq. 3.51 yields a number of scattered photons of about 0.5 per pulse. This is the expected absolute magnitude of the "direct" peak at photon energy 1.55 eV in Fig. 3.10a. Perfect phase matching is assumed since the tip radius is smaller than the wavelength of the high harmonic radiation. Taking for example the 7th harmonic around 11 eV photon

energy and taking the reduction of the intensity of the plateau compared to the response at the driving frequency from Fig. 3.10, we arrive at a yield of 7×10^{-4} of 7th harmonic photons per laser pulse or 56000 photons/s at a typical experimental repetition rate of 80 MHz. This corresponds to a total emitted power of 1×10^{-13} W, or a power conversion efficiency of about 10^{-11} , which suggests experimental detection to be difficult. We may compare HHG from a nanostructure to HHG from a gas of atoms, where the number of atoms in the laser focus is about 10^{10} , while the surface of a nano-tip of radius 10 nm only contains about 5000 atoms. This huge disparity in the number of emitters makes the observation of HHG from isolated nano-structures difficult. Likely, it is a main reason why high harmonic generation in the enhanced near-field of subwavelength structures is difficult to observe (for attempts and discussions see Kim et al. [2008]; Siviis et al. [2012]; Pfullmann et al. [2013]; Lupetti et al. [2013]). Partially, the decrease in signal can be set off by the increase in repetition rate for laser oscillators. Another way out of this dilemma may be the irradiation of large ensembles of nanostructures. Candidate systems include bow-ties on a surface [Kim et al., 2008], free-standing copper nanowires grown in polymer ion-track membranes [Maurer et al., 2006], or nano-patterned arrays of doped silicon tips [Swanwick et al., 2014].

In the above estimate, the emission characteristic of a nano-tip was modeled as a dipole oscillating along the tip axis. A more detailed calculation takes into account the field enhancement of the NIR pulse at the tip apex and assumes a scaling of the induced dipole moment at the n -th high harmonic frequency $d_n \propto F^{2n}$ with the near field. This scaling is also found to a good approximation in our TD-DFT calculation for intensities $I_{\text{eff}} \lesssim 1 \times 10^{13}$ W/cm². The Maxwell equations are then solved for an ensemble of radiating dipoles on the surface of the tip with the boundary element method (see chapter 2). The far-field emission characteristic is very similar to a dipole (Fig. 3.10d) with a slight shift of the maximum emission towards the back of the tip that we attribute mostly to the effect of the non-zero dielectric function of the tip on the dipole emission [Mertens et al., 2007]. On the other hand, taking into account an ensemble of dipoles on the tip surface instead of a single dipole has a smaller effect. The emission characteristic of a nano-structure differs markedly from HHG from an atomic gas where phase-matching provides a well-collimated XUV beam.

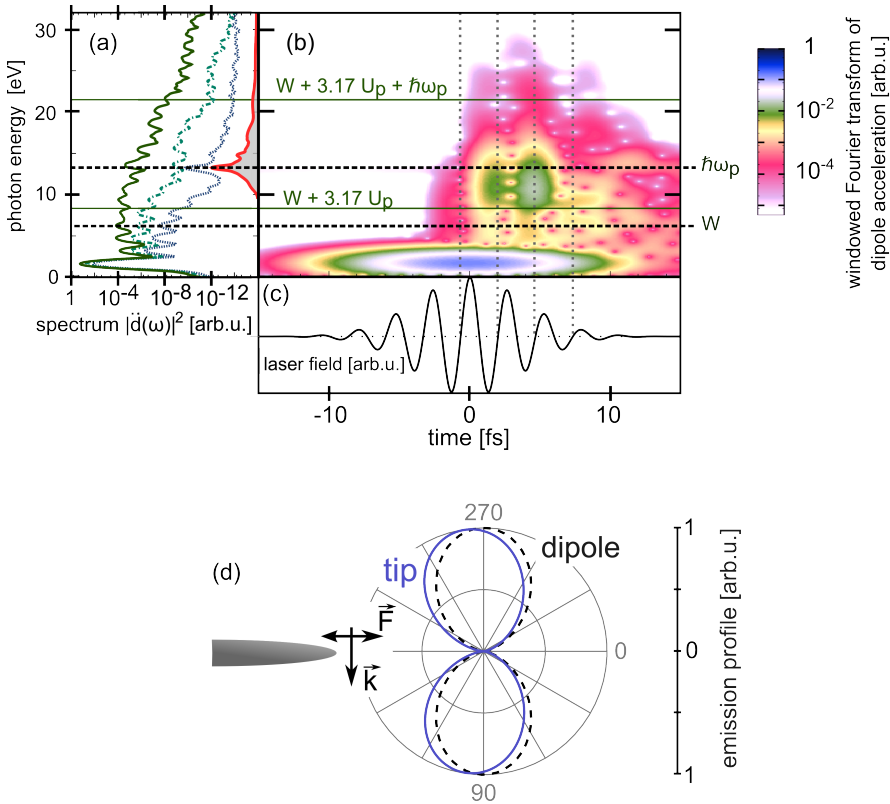


Figure 3.10: Calculated high harmonic spectra, time-frequency analysis, and emission characteristics. (a) Calculated high harmonic spectra from the dipole acceleration, $|d(\omega)|^2$, at different laser field strengths. Full green line: $F_{\text{eff}} = 0.018$ a.u.; dash-dotted turquoise line: $F_{\text{eff}} = 0.010$ a.u.; dotted blue line: $F_{\text{eff}} = 0.005$ a.u.; solid red line and shaded area: delta kick (scaled). (b) Time-frequency analysis of the surface dipole moment. The highest emitted photon energies are well above the classical cut-off. Emission of the highest photon energies is strongly asymmetric with respect to the laser pulse shape (c) and is localized in time around the zero crossings of the electric field where rescattering occurs (dotted horizontal lines). Horizontal dashed lines give positions of work function $W = 6.2$ eV plasmon energy $\omega_p = 13.6$ eV. Green horizontal solid lines give the position of the classical cut-off for $F_{\text{eff}} = 0.018$ a.u., $W + 3.17U_p = 8.35$ eV and the classical cut-off increased by the plasmon energy, $W + 3.17U_p + \omega_p = 22.0$ eV. (d) Angular high-harmonic emission characteristic of a nanotip (blue solid line) and a dipole (dashed line). The tungsten nanotip has a radius of 10 nm and opening angle 0 deg, 7th harmonic of 800 nm ($\epsilon_W(114 \text{ nm}) = 0.8 + 2.1i$ [Windt et al., 1988]). Inset: geometry of tip, propagation direction (\vec{k}), and polarization direction (\vec{E}) of the electric field. The emission profile is symmetric around the tip axis.

3.11 Conclusions and outlook

In this chapter, we have presented simulations for electron emission from metal nano tips as a prototypical system for electron emission from metal nano structures. The observed signatures of strong-field physics, namely the multi-photon peaks and the rescattering plateau in the electron spectra, were explained by a semi-analytical model based on the simple man's model. We have developed a microscopic description of the quantum surface dynamics at metal nanostructures based on time-dependent density functional theory that includes electron-electron interaction on the mean-field level. It successfully describes the tunneling of electrons near the maxima of the electric field and the nearly-free motion of the continuum electron wave packet near the metal nanostructure and subsequent rescattering from the first layer of surface atoms. We have demonstrated that our simulation is in excellent agreement with available experimental results and reproduces the delicate dependence of the electron spectra on details of the pulse shape. Our semi-classical model was used to interpret these carrier-envelope phase dependent electron spectra and disentangle the contributions from laser-field dependent tunneling and the motion of the wave packet in the continuum. We demonstrated that our simulation of quantum surface dynamics is capable of describing the microscopic field distribution at metal surfaces, which has recently become accessible to experimental scrutiny by the attosecond surface streaking technique. Our simulation predicts strong sensitivity of the electron spectra to the surface lattice structure and adsorbates for longer NIR laser wavelengths where the de Broglie wavelength of the recolliding electron becomes of the same order of magnitude as typical lattice constants and bonding distances. We discussed the possible emission of high-harmonic generation during rescattering and estimated the high harmonic yield that can be expected.

Future work will fall into three categories. First, the existing tools that were presented in this section can be employed to further improve the understanding of present experiments and to uncover physics in yet unexplored parameter regimes. The application of the semi-classical simple man's model to the carrier-envelope phase dependence of rescattering has already yielded promising results and a further extension including direct trajectories and interference terms along the classical trajectories may be able to explain even the fine structure in the electron spectra possibly enabling detailed pulse shape diagnostics. Along the same lines, a semi-classical model should be able to explain the additional interference structures seen at larger wavelengths in terms of contributions from "long" and "short" trajectories. An extension of both the quantum simulation and the semi-classical simulations to longer wavelengths where the inhomogeneity of the electric near-field is sampled by the photoemitted electrons is expected to reveal novel information about the near-field decay in the phase information encoded in the interference fringes. While we have already demonstrated that the magnitude of the electron spectra is sensitive to the surface potential on the atomic scale, we expect that also the scattering phase of the surface potential can be extracted

from the holographic information contained in the interferences of direct and rescattered electrons, perhaps aided by a selection of trajectories that maximize the overlap between direct and rescattered wave packets by advanced pulse shaping. Such delicate control of trajectories will also leave its marks in the high-harmonic response once it becomes accessible to experiment. The high sensitivity of electron spectra to the pulse shape and the laser intensity suggests that the electron spectra can be used to measure the magnitude of induced near-field at nano-structures, or alternatively, to map out the pulse shape within a laser focus to within nanometric precision by moving the tip with respect to the laser focus. First experiments on a nano-junction consisting of two tips placed at a controllable nanometric distance to each other have been reported [Savage et al., 2012], however in the linear response regime of low laser intensity. Extension of these experiments to the strong-field regime will lead to the observation of novel non-linear effects such as light-field induced currents through the nanojunction that can be described by the methods put forth in this chapter.

Secondly, work will be devoted to extending the present one-dimensional quantum simulations to three dimensions. While this can be done rather efficiently for the semi-classical model, the three-dimensional quantum simulations will become numerically challenging even for large supercomputers. While first simulations of coupled Maxwell and quantum dynamics described by TD-DFT have been reported by Yabana et al. [2012] for a high-symmetry flat surface, it will not be possible to extend such simulations to the full three-dimensional tip geometry in the foreseeable future. Instead, calculations employing a periodic surface unit cell in analogy to our one-dimensional jellium calculations will enable us to study the influence of the atomic structure of the surface on the electron emission and rescattering process from first principles. For example, such simulations can address the question where the electrons preferentially tunnel from, including the role of possible surface adsorbates, and elucidate differences in the dynamics of electrons coming from delocalized versus localized initial states like d-orbitals or surface states. Results may be compared with first experimental results of angle-resolved multiphoton emission spectra from solid surfaces [Sirotti et al., 2014]. Simulations and experiments of the fully angle-resolved electron spectra including electron rescattering can be used to image the surface structure as well as changes in the surface structure with sub-femtosecond precision. Finally, the microscopic electric field at interfaces can be studied both in the linear and non-linear regime and can be compared to attosecond surface streaking experiments.

Thirdly, work will be devoted to combine the semi-classical description of the simple man's model with the Maxwell simulations presented in chapter 2 and will enable us to study the time-dependent near-fields by their effects on photo-emitted electrons in three dimensions on the mesoscopic length scale. Photoemission can either be triggered by strongly non-linear tunneling-like electron emission from the apex as described by TD-DFT or alternatively by a sub-femtosecond XUV pulse synchronized to the incoming optical pulse (attosecond streaking). Both can be described

by a classical trajectory Monte Carlo simulation of electrons emitted from the nano-tip in the presence of the electromagnetic near-field. For strong-field photoemission from the tip apex, the focusing properties of the near-field of a nano-tip depending on the driving laser wavelength and the effects of the near-fields on the angular spectra of emitted electrons have been investigated by Herink et al. [2012] and Park et al. [2012] using a dipole field and a quasi-static approximation respectively. Our Maxwell simulations show that such approximations can only serve as first estimates of the fields near the tip apex. Recent TD-DFT simulations for strong-field electron emission by two-color pulses [Madlener, 2014] suggest that a strong variation in electron emission probability can be expected as a function of the phase shift between first and second harmonic. It remains to be seen if such sensitivity survives three dimensional averaging over the hot spot on a nano-tip and subsequent propagation of the emitted electrons in the enhanced near field. Along the same lines, the attosecond streaking technique will be extended from surfaces to nanostructures [Süssmann and Kling, 2011]. For electrons photo-excited by the XUV pulse inside the nano-tip, electron transport must be accounted for [Lemell et al., 2009]. In the XUV wavelength range, little or no field enhancement at the apex is expected, and electron emission by the single-photon process is equally probable from the whole illuminated surface area of the nano-tip. Therefore, exquisite focusing of the XUV radiation onto the tip apex will be necessary to reduce the background signal from the tip shank. Alternatively, tips of small opening angle may be used in conjunction with an XUV pulse that impinges along the tip axis, so that the geometrical cross section of the apex compared to the shank is increased.

Strong-field induced electron dynamics in bulk insulators

4.1 Introduction

We have demonstrated that intense few-cycle laser pulses trigger electron emission from metal nanostructures and can steer the electron motion on the sub-nanometer length and femtosecond time scale in the vicinity of the emitting nanostructure. This degree of control over the motion of electrons is exciting from a fundamental point of view and may be attractive for surface analysis due to the strong sensitivity to the surface structure and surface chemistry. However, experiments relying on electron emission require a high degree of control over the nanoscopic shape of the sample as well as its atomic structure and composition and must be performed in ultra-high vacuum. In this chapter, we investigate the complementary idea of using intense ultrashort optical laser pulses to trigger and control electron motion not outside but *inside* solid matter. Metals, due to their quasi-free conduction band electrons, are highly reflective at optical wavelengths and do not permit propagation of electromagnetic waves inside the metal beyond the skin depth of ~ 10 nm at optical frequencies. So far, time-dependent processes have been investigated only within the first few nanometers within the regime of the optical field near the surface [Cavaliere et al., 2007; Neppel et al., 2014]. On the other hand, large band gap insulators like window glass (SiO_2) are transparent for light at optical wavelengths and allow the propagation of an intense few cycle pulse through macroscopic lengths of bulk matter. Pioneering studies on the interaction of transparent dielectrics with intense laser pulses [Gertsvolf et al., 2008, 2010; Shih et al., 2009; Mitrofanov et al., 2011; Ghimire et al., 2011a,b] found a strongly non-linear response and first indications for electronic dynamics on the femtosecond time scale probed by optical readouts. Very recent transient absorption spectroscopy experiments employing attosecond pulses proved that

the optical properties of bulk insulators are modified on the time scale of femtoseconds [Schultze et al., 2013], and found a surprisingly high degree of reversibility of these changes. These findings point to possible ultrafast switching of optical properties of bulk matter by intense laser pulses on the femtosecond time scale. Strong-field interaction with condensed matter thereby promises to realize light-field electronics with devices operating in the femtosecond domain, several orders of magnitude faster than semiconductor-based electronics [Krausz and Stockman, 2014].

A substantial advance towards such “lightwave electronics” was achieved in very recent experiments that demonstrated direct control of macroscopic amounts of electric charge by nothing but the electric field of a laser pulse itself. Schiffrin et al. [Schiffrin et al., 2013, 2014; Paasch-Colberg et al., 2014] demonstrated that intense ultrafast few cycle laser pulses trigger currents in bulk dielectrics leading to a separation of charges collected by unbiased electrodes on the surface of the dielectric (Fig. 4.1). Control over the laser pulse shape determined by amplitude and carrier-envelope-phase translates into exquisite control over the magnitude and direction of the induced current.

In contrast to the electrical current and subsequent electron-avalanche breakdown that is induced by static fields or picosecond laser pulses [Sparks et al., 1981], the results by Schiffrin et al. indicate optical-field induced transient and reversible currents below the destruction threshold. Their findings suggest that the intense laser field strongly distorts the potential landscape, bond structure, and electronic band structure and thereby converts an insulator transiently into a metal on the (sub-) femtosecond time scale. This picture is supported by first modeling efforts based on independent-particle models [Apalkov and Stockman, 2012; Földi et al., 2013; Korbman et al., 2013; Schiffrin et al., 2013; Hawkins and Ivanov, 2013; Kruchinin et al., 2013; Schiffrin et al., 2014]. However, all previous approaches are based on one- or two-dimensional model equations and in large part contain phenomenological or fitting parameters. They neglect the microscopic bond structure of the sample, instead replacing the intricate three-dimensional electronic structure by, for example, model potentials that only reproduce selected properties like the band gap. Effectively, they average the ongoing physical processes over one unit cell and over the lattice directions so that a study of the three-dimensional electron dynamics within the unit cell has hitherto remained elusive, and the relation between the ultrafast dynamics and the microscopic lattice and electronic structure of the sample has remained unexplored. In contrast, experiments and theory for pulse-shape sensitive currents emitted from atomic gas targets [Milosevic, 2006] and nanostructures (chapter 3) trace the strong pulse-shape sensitivity of the currents to electron emission by tunneling and subsequent steering of the electron wavepacket in the continuum. The tunneling process is highly sensitive to details of the potential structure in the vicinity of the bound electron as demonstrated by strong-field experiments on molecules [Itatani et al., 2004; Meckel et al., 2008; Morishita et al., 2008; Haessler et al., 2011; Lock et al., 2012]. Therefore, we expect that a description of the electronic structure in three di-

mensions in real space is indispensable for the description of the strong-field response of bulk insulators.

In this chapter, we set out to give a microscopic description of strong-field induced currents in dielectrics. We employ state-of-the-art fully three-dimensional *ab-initio* quantum simulations based on time-dependent density functional theory in real space and real time. Our simulations capture the non-linear response of a bulk solid to a strong time-dependent perturbation by an electric field. They permit us to “look inside a unit cell” on the sub-nanometer length scale and sub-femtosecond time scale and resolve the microscopic spatio-temporal structure of the dynamically relevant microscopic quantities, the space and time dependent electron density and electrical current density.

We begin this chapter by a brief description of our formulation of TD-DFT for a bulk solid (section 4.2). We then discuss in detail our simulation of optical-field induced currents in α -quartz (SiO_2), starting with a discussion of the ground state electronic structure and the linear and low-order non-linear response to an electric field (sections 4.3 and 4.4). We next investigate the strongly non-linear response in the spirit of the experiment by Schiffrin et al. [2013] including the dependence on the laser intensity, carrier-envelope-phase, and direction of the laser polarization with respect to the crystal axes (section 4.5). We discuss the possible influence of the macroscopic shape of the sample and the electronic excitations remaining in the material after the end of the laser pulse and its ramifications for possible petahertz lightwave electronics applications. We then describe a strongly non-linear version of the “photo-galvanic effect”, i.e., ultrafast charge transfer along the non-inversion symmetric \hat{a} crystal direction that is *not* sensitive to the carrier-envelope phase (section 4.8). Finally, we turn to other observables accessible to our simulation besides the total transferred charge and study optical signals that carry the imprint of the ultrafast electron dynamics (section 4.9).

4.2 Time-dependent density functional theory for a bulk solid

We briefly describe our real-space, real-time formulation of time-dependent density functional theory for a periodic bulk solid [Yabana and Bertsch, 1996; Bertsch et al., 2000; Yabana et al., 2006; Otobe et al., 2009; Yabana et al., 2012; K. Yabana et al., 2013]. It has been applied to a number of different materials and observables [Otobe et al., 2008; Shinohara et al., 2010, 2012a; Otobe, 2012; Lee et al., 2014; Sato et al., 2014; Sato and Yabana, 2014]. Similar methods are being developed by other groups [Husser et al., 2011; Wang et al., 2013]. The large-scale collaborations *octopus* [Marques, 2003; Castro et al., 2006; Andrade et al., 2012] and *GPW* [Mortensen et al., 2005; Walter et al., 2008; Enkovaara et al., 2010] contain similar functionalities.

We consider an infinitely extended periodic system under the influence of a spatially uniform time dependent electric field $\mathbf{F}(t)$ corresponding to a vector potential $\mathbf{A}(t) = -\int_{-\infty}^t \mathbf{F}(t') dt'$. The electron dynamics within one unit cell are described by

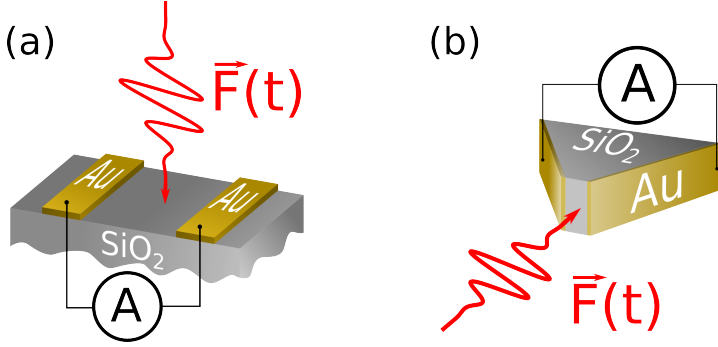


Figure 4.1: Experimental geometry for measuring optical field induced currents. An optical few-cycle laser pulse $\vec{F}(t)$ impinges onto a bulk insulator (SiO_2). The field-induced current leads to a charge separation along the polarization direction after each laser shot that is measured in the ammeter. **(a)** Stripe-shaped electrodes on flat sample. **(b)** Electrodes enclosing the sample and at an oblique angle with respect to each other. The pulse-sensitive field induced currents were measured for both sample geometries. The gap between the electrodes is between 50 – 500 nm, guaranteeing homogeneous illumination of the sample.

the time-dependent Kohn-Sham equations

$$i\partial_t\psi_i(\mathbf{r},t) = H_{\text{KS}}(\mathbf{r},t)\psi_i(\mathbf{r},t) \quad (4.1)$$

with the Kohn-Sham Hamiltonian

$$H_{\text{KS}}(\mathbf{r},t) = \frac{1}{2}(\mathbf{p} + \mathbf{A}_{\text{tot}})^2 + \hat{V}_{\text{ion}} + \int d\mathbf{r}' \frac{n(\mathbf{r},t)}{|\mathbf{r} - \mathbf{r}'|} + V_{\text{XC}}(\mathbf{r},t) \quad (4.2)$$

where the index i runs over the occupied orbitals, \mathbf{p} is the momentum operator, the lattice structure is included in terms of pseudopotentials \hat{V}_{ion} , the next term is the electrostatic potential from the electron density $n(\mathbf{r},t) = \sum_i |\psi_i(\mathbf{r},t)|^2$, and the last term is the exchange-correlation (XC) potential. For the latter, we again assume the adiabatic approximation employing the local density approximation (LDA) as well as a recently proposed advanced meta-generalized gradient approximation (GGA) functional that will be discussed in detail in the next section.

We employ the velocity gauge for the coupling to the electromagnetic field by $\mathbf{A}(t)$ so that the lattice periodicity of the scalar potential is conserved allowing the treatment of a single unit cell with periodic boundary conditions. The homogeneous electric field is represented by a vector potential $\mathbf{A}_{\text{tot}}(t)$ which includes the external vector potential $\mathbf{A}(t)$ from the laser field and can also include the induced vector potential from the accumulation of charge at the macroscopic boundaries of the sample. By default however, we employ the so-called “transverse” geometry, that is we treat a truly infinite system along the laser polarization direction and neglect any induced fields that stem from the surface charge so that the external field is equal to the total field. Neglecting the influence of the surface charge appears appropriate so as to model “ideal” metal electrodes that do not permit a surface charge patch to

form. The complimentary choice of a thin film target will be discussed in section 4.6. As the coupling to the external electric field enters in terms of the vector potential, the Hamiltonian (Eq. 4.2) can alternatively be viewed as the starting point of time-dependent *current* density functional theory [Vignale and Kohn, 1996; Vignale et al., 1997; Giuliani and Vignale, 2005] in the adiabatic approximation, neglecting the non-adiabatic exchange-correlation contribution to the vector potential \mathbf{A}_{XC} . This term plays a key role in describing relaxation and dissipation in an interacting many-body system [Wijewardane and Ullrich, 2005; D’Agosta and Vignale, 2006; Di Ventura and D’Agosta, 2007]. Explicit expressions for \mathbf{A}_{XC} have so far only become available in the linear response limit [Vignale and Kohn, 1996] and furthermore, the degree of improvement with respect to experiment that was achieved in first applications is still limited [Nazarov et al., 2007; Berger et al., 2007]. In view of the numerical complexity of the present simulation we neglect this term, neglecting relaxation phenomena from the outset. Relaxation sets in at a timescale of $\gtrsim 20$ fs so that the dynamics during and shortly after a few-cycle pulse are described correctly.

The initial state of the system is obtained by solving the ground state (static) Kohn-Sham equations ($\mathbf{A}(t) = 0$) by a conjugate gradient minimization before the time-dependent simulation. As the scalar potential is unit-cell periodic in space, Bloch’s theorem applies to the orbital wave functions during the simulation yielding periodic orbitals $u_{n,\mathbf{k}}(\mathbf{r}, t)$ defined by $\psi_i(\mathbf{r}, t) = e^{i\mathbf{k}\mathbf{r}}u_{n,\mathbf{k}}(\mathbf{r}, t)$ where the orbital index i is composed of the band index n and the crystal momentum \mathbf{k} . Eqs. 4.1 are solved on a uniform Cartesian grid in real and \mathbf{k} space. The space derivatives of the wave functions are calculated by high-order finite difference formulas [Chelikowsky et al., 1994] employing nine-point formulas for the first and second derivatives so that the application of the Hamiltonian to the wave function can be efficiently handled by standard methods for the multiplication of a sparse matrix with a vector. For the strong-field simulations, the real space grid is of order 0.2 a.u. along the laser polarization and 0.4 a.u. along the perpendicular directions, giving a total size of the real space grid around 40000 points. We employ a $4 \times 4 \times 4$ grid in \mathbf{k} -space ensuring convergence with test calculations up to $8 \times 8 \times 8$ \mathbf{k} -points. The time evolution is performed with a Taylor expansion of 4th order with a time step of 0.02 a.u. [Yabana and Bertsch, 1996]. Our implementation has efficient parallelization over the \mathbf{k} -point grid allowing simulations to be run on 64 cores in parallel. For the relatively large SiO_2 unit cell, further parallelization over the real space grid would be desirable. First steps to implementing a hybrid parallelization scheme (MPI over \mathbf{k} -points and OpenMP for the real-space grid) have been taken. In this work, hybrid parallelization has not been used for production results as we found that even though the wall clock time can be somewhat reduced, the computational cost would have increased by a significant fraction. The simulations presented below typically take up to 3 days on 64 cores (~ 2000 -5000 core-h on the Vienna supercomputers VSC1 or VSC2) for a single calculation. The total numerical cost of the results presented in this chapter is a few millions of core-h.

4.3 Ground state properties

The starting point for the calculation of the time-dependent electron dynamics driven by the electromagnetic field is the solution of the static Kohn-Sham equations. They yield the ground state distribution of electrons in the unit cell describing the chemical bonding. The input is the lattice structure of α -quartz. Each Si atom is tetrahedrally coordinated to four O atoms, and each O atoms is coordinated to two Si atoms (Fig. 4.2d, inset). The O-Si-O bonding angle is near a perfect tetrahedron (109.5 deg), however the Si-O-Si bonds are not linear but have a bond angle of 144 deg. The α -quartz lattice (space group $P3_121$) has two-fold rotation symmetry around the \hat{a} axis and three-fold rotation symmetry around the \hat{c} axis. As our implementation works in Cartesian coordinates, we are restricted to cuboid unit cells. The smallest cuboid unit cell of SiO_2 has dimensions $9.28 \times 16.05 \times 10.21$ a.u.³ along the \hat{a} , $\hat{a} \times \hat{c}$, and \hat{c} directions and contains six SiO_2 formula units with 16 valence electrons each (96 electrons or 48 orbitals in total). The $\text{O}1s^2$ and $\text{Si}1s^22s^22p^6$ cores are described by norm-conserving pseudopotentials [Troullier and Martins, 1991]. While the atomic configuration would be $\text{O}2s^22p^4$ and $\text{Si}3s^23p^2$, the covalent sp^3 -hybridized bonds in α -quartz are strongly polar so that mostly oxygen-like orbitals are occupied in the ground state. The density of states (Fig. 4.2a) contains two electrons per oxygen atom in a $2s$ -like state centered around the oxygen sites deeply bound at -18 eV (Fig. 4.2c, energy region marked ① in Fig. 4.2b). The density of electrons with energies from -10 to -4 eV corresponds to the $2p_z$ -like bonding orbitals extending along the Si-O-Si bond axis (②, Fig. 4.2d). The top of the valence band (-4 eV to the Fermi energy, ③,e) contains oxygen lone pair electrons that do not participate in the bonding oriented perpendicular to the bond axis ($2p_x, 2p_y$). Our calculation agrees well with literature results [Chelikowsky and Schlüter, 1977; Calabrese and Fowler, 1978; Gnani et al., 2002].

We employed two different approximations to the exchange-correlation potential. The local density approximation (LDA) [Perdew and Zunger, 1981] is known to underestimate the excitation gap in insulators. For our modeling of the strongly non-linear response and optical ionization of a bulk solid the excitation gap is of paramount importance for a correct and quantitative description of the response. We therefore also employ the recently proposed meta-GGA (generalized gradient approximation) Tran-Blaha modified Becke-Johnson (TB-mBJ) XC potential [Tran and Blaha, 2009; Koller et al., 2011, 2012]. It aims to correct the excitation gap by generating the XC potential not only from the local value of the density, but also from the gradient of the density and the local “kinetic energy density” $(1/2) \sum_i |\nabla \psi_i(\mathbf{r})|^2$. Effectively, the potential energy of the spatial regions corresponding to the unoccupied states is increased, leading to an increased excitation gap. The TB-mBJ XC potential contains a single free parameter $c_{\text{TB-mBJ}}$ with which the excitation gap monotonically increases. We follow the prescription by Tran and Blaha [2009] and set $c_{\text{TB-mBJ}} = 1$ for SiO_2 . Comparing the density of states of LDA and TB-mBJ XC potential, we find

only marginal differences in the occupied density of states indicating that the bonding and chemistry is described similarly by the LDA and TB-mBJ potentials. However, the unoccupied density of states (energy ≥ 0 in Fig. 4.2a,b) is shifted upwards in energy, giving a first indication that the optical gap is increased. While the ground state density is strongly localized in the unit cell around the oxygen atoms (Fig. 4.2a-c), the pseudo-density $\sum_i |\psi_i(\mathbf{r})|^2$ of the lowest unoccupied states in the unit cell (Fig. 4.2d) is much more de-localized along the Si-O-Si bond axes.

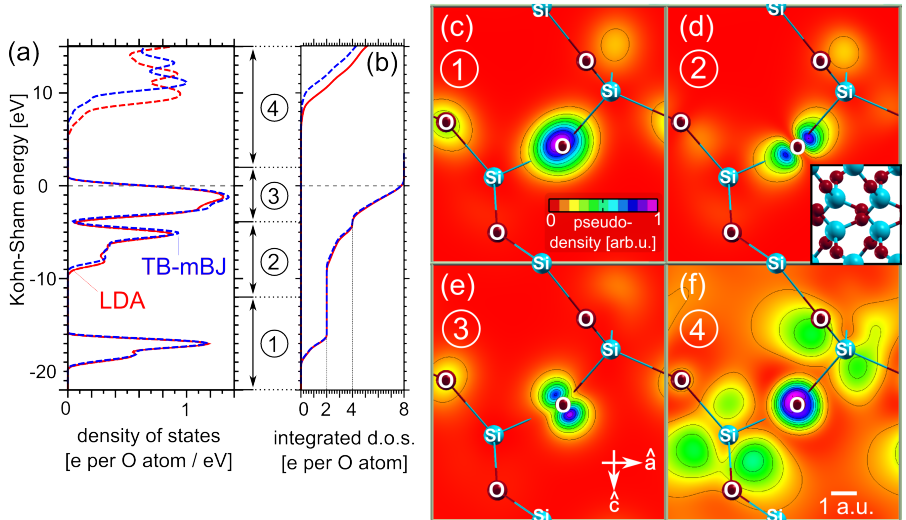


Figure 4.2: Ground state calculation of α -quartz (SiO_2) (a) Density of states for LDA (red solid) and TB-mBJ (blue dashed) XC potentials. The Fermi energy is at 0. (b) Integrated density of states in electrons per oxygen atom from the bottom of the valence band (below 0) and from the bottom of the conduction band (above 0). (c-f) Partial density corresponding to electrons in the lowest, bonding, antibonding, and conduction band (TB-mBJ functional, energy regions marked ①, ②, ③, ④ in (a) respectively). The \hat{a} - \hat{c} cut plane goes through the central oxygen atom, the other visible atoms are located above the oxygen atom. **Inset (d):** Projection of the lattice structure on the \hat{a} - \hat{c} plane.

4.4 Optical properties

In this section we investigate the linear and low-order non-linear response to optical excitation as prerequisite for the description of the highly non-linear response induced by intense few-cycle pulses. The linear response is extracted from a real-time simulation for a weak excitation [Yabana et al., 2012]. We evaluate the time- and space-dependent microscopic current density $\mathbf{j}(\mathbf{r}, t)$

$$\mathbf{j}(\mathbf{r}, t) = |e| \sum_i \frac{1}{2} [\psi_i^*(\mathbf{r}, t) (-i\nabla + \mathbf{A}(t)) \psi_i(\mathbf{r}, t) + \text{c.c.}] \quad (4.3)$$

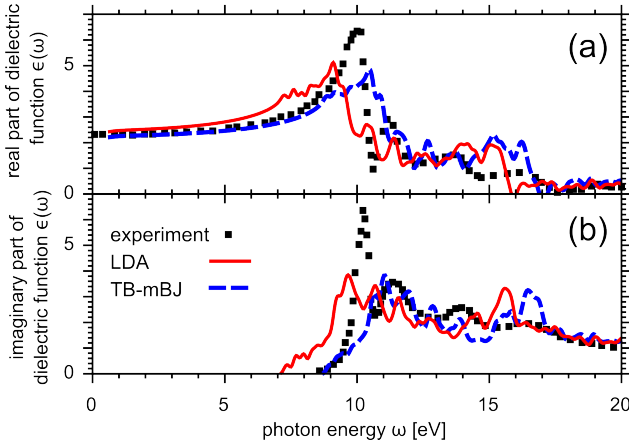


Figure 4.3: Optical properties of quartz. (a) Real part of dielectric function $\epsilon(\omega)$. Blue dashed: TB-mBJ exchange correlation functional; red: LDA; black squares: experiment [Philipp, 1966]. (b) Imaginary part of dielectric function $\epsilon(\omega)$.

and calculate the macroscopic current density $J(t)$ along the laser polarization direction $\mathbf{F}_0/|F_0|$ as the average of the microscopic current over one unit cell of volume Ω ,

$$J(t) = \frac{1}{\Omega} \int_{\Omega} d\mathbf{r} \mathbf{j}(\mathbf{r}, t) \cdot \mathbf{F}_0 / |F_0| \quad . \quad (4.4)$$

The proportionality constant between electric field and current is, according to Ohm's law, the conductivity $\sigma(\omega)$,

$$\sigma(\omega) = \frac{\int_{-\infty}^{\infty} dt e^{i\omega t} J(t)}{\int_{-\infty}^{\infty} dt e^{i\omega t} F(t)} \quad , \quad (4.5)$$

which is related to the dielectric function as

$$\epsilon(\omega) = 1 + \frac{4\pi i \sigma(\omega)}{\omega} \quad . \quad (4.6)$$

The resulting dielectric function agrees reasonably well with the experimental data for both LDA and TB-mBJ exchange-correlation functionals for optical frequencies ($\omega \lesssim 2$ eV, upper panel [real part] in Fig. 4.3). For higher photon energies, the LDA calculation underestimates the size of the excitation gap (imaginary part), giving a difference to the experimental value of the order of one photon energy ($hc/800 \text{ nm} \approx 1.55$ eV), which could significantly influence the response in the strong field regime by allowing lower order multi-photon processes. The optical gap is corrected by the TB-mBJ XC potential.

Recently, Nazarov and Vignale [2011] have argued that meta-GGA functionals such as TB-mBJ could be particularly well-suited for the calculation of optical spec-

tra. They point out that the kinetic energy density $(1/2)\sum_i |\nabla\psi_i(\mathbf{r})|^2$ is a non-local functional of the density $n(\mathbf{r}) = \sum_i |\psi_i(\mathbf{r})|^2$ and could therefore, in principle, capture the long-rangedness (“ultranonlocality”) of the XC potential. This would be particularly beneficial for the lowest peaks in the absorption spectra (at 10.3, 11.7 and 13.5 eV) that have been found to contain strong excitonic components [Chang et al., 2000]. A correct treatment of excitons requires more expensive methods typically based on the Bethe-Salpeter equation beyond standard functionals [Marini et al., 2003]. However, we do not observe that the TB-mBJ XC potential leads to a qualitative improvement of the shape of the calculated dielectric function compared with experiment in terms of reproducing the excitonic peaks. We instead find that the TB-mBJ exchange-correlation potential effectively shifts the LDA response to higher photon energies.

Our real-time method fully accounts for non-linear effects and is thus also suitable for the calculation of *non-linear* optical properties [Sipe and Shkrebtii, 2000]. For an isotropic medium that responds instantaneously to the driving field (that is lossless and without dispersion), the optical response $P(t)$ is expanded into a power series in the electric field strength $F(t)$ (SI units, [Boyd, 2003])

$$P(t) = \epsilon_0 \left[\chi^{(1)} F(t) + \chi^{(2)} F^2(t) + \chi^{(3)} F^3(t) + \dots \right] \quad (4.7)$$

where $\chi^{(i)}$ is the i -th order non-linear optical susceptibility. In our calculation, the polarization $P(t)$ is evaluated as the integral of the macroscopic current [Resta and Vanderbilt, 2007],

$$P(t) = \int_{-\infty}^t J(t') dt' \quad . \quad (4.8)$$

The non-linear optical susceptibilities are evaluated from a time-domain simulation for a short pulse (30 fs duration, \cos^8 envelope for a fast decay in frequency domain) by taking the ratio of the Fourier transforms of $P(t)$ and $F^i(t)$ around multiples of the laser frequency at a laser wavelength of 1064 nm for which high-quality experimental data are available [Bosshard et al., 2000; Gubler and Bosshard, 2000]. We checked that the first-order susceptibility agrees with the linear response (Eq. 4.6). The second-order susceptibility is zero for excitation along the \hat{c} axis due to symmetry. Along the \hat{a} axis, we find $\chi_{\text{LDA}}^{(2)} = 0.95$ pV/m for LDA and $\chi_{\text{TB-mBJ}}^{(2)} = 0.44$ pV/m for TB-mBJ while in experiment $\chi_{\text{exp}}^{(2)} = 0.60$ pV/m. Due to the reduced gap energy, the electrons in the LDA calculation are more polarizable, which also leads to an increased non-linear susceptibility that overestimates the experimental value almost by a factor two while the TB-mBJ calculation is somewhat closer to the experimental result. The best signal for $\chi^{(3)}$ is obtained along the \hat{c} direction where the $\chi^{(2)}$ signal is zero. We find $\chi_{\text{LDA}}^{(3)} = 4.2 \times 10^{-22} \text{m}^2/\text{V}^2$ for LDA and $\chi_{\text{TB-mBJ}}^{(3)} = 2.4 \times 10^{-22} \text{m}^2/\text{V}^2$ for TB-mBJ while in experiment $\chi_{\text{exp}}^{(3)} = 2.5 \times 10^{-22} \text{m}^2/\text{V}^2$. Again, the agreement is better for the TB-mBJ calculation than for LDA.

In conclusion, both linear and low-order non-linear optical properties are repro-

duced by our simulation to a good degree of accuracy. The TB-mBJ XC functional systematically improves agreement with experiment for all optical properties.

4.5 Optical-field induced currents in insulators

We now extend our investigations to the study of strongly non-linear field-induced currents by intense laser pulses⁸. We investigate the response of α -quartz to a strong few-cycle laser pulse defined by

$$\mathbf{A}(t) = -\frac{F_0}{\omega_L} \cos(\omega_L t + \phi_{CE}) \left[\cos\left(\frac{\pi}{2} \frac{t}{\tau_p}\right) \right]^2 \quad (4.9)$$

with amplitude $F_0 = |\mathbf{F}_0|$, photon energy ω_L , carrier-envelope phase (CEP) ϕ_{CE} , and pulse length τ_p (FWHM field; full pulse length is $2\tau_p$). At a moderate laser intensity of $5 \times 10^{12} \text{ W/cm}^2$ where the onset of the non-linear response is expected, the time-dependent polarization density $P(t)$ as calculated from Eq. 4.8 (Fig. 4.4a) follows approximately adiabatically the applied electric force as expected within linear response throughout the duration of the pulse. However, after the conclusion of the laser pulse (Fig. 4.4b), we observe small-scale and fast oscillations in the polarization density. This confirms earlier observations employing one-dimensional models [Korbman et al., 2013; Kruchinin et al., 2013], however with a reduced beating amplitude. This reduction is due to the three-dimensional rather than one-dimensional conduction band density of states and the self-consistent inclusion of screening. The dominant oscillation frequency of these “quantum beats” ($\sim 0.5 \text{ fs}$) corresponds to the beating frequency between states in the valence and conduction bands. Averaging over these oscillations, we observe a small but finite sustained polarization density after the pulse, much smaller than the maximum polarization density during the pulse corresponding to a transferred charge density of around $1 \times 10^{-7} e/(\text{atomiclength})^2$. Within the time interval covered by our propagation, we find that the transferred charge is approximately constant indicating the absence of a sustained current. The situation changes drastically for an increased laser intensity of $2 \times 10^{14} \text{ W/cm}^2$ (Fig. 4.4 a). During the laser pulse, the polarization density is distorted and phase shifted with respect to the laser field. After the pulse, the polarization density is still much smaller than the polarization density at the peak of the laser field. However, it behaves markedly different from the constant polarization found at low intensity: $P(t)$ shows an almost linear decrease, pointing to a constant current density flowing after the laser pulse is over. Signs of persistent currents after the laser pulse have also been found in one-dimensional model calculations [Kruchinin et al., 2013; Korbman et al., 2013]. Such a ballistic current will eventually relax due to dissipative processes such as electron-phonon coupling [Franco et al., 2007], impurity, and disorder scattering

⁸This section is expanded from the original description given by the author and co-workers in [Wachter et al., 2014b]; parts of the results presented in [Wachter et al., 2014b] can be found throughout this chapter.

on longer time scales neglected in the present simulation (mobility data suggest a relaxation after $\gtrsim 20$ fs [Williams, 1965; Goodman, 1967; Hughes, 1973]).

We correlate the observed polarization density for the high-intensity laser pulse (2×10^{14} W/cm²) with snapshots of the induced charge and current density within a unit cell of the material (Fig. 4.4c-f) taken around a representative oxygen atom with bond axes approximately in the \hat{a} - \hat{c} plane. Early during the laser pulse at a maximum of the electric field (at the time marked ① in Fig. 4.4a corresponding to snapshots c and f), when the response to the relatively low electric field strength is still approximately linear, we observe a dipole-like pattern of induced charge around the central oxygen atom. This is analogous to the quasi-static polarization of a single atom by an electric field. The dipole-like pattern is antisymmetric with respect to the central oxygen atom and slightly tilted with respect to the laser polarization (\hat{c} axis) as the electrons can move more easily along the bond axis oriented at an angle to the laser field. As the snapshot is taken at a maximum of the laser field, the electrons are maximally elongated and as a result the induced current (Fig. 4.4f) is zero. Conversely, at the time labeled ② in (Fig. 4.4a), the laser electric field goes through a zero crossing. As the electrons move from one side of the central oxygen atom to the other, the induced current density (Fig. 4.4g) is maximal. The current distribution is symmetric around the oxygen atom. The situation changes drastically around the maximum of the electric field in the regime of strongly non-linear response (Fig. 4.4e,f; label ③). The induced charge pattern (Fig. 4.4e) is oriented along the laser field and is markedly less symmetric, indicating a non-linear directional component to the induced charge density. At the same time, the current density (Fig. 4.4f) is no longer zero, indicating that a current is induced at the maximum of the electric field, in analogy to the tunnel ionization of an atom or a surface by a quasi-static field.

Within the strong-field ionization model the excitation process is governed by the magnitude of the Keldysh parameter $\gamma = \omega_L \sqrt{2\Delta}/F_0$ with Δ the excitation gap between valence and conduction bands of the dielectric [Keldysh, 1965]. For $\gamma \gg 1$, multi-photon transitions dominate while $\gamma \ll 1$ marks the regime of tunneling ionization. Accordingly, at an intensity of 2×10^{14} W/cm² the Keldysh parameter ($\gamma \approx 0.7$) is in the tunneling regime. The tunneling current is strongly anisotropic and is directed along the laser electric force ($-\hat{c}$ direction), forcing electrons to tunnel between neighboring atoms. However, while for an isotropic static potential landscape the tunneling current would be oriented strictly along the laser polarization, here the current is distinctly tilted due to the crystal potential, consistent with a charge transfer to the neighboring O and Si atoms and into the interstitial region. This directionality and the highly non-linear dependence of the tunneling current on the laser field strength lead to the observed charge transfer.

The time-average of the microscopic current after the laser pulse $|\mathbf{j}(\mathbf{r}, t > \tau_p)|$ maps out the excitation pattern within the unit cell (Fig. 4.5b). The quasi-free current comes with a population of de-localized conduction band states extending mainly along the Si-O-Si bonds along which the current flows. The excitation map obtained

from the time-averaged current after the pulse for the lower laser intensity is in stark contrast to the one for the higher intensity (Fig. 4.5a). Instead of a connected region de-localized over the unit cell, only a near-spherical region around the oxygen atom is activated, in analogy to atomic photoexcitation. At intermediate intensities, a smooth transition between the two extremal situations is found with both the de-localization of the current distribution in the unit cell as well as an appreciable contribution to the transferred charge from quasi-free currents emerging around $5 \times 10^{13} \text{ W/cm}^2$. The directionality of the tunneling process in real space leading to the quasi-free current leaves its marks also in momentum space. For low laser intensities, coupling to the conduction band is weak and (almost) fully reversible, and \mathbf{k} -points oriented parallel and anti-parallel to the laser amplitude are almost equally populated after the laser pulse (Fig. 4.5c) resulting in a vanishing free current. “Real” transitions to the conduction band set in when the instantaneous laser intensity surpasses the threshold for tunneling excitation. This threshold can be estimated from the field strength F_c where the electrostatic potential differences between the O and Si sites (distance $d_{\text{O-Si}} = 3.04 \text{ a.u.}$) reaches the order of magnitude of the excitation gap, $F_c d_{\text{O-Si}} \approx \Delta$. The resulting population of conduction band states after the laser pulse is orders of magnitude larger and shows energy-dependent forward-backward asymmetries as a result of the directional electron emission into the conduction band and the subsequent evolution (Fig. 4.5c).

The present simulations can be compared with the first experimental data [Schiffrin et al., 2013]. The total macroscopic charge transferred along the laser polarization direction after the laser pulse is calculated as

$$Q_L = P(t > \tau_p) \mathcal{A}_{\text{eff}} \quad (4.10)$$

where the time average over the polarization after the conclusion of the laser pulse at τ_p is calculated over $\sim 8 \text{ fs}$ before current damping would set in. \mathcal{A}_{eff} is the effective surface area perpendicular to the laser polarization of the crystal that is illuminated by the laser with near-peak field strength effectively contributing to the charge transfer to nearby electrodes. As \mathcal{A}_{eff} could not be determined in the experiment by Schiffrin et al. [2013], we choose \mathcal{A}_{eff} to match the experimental value of $Q_L = 0.6 \text{ Af}$ s at the intermediate intensity of $5 \times 10^{13} \text{ W/cm}^2$ for a comparison on an absolute scale, resulting in a scaling factor of $\mathcal{A}_{\text{eff}} = 8.7 \times 10^{-14} \text{ m}^2 \sim (300 \text{ nm})^2$. Keeping this scaling factor fixed, we find excellent agreement for the carrier-envelope phase maximized transferred charge Q_L without any adjustable parameters (Fig. 4.6a). The steep rise clearly indicates the transition from a reversible non-linear bound polarization current to the excitation of a quasi-free current. We checked that this result does not depend sensitively on the choice of XC functional by also performing calculations with the LDA. We attribute the weak dependence on the accurate value of the band gap to the strongly non-linear response beyond the lowest non-vanishing order of a multi-photon transition. In addition, we also performed test calculations starting from an LDA or TB-mBJ ground state calculation but with dynamical electron-

electron interactions switched off, i.e., the Hartree and XC terms of the Hamiltonian (Eq. 4.2) were kept at their ground state value. We found that the time-dependent polarization and transferred charge were slightly increased compared to the full calculation due to neglecting self-consistent screening but that the strongly non-linear intensity dependence is reproduced. For such independent-particle calculations, a highly efficient basis expansion has very recently been proposed that could decrease the numerical cost by two orders of magnitude [Sato and Yabana, 2014].

The experiment by Schiffrin et al. [2013] has furthermore demonstrated that for a wave-form controlled few-cycle pulse, exquisite light-field control translates into control over the charge transfer. In particular, Q_L varies sinusoidally with the carrier-envelope phase of the few-cycle pulse (Fig. 4.6b), clearly indicating that the field amplitude rather than the intensity is the parameter governing the charge transfer. We find excellent agreement with the experimental carrier-envelope phase dependence for a laser intensity of $5 \times 10^{13} \text{ W/cm}^2$. At high intensities, our simulations also agree to very recent results that determined the absolute value of the CEP rather than the CEP shift [Paasch-Colberg et al., 2014].

We also investigate the influence of the anisotropic electronic structure on the transferred charge by comparing simulations with laser polarization direction along the \hat{c} and \hat{a} crystal directions (Fig. 4.6b). We find that the dependence of Q_L on laser intensity and the CEP varies with laser polarization in the high-field regime ($I \sim 1 \times 10^{14} \text{ W/cm}^2$). At $5 \times 10^{13} \text{ W/cm}^2$, we observe a pronounced shift by $\sim \pi/4$ between the \hat{a} and \hat{c} axes. While the experiment by Schiffrin et al. [2013] was designed to be sensitive only to the CEP-dependent part of the transferred charge, we find an additional surprising CEP-independent contribution to Q_L for laser polarization along the \hat{a} axis (Fig. 4.6b) which we trace back to the broken inversion symmetry along the \hat{a} axis of the SiO_2 crystal leading to an average net charge transfer. This contribution to the charge transfer that does *not* sensitively depend on the laser pulse shape and persists even for non-CEP stabilized laser pulses (see section 4.8).

Hitherto, most experiments have been performed on amorphous samples, effectively averaging over the crystal directions. First experiments on single crystal targets indicate that the magnitude of the charge transfer is similar to amorphous targets [Schiffrin et al., 2013], but no systematic studies on the effect of the laser polarization direction in the unit cell have been performed. For our simulations, orientational averaging is prohibitively expensive as calculations for arbitrary laser polarization can be up to ten times more expensive than calculations for polarization along the Cartesian axes because several directions within the cuboid unit cell have to be discretized with a fine spacing. The numerical cost could be decreased by employing a smaller non-cuboid unit cell, a code for which is currently under development. However, in view of the sensitive dependence of charge transfer on laser polarization found in our simulations, experiments on single-crystal targets with well-defined intensity averaging and carrier-envelope phase control are called for. For both experiment and theory, investigations of other large-gap dielectrics with smaller unit cells and less

complicated three-dimensional structure like LiF, CaF₂ or BaF₂ will help elucidate the underlying mechanism of the CEP dependence.

Our simulation provides a simple and transparent picture of the optical-field induced current and charge transfer dynamics. At low laser intensity, well within the linear response regime ($I \leq 1 \times 10^{12} \text{ W/cm}^2$), neither a net current nor a charge displacement is induced. With increasing laser intensity, nonlinear effects become important. Starting from about $5 \times 10^{12} \text{ W/cm}^2$, our simulations show that a finite amount of charge is transferred by nonlinear polarization currents during the laser pulse, but no significant quasi-free current flows after the pulse, i.e. these polarization currents are completely reversible. Associating these currents with a field-induced AC conductivity $\sigma(\omega_L)$ at photon energy ω_L ,

$$J(t) = \sigma(\omega_L)F(t) , \quad (4.11)$$

the non-linear process of charge displacement can be viewed as a reversible (sub-) femtosecond insulator to “metal” transition where the conductivity $\sigma(\omega_L)$ is increased by more than 20 orders of magnitude. The character of the field-induced currents changes significantly once the laser intensity is sufficiently high such that a substantial amount of electrons are non-adiabatically excited into the conduction band by tunneling excitation. The onset of a ballistic macroscopic current in the material after the laser pulse is over is accompanied by a delocalized current density over the unit cell. This marks the precursor of dielectric breakdown for longer pulses. A finite conductivity, i.e., a transition from a femtosecond ballistic current to a dissipative current will be established only on longer time scales by dissipative processes such as electron-phonon and defect scattering. In our simulation, the transition from non-linear polarization to the regime where quasi-free ballistic currents dominate occurs at a laser intensity of about $5 \times 10^{13} \text{ W/cm}^2$. The amount of charge transferred is influenced by the laser intensity, pulse shape, and polarization direction of the laser pulse, indicating that the charge separation depends on the details of the potential landscape and bond structure.

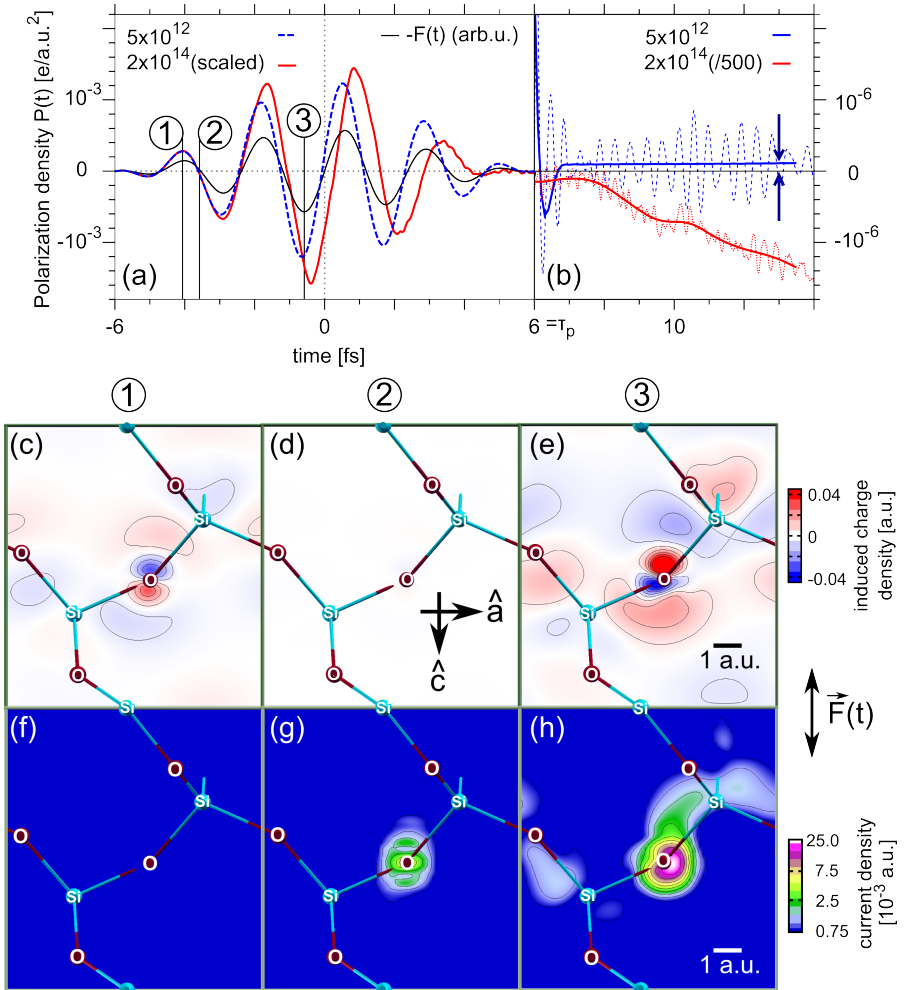


Figure 4.4: Time-dependent polarization density and snapshots of microscopic density and current density. (a,b) Time-dependent polarization density for low laser intensity (blue dashed, 5×10^{12} W/cm²) and high laser intensity (red solid, 2×10^{14} W/cm², scaled) during the pulse (12 fs full length, photon energy 1.7 eV, polarization along \hat{c} , black solid line). After the pulse (b) thick lines indicate temporal averages over fast oscillations (thin lines). Note the ordinate change from (a) to (b). (c-e) Snapshots of the induced electron density $n(x, t) - n(x, -\infty)$ for high laser intensity 2×10^{14} W/cm² at times marked ①, ②, ③ in (a) in an \hat{a} - \hat{c} plane cutting through the central oxygen atom (only the central Si-O-Si bond lies approximately in the cut plane). ①: At maximum of electric field (low field strength); ②: at zero crossing of electric field; ③: at maximum of electric field (high field strength). (f-h) Snapshots of the absolute value of the microscopic current density $|j(x, t)|$ (logarithmic scale) at the same times ①, ②, and ③.

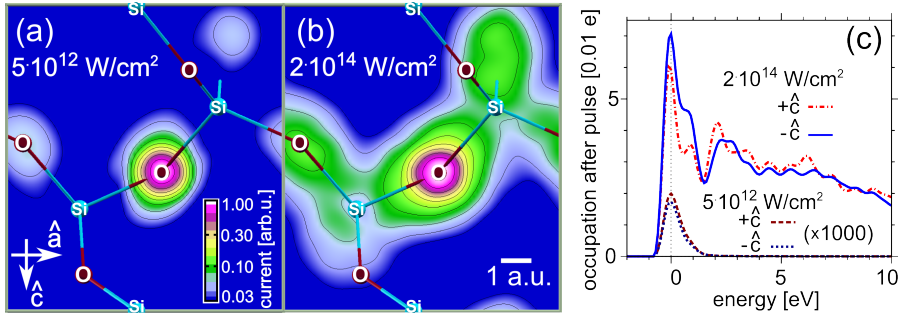


Figure 4.5: Time-averaged current and k-space occupation after the laser pulse. (a,b) Time-averaged current after the laser pulse in an \hat{a} - \hat{c} - plane cutting through the central oxygen atom for a laser intensity of $5 \times 10^{12} \text{ W/cm}^2$ (a) and $2 \times 10^{14} \text{ W/cm}^2$ (b). The laser pulse is polarized along the \hat{c} direction. (c) Occupation of conduction band states with positive (red lines) and negative (blue lines) projected \mathbf{k} -vectors compared to the laser polarization direction \hat{c} for $5 \times 10^{12} \text{ W/cm}^2$ (lower graphs, $\times 1000$) and $2 \times 10^{14} \text{ W/cm}^2$ (upper graphs).

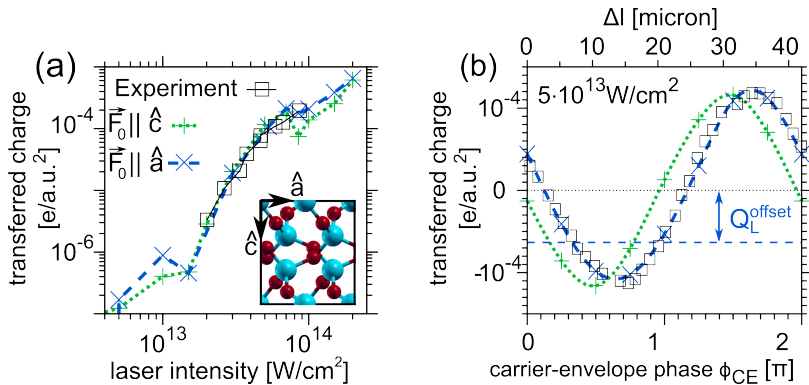


Figure 4.6: Intensity and carrier-envelope phase dependence. (a) Laser-induced charge transfer Q_L maximized over the CEP as function of the laser intensity for laser polarization along \hat{c} (green crosses), \hat{a} (blue Xes), and experiment (black boxes, amorphous target). **Inset:** Projection of lattice structure on the \hat{c} - \hat{a} -plane. (b) CEP dependence for fixed intensity $5 \times 10^{13} \text{ W/cm}^2$. Experimental data (black boxes) for a single crystal with polarization perpendicular to the \hat{c} axis plotted against the change Δl in optical path length through fused silica wedges. For laser polarization along \hat{a} , the simulation gives an additional ϕ_{CE} -independent offset (horizontal dashed blue line).

4.6 Influence of the macroscopic shape of the sample

The electronic response of an extended system to the laser field may depend on the macroscopic boundary conditions that are imposed on its surface that break the translational invariance. Pile-up of carriers at the boundary as a result of the current can contribute to the spatially homogeneous electric field expressed in the total vector potential $\mathbf{A}(t)$ in Eq. 4.2 [Kootstra et al., 2000; Berger et al., 2007; Yabana et al., 2012]. This induced field will depend on the macroscopic geometry of the sample and can contribute to screening of the field, or field enhancement (e.g. near the edges of the metal contacts). For the experimental samples with two metal electrodes at an oblique angle relative to each other (Fig. 4.1b) the induced field might not even be spatially homogeneous within the sample. In principle, another contribution due to the long-range XC potential is expected [Gonze et al., 1995]. By treating the sample as infinitely extended in the polarization direction, we model the electrodes as “ideal” sinks of electric charge that effectively do not permit a surface charge patch to form. This choice of “perfect” absorbers for comparison to the experiment at hand is corroborated by the following three points.

First, the sensitivity to the macroscopic shape of the sample was investigated experimentally by Schiffrin et al. [2013] for the wedge-like geometry and for a sample geometry where two stripes of metal electrodes were placed on the surface of a fused silica slab (Fig. 4.1). The experimental results were found to be insensitive to the macroscopic sample geometry indicating that the fields induced by the surface charges do not strongly influence the charge transfer.

Secondly, Schiffrin et al. [2013] also investigated the sensitivity to the size of the gap between electrodes and found that their results were not strongly influenced by the gap size. While for small gaps between the electrodes the surface charge acts back instantaneously on all unit cells in the gap, this approximation is only justified as long as the gap size divided by the speed of light is much smaller than the laser period (at $\omega_L = 1.7$ eV or 730 nm, 2.44 fs). In the experiment, the size of the gap between the electrodes was varied from 50 nm to 500 nm corresponding to a variation of the transit time by a factor of 10 between 7% and 70% of the optical period. The experimentally observed insensitivity to the gap size provides additional evidence that the induced surface charge plays only a minor role.

Thirdly, our simulations employing the identical geometry yield equally good agreement with the experiment both for low intensities where no free currents after the laser pulse are generated as well as for higher intensities where the surface charge accumulated by the currents could possibly influence the dynamics more strongly. We take this as an additional indication that the comparison between experiment and simulation is not strongly influenced by boundary effects.

To check on possible boundary effects we have performed also simulations in the so-called longitudinal geometry [Yabana et al., 2012]. Effectively, we assume the macroscopic shape of a thin film so that the surface charge acts back instantaneously

on all unit cells, and neglect any influence of the electrodes, thereby giving a complementary limit to the calculations for the “transverse” geometry modeling an infinitely extended solid and perfectly absorbing electrodes. The pile-up of charge at the surface of the dielectric leads to an additional induced field described by the vector potential $\mathbf{A}_{\text{ind}}(t)$ with

$$\frac{d^2 \mathbf{A}_{\text{ind}}(t)}{dt^2} = \frac{4\pi}{c} \mathbf{J}(t) \quad , \quad (4.12)$$

and the total vector potential entering Eq. 4.1 is given by $\mathbf{A}_{\text{tot}}(t) = \mathbf{A}(t) + \mathbf{A}_{\text{ind}}(t)$. Thereby, the external laser field is screened by about a factor of $\epsilon(\omega_L) \approx 2.2$ (Fig. 4.7c). This reduction in effective electric field strength leads to a reduced transferred charge that is about a factor 50 smaller than in the transverse geometry where $\mathbf{A}_{\text{tot}}(t) = \mathbf{A}(t)$ (Fig. 4.7a). To numerically resolve this lower signal, we employ pulses with a faster decay in frequency space with a \cos^6 envelope while the calculations for transverse geometry are converged even employing a \cos^2 envelope down to intensities of $\sim 1 \times 10^{13} \text{ W/cm}^2$. Qualitatively, we find the polarization response unchanged. The mechanism for charge transfer is the same as discussed for the transverse geometry. Due to the lower absolute field strength, tunneling is less apparent than in the transverse calculation, but the asymmetry in the total microscopic current near the maxima of the laser field is still visible (Fig. 4.7b, compare Fig. 4.4 g and h). As for the transverse calculations, after the pulse there remains a sustained polarization and a quasi-free current as well as fast quantum beat oscillations (Fig. 4.7c). The magnitude of the latter is reduced due to the inclusion of macroscopic screening. The linear decrease of polarization after the pulse leads to a finite macroscopic electric field after the pulse that acts against the current. The resulting field is, however, about two orders of magnitude weaker than the peak electric field during the pulse and does not appreciably change the flow of the current within the first few femtoseconds after the pulse.

The intensity dependence of the transferred charge agrees well to experiment for calculations with both longitudinal and transverse geometry (Fig. 4.7a). The transverse geometry calculations show a somewhat faster decay at low intensities and a stronger saturation at high intensities, showing slightly better agreement with experiment. The results presented in the remainder of this chapter are for the transverse geometry.

4.7 Number of excited electrons and petahertz electronics

We investigate the degree of excitation of the system after the laser pulse quantified by the total number of electrons in the conduction band and the energy deposited into the sample. The number of excited electrons is calculated as the number of electrons

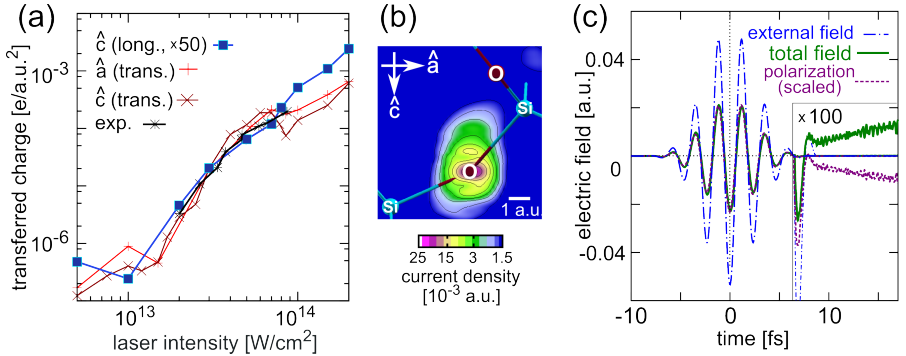


Figure 4.7: Comparison of longitudinal (slab) and transverse (infinite) geometry. (a) Carrier-envelope phase maximized transferred charge along the \hat{c} (dark red Xes) and \hat{a} (red crosses) directions in the transverse geometry (no surface charge); along the \hat{c} direction in the longitudinal geometry (surface charge included via Eq. 4.12, blue squares), and experiment (black stars). (b) Microscopic current density $|\mathbf{j}(\mathbf{r}, t)|$ around O atom near the maximum of the electric field (intensity $2 \times 10^{14} \text{ W}/\text{cm}^2$, longitudinal geometry). (c) Typical electric fields and polarization response for intensity $1 \times 10^{14} \text{ W}/\text{cm}^2$ (longitudinal geometry). External electric field (blue dash-dotted); total field (green solid); time-dependent polarization density (violet dashed; scaled). After the laser pulse, the scale is magnified by a factor 100.

removed from the ground state after the laser pulse,

$$n_{\text{exc}}(t) = \sum_i^N \left\{ 1 - \sum_j^N \left| \langle \psi_j(0) | \psi_i(t) \rangle \right|^2 \right\}, \quad (4.13)$$

where the sums extend over the occupied orbitals, $|\psi_j(0)\rangle$ are the ground-state orbitals, and $|\psi_i(t)\rangle$ are the time-dependent orbitals. We observe that for laser polarizations along both \hat{a} and \hat{c} axes the number of excited electrons scales as $\sim I^{4.5}$ at low intensities, roughly corresponding to the number of photons necessary to bridge the band gap (Fig. 4.8b). For higher laser intensities $\gtrsim 2 \times 10^{13} \text{ W}/\text{cm}^2$, the number of excited electrons increases more slowly and starts to saturate.

Similarly, we find that the CEP maximized transferred charge scales approximately as I^4 at lower intensities ($1 \times 10^{13} \text{ W}/\text{cm}^2$ to $5 \times 10^{13} \text{ W}/\text{cm}^2$). The saturation at large intensities is more abrupt and, in general, the transferred charge displays more fine structure, indicating that the number of excited electrons alone is not responsible for the magnitude of transferred charge but that it is the interplay of ionization and steering of the ionized electrons by the remainder of the laser pulse that leads to this intensity dependence of the transferred charge. We also present the carrier-envelope phase maximized transferred charge *including* the carrier-envelope phase independent offset to which the experiment has hitherto not been sensitive (Fig. 4.8a). The latter is of similar order of magnitude as the carrier-envelope phase dependent signal for intensities larger than $5 \times 10^{13} \text{ W}/\text{cm}^2$ even for the short pulses employed by Schiffrin et al. [2013] and appears to scale differently than the carrier-envelope phase dependent transferred charge. Before we investigate the origin of this

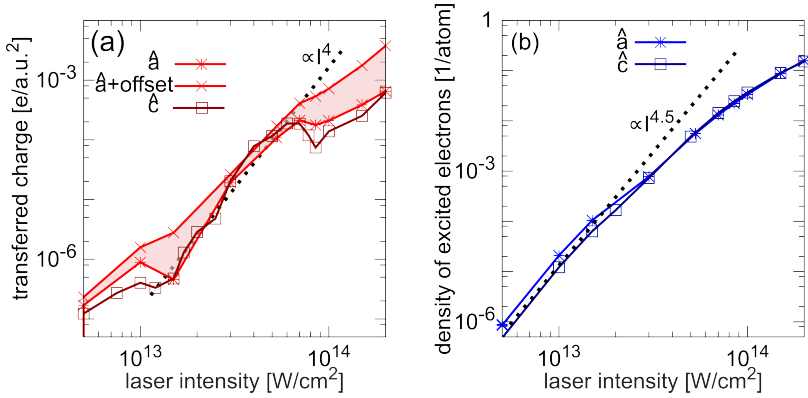


Figure 4.8: Transferred charge and number of excited electrons. (a) Laser-induced charge transfer Q_L maximized over the carrier-envelope phase as function of the laser intensity for laser polarization along \hat{c} (dark red rectangles), \hat{a} (without offset, red stars; with offset, red Xes). (b) Density of excited electrons per atom (electrons not in the ground state) after the laser pulse for laser polarization along \hat{c} (boxes) and along \hat{a} direction (stars).

offset in the next section, we explore consequences of the excitation with respect to the thermal stability of possible petahertz lightwave electronics circuits.

Modern electronics and information technology relies on the control of electric and optical properties of semi-conductors by microwave fields. It has been suggested that the same concepts can be extended to optical frequencies by employing wideband materials that require strong fields to change their properties. A candidate process for optical switching is the generation of optical field-induced currents where a strong few-cycle laser pulse is employed to change the properties of the bulk material from an insulator to a semi-metal with switch-on times on the femtosecond scale. This ultrafast switching time could, in principle, surpass today's semiconductor technology where the fastest transistors operate on the (sub)THz frequency or on the time scale $\gtrsim 1$ ps by several orders of magnitude [Krausz and Stockman, 2014]. A key factor for the realization of such devices is the amount of deposited energy density per transmitted signal, as this energy is eventually dissipated to the lattice of the sample or integrated circuit and must be removed by cooling in order to keep the device functional and below melting temperature. Here, we estimate the energy deposition per laser pulse and compare it to the dissipated power per switching cycle for semiconductor technology, following the estimates given in [Krausz and Stockman, 2014]. For laser intensity $5 \times 10^{13} W/cm^2$ in the transition regime from non-linear polarization to free currents, the number density of excited electrons after the laser pulse is $0.02 e/[0.33 \text{ nm}]^3$ (Fig. 4.8) where $[0.33 \text{ nm}]^3$ is the volume per SiO_2 formula unit. As most electrons are excited to low-lying conduction band states for low to intermediate intensities (Fig. 4.5c), the total excitation energy can be estimated from the number density of excited electrons times the excitation gap ($\sim 10 \text{ eV}$). The total deposited energy per switching device is given by the excitation energy den-

sity multiplied by the volume of the device. For the current experiment (electrode gap distance ~ 50 nm, transverse area $A_{\text{eff}} \sim (300 \text{ nm})^2$), we find that a single laser pulse deposits a “switching” energy of about $E_{\text{switch}} (5 \times 10^{13} \text{ W/cm}^2) \approx 6500$ fJ into the electronic system of the sample. The same order of magnitude can be obtained from independent calculations by Mark Stockman [Krausz and Stockman, 2014] giving $E_{\text{switch}}^{\text{M.S.}} (5 \times 10^{13} \text{ W/cm}^2) \approx 1000$ fJ. Today’s semiconductor technology operates with a drastically lower switching energy $E_{\text{switch}}^{\text{transistor}} \approx 0.1\text{-}1$ fJ and still, cooling is already the limiting factor even at GHz clock speeds. Therefore, the total amount of deposited energy must be drastically reduced to achieve operability on the PHz time scale. A reduction of the laser intensity down to the non-linear polarization regime $\sim 2 \times 10^{13} \text{ W/cm}^2$ reduces the number of excited electrons at the cost of the current signal (and concomitantly the change in dielectric properties) which was, however, still found to be measurable in experiment. Keeping the volume of the signal processing unit fixed, we find $E_{\text{switch}} (2 \times 10^{13} \text{ W/cm}^2) \approx 35$ fJ per signal, still 2-3 orders above semiconductor technology. Clearly, miniaturization of the signal processing unit to the nanometer length scale is paramount. Hypothetical miniaturization to a cube of volume $(20 \text{ nm})^3$, comparable to the miniaturization achievable by industry-grade contemporary semiconductor technology, results in an theoretical optimum of $E_{\text{switch}}^{\text{opt}} \sim 0.06$ fJ. This value is still not much better than $E_{\text{switch}}^{\text{transistor}} \approx 0.1\text{-}1$ fJ. This unavoidable energy deposition will be a challenge for achieving petahertz signal processing. Effective miniaturization may employ plasmonic confinement of light to the nanoscale for signal transmission between switches. Exploring longer wavelengths could substantially reduce the number of excited electrons. However, it is currently an open question if the strongly non-linear response and charge transfer persist for other laser parameters.

4.8 Non-linear ultrafast bulk photogalvanic effect

We now investigate the CEP-*independent* charge transfer found in section 4.5 for laser polarization along the \hat{a} axis. The generation of a current by homogeneous illumination of an infinitely extended bulk material by a linearly polarized laser field bears resemblance to the so-called “bulk photogalvanic effect” (PG) [Glass et al., 1974; Belinicher and Sturman, 1980; Sturman, 1992; Fridkin, 2001]. Phenomenologically, the lowest order photogalvanic effect is described as

$$j_k^{\text{PG}} = \beta_{kln} F_l E_n^* , \quad (4.14)$$

i.e., the observed current, a second-order effect in the electric field, is linear in the time-averaged laser intensity $I \propto F_l F_l^*$. For linear polarization, the bulk photogalvanic tensor β_{kln} (sometimes also called Glass coefficient, a close cousin of the piezoelectric tensor) is finite only in non-centrosymmetric crystals. Some authors refer to the bulk photogalvanic effect as “anomalous photovoltaic effect” to indicate that the induced photovoltage can be larger than the excitation gap, in contrast to traditional

photovoltaic materials. The latter are typically inhomogeneous (doped) structures employing the electric field at a p - n -junction to separate electrons and holes, and can generate voltages only up to the semiconductor gap. Often, the effect described by Eq. 4.14 is termed “bulk” photogalvanic effect to distinguish it from the so-called Dember effect [Dember, 1931] caused by inhomogeneous illumination of a semiconductor with differing electron and hole mobilities that can also lead to a current and voltage.

Depending on the material, the microscopic processes underlying the phenomenological bulk photogalvanic effect (Eq. 4.14) can include photo-excitation, scattering at impurities or phonons, and relaxation and recombination that may occur with different probabilities for electrons moving in one or the other direction leading to a net current [Belinicher and Sturman, 1980]. If slow processes like phonon scattering or relaxation processes are the main drivers of the photogalvanic effect, the latter takes place on rather long time scales ($\gtrsim 20$ fs) and does not depend on the initial photoexcitation. The photo-galvanic contribution from optical photoexcitation on the femtosecond time scale has been derived by perturbative analysis of the non-linear response of a bulk solid to an electromagnetic field [Sipe and Shkrebtii, 2000]. In quartz, photogalvanic currents from optical excitation are typically caused by asymmetric excitations of F center impurities (a neutral crystal defect in which an anionic vacancy is replaced by electrons), and the bulk photogalvanic effect was shown to be much smaller for synthetic samples with a reduced number of defects [Dalba et al., 1995]. To our knowledge, at present there are no measurements of the photogalvanic coefficient in the visible for defect-free quartz. One important candidate mechanism for the generation of the photo-galvanic current that also applies to defect-free materials is the so-called “shift current” contribution to the non-linear current response [Sipe and Shkrebtii, 2000]. This shift current is caused by the shift of the center of charge of the valence electrons and the center of charge of excited (conduction-band) density of states. This shift current has been predicted to be important in several semi-conductors [Sipe and Shkrebtii, 2000; Nastos and Sipe, 2006, 2010]. Recently, a first direct comparison of ab-initio calculations for the shift current contribution to experiments for the ferroelectrics BaTiO_3 and PbTiO_3 has found good agreement to experimentally measured tensor components in magnitude and spectrum profile [Young et al., 2012]. A first prediction of symmetry properties of a non-linear bulk photogalvanic effect depending on the symmetry properties of the lattice has been given by Alon [2003].

To systematically investigate the CEP-independent charge transfer and elucidate its relation to the photogalvanic effect, we performed a series of calculations for irradiation of α -quartz along the \hat{a} direction with varying laser intensity and pulse length. The total amount of transferred charge was split into a CEP-dependent part and a CEP-independent part by performing simulations for several CE-phases. We found that the CEP-dependent part tends to decrease with increasing pulse length (Fig. 4.9b). The amplitude of the CEP-independent transferred charge, on the other

hand, increases monotonically with increasing pulse length. For full pulse length $\gtrsim 15$ fs (FWHM intensity 5.5 fs), the CEP-independent signal is approximately proportional to the pulse duration as would be expected for the photogalvanic effect. While a CEP-dependent signal is still present, the CEP-independent signal is about one order of magnitude larger.

The CEP-independent transferred charge increases non-linearly with increasing intensity, following a power law of about $I^{2.8}$ (Fig. 4.9a). This can be contrasted with the I^4 power law observed for the CEP-dependent transferred charge for shorter pulses and the I^1 dependence of the lowest order photogalvanic effect (Eq. 4.14). The absolute magnitude of the transferred charge is similar to the CEP-dependent charge transfer by shorter pulses discussed in section 4.5. Therefore, we expect that a similar experimental setup as used by Schiffrin et al. [2013] could be employed to investigate the non-linear photogalvanic effect.

Surprisingly, we observe a sign change in the transferred charge with increasing intensity, i.e., electron particle current flows along the $+\hat{a}$ axis for low intensities $I \lesssim I^* = 4 \times 10^{13}$ W/cm² while electrons are transferred along the $-\hat{a}$ for higher intensities beyond I^* . Introducing an effective non-linear Glass coefficient $\tilde{\beta}_{\hat{a}}(I)$ in analogy to Eq. 4.14,

$$j_{\hat{a}}^{\text{NL-PG}} \approx \tilde{\beta}_{\hat{a}}(I) I^{2.8}, \quad (4.15)$$

we find that the sign of the non-linear Glass coefficient depends on the laser intensity. We elucidate the microscopic mechanism for the sign change by analysis of the spatio-temporal charge dynamics on the atomic length and time scales. At lower intensities $I \lesssim I^*$, we observe a multi-photon-like excitation into low-lying conduction band states predominantly localized around the oxygen atoms, in analogy to the results for shorter pulses. The excitation pattern derived from the time-averaged density fluctuations after the laser pulse shows an accumulation of charge between the Si-O-Si bond axes (Fig. 4.10f). This implies the formation of atomic-scale dipoles around the oxygen atoms, in analogy to the Clausius-Mossotti picture of matter composed of microscopic dipoles [Mossotti, 1850]. Corroborating this picture, we observe that the dipole moment per oxygen atom averaged over the simulation time after the laser pulse

$$\langle d_O \rangle \propto \int_{\tau_p}^{\infty} dt \int d^3\mathbf{r} (\mathbf{r} \cdot \hat{a}) \Delta n(\mathbf{r}, t) \quad (4.16)$$

is positive⁹, consistent with a net movement of electrons along the $+\hat{a}$ direction. We thus interpret the non-linear electron transfer along the $+\hat{a}$ direction as the strong-field version of the shift current mechanism in the multi-photon regime. Excitations

⁹ In a bulk dielectric, the induced dipole moment per unit cell or polarization density is not well defined by Eq. 4.16 as the result can depend on the choice of coordinate system [Purcell and Morin, 2013]. A more general definition is given by the “modern theory of polarization”, i.e. $P(t) = \int_{-\infty}^t dt' J(t')$ (Eq. 4.8, [Resta and Vanderbilt, 2007]). In the special case discussed here, the density fluctuations are well localized around the oxygen atoms, and the oxygen atoms are sufficiently far away from the unit cell boundaries. Therefore, the former expression indeed gives the average induced dipole moment around the oxygen atoms, corroborating the physical picture laid out above.

are essentially vertical in character and remain localized around individual Si-O-Si bonds, but due to the different center of mass of the valence and excited conduction band states induced by the non-equivalent $+\hat{a}$ and $-\hat{a}$ directions a net shift of charge along the $+\hat{a}$ axis occurs. For higher laser intensities, on the other hand, the predominant charge transfer mechanism becomes tunneling. Tunneling significantly depends on the local potential landscape. We find tunneling is enhanced if the bond direction is aligned with the laser field (labeled O atoms in Fig. 4.10c) as evidenced by a strongly asymmetric current density at times near the maxima of the electric field (Fig. 4.10d,e). Tunneling ionization is more efficient along the $-\hat{a}$ axis where the O-Si bond is more aligned to the laser field (25.3 deg) while in $+\hat{a}$ direction tunneling is suppressed (51.5 deg; the other bonds are at similar or larger angles with respect to the laser field). The transition from multi-photon excitation to tunneling therefore corresponds to a sign change of the non-linear photogalvanic coefficient and of the transferred charge. After ionization, the current is mainly driven along the helical channel formed by the O-Si-O-Si-O chain along the \hat{a} direction (labeled atoms in Fig. 4.10c and light contours in d, e). For both low and high laser intensities, the CEP-independent charge transfer happens *during* the laser pulse (Fig. 4.10a), even though a small persistent current is also observed at high intensities (slope of $P(t)$ in Fig. 4.10a). The charge transfer is strongest around the maxima of the laser field. The time-dependence of the tunneling current can be illustrated by the “non-linear” current $j_{\text{NL}}(t)$ defined as the difference between the current and the scaled linear response current (Fig. 4.10 b). At the beginning of the pulse, the non-linear current is zero (linear response for low field strength). However, once a significant field strength sufficient for tunneling between neighboring atoms is reached at around -3 fs, the non-linear current shows strong spikes. While the linear response current is, to a good approximation, 90 degrees out of phase with the electric field (so that $P(t) = \int_{-\infty}^t dt' J(t')$ is in phase with $F(t)$), the non-linear current shows spikes at the maxima of the laser field, indicative of tunneling. At later times (from -1 fs), the “non-linear” current is in phase with the laser field but is, to a good approximation, proportional to the laser field, indicative of a conductor-like linear response $J(t) = \sigma F(t)$ with a Drude (free carrier-like) conductivity σ ascribed to the tunneling-induced electron population in the conduction band.

Our results indicate that the non-linear photogalvanic effect can be employed for light-field controlled charge separation on the femtosecond time scale. Compared to the CEP-dependent currents discussed in the previous section, the requirements for the driving laser are lower. Even many-cycle pulses with a duration much longer than the optical period and without CEP stabilization can be used to induce charge transfer because the lattice structure instead of the CEP is employed to break the inversion symmetry along the laser polarization axis. The amount of transferred charge per shot can be adjusted by tuning the laser intensity or the laser pulse length. The photogalvanic effect is conceptually simpler than the carrier-envelope phase dependent charge transfer since no elaborate steering of the conduction band electrons is

necessary. Therefore, the mechanism is robust against small changes in the laser pulse parameters.

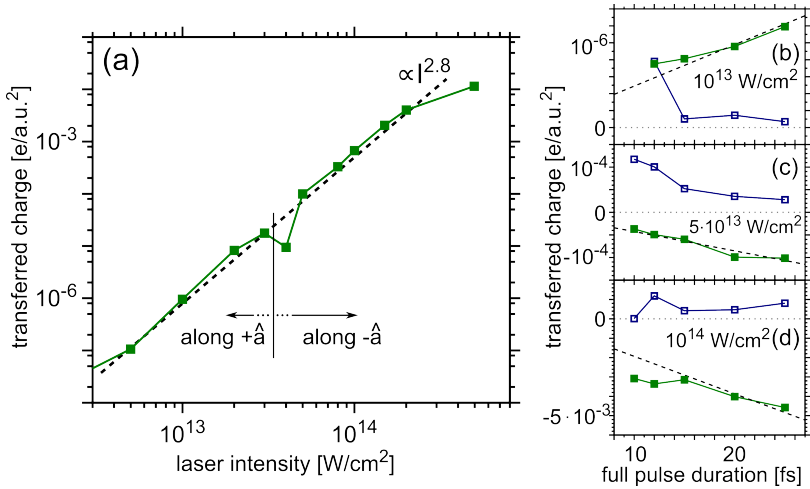


Figure 4.9: Non-linear photogalvanic effect. (a) Amplitude of carrier-envelope phase (CEP) independent transferred charge as a function of laser intensity for pulses with $\hbar\omega = 1.7$ eV photon energy and full pulse duration 20 fs (FWHM intensity 7.3 fs) polarized along the \hat{a} crystallographic direction. The transferred charge increases approximately with $I^{2.8}$ (dashed line); electrons are transferred along $+\hat{a}$ for lower laser intensity and along $-\hat{a}$ for higher laser intensity ($\geq 4 \times 10^{13}$ W/cm²). (b-d) Pulse length dependence of transferred charge at intensities 1×10^{13} W/cm², 5×10^{13} W/cm², and 1×10^{14} W/cm². The CEP dependent part (blue open squares) tends to decrease for longer pulses (full pulse length) while the CEP independent part (green full squares) increases approximately linearly for long pulse lengths (dashed line goes through the origin).

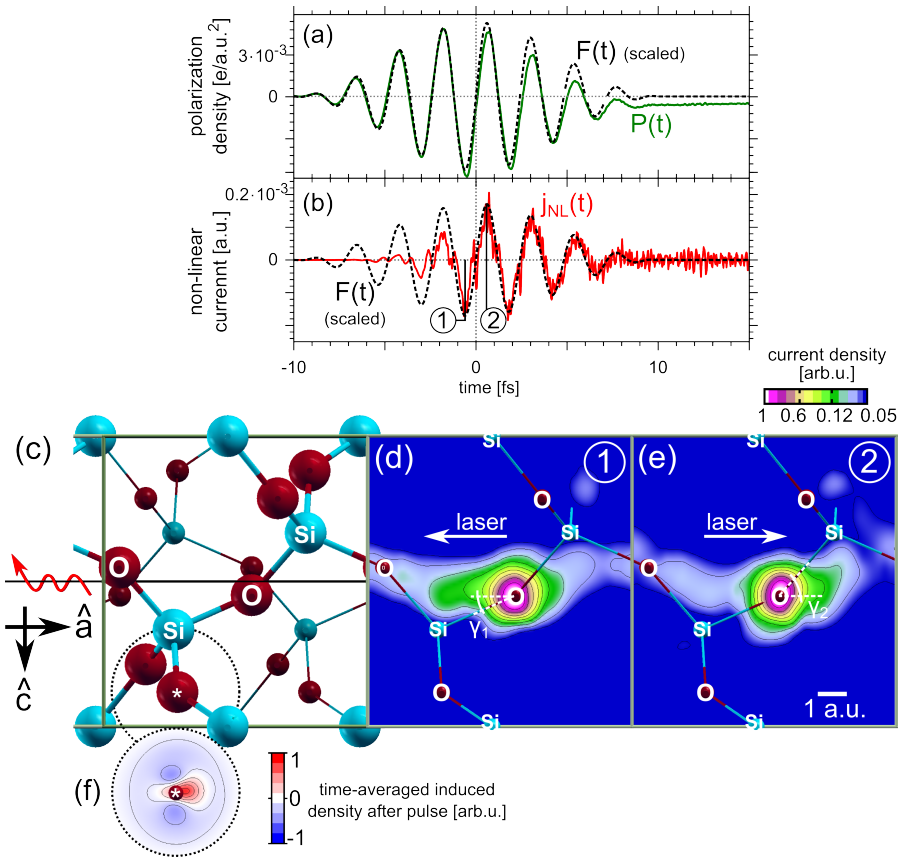


Figure 4.10: Mechanism for charge transfer (a) Time-dependent polarization density $P(t)$ (solid green) along the laser polarization direction \hat{a} and laser field $F(t)$ (black dashed, scaled) for a 20 fs pulse with photon energy 1.7 eV and intensity 1×10^{14} W/cm 2 . (b) Time-dependent non-linear current, defined as the difference between the current and the current from a low intensity simulation scaled to the high laser intensity (red solid). (c) α -quartz lattice structure. Big atoms are closer to the reader than small atoms (in the “closer” half of the unit cell); labeled atoms form a helix (compare red arrow) along the \hat{a} direction while unlabeled atoms have bonds with large angles on the viewing plane. The non-linear photogalvanic effect is observed along the \hat{a} axis since the lattice is not symmetric with respect to an inversion $\hat{a} \rightarrow -\hat{a}$. (d-e) Snapshot of the current density in an $\hat{a}-\hat{c}$ cut plane going through the central oxygen at a time when the non-linear current is directed into the $-\hat{a}$ direction (marked ① in (b)) for (d) and into the $+\hat{a}$ direction (marked ② in (b)) for (e). The angle between electric field and the O-Si bond is $\gamma_1 = 25.3$ deg and $\gamma_2 = 51.5$ deg. (f) Time-averaged density fluctuation after the laser pulse in a cut plane through the oxygen atom marked by a star for a lower laser intensity of 1×10^{13} W/cm 2 .

4.9 Optical signal of ionization and non-linear polarization

As an alternative to the optical-field induced charge transfer, optical probes can be used to scrutinize strong-field electron dynamics in the bulk. Pioneering studies by Gertsvolf et al. [2008] found that multiphoton ionization in the bulk depends on the orientation of the laser polarization with respect to the crystal axis as revealed by non-linear absorption. Attosecond (sub-cycle) dynamics were first demonstrated in the change in ellipticity between incident and transmitted beams [Gertsvolf et al., 2010]. Another manifestation of the ionization dynamics was observed for gas targets in terms of signals at additional frequencies [Verhoef et al., 2010] and could be extended to the study of bulk solids [Mitrofanov et al., 2011]. The laser field changes the dielectric response of matter around the extrema of the laser field due to ionization of electrons on a time scale much shorter than the optical period. This ionization happens twice per laser cycle, i.e., with frequency $2\omega_1$ where ω_1 is the pump laser photon energy. To spatially, temporally, and spectrally isolate the ionization-related signal from concomitant non-linear optical responses, a non-collinear cross-polarized pump-probe setup was employed (Fig. 4.11a) that consists of a pump pulse (henceforth index 1) and a weaker, cross-polarized probe pulse (index 2) that overlap in the target under a non-collinearity angle ϕ_{NC} . The optical signal related to ionization was observed at frequency $\omega_{\text{ion}} = 2\omega_1 + \omega_2$ in the direction of the probe pulse \mathbf{k}_2 and polarized along the probe direction. Concomitant optical responses include third harmonic generation by the pump pulse (at $\omega_{3\text{H}} = 3\omega_1$, along \mathbf{k}_1 , in pump polarization direction) and other third-order responses like cross-phase modulation (XPM) $P_{\text{XPM};2}^{(3)} = \chi_{112}^{(3)} F_1^2 F_2$ at frequency $\omega_{\text{XPM}} = 2\omega_1 + \omega_2$ in direction $2\mathbf{k}_1 + \mathbf{k}_2$ polarized along the probe direction. This latter third-order response is excluded in experiment by collecting only the light emitted into a narrow angle around the probe direction, and in experiment ω_1 and ω_2 were chosen such that the third order harmonic generation in probe direction ($3\omega_2$) is spectrally separable from the ionization signal.

Within our present simulation of time-dependent electronic dynamics not including propagation of the electromagnetic wave in the material, it is not possible to spatially separate the signals propagating in different directions \mathbf{k}_1 , \mathbf{k}_2 , and $2\mathbf{k}_1 + \mathbf{k}_2$ as in experiment. While first results coupling TD-DFT quantum dynamics within a single unit cell to a Maxwell solver were recently achieved [Yabana et al., 2012], extension to more than one dimension is presently prohibited by the numerical complexity. However, we may investigate the optical response resolved by polarization direction \hat{n} and frequency ω , i.e., the energy radiated per laser pulse per unit frequency interval per solid angle by a single unit cell and without phase matching. It is according to Larmor's formula [Jackson, 1998] proportional to

$$S_{\hat{n}}^{\text{opt}}(\omega) = \omega^2 \left| \int_{-\infty}^{\infty} \mathbf{J}(t) \cdot \hat{n} e^{-i\omega t} dt \right|^2 \quad (4.17)$$

where $\mathbf{J}(t)$ is the time-dependent macroscopic current in a unit cell (see Eq. 4.4).

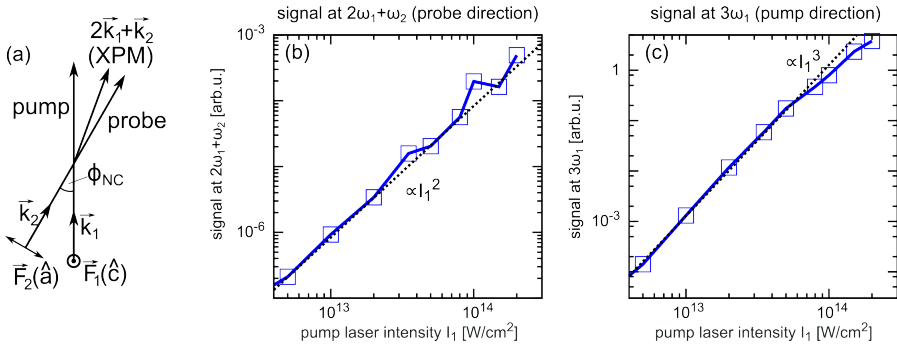


Figure 4.11: Optical signal in a non-collinear cross-polarized pump-probe setup. (a) Sketch of non-collinear cross-polarized pump-probe setup. A strong (pump, index 1, $\omega_1 = 1.65$ eV, polarized along \hat{c}) and a weak (probe, index 2, $\omega_2 = 1.46$ eV, $I_2 = 1 \times 10^{10}$ W/cm², pulse duration 5.8 fs for both) laser pulse overlap with a non-collinearity angle of ϕ_{NC} . In the simulation, we simulate only a single unit cell so that the concomitant signals in pump, probe, and $2\vec{k}_1 + \vec{k}_2$ directions are not disentangled. (b) Optical signal at $2\omega_1 + \omega_2$ in probe direction (blue boxes), I_1^2 scaling (dotted line). (c) Optical signal at $3\omega_1$ in pump direction (blue boxes, same units as (b)), I_1^3 scaling (dotted line).

In pump polarization direction (\hat{c}), we find that the perturbative expansion $P_{3H,1}^{(3)} = \chi_{111}^{(3)} F_1^3$ remains valid up to about 5×10^{13} W/cm² (Fig. 4.11c). In probe direction, the optical signal at low intensities scales as I_1^2 , consistent with the dominance of cross-phase modulation. We confirmed that the signal in probe direction is maximal at $2\omega_1 + \omega_2$ for various photon energies ω_1 and ω_2 and that the signal vanishes for non-overlapping pump and probe pulses. Further, the signal is suppressed for circular pump polarization. We find that the optical signal departs from the pure χ^3 effect starting from about 5×10^{13} W/cm². This intensity coincides with the appearance of tunneling-like ionization and quasi-free currents in the material. However, within our simulation it is not possible to unambiguously discern the optical signal stemming from the quasi-periodic ionization. We note that in experiment [Mitrofanov et al., 2011] the maximum laser intensity was $< 2 \times 10^{13}$ W/cm² which was found to be already close to the optical damage threshold for the samples employed. However, other measurements find a much increased optical breakdown threshold of 9×10^{13} W/cm² [Schultze et al., 2013].

The sub-cycle dynamics of the non-linear polarization can be further scrutinized in the time domain. Schiffrin et al. [2013] investigated the dynamics of ultrafast currents by a collinear cross-polarized pump-probe setup ($\phi_{NC} = 0$) where the wave form of the strong pump pulse and the weak probe pulse were identical copies of one another ($\omega_1 = \omega_2 = 1.7$ eV) however with adjustable amplitudes and time delay. It was demonstrated that the optical-field induced currents were controlled by this time delay. Schiffrin et al. [2013] argued that the strong (pump) pulse injects carriers into the conduction band that can subsequently be steered by the weak (probe) pulse. Within our simulation, we can disentangle the “linear” polarization, that is the

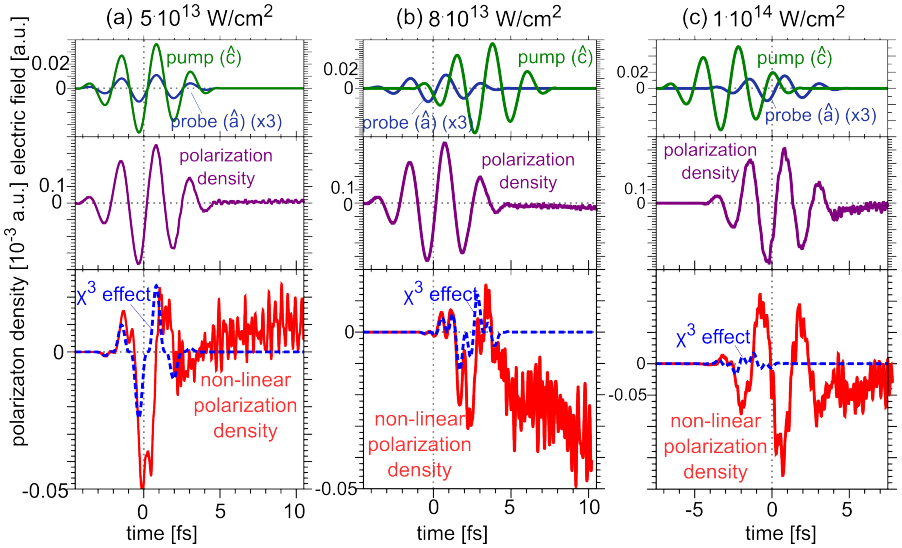


Figure 4.12: Non-linear polarization in pump-probe setup. Top panels: Electric field strength in pump (green, along \hat{c}) and probe (blue, along \hat{a}) direction. Middle panels: Time-dependent polarization density in probe direction. Bottom panels: Time-dependent non-linear polarization density, defined as the additional polarization density induced by the presence of the pump pulse (red solid line); corresponding third-order effect $P^{(3)}(t) = \chi_{\text{acc}F_c}^{(3)}(t)^2 F_a(t)$ (blue dashed line). **(a)** Pump intensity $5 \times 10^{13} \text{ W/cm}^2$, delay 0 fs. Probe intensity is a factor 100 lower than pump intensity in this plot, both pump and probe pulse duration is 3.5 fs at photon energy 1.7 eV. **(b)** Pump intensity $8 \times 10^{13} \text{ W/cm}^2$, delay -3 fs. **(c)** Pump intensity $1 \times 10^{14} \text{ W/cm}^2$, delay $+3$ fs.

polarization elicited by the probe pulse alone, from the “non-linear” polarization due to both pump and probe pulses (Fig. 4.12). We compare this non-linear polarization to the lowest-order non-linear effect, the cross-phase modulation, where the proportionality constant $\chi_{\text{XPM}}^{(3)}$ was obtained from simulations at low pump and probe intensities. At relatively low intensities of $5 \times 10^{13} \text{ W/cm}^2$, the non-linear polarization response at first follows the $\chi^{(3)}$ prediction (Fig. 4.12a bottom). However, as the laser pulse changes the non-linear dielectric properties of the dielectric, the non-linear polarization departs from the $\chi^{(3)}$ prediction. The magnitude of the non-linear polarization is twice that of the $\chi^{(3)}$ effect. The non-linear polarization that builds up after the laser pulse along the \hat{a} direction induced by the laser field in \hat{c} direction is caused by a separate non-linear effect permitted by the lattice symmetry similar to the non-linear photogalvanic effect. In Fig. 4.12a, the pump and probe pulses are perfectly on top of each other, so that is not possible to say if the non-linear response is switched on by one or the other. In a second simulation run, the pump pulse was delayed with respect to the probe pulse by 3 fs (Fig. 4.12b) so that the maximum of the pump pulse is approximately at a zero crossing of the probe pulse. Again, the non-linear polarization response at first follows the χ^3 prediction. The polarization

response strongly departs from the χ^3 prediction in coincidence with the maximum of the pump laser. This indicates that the non-linear optical properties of the material are strongly changed by the pump laser field on a sub-cycle time scale. This observation might be related to the so-called “adiabatic metalization” predicted for thin films [Durach et al., 2010, 2011; Apalkov and Stockman, 2012]. On the other hand, if the probe is delayed with respect to a strong pump pulse, the non-linear response is dominated by a free-carrier like contribution (in phase with the vector potential), indicating that the pump pulse has permanently changed the dielectric properties of the material (see also Sato et al. [2014]). Equating the non-linear polarization density incurred during the pulse to an effective dielectric function during the laser irradiation, first results indicate that the dielectric function is changed by 2 – 10 % between $5 \times 10^{13} \text{ W/cm}^2$ and $1 \times 10^{14} \text{ W/cm}^2$. This ultrafast change of dielectric properties on the sub-cycle time scale will be reflected in an ultra-broad spectral response beyond low-order non-linear processes. The generation of high harmonics employing pump pulses in the optical wavelength range in quartz and other solids can be envisioned.

4.10 Conclusions and outlook

In this chapter, we have studied optical-field induced electron dynamics in dielectrics by ab-initio fully three-dimensional time-dependent density functional theory simulations in real space and real time for a periodic unit cell of α -quartz. Employing a recently proposed meta-GGA approximation to the exchange-correlation functional capable of correcting the value of the band gap, we found linear and low-order non-linear optical properties in good agreement with experiment. We then focused on investigating optical field-induced currents in dielectrics stimulated by very recent experiments by Schiffrin et al. [2013]. Employing our simulation to resolve the microscopic charge and current dynamics on the atomic length and time scales within a unit cell, we found a transition from non-linear polarization currents to the regime of tunneling excitation where the intense electric field forces electrons to tunnel between neighboring atoms leading to quasi-free currents that persist even after the laser pulse. Our simulation agrees with the first experimental data for the intensity dependence as well as the carrier-envelope-phase dependence. Additionally, we found that the non-linear current response is also sensitive to the laser polarization in the unit cell and thereby on details of the chemical bonds and lattice structure. Such strong-field physics of dielectrics are a promising candidate for optical signal processing on the femtosecond (petahertz) time scale. We discussed the thermal load in such a device resulting from the electronic excitation and found that minimization of “real” excitations and miniaturization of switching devices down to the nanoscale will be of paramount importance for realizing operable petahertz circuits. We then discussed a novel process that we termed “non-linear photogalvanic effect” in analogy to the conventional photogalvanic effect that describes generation of electrical currents by a linearly polarized cw laser field along a non-inversion symmetric crystal direction.

Instead of the linear intensity scaling we found a strongly non-linear intensity dependence. At high laser intensity, electron tunneling that is enhanced along the bonding direction and suppressed when the bond is oriented at a larger angle to the laser field. Here, the transition from multiphoton excitation at low intensity to tunneling at high intensity leads to a reversal in the sign of the transferred charge. Finally, we discussed signatures of ionization and tunneling that can be found in the light emitted from a dielectric under irradiation and demonstrated that the non-linear optical properties of a dielectric are changed on the femtosecond time scale by a strong laser field.

Future work will fall into three categories. Firstly, the simulations presented in this chapter will be extended to other laser pulse shapes and materials. A systematic study of the cross-polarized pump probe setup following the second set of experiments by Schiffrin et al. [2013] will allow consistent interpretation of both experiments in terms of the spatio-temporal charge dynamics induced by ultrashort laser pulses, possibly including the transition from ballistic to dissipative electron transport. Another interesting class of laser pulse shapes for which charge transfer is expected due to the broken inversion symmetry are two-color pulses. Along the same lines, a set of several large bandgap dielectrics, including ionic crystals with a simpler lattice structure like LiF, will be studied to elucidate the connection between lattice structure, laser intensity, excitation mechanism, and steering of the electron wave packet in the conduction band in both one-pulse and pump-probe setups. For comparison to future experiments, knowledge of the experimental parameter \mathcal{A}_{eff} will allow comparison on an absolute scale and, eventually, allow assessment of the influence of the macroscopic sample shape on the charge dynamics.

Secondly, detailed scrutiny of some issues discussed in this chapter will require extension of the present theoretical framework. Two major extensions will be needed. Firstly, multi-scale simulations coupling time-dependent density functional theory simulations for the microscopic dynamics with a Maxwell solver for the macroscopic dynamics of the electromagnetic field have recently been presented by Yabana et al. [2012]. While the numerical cost of such simulations is, typically, two to three orders of magnitude larger than the simulations presented above since 100 to 1000 microscopic simulations have to be coupled to each other, such simulations will answer a number of important questions. They will be used to investigate at which depth in the sample the charge transfer occurs (i.e., if the charge transfer is mostly a surface or mostly a bulk effect). This should also be confirmed experimentally by varying the sample shape and thickness. Further, the highly non-linear re-shaping of the incident laser pulse will be investigated, which can also impact on the non-linear charge transfer in the bulk. Finally, such coupled microscopic-macroscopic simulations will also provide the two-dimensional phase matching needed for the separation of the ionization signal from concomitant non-linear optical responses in section 4.9. Possibly, a recently proposed efficient basis expansion can be employed to render the numerical effort more tractable [Sato and Yabana, 2014]. The second important improvement to the present description is the inclusion of dissipation of the quasi-free currents by

electron-electron, electron-impurity, and electron-phonon scattering. Dissipation can be included most easily by employing a phenomenological description of “quantum friction” [Neuhauser and Lopata, 2008]. In the long term, ab-initio approaches will be called for. For electron-phonon scattering existing approaches may be extended [Kreibich and Gross, 2001; Kreibich et al., 2004, 2008; van Leeuwen, 2004; Butriy et al., 2007; Franco et al., 2007; Andrade et al., 2009; Shinohara et al., 2010, 2012b], and/or an improved description of dissipation in the electronic degree of freedom can be achieved employing time-dependent *current* density functional theory [Wijewardane and Ullrich, 2005; D’Agosta and Vignale, 2006].

Thirdly, the present toolbox for description of intense laser-matter interaction will be extended to the study of qualitatively different systems and observables. Non-linear optical properties of bulk defects like color centers will be studied. A simulation for the first surface layer, either employing a supercell or by a dedicated new software solution specifically designed for surfaces, will be used to investigate if the field-induced current is larger within the first layer of the surface than below and how the field-induced currents depend on the surface structure and composition. In principle, such a surface simulation can also be used for investigating the strong-field response and electron emission from metal surfaces and nanostructures (chapter 3). Studies of optical properties of dielectrics slabs and the transition from vacuum to bulk dielectric properties have been restricted to the linear regime [Giustino et al., 2003; Giustino and Pasquarello, 2005; Shi and Ramprasad, 2005, 2006; Wakui et al., 2008] and will be extended to the non-linear regime, possibly involving applications of hot-electron assisted surface femtochemistry [Gavnholt et al., 2009; Mukherjee et al., 2013]. High harmonic radiation from bulk semiconductors has been observed and has been interpreted in terms of dynamical Bloch oscillations, i.e. reflections at the Brillouin zone boundary, for a ZnO crystal at an infrared wavelength of 3250 nm [Ghimire et al., 2011a, 2012] including its dependence on the crystal orientation and in GaSe at 10 μm (30 THz) [Schubert et al., 2014]. First theoretical efforts based on the non-equilibrium Keldysh formalism predict Bloch oscillations are a robust mechanism for high harmonic generation insensitive to scattering by impurities and phonons [Kemper et al., 2013] (see also Földi et al. [2013]; Korbman et al. [2013]; Vampa et al. [2014]). First TD-DFT ab-initio calculations for diamond [Otobe, 2012] have been performed at visible wavelengths. However, the role of Bloch oscillations in the parameter regime important for high harmonic generation is yet unresolved. While we have shown in section 4.9 that the *non-linear* optical properties in dielectrics can be controlled on the femtosecond time scale, the *linear* optical properties show a much smaller contrast in the range of only a few per cent of the value of the dielectric function. Extension to other pump and probe wavelengths may lead to improved contrast also for the linear response, possibly leading to all-optical femtosecond switching of light by light. For example, pump wavelengths in the infrared can be employed to modify the value of the gap and switch transmission of ultra-fast few-cycle probe pulses with photon energies at or near the gap energy ($\sim 10 \text{ eV} \sim 120 \text{ nm}$) of large-gap dielectrics,

anticipating development of such laser pulses within the next few years. Alternatively, lower-gap materials and laser pulses that are currently achievable (~ 4 eV with FWHM 3 fs [Graf et al., 2008; Reiter et al., 2010]) could serve a similar purpose. Up to now, strong field experiments on bulk solids rely on high-power amplified lasers. As we have demonstrated in chapter 3, electromagnetic near-field enhancement can substantially lower the necessary laser intensity and permit the use of low-power oscillators with high repetition rates. To achieve a similar effect for the optical-field induced response in dielectrics, composite systems of dielectrics and nanoparticles (possibly employing a plasmonic metal) may be investigated. Novel two and three-dimensional nanoscale fabrication methods abound thanks to vigorous interest in meta-materials [Liu and Zhang, 2011] and photonic crystals [Soukoulis, 2002; von Freymann et al., 2013]. Candidate systems include nano-spheres or nano-ellipsoids embedded into dielectrics like glass, which have already been employed to tune the low-order non-linear response [Chen et al., 2011; Mohan et al., 2012; Can-Uc et al., 2013], or novel template-assisted lithography methods allowing production of almost arbitrary nano-structures on large-area surfaces [Tang and Wei, 2012; Zhao et al., 2014] or in stacked layers [Atwater and Polman, 2010]. An attractive alternative for obtaining strong field physics at low nominal field strengths besides composite systems are *dielectric* nanoparticles of *mesoscopic* size leading to a nano-focusing at the back side of the particle [Münzer et al., 2001; Gérard et al., 2008; Devilez et al., 2009; Mendes et al., 2011]. First test calculations with Maxwell solvers in the linear response regime suggest that silicon dioxide nanospheres with a radius equal to the optical wavelength lead to a maximal intensity enhancement of up to 40 times the nominal intensity at the back side of the particle. Similar effects may be achievable in reduced dimensions by nano-wires or arrays of nano-wires [Grzela et al., 2014], for which fully coupled TD-DFT/Maxwell calculations appear feasible.

Molecular near fields and attosecond streaking of endohedral fullerenes

5.1 Introduction

We now turn to the study of a much smaller system, a C_{60} molecule, that is exposed to few-cycle laser pulses as a test bed system for the ab-initio description of field enhancement.

Field enhancement occurs at structures much smaller than the optical wavelength of 800 nm. However, nanostructures are typically still very large compared to the atomic length scale. A nano-sphere of 10 nm radius contains about 50000 atoms, so that an ab-initio treatment of the corresponding near-fields and field enhancement is not feasible. In this chapter, we study the molecular near-field response of a C_{60} molecule that is at once large enough to show such near-fields and field enhancement and at the same time is still small enough so that a full ab-initio treatment becomes possible. Furthermore, buckminsterfullerene C_{60} [Kroto et al., 1985] is relatively easy to synthesize and isolate [Krättschmer et al., 1990]. The electrons are arranged in a shell, and its near-spherical symmetry is ideal for comparison to the analytically solvable model for field enhancement of a dielectric sphere in a static electric field.

It has been suggested that such near-fields of nanoparticles can be studied by attosecond streaking. The near-fields are probed by their effect on electrons photoemitted by an attosecond XUV pump pulse timed with respect to a NIR probe pulse [Skopalová et al., 2011; Süssmann and Kling, 2011]. In attosecond streaking experiments on solid surfaces, sensitivity to the local electric field that is rapidly screened inside the solid has been demonstrated ([Cavaliere et al., 2007; Neppel and et al., 2014]

and section 3.7). These experiments rely on surface preparation techniques on the sub-nm length scale by deliberately placing different atomic species at engineered positions in the sample, leading to a sub-nanometer localized source of electrons that can be distinguished in the streaking spectra by their final energies. For analysis of the molecular near-fields of C_{60} by attosecond streaking, a similar localized source of electrons can be provided by doping C_{60} with another atomic species. Such doping schemes have been investigated almost since the first detection of C_{60} [Heath et al., 1985] leading to so-called “endohedral fullerenes” or endofullerenes that are denoted by an @ sign, for example $Ne@C_{60}$. While metal dopants can adsorb to different sites inside the C_{60} “cage”, it has been found that the chemically inert rare gases like He and Ne are located at its center. As endohedral atom, we chose $Ne@C_{60}$ as its $2s$ line is sufficiently well separated from the C_{60} lines to allow spectral separation. We expect that our conclusions are also valid for other rare gases.

We begin this chapter by briefly reviewing some specifics of the TD-DFT implementation employed for finite 3D systems (section 5.2). We then present the ground state and linear response properties of fullerenes and endohedral fullerenes, putting emphasis on the change in the electron density that is induced by an optical laser pulse and the electric near field distribution derived from it (sections 5.3, 5.4, and 5.5). We then study the molecular near-fields depending on the orientation of the polarization vector of the laser pulse relative to the molecule to elucidate how bonding affects the near-fields (section 5.6). Taking advantage of our real-time formulation, we investigate the onset of non-linear field enhancement at higher laser intensities (section 5.7). In the second part of this chapter, we demonstrate how the time and space dependent near fields can be scrutinized by the attosecond streaking technique. The ab-initio near-field serves as input for a classical-trajectory Monte Carlo simulation. We study the effect of the molecular orientation and the presence of an endohedral atom on the streaking observables (section 5.8). In the final section, we substitute the NIR laser pulse by a UV pulse that populates the lowest excited states of the molecule. The coherently launched electronic wave packet leads to an oscillating time-dependent dipole moment of the molecule even after the laser pulse is over. We show that, in this configuration, the streaking signal yields a direct measurement of the time evolution of the molecular dipole moment and discuss possible ramifications for studying the onset of dephasing and decoherence on the electronic time scale.

5.2 TD-DFT simulation of fullerenes and endohedral fullerenes

We perform ab-initio simulations of fullerenes and endohedral fullerenes with time-dependent density functional theory for a finite system. The simulation was described in detail by Yabana and Bertsch [1996] and Kawashita et al. [2009]. We in-

tegrate the time-dependent Kohn-Sham equations

$$\begin{aligned}
 i\partial_t\psi_i(\mathbf{r},t) &= \left\{ -\frac{1}{2}\nabla^2 + V(\mathbf{r},t) \right\} \psi_i(\mathbf{r},t) = \\
 &= \left\{ -\frac{1}{2}\nabla^2 + V_{\text{ion}} + V_{\text{ext}}(\mathbf{r},t) + \int d\mathbf{r}' \frac{n(\mathbf{r}',t)}{|\mathbf{r}-\mathbf{r}'|} + V_{\text{XC}}[n(\mathbf{r},t)] \right\} \psi_i(\mathbf{r},t) .
 \end{aligned}
 \tag{5.1}$$

The potential of the ionic cores V_{ion} is included in terms of norm-conserving pseudopotentials [Troullier and Martins, 1991] for the $1s^2$ cores of carbon and neon. The external potential

$$V_{\text{ext}}(\mathbf{r},t) = F_L(t)z \tag{5.2}$$

describes the coupling to the time-dependent electric field $F_L(t)$ of the laser polarized in z direction in length gauge within the dipole approximation. Throughout this chapter, we use the adiabatic LDA to the XC potential V_{XC} . In total, we treat 240 electrons (120 orbitals) in a cuboid box with a space discretization of 0.5 a.u. for C_{60} and 248 electrons (124 orbitals) with a discretization of 0.4 a.u. for Ne@C_{60} . The induced density $\Delta n(\mathbf{r},t) = n(\mathbf{r},t) - n(\mathbf{r},-\infty)$ leads to an induced dipole moment along the laser polarization direction z

$$d(t) = \int d\mathbf{r} z \Delta n(\mathbf{r},t) . \tag{5.3}$$

The microscopic electric field is defined as the negative gradient of the induced potential $V(\mathbf{r},t) - V(\mathbf{r},-\infty)$ that results from the induced density.

5.3 Geometry and ground-state properties

C_{60} or buckminsterfullerene has the shape of a truncated icosahedron where the carbon atoms occupy the 60 vertices (Fig. 5.1a). The 32 faces comprise 20 hexagons and 12 pentagons. Pentagons are surrounded by hexagons only, and each hexagon is surrounded by three hexagons and three pentagons. Therefore, there are only two different kinds of edges, namely edges between two hexagons (6-6) and edges between a hexagon and a pentagon (5-6). All carbon atoms are equivalent (each borders on one pentagon and two hexagons). Per default, we take the coordinate axes aligned with mirror planes of the C_{60} molecule. The faces of C_{60} can be visualized in a Schlegel diagram (Fig. 5.1b, Schlegel [1883]), i.e., the projection of the atom sites from a point above the C_{60} onto a plane below the C_{60} .

The electronic structure of C_{60} was predicted [Osawa and Yoshida, 1971; Bochvar and Gal'pern, 1973] well before first experimental hints of its detection [Kroto et al., 1985; Krätschmer et al., 1990] and has been discussed in detail thereafter [Haddon et al., 1986; Yabana and Bertsch, 1993; Rioux, 1994; Liebsch et al., 1995] so we only give a brief overview here. The ground state electron density is localized around the

carbon cores at a radius of 6.66 a.u. from the center of the cage (Fig. 5.2 and inset). Of the four carbon valence electrons (configuration $2s^2 2p^2$), three form sp^2 -hybridized bonds between the carbon atoms of lower energy (about -25 to -10 eV). These σ electrons have maximum probability on the carbon shell (e.g. Fig. 5.2e②). The remaining electrons occupy π states of higher energy (e.g. the HOMO in Fig. 5.2e⑤) with a node on the carbon shell. In our LDA calculation, the highest occupied orbital is at -6.11 eV while the experimental electron removal energy is 7.5 eV. The total ground state Kohn-Sham potential at the center of the C_{60} is slightly attractive (about -2 eV in our calculation, Fig. 5.2b inset).

We may now inquire into the effect of an added neon rare gas atom into the center of the C_{60} molecule. The density, potential, and density of states of an isolated Ne atom without a C_{60} cage is shown in Fig. 5.2¹⁰ along with the corresponding quantities for C_{60} and the combined Ne@ C_{60} . The ground state density, potential, and density of states of C_{60} are only marginally disturbed by the presence of the neon atom. The states corresponding to the Ne atom are slightly shifted to lower energy by about 2 eV compared to the free atom (Fig. 5.2d①,③). This shift is attributed to the attractive potential in the center of the C_{60} molecule. We find only minimal hybridization between Ne and C_{60} orbitals. The Ne $2s$ orbital (-37.3 eV) has such low energy that there are no C_{60} states available for hybridization (Fig. 5.2d,e①). The Ne $2p$ states (-14.5 eV, Fig. 5.2d,e③) do not hybridize with the C_{60} states of similar energy because these states are still predominantly of σ character. There is, however, a slight hybridization between Ne $2p$ states and C_{60} π states of somewhat higher energy around -12 eV (Fig. 5.2d,e④). This hybridization leads to a tiny distortion in the density of states of the Ne@ C_{60} compared to C_{60} (Fig. 5.2d④). We conclude that the chemical ground-state structure of C_{60} is, for practical purposes, not changed by the additional Ne atom in its center.

5.4 Absorption and polarizability

We now inquire into the linear response properties of C_{60} and Ne@ C_{60} by applying a weak excitation with a wide frequency spectrum at the start of the simulation and propagating the system in time. To check the numerical accuracy of the simulation, we evaluated the oscillator strength distribution for C_{60} and Ne@ C_{60} and verified that it agrees with literature results (Kawashita et al. [2009], Fig. 5.3a) which show good agreement to experimental absorption spectra. The dominant structures in the spectra are peaks around ~ 6 eV and ~ 20 eV. These peaks can be loosely assigned to plasmon excitations of the π and σ electron systems within a two-fluid model [Barton and Eberlein, 1991]. The lowest dipole-allowed excitations correspond to transitions from the HOMO (symmetry h_u) and HOMO-1 (h_g) to the LUMO (t_u), LUMO+1 (t_g)

¹⁰ In our LDA calculation, the energy levels of an isolated neon atom are at -36 eV ($2s^2$) and -13.5 eV ($2p^6$), in agreement to literature values [Gaiduk et al., 2012]. The ionization energy calculated by the total energy difference between the neutral and ionic species is 22.7 eV, in agreement to literature values [Parr, 1994] and in better agreement to the experimental electron removal energy (21.7 eV).

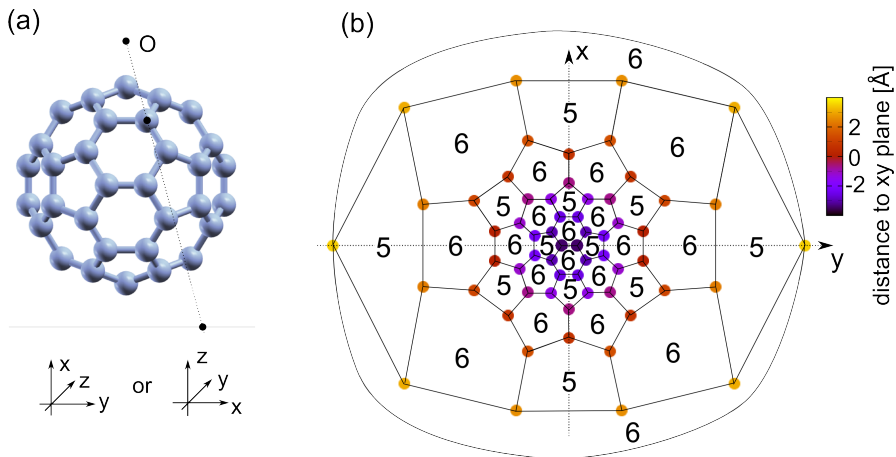


Figure 5.1: Geometry of the C_{60} molecule (a) Geometry of the C_{60} molecule (projection onto the xy or xz plane, see coordinate systems. Illustration of a Schlegel projection [Schlegel, 1883] of the C_{60} structure onto the xy plane. (b) Schlegel projection of the C_{60} structure onto the xy plane with the distance from the z axis as color code (20 hexagons, 12 pentagons).

and LUMO+2 (h_g) [Bertsch et al., 1991] and are visible as peaks in the polarizability starting from 3.6 eV (Fig. 5.3b; experiment: 3.76 eV [Heath et al., 1987; Ajie et al., 1990; Yasumatsu et al., 1996]). The excitation spectrum for Ne@ C_{60} agrees with the excitation spectrum of C_{60} in great detail, underlining that the electronic properties are not appreciably changed by the presence of the endohedral atom. We find a static polarizability of about 82 \AA^3 in good agreement to literature results [Zope et al., 2008]. A free Ne atom has a static polarizability of around 0.40 \AA^3 in experiment and 0.45 \AA^3 in LDA [Gisbergen et al., 1996]. We find that the combined polarizability for Ne@ C_{60} is lower than the sum of the free polarizabilities of Ne and C_{60} . This is because the C_{60} screens the external field even at optical frequencies. The small residual field inside the C_{60} cage reduces the small contribution of the Ne to the total polarizability. Outside the C_{60} shell we observe field enhancement. The maximal field is attained at a distance of about 10 a.u. from the center, significantly outside the carbon cores (6.66 a.u.), with field enhancement between 2 and 3.

5.5 Density change and near field induced by few-cycle laser pulses

The mechanism of screening and field enhancement is visualized by a snapshot of the induced density and near field around C_{60} and Ne@ C_{60} molecules during a few-cycle laser pulse of central wavelength 800 nm (Fig. 5.4). The time-dependent electric field moves electron density so that a polarization charge layer forms at the surface of the carbon cage. The induced surface charge (Fig. 5.4c) is the quantum mechan-

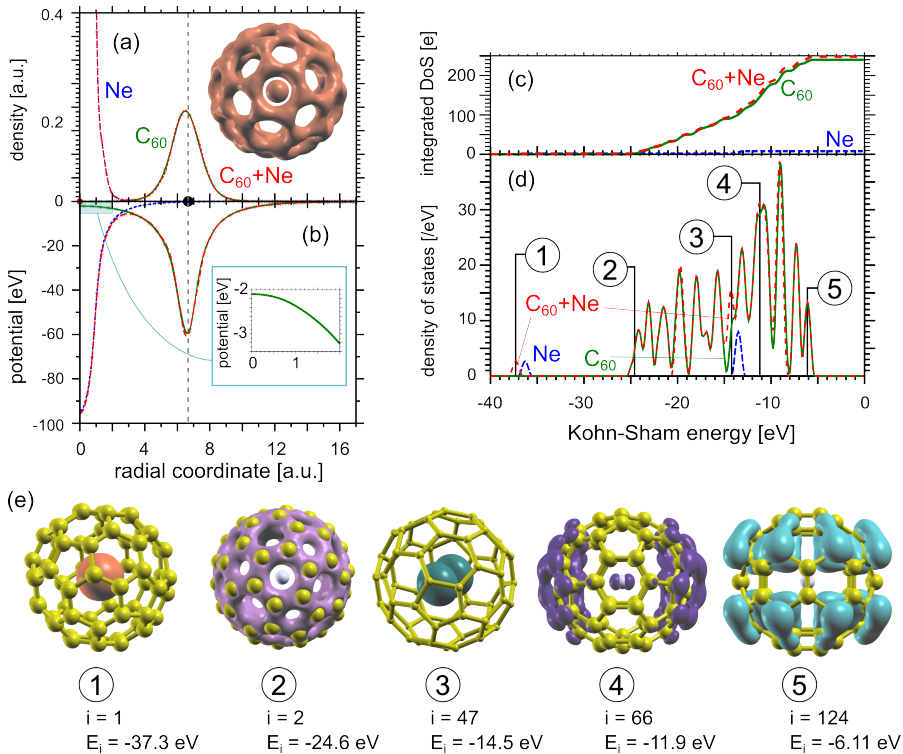


Figure 5.2: Ground state density and potential of C_{60} and $Ne@C_{60}$ (a) Ground state density of Ne (blue closely dashed), C_{60} (green solid), and $Ne@C_{60}$ (red dashed) averaged over the solid angle. **Inset:** 3D-isocour surface of the ground state density of $Ne@C_{60}$. (b) Ground state local Kohn-Sham potential. **Inset:** C_{60} potential around the center (turquoise rectangle). (c) Integrated density of states ($Ne@C_{60}$ has in total 248 valence electrons) and (d) density of states. (e) Kohn-Sham orbitals $|\psi_i(\mathbf{r}, t = -\infty)|^2$ of $Ne@C_{60}$ corresponding to the energies marked 1...5 in (d): (1) Ne $2s$ orbital, (2) lowest C_{60} orbital, (3) Ne $2p$ orbital, (4) slightly hybridized C_{60} / Ne $2p$ orbital, (5) highest occupied orbital, with corresponding orbital index (between 1 and 124) and Kohn-Sham eigenenergy.

ical analog of the surface charge on the dielectric sphere in a constant electric field (Fig. 2.1c). The polarization charge layer has a thickness of several a.u. and is localized predominantly outside the carbon cores even though the ground state density (Fig. 5.4a) assumes maximum probability density at the position of the cores. As a result, the electric field is already screened at the position of the carbon atoms in analogy to screening at a metal surface (section 3.7). The electric field inside the sphere is strongly screened to a factor of about 0.15 of the incident field and the field outside is dominated by a dipole pattern. Convergence to the asymptotic dipole field $1 + 2\alpha_0/|z|^3$ is already attained at 20 a.u., about twice the effective radius of the sphere (Fig. 5.4e). The finite width of the polarization charge layer smears out the near-field, resulting in a reduced field enhancement compared to macroscopic elec-

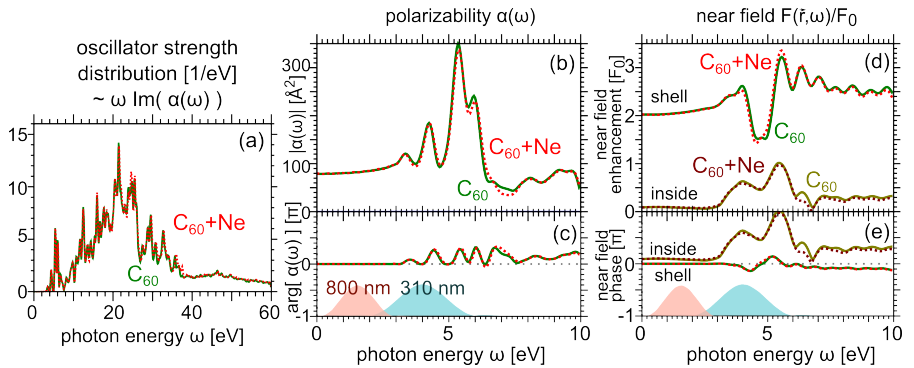


Figure 5.3: Frequency response of C_{60} and $Ne@C_{60}$. (a) Oscillator strength distribution of C_{60} (green solid line) and $Ne@C_{60}$ (red dotted line) over a wide frequency range, see also Kawashita et al. [2009]. (b) Absolute value of the frequency-dependent polarizability up to 10 eV for C_{60} and $Ne@C_{60}$. (c) Phase of the frequency-dependent polarizability up to 10 eV. Inset: Laser spectra for an 800 nm few-cycle pulse and a 310 nm few-cycle pulse (repeated in (e)). (d) Absolute value of the local frequency-dependent near field enhancement (upper graphs, “shell”, taken at 10 a.u. along the laser polarization direction) and screened field inside (lower graphs, “inside”, taken at 5 a.u. along the laser polarization direction). (e) Phase of the local electric field.

tromagnetism where the polarization charge layer is assumed to be infinitely thin. The density response of C_{60} and $Ne@C_{60}$ is almost completely equal at distances further than 3 a.u. from the center. Accordingly, the near field distribution is influenced only marginally by the Ne atom. The endohedral atom results in small fluctuations of magnitude $\sim 0.1F_0$ inside the cage while the screening, field enhancement, and decay are virtually identical for C_{60} and $Ne@C_{60}$.

5.6 Dependence on the orientation of the molecule

Optical near-fields around metallic nano-particles have been studied with quantum mechanical methods within the jellium approximation [Zuloaga et al., 2009, 2010; Stella et al., 2013] and very recently sodium dimers have been simulated including their atomic structure [Zhang et al., 2014]. The near-field of C_{60} in a static electric field has been studied by Delaney and Greer [2004]. We investigate the effect of the C_{60} bonds on the near field distribution at optical frequencies by changing the alignment of the C_{60} with respect to the laser along 5 high-symmetry directions where the strongest change in dielectric response is expected (Fig. 5.5b). We find that the asymptotic behavior, i.e., the polarizability, is approximately the same, as well as the field inside the cage. Significant differences appear around the position of the carbon cores and slightly outwards. For laser polarization pointing towards a carbon atom or covalent bonds (Fig. 5.5a) we find similar field distributions near the surface. On the other hand, when the laser field points towards the center of a hexagon or pentagon with smaller ground state electron density, the field enhancement is reduced as

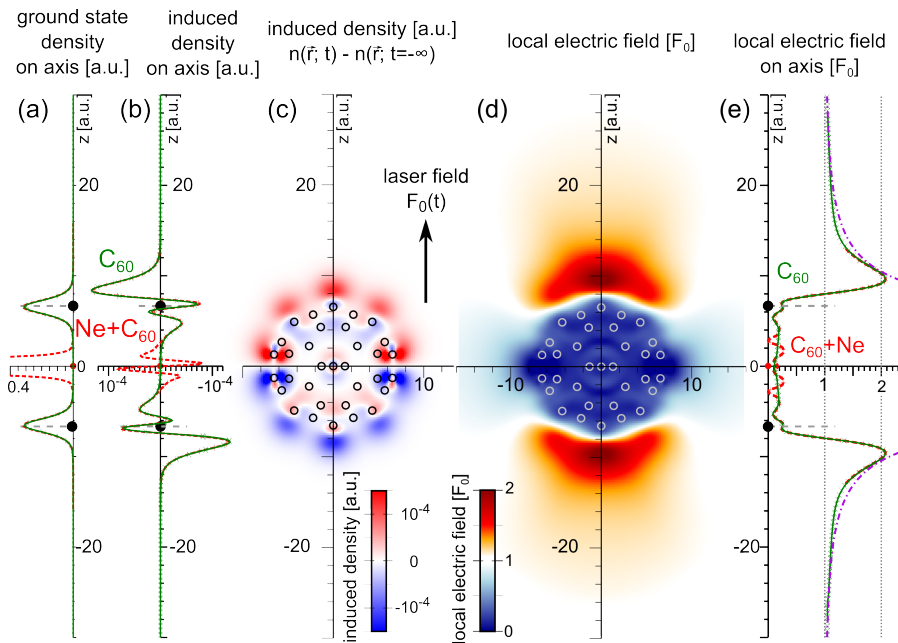


Figure 5.4: Induced density and near field enhancement around C₆₀ and Ne@C₆₀. (a) Ground state density of C₆₀ (green) and Ne@C₆₀ (red dashed) on the z axis parallel to the laser polarization direction where the coordinates x, y, z are defined as in Fig. 5.1. Horizontal grey dashed lines mark the radius of the carbon cores. Laser field points upwards. (b) Induced density due to optical excitation (800 nm, $F_0(t) = 0.0013$ a.u.) on the z axis. (c) Induced density of Ne@C₆₀ in the xz plane. Circles mark the positions of the carbon atoms. (d) Local electric field of Ne@C₆₀ in the xz plane. (e) Line out of local electric field in C₆₀ and Ne@C₆₀ along the z axis. Purple dash-dotted line: dipole field $1 + 2\alpha_0/|z|^3$ with $\alpha_0 \sim 84 \text{ \AA}^3$.

fewer electrons are available to respond. The value of the field enhancement factor varies between 1.7 and 2.1. This significant change by more than 20 % indicates that the near field distribution and enhancement around molecules is strongly affected by the atomic composition of the molecule, the bonds and bond strengths between the atoms, and conceivably the electronic state (ground state or excited state) of the electrons that make up the bond. Non-linear processes like electron tunneling are expected to be localized at the molecular sites with the largest near-field. On the other hand, the field distribution inside the carbon cage is largely unaffected by the direction of the electric field and shows only minor fluctuations if an additional Ne atom is present.

5.7 Dependence on the laser intensity

The above results were obtained at low laser intensities where the molecular response is linear in the laser field. Our real-time formalism also allows us to investigate the

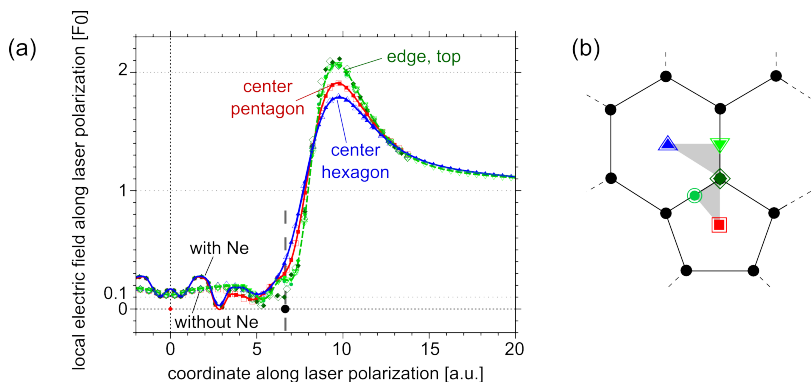


Figure 5.5: Dependence of near field on the laser polarization direction relative to the molecule orientation. (a) Electric near field along the laser polarization direction for C_{60} (open symbols) and $Ne@C_{60}$ (full symbols) for laser polarization direction oriented along the directions indicated in (b). Linear response calculation with laser intensity 1×10^{11} W/cm². Vertical gray dashed line indicates the radius of the carbon cores. (b) Sketch of C_{60} surface with irreducible unit cells (gray triangles) and high-symmetry points. Blue upwards triangle: center of hexagon; green downwards triangle: center of hexagon-hexagon edge; green circle: center of hexagon-pentagon edge; dark green diamond: on top of carbon atom; red square: center of pentagon.

non-linear response of C_{60} and $Ne@C_{60}$ for higher laser intensities. In bulk solids, the transition from linear to non-linear response can be described perturbatively [Bloembergen, 1996; Boyd, 2003]. To lowest order, the dominant contribution for centrosymmetric materials is the Kerr effect where the response function $\chi(\omega_L)$ acquires a non-linear contribution $\chi \rightarrow \chi^{(1)} + \chi^{(3)} |F_0(\omega_L)|^2$ that scales with the laser intensity. The third-order nonlinear coefficient is positive so that the refractive index increases with increasing intensity leading to spectacular effects like self-focusing. The nonlinear susceptibility of C_{60} is also positive [Wang and Cheng, 1992; Quong and Pederson, 1992; Jensen and Van Duijnen, 2005]. Near-field enhancement by the lightning-rod effect in general increases with increasing dielectric constant or polarizability. Therefore, one could expect that near field enhancement *increases* at higher laser intensities. On the other hand, a stronger laser field will lead to a smearing out of the polarization charge over a larger volume as the bonding potential becomes weaker so that the field enhancement may *decrease* compared to lower intensities. Experimental measurements of field enhancement, for example near metal nanostructures, have been restricted to the linear response regime [Thomas et al., 2013]. Theoretical treatments of non-linear effects for field enhancement have so far been scarce due to the lack of a theoretical framework for a reliable inclusion of non-local and non-linear effects for arbitrary laser intensities into the macroscopic Maxwell equations. Our ab-initio simulation of the C_{60} molecule can serve as a first step towards a microscopic understanding of non-linear field enhancement. We expect that the trends retrieved from this model system will be applicable to the intensity dependence of field enhancement for other molecules, nano-particles, and nano-structures.

To investigate the intensity dependence of field enhancement, we discuss snap-

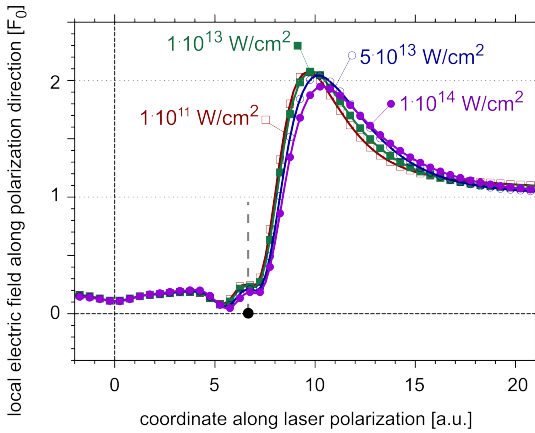


Figure 5.6: Dependence of near field on the laser intensity. (a) Electric near field along the laser polarization direction for C_{60} for laser intensities from the linear response regime $1 \times 10^{11} \text{ W/cm}^2$ to the regime of strong ionization $1 \times 10^{14} \text{ W/cm}^2$. Laser polarization is taken from the center of the C_{60} towards the hexagon-hexagon edge (see Fig. 5.5). Vertical grey dashed line indicates the radius of the carbon cores.

shots of the microscopic electric field in the C_{60} molecule at the time of the laser field maximum (Fig. 5.6) for increasing intensities from $1 \times 10^{11} \text{ W/cm}^2$ in the linear response regime up to $1 \times 10^{14} \text{ W/cm}^2$ where in experiment already several electrons can be ionized even by a short femtosecond pulse [Becker et al., 2006]. The snapshots are taken at the first large peak of the electric field, so that no significant ionization has yet occurred. For an intensity of $1 \times 10^{13} \text{ W/cm}^2$, we still find excellent agreement to the linear-response calculation. As the laser intensity is increased to $5 \times 10^{13} \text{ W/cm}^2$ and $1 \times 10^{14} \text{ W/cm}^2$, we observe that the maximum of the field is somewhat reduced and that the field distribution is shifted outward. Both observations are consistent with an increased spill-out of the electronic charge for high intensities. It leads at the same time to an increased dipole moment (polarizability, susceptibility) for higher intensities that is consistent with the Kerr effect, but also to a reduced maximum field enhancement.

5.8 Streaking of endohedral fullerenes in few-cycle optical laser pulses

Near field enhancement can be indirectly observed by the enhanced probability of non-linear processes. Alternatively, steady-state plasmon modes around nanostructures may be studied by their effect on electron trajectories in electron energy loss spectroscopy [Hörl et al., 2013]. Similarly, we here investigate near-fields by their effect on electrons as probe particles which are, however, emitted from the molecule itself with sub-femtosecond timing by an attosecond XUV pulse ($\omega_{\text{XUV}} \approx 100 \text{ eV}$) synchronized to the few-cycle pulse driving the linear response. The space- and time-

dependent near-field is thereby encoded into the momentum spectrum of the photoemitted electrons as a function of the delay between XUV and NIR pulse. For a pure laser field without near-field, the momentum shift acquired by electrons from their photoemission at time t^* until the end of the laser pulse is $\Delta\mathbf{p}(t^*) = -\int_{t^*}^{\infty} \mathbf{F}(t)dt = \mathbf{A}(t^*)$ equal to the vector potential $\mathbf{A}(t^*)$ at photoemission. Varying the time delay Δt between NIR and XUV pulse allows extraction of the wave form of the laser field [Goulielmakis et al., 2004]. A modification of this relation was found for rare-gas atoms where signals from different initial states are shifted with respect to one another by a few attoseconds so that the streaking signal is approximately $\mathbf{A}(t^* + \Delta t)$ (Schultze et al. [2010]; see Pazourek et al. [2014] for a recent review). This apparent “time shift” Δt stems in part from the quantum mechanical photoemission process where the formation time of the outgoing electron wave packet is identified with the energy derivative of the phase of the dipole matrix element called Eisenbud-Wigner-Smith time delay [Eisenbud, 1948; Wigner, 1955; Smith, 1960]. Along the trajectory of the liberated electron additional mechanisms contribute to the effective shift Δt . The trajectory of the outgoing electron can be modified by the atomic dipole moment of the residual ion [Pazourek et al., 2012], in analogy to the time-dependent near-field of a larger molecule or nanostructure. Analogously, attosecond *surface* streaking [Cavaliere et al., 2007; Neppel and et al., 2014] has found photoelectron spectra to be highly sensitive to the atomic-scale electric field distribution near the surface. These encouraging results nurture the hope that attosecond streaking can also yield information on near-fields in nano-size systems. While early numerical models have promised feasibility of this “nano-plasmonic streaking” [Skopalová et al., 2011; Süßmann and Kling, 2011], hitherto no experimental evidence has been presented. Likely, this is due to electron emission from deeper regions in the material on the length scale of the inelastic mean-free path $\lesssim 10$ nm [Lemell et al., 2009] that smears out the streaking signal. In recent surface streaking experiments, this has been counteracted by placing different atomic species at engineered positions in the sample so that individual photoemission lines are correlated with the spatial position of the initial wave functions of the electrons. Thereby, space resolution on the atomic length scale has been achieved [Neppel and et al., 2014].

In this section, we study attosecond streaking of Ne@C₆₀. While the dielectric properties of Ne@C₆₀ are essentially unchanged compared to C₆₀, we employ the central atom as a well-localized source of electrons to prevent smearing out of the streaking spectra over the size of the molecule. The electrons from the neon atom are distinguished by their final energy, $E_{\text{fin}} \approx \omega_{\text{XUV}} - E_{\text{Ne}2s}$ with $E_{\text{Ne}2s} = 48.5$ eV from the C₆₀ electrons that have less binding energy. Previous studies [Wais, 2014] found that the streaking spectra of this composite system can be described by the vector potential and an effective time shift $\langle \mathbf{p} \rangle(t) = \mathbf{p}_0 + \mathbf{A}(t + \Delta t)$ with $p_0 = \sqrt{2E_{\text{fin}}}$. The time shift Δt was found to be the sum of quantum mechanical contributions, the apparent time shift due to the influence of the Coulomb field on the electron trajectory (Coulomb-laser coupling), and an apparent time shift due to the influence

of the near field on the electron trajectory. Here, we focus on this latter contribution that itself results from two mechanisms. First, the external electric field of the laser is screened inside C_{60} , so that the photoemitted electron effectively appears later in the continuum and the streaking signal is delayed by the electron run time of $t_{\text{run}} \sim R_{C_{60}}/p_0 \approx 0.12$ fs. Secondly, upon traversing the C_{60} shell, the electron is accelerated by the enhanced near field at the pole caps, thereby reducing the apparent time shift to a value around $\Delta t = 0.01$ fs.

We employ as input near-fields derived from TD-DFT simulations as presented in the preceding sections for simulations of the classical electron trajectory through the near-field. We study the dependence of the apparent time shift Δt on (1) the orientation of the molecule with respect to the laser polarization, (2) the effect of the endohedral neon atom on the apparent time shift, and (3) the sensitivity of the time shift in the streaking spectra to details of the electric near field by comparing the ab-initio result with a dielectric sphere model. In a first step, we neglect additional reaction channels like elastic scattering from the carbon cores and inelastic losses from electron-electron collisions with the C_{60} electrons. Perhaps the largest source of uncertainty in our simulation comes from not explicitly including the photoionization process in our treatment of the optical response of $\text{Ne}@C_{60}$. On the time scale of the photoionization and photoelectron motion through the cage, the C_{60} spectator electrons will start to feel the additional Coulomb potential from the Ne core. Eventually the Ne core-hole state Ne^+C_{60} will relax radiatively or by an Auger-like transition to a final state $\text{Ne}@C_{60}^{n+}$. The time scale after which the C_{60} spectator electrons start to move can be estimated from TD-DFT calculations for the dynamic screening of classical point charges to be around 10 a.u. (0.25 fs) [Muiño et al., 2011; Koval et al., 2012a,b]. This is also the time scale on which the dielectric properties of the C_{60} molecule will change. Traversal of the C_{60} radius takes about 0.12 fs. Therefore, the electron will already be at some distance from the C_{60} molecule at the time when the dielectric properties of the latter begin to change. However, it might be possible to study the ultrafast screening motion of the C_{60} electrons with smaller XUV photon energies, or alternatively by employing larger fullerenes.

We simulate streaking of endohedral fullerenes by three-dimensional classical trajectory Monte Carlo calculations [Lemell et al., 2009, 2013]. Electrons start from the center of the C_{60} cage with an initial velocity vector chosen randomly from a cosine distribution and with initial energy given by the photoelectric effect taking into account spectral broadening by the attosecond XUV pulse (100 as). The ionization probability is assumed to be proportional to the instantaneous XUV intensity. The electrons are then propagated in the time-dependent near-field derived from the TD-DFT calculation and their final momentum after the laser pulse is recorded. Alternatively, to test the sensitivity of the simulation to details of the near field distribution, we also performed simulations in a model near field of a dielectric sphere in a homogeneous

laser field $\mathbf{F}(t)$ with instantaneous dipole moment $\mathbf{d}(t)$,

$$F_{\text{total}}(\mathbf{r}, t) = \mathbf{F}(t) + \begin{cases} -\mathbf{d}(t)/R_{\text{sphere}}^3 & \text{for } r < R_{\text{sphere}} \\ -\mathbf{d}(t)/r^3 + 3\frac{\mathbf{d}(t)\cdot\mathbf{r}}{r^5}\mathbf{r} & \text{for } r > R_{\text{sphere}} \end{cases}. \quad (5.4)$$

Here, $\mathbf{F}(t)$ and $\mathbf{d}(t)$ are taken from the TD-DFT simulation, and we use $R_{\text{sphere}} = 10$ a.u. for the effective electronic surface. The momentum spectrum at each XUV-NIR delay is calculated by an ensemble average over electron trajectories that end up with a final velocity within an acceptance angle of 10 degrees to the laser polarization direction. The spectra recorded for many delay times t give the streaking spectrogram (Fig. 5.7a). The time shift Δt due to the near field between the vector potential and the streaking signal $\langle p \rangle(t)$ is extracted by fitting $\langle p \rangle(t) = a \times A(t + \Delta t) + b$ where the amplitude a is roughly 1.

We performed simulations for several different molecule orientations (Fig. 5.7b), each with and without endohedral atom (C_{60} vs. Ne@C_{60}) and for both the ab-initio derived near field distribution (“full”) vs. the simplified near-field distribution by virtue of Eq. 5.4 (“dipole”). In all cases, the orientation of the molecule has a negligible effect on the streaking delay on the order of 1 as. The changes in the near fields due to the presence of the endohedral atom also give only negligible contribution to the streaking delay on the order of 1 as. However, we find a sizable change of the streaking delay on the order of 7 as between the full simulations employing the ab-initio derived near fields and the simulations employing the simplified model for the near fields (Eq. 5.4). Our results demonstrate that details of the near-field distribution can influence the extracted streaking delay by a few attoseconds even if they have the same asymptotic behavior.

5.9 Streaking of dipole excitations

When a molecule is subjected to a time-dependent field, the laser field can induce either “virtual” excitations, i.e., an induced dipole moment that adiabatically follows the driving field according to $d = \alpha F$ with a real polarizability α , or “real” excitations, i.e., photoabsorption. The latter corresponds to a sustained energy transfer from the laser pulse to the molecule. Photoabsorption is indicated by an imaginary part of the polarizability (see Fig. 5.3). The weak 800 nm NIR pulse employed in the preceding section has only negligible components in the region where photoabsorption takes place. Therefore, the dipole moment induced during the laser pulse goes back to zero after the pulse. This formation of a transient electronic dipole on the attosecond time scale has recently been scrutinized experimentally and theoretically by Neidel et al. [2013]. Radiation of higher energy that can access low-lying electronic excitations of the molecule leads to “real” excitations that remain after the laser pulse. The coherent population of excited states can lead to an oscillating time-dependent dipole moment

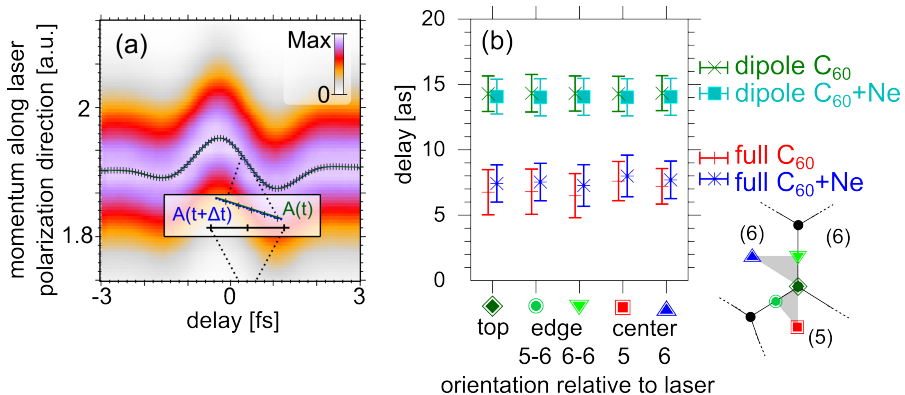


Figure 5.7: Streaking of C_{60} and $\text{Ne}@C_{60}$. (a) Typical electron momentum histogram as function of delay between ionizing XUV pulse and NIR pulse driving the near-field response (“streaking spectrogram”). Laser polarization toward the center of a hexagon-hexagon edge, Eq. 5.4 was used for the near field. Laser intensity $1 \times 10^{11} \text{ W/cm}^2$ and photon energy $\omega_{\text{XUV}} = 100 \text{ eV}$. Green and blue line: vector potential $A(t)$ and fit to vector potential with time delay $A(t + \Delta t)$ (almost on top of each other). **Inset:** Enlarged view of the region of the spectrogram with best contrast. The extracted delay for this simulation run is $\Delta t = 14.3 \pm 1.3 \text{ as}$. (b) Dependence of the time delay on: (1) the orientation of the laser polarization axis with respect to the molecule (horizontal axis, see inset); (2) the presence of the central Ne atom ($\text{Ne}@C_{60}$ versus C_{60}); (3) near-field distribution derived from ab-initio calculations (“full”) vs. simplified near-field distribution for a polarized sphere (Eq. 5.4, “dipole”). The error bars reflect the quality of the fit of the streaking signal to the time-shifted vector potential. **Inset:** Sketch of the laser polarization direction with respect to the C_{60} surface.

that continues to oscillate even after the laser pulse is over.¹¹

In this section, we will show for the paradigmatic example of C_{60} that such a time-dependent dipole moment after the pulse leads to an appreciable signal in the streaking spectra taken *after* the end of the NIR laser pulse. We find that the streaking signal is, to a good approximation, proportional to the instantaneous dipole moment after the laser pulse. This enables the study of electronic excitations and their evolution and eventual decay in real time with sub-femtosecond time resolution. While we still apply the streaking protocol of time-delayed NIR and XUV pulses, the role of pump and probe is reversed compared to the preceding section. There, the XUV pulse photoemits an electron and the NIR pulse probes the emission time of the electron. Here, the NIR pulse excites the molecule, and the XUV pulse is used to probe the near-field associated with this excitation (“self-streaking”). In this sense, the proposed protocol bears more similarity to attosecond transient absorption [Pfeifer et al., 2008; Goulielmakis et al., 2010; Wirth et al., 2011] and can be viewed as a variant of time-resolved photoelectron spectroscopy for the sub-femtosecond time scale [Stolow et al., 2004; De Giovannini et al., 2013]. Alternatively, it can also be viewed as the generalization of the “nanoplasmonic-field microscope” proposed by Stockman et al. [2007] from surface plasmons to the study of single molecules. A somewhat similar idea has recently been proposed by Mignolet et al. [2014] for the study of the onset of

¹¹This is analogous to the “quantum beats” observed for laser excitation of SiO_2 described in section 4.5. There, however, the excitation was produced by a strong laser field in a multi-photon process.

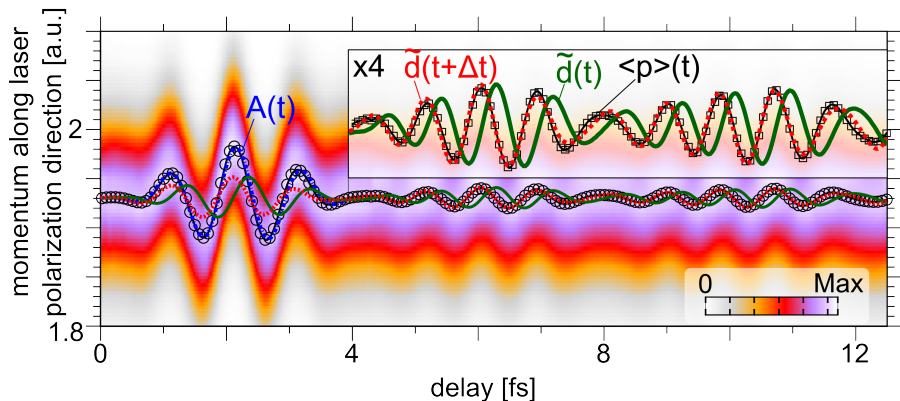


Figure 5.8: Streaking of excited C_{60} . Spectrogram of C_{60} streaked by a few-cycle UV pulse (central wavelength 310 nm, 4 fs pulse length, FWHM intensity pulse length $\lesssim 2$ fs, 9×10^{11} W/cm 2). During the few-cycle pulse, the streaking signal $\langle p \rangle(t)$ (center of momentum of the ionized electrons, circles) follows approximately the vector potential $A(t)$ as for a NIR streaking pulse (blue dash-dotted line). As the laser excites the low-lying dipole-allowed transitions, the dipole moment of the C_{60} shows oscillations even after the laser pulse is over (green solid line). After the pulse, the streaking signal traces the oscillations of the dipole moment with a negative delay (advancement) of -203 ± 2.3 as (red dashed line) and a scaling factor of $\tilde{d}/d_0 = 0.00504 \pm 8.1 \times 10^{-5}$. **Inset:** 4 times magnified view of delay times larger than the pulse duration.

strong-field excitation, however employing an attosecond pulse train with time delay between the attosecond pulses adjusted to the quantum beat period as a frequency filter.

Eventually, the excess energy in the electronic system will decay either radiatively (typically on a time scale of nanoseconds) or diffuse into other degrees of freedom (coupling to transverse degrees of freedom or electron-hole excitations in the electronic system and coupling to the lattice on the sub-picosecond time scale). For C_{60} , experimental and theoretical studies suggest that the dominant decay mechanism is vibronic coupling on a time scale of down to 20 fs [Gunnarsson et al., 1995; Hands et al., 2008; Iwahara et al., 2010; Faber et al., 2011]. Currently, ab-initio descriptions including coupling to the nuclear degrees of freedom in real time are being developed [Rozzi et al., 2013; Falke et al., 2014; Fischer et al., 2014], and dissipation in the electronic system may be included eventually by extension to time-dependent current density functional theory [Wijewardane and Ullrich, 2005; D’Agosta et al., 2007]. Here, we restrict ourselves to modeling the ultrafast excitation within TD-DFT and focus on investigating the signatures of the molecular dipole and microscopic electric field distribution in the streaking spectrograms. We point out, however, that reproducing the time-dependent dipole moment of such a complicated system including decoherence presents a challenging benchmark for the predictive power of ab-initio theories.

The combined TD-DFT and classical trajectory Monte Carlo simulations proceed as described in the preceding section, however the NIR laser field is replaced by

higher energy radiation (310 nm). These laser parameters are similar to what is achievable in contemporary experiments [Graf et al., 2008; Reiter et al., 2010]. During the pulse, the streaking signal traces the vector potential of the external field (Fig. 5.8). The time-dependent dipole moment continues its evolution after the pulse. The dominant oscillation frequency $\sim 1/(1 \text{ fs})$ corresponds to the excitation energy of the lowest dipole-allowed states $\sim 4 \text{ eV}$. The beating frequency $\sim 1/(5 \text{ fs})$ corresponds to the energy difference between individual excited states $\sim 1 \text{ eV}$ (see the excitation spectrum in Fig. 5.3). The oscillations in the dipole moment are mirrored in the observed streaking signal. After the pulse, the streaking signal shows oscillations that coincide to good accuracy with the scaled and delayed dipole moment $\tilde{d}(t) = a \times d(t + \Delta t) + b$. Here $b = 1.93 \text{ a.u.}$ is the momentum of the emitted electron in the absence of laser field and dipole, $a = 0.00504$ is a scaling factor, and $\Delta t = -0.203 \text{ fs}$ is the time shift. We numerically find that the streaking signal amplitude a scales linearly with the applied electric field strength. While these results were obtained using the full time-dependent near-field derived from ab-initio calculations, we verified that qualitatively similar streaking spectra are obtained for the simplified near field distribution of a polarized sphere (Eq. 5.4), however with slightly different fit parameters a , b , and Δt but with a similar quality of the fit. Therefore, our results illustrate that the mechanism that maps the time-dependent dipole moment onto the streaking signal is independent of details of the near-field distribution.

The streaking spectrum can be understood as follows. We consider an electron emitted along the laser polarization direction z in the near-field distribution Eq. 5.4 with no external field $F(t) = 0$ but with a finite dipole moment $d(t)$. Notably, this field distribution is symmetric around the origin and the corresponding potential is antisymmetric. Therefore, the potential at the center of the cage and at infinite distance is zero. This implies that no momentum shift is incurred in emission from the center of a *static* polarized sphere. However, the dipole moment changes on a time scale of $T_{\text{dip}}/4 \approx 0.23 \text{ fs}$ which is of the same order as the electron traversal through the C_{60} radius, $R_{C_{60}}/p_0 \approx 0.12 \text{ fs}$. Therefore, the electron samples a changing near field along its trajectory that can give rise to a net momentum shift. The largest momentum shift is acquired when the electron is emitted around the zero of the dipole moment so that only little deceleration is incurred during the traversal of the C_{60} cage and optimal near-field acceleration is acquired after the electron emerges from the cage. The streaking signal therefore lags behind the dipole moment by about 90 deg (Fig. 5.8). The amplitude of the streaking momentum shift is of order $d/R_{\text{sphere}}^2 \sim 0.005 \text{ a.u.}$ in good agreement to full calculation ($\sim 0.01 \text{ a.u.}$).

In experiment, the C_{60} molecules would likely be randomly oriented. As the excitation spectrum and polarizability are weakly orientation dependent, the individual dipole moments evolve slightly differently and will eventually be out of phase. The signal will vanish on a time scale associated with this dephasing (“inhomogeneous broadening”). Performing simulations for several molecule orientations, we found that during the simulation time the dipole moments are to a good approxima-

tion equal and their time shift with respect to each other 8 fs after the pulse is only $\lesssim 0.05$ fs.

Our model indicates that a dipole excitation in a molecule leaves its trace in the streaking spectra. The effect is independent of how the dipole is excited. In particular, we verified that also longer UV pulses up to a few fs pulse length lead to similar shapes of the dipole moment after the pulse is over as the dipole signal in time domain is reconstructed from the convolution of the C_{60} response with the incident laser spectrum (Fig. 5.3). The dipole excitation could also be created by a strong laser-pulse [Li et al., 2014] or by shifting the excitation spectrum of the C_{60} down into the optical range by an adatom layer [Rubio et al., 1994].

For endohedral fullerenes, the central rare gas atom provides a well-localized source of distinguishable streaking electrons. For studying processes in more complex compounds, for example in organic molecules containing several atomic species, contributions from different locations within the molecule can be disentangled by the final electron energy. We may envision time-domain visualization of charge-transfer processes [Kuleff et al., 2013; Falke et al., 2014] and hot electron dynamics in small clusters and nanoparticles [Schlipper et al., 1998; Klamroth and Nest, 2009; Nest, 2010] with sub-femtosecond time resolution.

5.10 Conclusions and outlook

In this chapter, we have studied near fields induced by optical laser pulses in fullerenes and endohedral fullerenes. While still tractable by ab-initio simulation, these large molecules bridge the gap from atoms and molecules to nano-particles and nano-structures. The electric near-field induced inside the molecule is reduced (screening) and increased outside the molecule (field enhancement). We found a strong dependence of field enhancement on the orientation of the molecule of the order of 20 % that can lead to dramatic localization of non-linear processes on the C_{60} surface. Our real-time method incorporates non-linear effects and thus allowed us to study the intensity dependence of field enhancement from first principles. We found that, somewhat surprisingly, field enhancement is slightly reduced with increasing intensity due to the increased smearing out of the polarization charge. We demonstrated that the linear response result remains a good approximation to the near fields for the early stage of laser-matter interaction also at higher intensities up to 1×10^{14} W/cm². For all investigated properties, we found that Ne@ C_{60} behaves very similarly to C_{60} . In the second part of this chapter, we studied a proposed protocol to scrutinize the molecular near field with attosecond streaking. We found that the near fields significantly influence the streaking spectra leading to an effective time shift between the streaking signal and the vector potential. We found little dependence of the streaking spectra on the molecular orientation, but some dependence on details of the near field distribution comparing a polarizable sphere model with the ab-initio results. In the final section, we turned from studying the “virtual” excitations, the adiabatic fol-

lowing of the driving laser field during the pulse, to “real” excitations that persist even after the laser pulse is over. We employed an UV pulse as a pump to launch an oscillating electron wave packet and the XUV pulse to probe the excited electron dynamics after the pulse. We showed that the amplitude of the streaking signal traces, to a very good approximation, the instantaneous time-dependent dipole moment of the molecule. The shape and amplitude of the streaking spectra can be understood with a model based on a polarized sphere and the streaking spectra do not sensitively depend on details of the near field distribution. This suggests extension to other molecules, nano-particles, and nano-structures to study the onset of dephasing and decoherence on the electronic time scale.

Further work will fall into two categories. Firstly, molecular near fields will be studied in more detail. We will study other molecular species to find out if the physical picture derived from C_{60} is transferable. First results for benzene and other aromatic molecules point into this direction. However, the details of the molecular near-field enhancement depending on the constituting atoms and bond structure have only begun to be understood. Comparison of the density-functional theory results with high-level quantum chemistry methods is desirable and can be most easily achieved for a static electric field. Extension from the single-molecule level to the study of nano-structures on surfaces can proceed, for example, through study of pyramidal structures made from a few palladium or platinum atoms on the surface of nanometric tips [Kuo et al., 2004] possibly employing embedding schemes to account for the influence of the infinite surface [Huang et al., 2014; Libisch et al., 2014]. Another possibility to extend the present simulations to the mesoscopic scale is the study of static field emission or strong-field photoemission from carbon nanotubes where large-scale TD-DFT calculations could reach spatial extension on the nanoscale [deHeer et al., 1995; Saito and Uemura, 2000; Han et al., 2002; Zheng et al., 2004; Driscoll et al., 2011]. Due to the spatial inhomogeneity of the molecular near fields, strong localization of non-linear effects such as electron emission by tunneling is likely. The emitted electron spectra from molecules or nano-structures are therefore expected to carry the imprint of these near-fields. Such electron spectra may be calculated from the present simulations by the methods discussed in chapter 3. Experiments employing rescattering could be used to investigate the near-fields. The influence of near fields could also have spectacular consequences for electrons photoemitted by circularly polarized fields, modifying the “attoclock” principle [Eckle et al., 2008b,a; Pfeiffer et al., 2012].

Secondly, the study of molecular near field imaging by attosecond streaking will be extended. For C_{60} , potentially important contributions to the experimentally measurable time shift stemming from the quantum mechanical delay as well as from elastic collisions of the streaking electrons with the C_{60} cores and electrons have to be investigated in more detail. On their way out, streaked electrons may also undergo inelastic scattering events with the C_{60} shell electrons, and streaking may be able to study the excitation of plasmons in real time. To some degree, such additional pro-

cesses will be incorporated into the classical transport theory simulations presented above. Streaking from larger molecules or nano-particles should include electron transport effects [Lemell et al., 2009]. Investigations of other molecular species will show if streaking of dipole moments can be generalized and how its features depend on the molecular bond structure and composition. The study of electrons emitted into other directions than along the laser polarization may allow reconstruction of the time-dependent near field within the molecule. Attosecond streaking of resonant dipolar excitations as demonstrated in the final section opens the door to the study of the onset of decoherence and decay in molecules, nano-particles, and nano-structures with unprecedented time resolution.

Conclusions and outlook

This monograph has been dedicated to the study of the strongly non-linear electron dynamics occurring when condensed matter is irradiated with intense few-cycle laser pulses. The availability of intense laser pulses of custom-tailored shape and duration allows the observation and control of electron motion and the corresponding high-order non-linear response of matter with unprecedented accuracy. We have focused on the description of the non-linear response of many-electron systems to such strong time-dependent perturbations on the femtosecond time scale. Our work horse theory was time-dependent density functional theory (TD-DFT) in real space and real time that permits an ab-initio description of the time-dependent many-body problem on the mean field level including non-linear response to all orders. As the study of such high-order non-linear response of solid matter is still in its infancy and theoretical tools are being developed as experimental technology progresses, we emphasized comparison with experimental results where available to establish that TD-DFT can give a realistic description of processes in matter even under such violent perturbations. Overall, we found that TD-DFT captures the essential physics very well. While TD-DFT gives accurate results for experimental observables, interpretation of the results and understanding of the underlying processes is often complicated by the wealth of processes that take place at the same time and by the complexity of the quantum-mechanical description. Wherever possible, we illuminated the quantum calculations by comparing with simpler models based on back-of-the-envelope estimates, classical electrodynamics, semi-classical methods, and classical trajectory Monte Carlo methods.

In the course of this voyage through the world of strong-field response of solid matter, we applied our theoretical framework to three realistic systems. Firstly, we

investigated the interaction of ultrashort laser pulses with metal nano-structures, specifically nano-tips, in chapters 2 and 3. The impinging few-cycle pulse is enhanced and slightly distorted near the apex of the tip by the dynamic lightning-rod effect described by macroscopic electrodynamics, leading to electron photoemission from a nanometrically confined area. Experimental control over the tip design parameters affords control of the electromagnetic response. The local electric field at the tip apex enters a quantum simulation of the emission and motion of electrons along the laser direction in the vicinity of the metal nanostructure with TD-DFT. The time-dependent electric field controls the motion of the emitted electron wave packet on the sub-nanometer length scale and sub-femtosecond time scale and can lead to a return of the electron to the surface where it can scatter from the first layer of surface atoms, leaving characteristic marks in the energy spectra of emitted electrons. This exquisite control of electron motion leads to a distinctive dependence of the electron spectra on the laser pulse shape. Its origin was interpreted by comparison with a semi-classical model as interplay of highly non-linear ionization near the laser pulse maximum and the probability for rescattering along a classical trajectory. Our simulation can resolve the time-dependent screening charge layer on the surface that is smeared out by quantum mechanical uncertainty or, equivalently, the atomic-scale variations of the local electric field, in agreement with very recent experimental results obtained by attosecond streaking of metal surfaces. We extended our simulations to parameter regimes where experiments will become available in the near future and predict sensitivity of the electron spectra to the detailed surface structure for longer wavelength radiation (1600 nm) and discussed possible high harmonic emission from metal tips.

Secondly, we investigated strong-field induced electron dynamics in dielectrics (chapter 4). Recent experiments have established that the properties of dielectrics can be changed on the femtosecond time scale in a controlled and reversible manner by ultrafast intense laser pulses, holding the promise of ultrafast optical circuits that can, in principle, operate with petahertz clock rates, several orders of magnitude faster than conventional semiconductor electronics. We focused on studying a very recent set of experiments by Schiffrin et al. [2013] that has demonstrated charge transfer inside a dielectric by virtue of the electric field alone. Our fully three-dimensional ab-initio calculations permit scrutiny of the electron dynamics on the atomic length scale and sub-femtosecond time scale. We found that the observed strongly non-linear increase of transferred charge with increasing laser intensity is connected to a change in the excitation mechanism from vertical excitations to the tunneling regime where electrons are forced to tunnel between neighboring atoms within the solid. The directionality of the tunneling process can lead to quasi-free currents that persist even after the laser pulse is over before equilibrium is established on longer time scales in the 100 fs range by dissipative processes. An inherently local process, tunneling is strongly influenced by the three-dimensional bond structure, and we found a novel non-linear bulk photogalvanic effect relying on this mechanism that may permit ultrafast charge transfer in a dielectric even without the need for pulse-shape con-

trolled laser pulses. We used our simulation to estimate the feasibility of petahertz signal processing and found that dissipation of the thermal load will be a main design constraint. Employing a pump-probe setup to investigate the transient properties of matter during irradiation, we found that the non-linear optical properties of matter are changed drastically on the femtosecond time scale while the linear response is changed on the level of a few per cent for laser intensities slightly below the damage threshold.

Thirdly, we studied the response of fullerenes and endohedral fullerenes to ultra-short laser pulses as a realistic nano-sized model system where field enhancement and screening are still tractable by ab-initio simulations (chapter 5), extending our studies of mesoscopic metal nanostructures in the previous chapters 2 and 3 where field enhancement and quantum response had to be treated separately. Even though C_{60} contains only 60 atoms arranged in a spherical shell of solid-state density with a diameter of merely 0.7 nm, we found that many aspects of its response to ultrashort optical laser pulses can be understood by comparison to the classical electrodynamic textbook example of a sphere in a static electric field. We found the laser field is screened inside the C_{60} that essentially works as a Faraday cage, and that the field is enhanced near the poles of the sphere. The main difference to macroscopic electromagnetism is a smearing out of the near-fields on the atomic length scale. Taking advantage of our real-time formalism, we studied the onset of nonlinearities as a function of laser intensity as well as the dependence of near-fields on nearby molecular bonds. These time-dependent molecular near-fields can be scrutinized by their effect on electrons ejected from the endohedral atom by an attosecond pulse in the framework of attosecond streaking chronoscopy. For somewhat higher photon energies of the streaking field in the UV range that can access the first excited states of C_{60} , excited states are coherently populated and oscillations of the time-dependent dipole moment continues after the laser pulse is over. We propose to make these coherent oscillations accessible to experiment by applying the well-established streaking protocol. We found a significant signal in the streaking spectra that essentially follows the time-dependent dipole moment and elucidated its origin. Our proposed protocol may allow experimental observation of complex processes like charge migration and the onset of dissipation and decoherence from small molecules to mesoscopic nano-particles.

We have demonstrated that time-dependent density functional theory provides a good starting point for the description of the strongly non-linear response of matter for a great variety of systems ranging from a bulk insulator to a metal surface to a large molecule. A realistic description of the three-dimensional atomic structure and bonding in real space is key to capturing the strongly non-linear response in the non-adiabatic tunneling regime that is strongly influenced by local fluctuations in the bonding environment. The concepts and methods presented in this work will provide a realistic description for many applications becoming accessible to experiment in the coming years, several of which are highlighted in the conclusions of the

individual chapters. On a broader scale, we foresee three main upcoming challenges for a successful theoretical description of ultrashort pulse physics.

Firstly, a consistent and tractable description of the coupling between the macroscopic dynamics of light propagation and the microscopic electron dynamics must be developed. First promising efforts into this direction by Yabana et al. [2012] are, up to now, feasible only for the simplest of macroscopic sample geometries even while employing the largest of supercomputers. Extension to more complicated geometries will require improvements in efficiency or effectivity.

The second challenge for a theoretical description is the inclusion of decoherence and dissipative processes, that is coupling to a bath of many degrees of freedom describing the influence of macroscopic boundaries, defects, and impurities, as well as the motion of the atomic cores both for an infinite solid as well as for a molecule. Such effects will become important on the time scale of 10-100 fs and their tractable inclusion into TD-DFT beyond a phenomenological description of “quantum friction” is presently an open question. In fact, the main driving mechanism of decoherence and dissipation for individual systems is often not known a priori as it can depend on, for example, the number density of different types of defects and impurities, surface quality, etc. One desirable outcome of the study of the interactions of intense laser pulses with matter is an improved understanding of these relaxation processes for realistic systems in real time that have so far remained unexplored. Experiments that provide access to, for example, the relaxation dynamics of the quasi-free currents discussed in chapter 4 or the time-dependent dipole moment of large molecules as discussed in chapter 5 will provide important benchmarks for a successful description of the underlying processes.

The third challenge for theory is the inclusion of strong dynamic electron correlation into the quantum description of realistic systems with more than a handful degrees of freedom. Recent improvements to the static exchange-correlation functionals and the development of suitable extensions of the mean-field description in terms of many-body perturbation theory and the Bethe-Salpeter equation for *static* density functional theory have lead to great progress in the description of electron correlation to a degree where chemical accuracy can routinely be reached for many relevant materials. For *time-dependent* density functional theory, such a level of accuracy is not yet obtainable and a large number of processes involving single-particle excitations far from the mean field are at present not included. Examples that were in part encountered in the course of this work include photoionization of an electron by an XUV pulse, charge transfer, Auger decay, electron impact ionization in a solid or in non-sequential double ionization of atoms and molecules by short laser pulses, or excitation of intrinsic and extrinsic plasmons and inelastic loss as an electron traverses a bulk metal or a C₆₀ shell. An ab-initio description of these processes in real time is, in general, currently not feasible. For such cases, theory resorts to lower-level methods like the estimation of reaction rates and classical transport theory taking quantum mechanical information as input along the lines of section 5.8. The underlying reason

for this failure of the, in principle, exact reformulation of time-dependent many-body dynamics by TD-DFT has been in most part traced to the neglect of memory, or in linear response, equivalently the frequency dependence of the exchange-correlation potential [Lein and Kümmel, 2005; Wijewardane and Ullrich, 2005; Ullrich and Tokatly, 2006; Ramsden and Godby, 2012; Elliott et al., 2012; Fuks et al., 2013; Thiele and Kümmel, 2014]. Identifying the main mechanisms that lead, within a mean-field scheme, to a correct description of these processes has so far remained elusive even as sustained interest has sparked much work on the subject over the last decades. One possible conclusion is that a mean-field description, even though *in principle* exact, is ill-equipped for capturing such physics. Besides optimal basis expansions for treating the full time-dependent Schrödinger equation [Meyer, 2012], a way out might be provided by recent advances in approximate methods that take the two-body reduced density matrix instead of the one-body density as basic quantity [Akbari et al., 2012; Lackner, 2014]. Such approaches have yielded first promising results, however for small low-dimensional model systems.

Resolution of the three challenges laid out above will occupy physicists in the decades to come. Being aware of these difficulties, we have demonstrated in this work that a large variety of realistic systems can be treated with presently available time-dependent density functional theory in good agreement to first available experimental results. The vigorous interest in extending intense few-cycle laser pulse physics to ever more complex molecular and solid-state targets will afford ample opportunity to apply the concepts and methods of this work to more and more systems. The promise of femtosecond strong-field physics to observe and control the motion of electrons within almost arbitrarily complex targets on the natural electronic time scale remains to be realized.

Appendix

Simulation of plasmonic tips with the boundary element method

In this section, we show how the boundary element method can be used to reliably extract the complex field enhancement factor for mesoscopic structures made from plasmonic metals. In contrast to the results for tungsten presented in the main text, some subtleties have to be noted. The dielectric function of tungsten has a large imaginary part over the whole range presented in section 2.5. This imaginary part leads to a rapid decay of surface plasmons that are excited at the apex of the nanotip and propagate along the tip shaft. For example, the propagation length of surface plasmons along a tungsten cylinder of 20 nm radius is only ~ 150 nm for tungsten at a wavelength of 800 nm [Sarid and Challener, 2010]. It is therefore sufficient to extend the numerical tip somewhat out of the laser focus to reach convergence. The situation changes drastically for “plasmonic” materials like gold which have a lower imaginary part of the dielectric function at optical frequencies ($\epsilon_{\text{Au}}(\lambda = 800 \text{ nm}) \sim -26.4 + 1.46i$, Palik [1991]; Olmon et al. [2012]) yielding a much increased propagation distance of $\sim 3.5 \mu\text{m}$ or up to several tens of micron for cylinder radii in the 100 nm range. The simulation of tips of several tens of microns in size is typically not feasible numerically. With other simulation methods, such as finite-differences-time-domain or finite element simulations, numerical absorbers like perfectly matched layers can be employed to model the response of an infinitely extended tip shaft and absorb such excitations [Taflove and Hagness, 2005]. Such absorbing boundary conditions are unfortunately conceptually absent from the boundary element method restricted to material configurations with piecewise constant material properties¹². However, plasmonic materials can still be simulated with

¹²Likely, numerical “absorbers” could also be built from well-designed material configurations with piecewise constant dielectric function simulating, for example, the gradual turning on of an imaginary part of the dielectric function at the cost of a larger number of materials and material boundaries in the simulation.

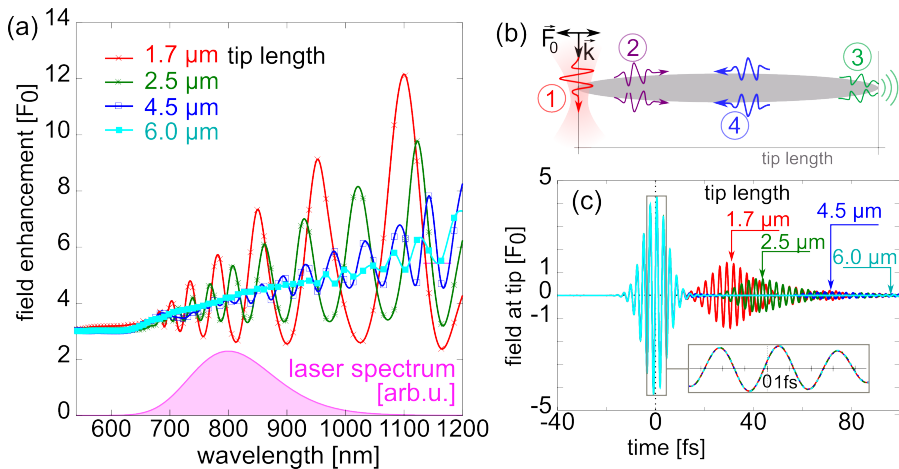


Figure A.1: Simulation of plasmonic materials. (a) Frequency-domain response of gold rods of varying length (radius 20 nm, opening angle 0 deg). Red crosses: 1.7 micron, green crosses: 2.5 micron, blue open squares: 4.5 micron; turquoise filled squares: 6.0 micron. Pink shaded region: spectrum of a typical few-cycle laser pulse (800 nm, 8 fs). (b) Sketch of the mechanism giving rise to the interference fringes in (a). (1) Excitation of surface plasmons at the tip apex; (2) propagation of surface plasmons along tip shaft; (3) reflection of surface plasmons at the back side of the tip (and possibly out-coupling), (4) propagation back to the tip apex. (c) Time-domain response of gold tips of varying length. The arrows indicate the revival time of the reflected surface plasmon wave packet for the tip lengths employed. **Inset:** Magnified view around time zero (grey rectangle). The short-time responses of all tip lengths agree perfectly (dashed lines in inset for easier viewing).

the boundary element method as demonstrated in the following.

As a few-cycle laser pulse reaches the apex of the nanotip, a surface plasmon wave packet is launched along the tip shaft (Fig. A.1b). The plasmon wavepacket is dispersed and damped along its way to the back end of the numerical tip. Depending on the shape employed for the back end of the tip, the surface plasmon wave packet is reflected and can also couple to delocalized modes leading to irradiation of light from the back end of the tip and further damping of the surface plasmon wave packet. After reflection, the surface plasmon wave packet propagates back to the tip apex, where its arrival time depends on the tip length and details of the shape of the tip (Fig. A.1 c). The arrival time is of the order of twice the tip length divided by the speed of light ($c = 299.9 \text{ nm/fs}$) so that for a tip length of 2 micron the total travel time of the plasmon wave packet is about $\sim 13 \text{ fs}$. The tip length should be chosen long enough so that the revival of the plasmon wave packet is clearly separated in time from the incoming laser pulse. On the other hand care must be taken to resolve the surface plasmon wavelength along the geometry. The near-field response at short times is not affected by the revival dynamics at later times (inset of (Fig. A.1c) so that field enhancement and phase shift are converged and can be extracted by fitting to a short pulse shape or by doing a windowed Fourier transform around the short-time response. In frequency space, the signature of the two wave packets reaching the

apex delayed in time relative to each other are interference fringes in the conjugated variable, the laser frequency (“antenna resonances”, Fig. A.1 a). This mechanism is analogous to the interference of *particle* waves described by the simple man’s model for nanotips described in section 3.2. The distance of the interference fringes is inversely related to the time delay between the two wave packets, and the visibility of the fringes is a measure for the damping of the surface plasmon wave packet as it travels from the apex to the back end of the tip and back again. Taking only the short-time response into account for the evaluation of the field enhancement and phase shift (low-pass filter in the time domain) corresponds to filtering out the high frequencies in frequency space, i. e., smearing out the interference fringes over the spectrum of the laser pulse.

While the calculation of plasmonic materials is more costly as simulations must be run at several frequencies, the qualitative behavior including field enhancement and phase shift is similar to that of tungsten or non-plasmonic dielectrics. However, first results indicate stronger field enhancement and a maximum field enhancement at smaller opening angles that decreases as the dielectric function decreases ($\epsilon \rightarrow -\infty$). In simulations for gold at intermediate tip angles near the maximum field enhancement, we observe that the charge density distribution along the tip shaft is strongly localized at the apex and is phase shifted compared to the incident field. This localization of the charge density distribution suggests that the incident field couples to a surface plasmon mode localized at the tip apex. The importance of surface plasmons is further corroborated by the work of Issa and Guckenberger [2007] who numerically investigate the field enhancement at the apex of a nano-tip due to adiabatic nano-focusing of surface plasmons along the shaft [Babadjanyan et al., 2000; Stockman, 2004]. They obtain maximum field enhancement at intermediate tip opening angles in analogy to our results, indicating that surface plasmons also play a role for field enhancement due to illumination by a laser beam. Finally, Vincent et al. [2011] have investigated the relation between the surface plasmon resonance localized at a singularity and the dielectric properties of the surrounding material. The resonance condition for a cone with semiangle α_0 is

$$\cos(\alpha_0) = \frac{\epsilon + 1}{\epsilon - 1}. \quad (\text{A.1})$$

The resonance wavelength λ_0 for a given tip opening angle is given by the solution of the above equation for $\epsilon(\lambda_0)$. Eq. A.1 has also been given by Goncharenko et al. [2006]. Notably, the resonance condition cannot be satisfied for dielectric tips where $\text{Re}(\epsilon) > 0$ and the right hand side is > 1 . The resonant angle is attained around $\alpha_0 \sim 20$ deg for typical plasmonic materials in the optical wavelength range. For materials in the infra-red where $\text{Re}(\epsilon) \rightarrow -\infty$, the optimal angle approaches 0 deg. First results comparing the resonance angle of the localized surface plasmon predicted by Eq. A.1 to the optimum angle resulting from our simulations as a function of the real part of the dielectric function appear to substantiate that this resonance is indeed the root

cause for the larger field enhancement at smaller tip opening angles for plasmonic materials. Despite this apparent resonance behavior, we find for most geometrical parameters that the time-domain field is still only enhanced and phase shifted as for dielectrics except near the optimal angle α_0 at very small tip radii ($\lesssim 5$ nm). This is an indication that the tip resonance is strongly coupled to the propagating surface plasmon modes at the tip that guide the excitation away from the tip apex efficiently before a localized resonance develops so that broadband field enhancement is still provided. Importantly, the electric field can, to a good approximation, couple to the plasmon modes only at the tip apex so that there are no plasmons propagating towards the apex in the absence of specifically designed gratings [Giugni et al., 2013]. This is in contrast to results from nano-particles and nano-fabricated metal structures where localized plasmonic resonances are excited (see e.g. Feist et al. [2013], Feichtner et al. [2012], Dombi et al. [2013]). Such localized resonances typically provide stronger field enhancement at the cost of a sharp resonance that leads to a much longer near-field response in the time domain. To provide well-controlled few-cycle laser pulses at the surface of such a nano-structure, advanced pulse-shaping techniques would be required, and experiments relying on exquisite control of the laser pulse shape would be harder because the temporal pulse shape at the surface may strongly depend on details of the geometry [Foldi et al., 2014].

Scientific environment

This section is devoted to a basic statistical evaluation of the population of scientists I encountered during my PhD. The statistical sample consists of about $n = 104$ “collaborators”. To gain reasonable statistics, the term “collaborator” was used very liberally and includes all persons I published a paper, a poster, or an abstract with. It also includes all persons I was in correspondence with with the eventual goal of doing any of the former. The statistical uncertainty of the results presented is of the order of $1/\sqrt{N} \sim 10\%$.

My experience confirms the infamous gender gap in physics (Fig. B.1a) with a male-to-female ratio of about 4-1. This is about average among physicists: In the US in 2010, the fraction of PhDs earned by women was only 20 % and fraction of female professors is substantially below this value (e.g., 7 % full professors) [American Physical Society, 2014]. The situation of women in physics is illustrated by the fact that among my collaborators there is only a single scientist who is at the same time female, permanently employed, and neither French nor Belgian: Stefanie Gräfe received an offer from Jena University as a full professor in 2012. Congratulations again!

For reasons unknown to me, physicists like to part themselves into experimentalists and theorists. I worked with more experimentalists than theorists (2-1, Fig. B.1b). While I like to think this reflects my drive to pursue applied topics with a direct connection to experiment, it also reflects the baseline statistics. For example, at the IMPRS-APS the ratio of theory groups to experimental groups is 13-6, at TU Wien there are 3 experimental institutes and 1 theory institute, and a recent study also found a ratio of about 2-1 [Boninsegni, 2008].

I worked with people from 11 different countries (counting affiliations, not nationalities; Fig. B.1e). The largest fraction of collaborators comes from Germany. The

large role of Germany is explained by my affiliation with the IMPRS-APS (International Max Planck Research School for Advanced Photon Science) of the Max Planck Institute of Quantum Optics (MPQ) in Garching / Munich. Regular meetings with people from MPQ fostered almost half of my collaborations (Fig. B.1d). Austria is second, with collaborations mainly within Prof. Burgdörfer's group and with other groups at TU Wien.

A typical career in physics involves getting a PhD, doing a number of post-docs, and eventually securing a permanent position as an assistant professor or a full professor (group leader). The latter account for about a third of people I have worked with (Fig. B.1c), which reflects the large number of different publications full professors tend to be involved in. Professors are usually funded permanently while PhD students and post-docs have temporary contracts (Fig. B.1f). The "average" scientist I encountered was a male German experimentalist group leader at MPQ Garching with a temporary position, as realized by Peter Hommelhoff before he was appointed professor at Erlangen.

The scientific population pyramid as viewed from my perspective is given in Fig. B.1e. The overwhelmingly young population ($\text{PhD} \leq 2010$) is decimated along the scientific career path until it converges around PhD 1995-99. Recent statistics from England [Harris, 2012] suggest a two-step mechanism for the decline. First, a little more than half of the PhD students go off to pursue careers outside science after their PhD. Next, more than 90% of early career researchers (post-docs) eventually end up in careers outside of universities with the majority flocking to jobs outside of science. A recent PhD graduate who has decided to pursue a research career has a statistical likelihood of about 7.5% to obtain a permanent position at a university, and the chance of becoming a professor is 1%.

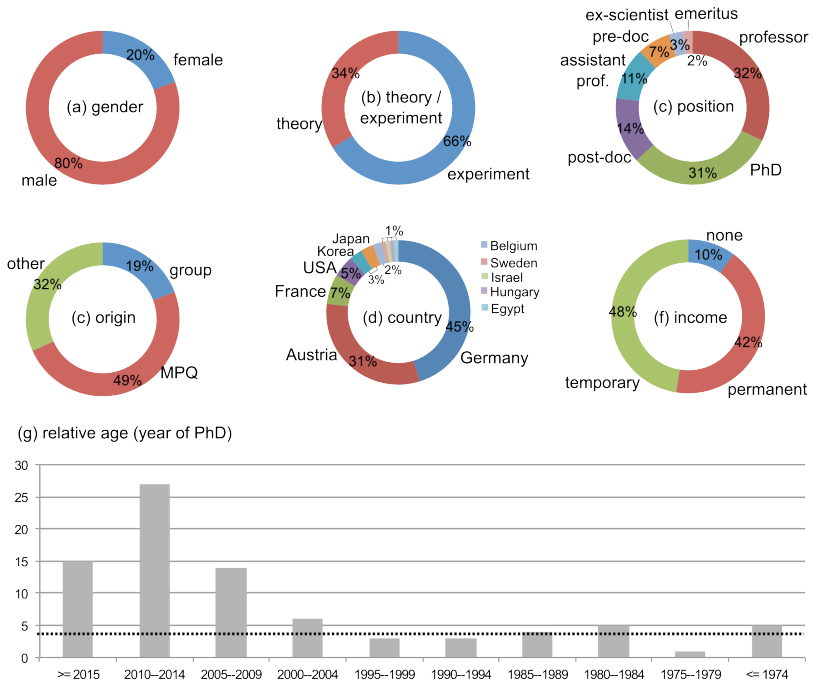


Figure B.1: Scientific environment. (a) Gender. (b) Theorists vs. experimentalists. (c) Position along the scientific career path. (d) Origin of collaboration (MPQ = Max Planck Institute for Quantum Optics). (e) Country. (f) Income. (g) Population pyramid by year of PhD defense.

List of Figures

2.1	Field enhancement near a nano-sphere	10
2.2	Near-field around nano-tips	15
2.3	Field enhancement in time and frequency domain	16
2.4	Geometry dependence of near-field response	19
2.5	Field distribution around a pair of nano-tips	20
3.1	Typical experimental electron spectrum	26
3.2	Simple man's model for nanostructures	32
3.3	Sample simulation with time-dependent density functional theory	43
3.4	Appearance of plateau for high intensities	44
3.5	Carrier-envelope phase dependence of rescattering	46
3.6	Microscopic electric field near the surface	48
3.7	Wavelength dependence of simulated electron spectra.	51
3.8	Sensitivity of rescattering to the empirical surface potential	53
3.9	Sensitivity of rescattering to the surface structure	54
3.10	High harmonic emission from a nano-tip	60
4.1	Experimental geometry for light-induced currents.	68
4.2	Ground state	71
4.3	Optical properties	72
4.4	Time-dependent polarization density and simulation snapshots	79
4.5	Time-averaged current after the pulse	80
4.6	Intensity and carrier-envelope phase dependence	80
4.7	Longitudinal versus transverse geometry	83
4.8	Number of excited electrons	84
4.9	Non-linear photogalvanic effect	89

4.10	Mechanism for charge transfer	90
4.11	Optical signal of ionization	92
4.12	Non-linear polarization in pump-probe setup	93
5.1	Geometry of the fullerene molecule	103
5.2	Ground state density and potential	104
5.3	Near-field response in frequency space	105
5.4	Induced density and near field around C_{60} and $Ne@C_{60}$	106
5.5	Dependence of near-field on the laser intensity	107
5.6	Dependence of laser polarization direction	108
5.7	Streaking of $Ne@C_{60}$	112
5.8	Streaking of dipole excited C_{60}	113
A.1	Field enhancement for plasmonic materials	128
B.1	Statistics of scientific environment	133

Table B.1: Symbols often employed

Symbol	Meaning
\mathbf{r}	position vector (bold quantities are vectors)
t	time
F	electric field
e	electron charge
F_0	electric field amplitude (in vacuum)
F_{eff}	electric field amplitude ($_{\text{eff}} \rightarrow$ including field enhancement)
F_{dc}	static electric field (for “direct current”)
$F_{\text{local}}(\mathbf{r})$	local microscopic electric field
A	vector potential ($A(t) = -\int_{-\infty}^t F(t')dt'$)
I	laser intensity ($[I[\text{W}/\text{cm}^2] = (F_0[\text{a.u.}]^2)/5.338 \times 10^{-9}$)
λ	(central) laser wavelength
ϕ_{CE}	carrier-envelope phase
ω, ω_L	photon energy of laser
ω_{XUV}	XUV photon energy
τ	pulse length
T	laser period ($T = 2\pi/\omega$)
\mathbf{p}	dipole moment
\mathbf{d}	dipole moment
A_s	shape factor of a spheroid
$R(R_{\text{tip}})$	radius (of curvature of a nano-tip)
α_{tip}	half opening angle of a nano-tip
ϵ	dielectric function
ζ_{FE}	field enhancement
W	work function
I_p	ionization potential
E_F	Fermi energy
$n(\mathbf{r}, t)$	charge density at \mathbf{r} at time t
$n_0(\mathbf{r})$	ground state density ($n(\mathbf{r}, t = -\infty)$)
Δn	induced charge density ($n(\mathbf{r}, t) - n_0(\mathbf{r})$)
\mathbf{j}	(microscopic) current density
\mathbf{J}	(macroscopic) current density

Table B.1: Symbols often employed

Symbol	Meaning
P	polarization density ($P(t) = \int_{-\infty}^t J(t') dt'$)
U_p	ponderomotive energy ($U_p = [F_0 / (2\omega)]^2$)
γ	Keldysh parameter ($\gamma = \omega\sqrt{2W}/F_0 = \sqrt{W/(2U_p)}$)
α_{quiver}	quiver radius ($\alpha_{\text{quiver}} = F_0/\omega^2$)
p	(electron) momentum
v	(electron) velocity
k	wave vector (electron or photon)
E	energy
E_i	energy eigenvalue labeled i (often $i = n, \mathbf{k}$, band index and wave vector)
H	Hamiltonian
V	potential
V_{GS}	ground state potential
V_{es}	electrostatic potential
V_{XC}	exchange correlation potential
V_{ext}	external potential
ψ	(time-dependent) wave function
ϕ	(time-independent) wave function
z_{im}	position of image plane
$\langle A(b) \rangle_b$	average of quantity $A(b)$ over b , $\langle A(b) \rangle_b = \int_{b_1}^{b_2} A(b) db / (b_2 - b_1)$ For probability distribution $S(x)$, $\langle A \rangle = \int A(x) S(x) dx / \int S(x) dx$
r_s	Wigner-Seitz radius
ω_p	plasma frequency
$\chi^{(i)}$	i -th order susceptibility
Q_L	laser-induced transferred charge
\mathcal{A}_{eff}	effective surface area
α	polarizability
Δp	momentum shift
Δt	time shift

Acronyms

ADK – Ammosov, Delone, and Krainov
BEM – boundary element method
CEP or CE-phase – carrier-envelope phase
CTMC – classical trajectory Monte Carlo
FDTD – finite differences time domain
FEM – finite element
FWHM – full width at half maximum
HHG – high-harmonic generation
IR – infrared (here used loosely for radiation of 750 nm - 10 μm wavelength)
LDA – local density approximation
NIR – near-infrared (700 nm - 1400 nm wavelength)
SMMN – simple man’s model for nanostructures
TD-DFT – time-dependent density functional theory
TDSE – time-dependent Schrödinger equation
UV – ultraviolet (100 nm - 300 nm wavelength)
VIS – visible (300 nm - 700 nm wavelength)
XUV – extreme ultraviolet (\sim 10 nm - 100 nm wavelength)

- Agostini, P., Fabre, F., Mainfray, G., Petite, G., and Rahman, N. K. (1979). Free-free transitions following six-photon ionization of xenon atoms. *Phys. Rev. Lett.*, 42(17):1127.
- Ajje, H., Alvarez, M. M., Anz, S. J., Beck, R. D., Diederich, F., Fostiropoulos, K., Huffman, D. R., Kraetschmer, W., Rubin, Y., et al., . (1990). Characterization of the soluble all-carbon molecules C_{60} and C_{70} . *J. Phys. Chem.*, 94(24):8630.
- Akbari, A., Hashemi, M. J., Rubio, A., Nieminen, R. M., and van Leeuwen, R. (2012). Challenges in truncating the hierarchy of time-dependent reduced density matrices equations. *Phys. Rev. B*, 85(23):235121.
- Alon, O. (2003). Bulk photogalvanic effects beyond second order. *Phys. Rev. B*, 67(12).
- American Physical Society (2014). Gender equity conversations. (http://www.aps.org/programs/women/workshops/gender-equity/sitevisits/upload/GE_CONVERSATIONS_Final.pdf).
- Ammosov, M. V., Delone, N. B., and Krainov, V. P. (1986). Tunnel ionization of complex atoms and of atomic ions in alternating electromagnetic fields. *Zh. Eksp. Teor. Fiz.*, 90:2008.
- Andrade, X., Alberdi-Rodríguez, J., Strubbe, D. A., Oliveira, M. J. T., Nogueira, F., Castro, A., Muguerza, J., Arruabarrena, A., Louie, S. G., Aspuru-Guzik, A., Rubio, A., and Marques, M. A. L. (2012). Time-dependent density-functional theory in massively parallel computer architectures: the octopus project. *J. Phys. Condens. Matter*, 24(23):233202.
- Andrade, X., Castro, A., Zueco, D., Alonso, J. L., Echenique, P., Falceto, F., and Rubio, A. (2009). Modified ehrenfest formalism for efficient large-scale ab initio molecular dynamics. *J. Chem. Theory Comput.*, 5(4):728.
- Apalkov, V. and Stockman, M. I. (2012). Theory of dielectric nanofilms in strong ultrafast optical fields. *Phys. Rev. B*, 86:165118.
- Apolonski, A., Dombi, P., Paulus, G., Kakehata, M., Holzwarth, R., Udem, T., Lemell, C., Torizuka, K., Burgdörfer, J., Hänsch, T., and Krausz, F. (2004). Observation of light-phase-sensitive photoemission from a metal. *Phys. Rev. Lett.*, 92(7):073902.
- Arbó, D. G., Ishikawa, K. L., Schiessl, K., Persson, E., and Burgdörfer, J. (2010a). Diffraction at a time grating in above-threshold ionization: The influence of the Coulomb potential. *Phys. Rev. A*, 82(4):043426.
- Arbó, D. G., Ishikawa, K. L., Schiessl, K., Persson, E., and Burgdörfer, J. (2010b). Intracycle and intercycle interferences in above-threshold ionization: The time grating. *Phys. Rev. A*, 81(2):021403.
- Arbó, D. G., Yoshida, S., Persson, E., Dimitriou, K. I., and Burgdörfer, J. (2006). Interference oscillations in the angular distribution of laser-ionized electrons near ionization threshold. *Phys. Rev. Lett.*, 96(14):143003.
- Arbouet, A., Houdellier, F., Marty, R., and Girard, C. (2012). Interaction of an ultrashort optical pulse with a metallic nanotip: A green dyadic approach. *J. Appl. Phys.*, 112(5):053103.
- Atwater, H. A. and Polman, A. (2010). Plasmonics for improved photovoltaic devices. *Nat. Mater.*, 9(3):205.
- Babadjanyan, A. J., Margaryan, N. L., and Nerkararyan, K. V. (2000). Superfocusing of surface polaritons in the conical structure. *J. Appl. Phys.*, 87(8):3785.
- Barton, G. and Eberlein, C. (1991). Plasma spectroscopy proposed for C_{60} and C_{70} . *J. Chem. Phys.*, 95(3):1512.
- Barwick, B., Corder, C., Strohaber, J., Chandler-Smith, N., Uiterwaal, C., and Batelaan, H. (2007).

- Laser-induced ultrafast electron emission from a field emission tip. *New J. Phys.*, 9(5):142.
- Baum, P., Yang, D.-S., and Zewail, A. H. (2007). 4d visualization of transitional structures in phase transformations by electron diffraction. *Science*, 318(5851):788.
- Becker, A. J., Becker, A., and Faisal, F. H. M. (2006). Saturated ionization of fullerenes in intense laser fields. *Phys. Rev. Lett.*, 96:143006.
- Becker, W., Liu, X., Ho, P. J., and Eberly, J. H. (2012). Theories of photoelectron correlation in laser-driven multiple atomic ionization. *Rev. Mod. Phys.*, 84:1011.
- Belinicher, V. I. and Sturman, B. I. (1980). The photogalvanic effect in media lacking a center of symmetry. *Soviet Physics Uspekhi*, p. 199.
- Berger, J., de Boeij, P., and van Leeuwen, R. (2007). Analysis of the vignale-kohn current functional in the calculation of the optical spectra of semiconductors. *Phys. Rev. B*, 75(3):035116.
- Bertsch, G. F., Bulgac, A., Tománek, D., and Wang, Y. (1991). Collective plasmon excitations in C_{60} clusters. *Phys. Rev. Lett.*, 67(19):2690.
- Bertsch, G. F., Iwata, J. I., Rubio, A., and Yabana, K. (2000). Real-space, real-time method for the dielectric function. *Phys. Rev. B*, 62(12):7998.
- Bian, X. B. and Bandrauk, A. D. (2012). Attosecond time-resolved imaging of molecular structure by photoelectron holography. *Phys. Rev. Lett.*, 108:263003.
- Bian, X. B., Huismans, Y., Smirnova, O., Yuan, K. J., Vrakking, M. J. J., and Bandrauk, A. D. (2011). Subcycle interference dynamics of time-resolved photoelectron holography with midinfrared laser pulses. *Phys. Rev. A*, 84:043420.
- Bladel, J. V. (1996). *Singular Electromagnetic Fields and Sources*. Ieee, New York; Oxford; New York.
- Bloembergen, N. (1996). *Nonlinear Optics*. World Scientific Pub Co Inc, Singapore; River Edge (N.J.); London etc., 4 edition edition.
- Bochvar, D. and Gal'pern, E. (1973). Carboradecahedron, s-icosahedron, and carbo-s-icosahedron hypothetical systems. *Doklady Akademii Nauk SSSR*, 209(3):610.
- Bohren, C. F. and Huffman, D. R. (1998). *Absorption and Scattering of Light by Small Particles*. Wiley-VCH. Published: Paperback.
- Boninsegni, M. (2008). Golden ratio (blog post). <http://expbook.wordpress.com/2008/04/04/golden-ratio>.
- Bormann, R., Gulde, M., Weismann, A., Yalunin, S. V., and Ropers, C. (2010). Tip-enhanced strong-field photoemission. *Phys. Rev. Lett.*, 105(14):147601.
- Bosshard, C., Gubler, U., Kaatz, P., Mazerant, W., and Meier, U. (2000). Non-phase-matched optical third-harmonic generation in noncentrosymmetric media: Cascaded second-order contributions for the calibration of third-order nonlinearities. *Phys. Rev. B*, 61:10688.
- Botti, S., Schindlmayr, A., Sole, R. D., and Reinig, L. (2007). Time-dependent density-functional theory for extended systems. *Rep. Prog. Phys.*, 70(3):357.
- Bouhelier, A., Beversluis, M. R., and Novotny, L. (2003). Near-field scattering of longitudinal fields. *Appl. Phys. Lett.*, 82(25):4596.
- Boyd, R. W. (2003). *Nonlinear Optics*. Academic Press.
- Brongersma, M. L. and Kik, P. G., editors (2007). *Surface Plasmon Nanophotonics*, volume 131 of *Springer Series in Optical Sciences*. Springer.
- Burgdörfer, J. (1994). Atomic collisions with surfaces. In Lin, C. D., editor, *Review of fundamental processes and applications of atoms and ions*, p. 517. World Scientific Pub Co Inc.
- Butry, O., Ebad, H., de Boeij, P. L., van Leeuwen, R., and Gross, E. K. U. (2007). Multicomponent density-functional theory for time-dependent systems. *Phys. Rev. A*, 76(5):052514.
- Calabrese, E. and Fowler, W. B. (1978). Electronic energy-band structure of α quartz. *Phys. Rev. B*, 18:2888.
- Can-Uc, B., Rangel-Rojo, R., Rodriguez-Fernandez, L., and Oliver, A. (2013). Polarization selectable nonlinearities in elongated silver nanoparticles embedded in silica. *Opt. Mater. Express*, 3(12):2012.
- Casida, M. E. and Huix-Rotllant, M. (2012). Progress in time-dependent density-functional theory. *Ann. Rev. Phys. Chem.*, 63(1):287.
- Castro, A., Appel, H., Oliveira, M., Rozzi, C. A., Andrade, X., Lorenzen, F., Marques, M. a. L., Gross, E. K. U., and Rubio, A. (2006). octopus: a tool for the application of time-dependent density functional theory. *Phys. Status Solidi B*, 243(11):2465.
- Cavalleri, A. L., Muller, N., Uphues, T., Yakovlev, V. S., Baltuska, A., Horvath, B., Schmidt, B., Blumel, L., Holzwarth, R., Hendel, S., Drescher, M., Kleineberg, U., Echenique, P. M., Kienberger, R., Krausz, F., and Heinzmann, U. (2007). Attosecond spectroscopy in condensed matter. *Nature*, 449(7165):1029.
- Chang, D. E., Sørensen, A. S., Hemmer, P. R., and Lukin, M. D. (2007). Strong coupling of single emitters to surface plasmons. *Phys. Rev. B*, 76(3):035420.
- Chang, D. E., Thompson, J. D., Park, H., Vuletić, V., Zibrov, A. S., Zoller, P., and Lukin, M. D. (2009). Trapping and manipulation of isolated atoms using nanoscale plasmonic structures. *Phys. Rev. Lett.*, 103(12):123004.
- Chang, E. K., Rohlfing, M., and Louie, S. G. (2000). Excitons and optical properties of α -quartz. *Phys. Rev. Lett.*, 85:2613.
- Chelikowsky, J. R., Leeor Kronik, and Igor Vasiliev (2003). Time-dependent density-functional calculations for the optical spectra of molecules, clusters, and nanocrystals. *J. Phys. Condens. Matter*, 15(35):R1517.
- Chelikowsky, J. R. and Schlüter, M. (1977). Electron states in α -quartz: A self-consistent pseudopotential calculation. *Phys. Rev. B*, 15:4020.

- Chelikowsky, J. R., Troullier, N., Wu, K., and Saad, Y. (1994). Higher-order finite difference pseudopotential method: An application to diatomic molecules. *Phys. Rev. B*, 50(16):11355.
- Chen, F., Dai, S., Xu, T., Shen, X., Lin, C., Nie, Q., Liu, C., and Heo, J. (2011). Surface-plasmon enhanced ultrafast third-order optical nonlinearities in ellipsoidal gold nanoparticles embedded bismuthate glasses. *Chem. Phys. Lett.*, 514(1–3):79.
- Chen, J., Thygesen, K. S., and Jacobsen, K. W. (2012). Ab-initio non-equilibrium quantum transport and forces with the real space projector augmented wave method (arxiv:1204.4175).
- Chen, Z., Le, A. T., Morishita, T., and Lin, C. D. (2009). Quantitative rescattering theory for laser-induced high-energy plateau photoelectron spectra. *Phys. Rev. A*, 79:033409.
- Chini, M., Zhao, K., and Chang, Z. (2014). The generation, characterization and applications of broadband isolated attosecond pulses. *Nat. Phot.*, 8(3):178.
- Chulkov, E. V., Silkin, V. M., and Echenique, P. M. (1999). Image potential states on metal surfaces: binding energies and wave functions. *Surf. Sci.*, 437(3):330.
- Ciappina, M. F., Pérez-Hernández, J. A., Shaaran, T., Lewenstein, M., Krüger, M., and Hommelhoff, P. (2014). High-order-harmonic generation driven by metal nanotip photoemission: Theory and simulations. *Phys. Rev. A*, 89(1):013409.
- Corkum, P. (1993). Plasma perspective on strong field multiphoton ionization. *Phys. Rev. Lett.*, 71(13):1994.
- Corkum, P. B. and Krausz, F. (2007). Attosecond science. *Nat. Phys.*, 3(6):381.
- D'Agosta, R., Di Ventra, M., and Vignale, G. (2007). Electronic viscosity in a quantum well: A test for the local-density approximation. *Phys. Rev. B*, 76:035320.
- D'Agosta, R. and Vignale, G. (2006). Relaxation in time-dependent current-density-functional theory. *Phys. Rev. Lett.*, 96(1):016405.
- Dalba, G., Soldo, Y., Rocca, F., Fridkin, V. M., and Sainctavit, P. (1995). Giant bulk photovoltaic effect under linearly polarized x-ray synchrotron radiation. *Phys. Rev. Lett.*, 74(6):988.
- De Giovannini, U., Brunetto, G., Castro, A., Walkenhorst, J., and Rubio, A. (2013). Simulating pump-probe photoelectron and absorption spectroscopy on the attosecond timescale with time-dependent density functional theory. *ChemPhysChem*, 14(7):1363.
- De Giovannini, U., Varsano, D., Marques, M. A. L., Appel, H., Gross, E. K. U., and Rubio, A. (2012). Ab initio angle- and energy-resolved photoelectron spectroscopy with time-dependent density-functional theory. *Phys. Rev. A*, 85(6):062515.
- de Morisson Faria, C. F. and Liu, X. (2011). Electron-electron correlation in strong laser fields. *J. Mod. Opt.*, 58(13):1076.
- deHeer, W. A., Bacsá, W. S., Châtelain, A., Gerfin, T., Humphrey-Baker, R., Forro, L., and Ugarte, D. (1995). Aligned carbon nanotube films: Production and optical and electronic properties. *Science*, 268(5212):845.
- Delaney, P. and Greer, J. C. (2004). C₆₀ as a Faraday cage. *Appl. Phys. Lett.*, 84(3):431.
- Dember, H. (1931). Über eine photoelektronische Kraft in Kupferoxydul-Kristallen. *Physikalische Zeitschrift*, (32):554.
- Descobes, S., Durochat, C., Lanteri, S., Moya, L., Scheid, C., and Viquerat, J. (2013). Recent advances on a DGTD method for time-domain electromagnetics. *Photonics and Nanostructures - Fundamentals and Applications*, 11(4):291.
- Devilez, A., Bonod, N., Wenger, J., Gérard, D., Stout, B., Rigneault, H., and Popov, E. (2009). Three-dimensional subwavelength confinement of light with dielectric microspheres. *Opt. Express*, 17(4):2089.
- Di Ventra, M. and D'Agosta, R. (2007). Stochastic time-dependent current-density-functional theory. *Phys. Rev. Lett.*, 98(22).
- Dinh, P. M., Romaniello, P., Reinhard, P. G., and Surraud, E. (2013). Calculation of photoelectron spectra: A mean-field-based scheme. *Phys. Rev. A*, 87:032514.
- Dombi, P., Apolonski, A., Lemell, C., Paulus, G. G., Kakehata, M., Holzwarth, R., Udem, T., Torizuka, K., Burgdörfer, J., Hänsch, T. W., and Krausz, F. (2004). Direct measurement and analysis of the carrier-envelope phase in light pulses approaching the single-cycle regime. *New J. Phys.*, 6(1):39.
- Dombi, P., Hörl, A., Rácz, P., Márton, I., Trügler, A., Krenn, J. R., and Hohenester, U. (2013). Ultrafast strong-field photoemission from plasmonic nanoparticles. *Nano Lett.*, 13(2):674.
- Draine, B. T. and Flatau, P. J. (2012). User guide for the discrete dipole approximation code DDSCAT 7.2 (arxiv:1202.3424).
- Driscoll, J. A., Bubin, S., and Varga, K. (2011). Laser-induced electron emission from nanostructures: A first-principles study. *Phys. Rev. B*, 83:233405.
- Durach, M., Rusina, A., Kling, M. F., and Stockman, M. I. (2010). Metallization of nanofilms in strong adiabatic electric fields. *Phys. Rev. Lett.*, 105(8).
- Durach, M., Rusina, A., Kling, M. F., and Stockman, M. I. (2011). Predicted ultrafast dynamic metallization of dielectric nanofilms by strong single-cycle optical fields. *Phys. Rev. Lett.*, 107(8).
- Eckle, P., Pfeiffer, A. N., Cirelli, C., Staudte, A., Dörner, R., Müller, H. G., Büttiker, M., and Keller, U. (2008a). Attosecond ionization and tunneling delay time measurements in helium. *Science*, 322(5907):1525.
- Eckle, P., Smolarski, M., Schlup, P., Biegert, J., Staudte, A., Schöffler, M., Müller, H. G., Dörner, R., and Keller, U. (2008b). Attosecond angular streaking. *Nat. Phys.*, 4(7):565.
- Eguiluz, A. G., Campbell, D. A., Maradudin, A. A., and Wallis, R. F. (1984). Static response of a jellium surface: The image potential and indirect interaction between two charges. *Phys. Rev. B*, 30(10):5449.

- Einstein, A. (1905). Über einen die Erzeugung und Verwandlung des Lichtes betreffenden heuristischen Gesichtspunkt. *Ann. Phys.*, 322(6):132.
- Einstein, A. (1917). Zur Quantentheorie der Strahlung. *Physikalische Zeitschrift*, 18:121.
- Eisenbud, L. (1948). *Formal properties of nuclear collisions*. Princeton University.
- Elliott, P., Fuks, J. I., Rubio, A., and Maitra, N. T. (2012). Universal dynamical steps in the exact time-dependent exchange-correlation potential. *Phys. Rev. Lett.*, 109(26):266404.
- Enkovaara, J., Rostgaard, C., Mortensen, J. J., Chen, J., Dulak, M., Ferrighi, L., Gavnholt, J., Glinsvad, C., Haikola, V., Hansen, H. A., Kristofersen, H. H., Kuisma, M., Larsen, A. H., Lehtovaara, L., Ljungberg, M., Lopez-Acevedo, O., Moses, P. G., Ojanen, J., Olsen, T., Petzold, V., Romero, N. A., Stausholm-Møller, J., Strange, M., Tritsarolis, G. A., Vanin, M., Walter, M., Hammer, B., Häkkinen, H., Madsen, G. K. H., Nieminen, R. M., Nørskov, J. K., Puska, M., Rantala, T. T., Schiøtz, J., Thygesen, K. S., and Jacobsen, K. W. (2010). Electronic structure calculations with GPAW: a real-space implementation of the projector augmented-wave method. *J. Phys.: Condens. Matter*, 22(25):253202.
- Esteban, R., Borisov, A. G., Nordlander, P., and Aizpurua, J. (2012). Bridging quantum and classical plasmonics with a quantum-corrected model. *Nat. Commun.*, 3:825.
- Faber, C., Janssen, J. L., Côté, M., Runge, E., and Blase, X. (2011). Electron-phonon coupling in the C_{60} fullerene within the many-body GW approach. *Phys. Rev. B*, 84(15):155104.
- Faisal, F. H. M., Kamiński, J. Z., and Saczuk, E. (2005). Photoemission and high-order harmonic generation from solid surfaces in intense laser fields. *Phys. Rev. A*, 72(2):023412.
- Falke, S. M., Rozzi, C. A., Brida, D., Maiuri, M., Amato, M., Sommer, E., Sio, A. D., Rubio, A., Cerullo, G., Molinari, E., and Lienau, C. (2014). Coherent ultrafast charge transfer in an organic photovoltaic blend. *Science*, 344(6187):1001.
- Feichtner, T., Selig, O., Kiunke, M., and Hecht, B. (2012). Evolutionary optimization of optical antennas (arxiv:1204.5422).
- Feist, J., Reid, M. T. H., and Kling, M. F. (2013). Nanoplasmonic near-field synthesis. *Phys. Rev. A*, 87:033816.
- Fennel, T., Meiwes-Broer, K.-H., Tiggesbäumker, J., Reinhard, P.-G., Dinh, P. M., and Suraud, E. (2010). Laser-driven nonlinear cluster dynamics. *Rev. Mod. Phys.*, 82(2):1793.
- Fiolhais, C., Nogueira, F., and Marques, M. A. L. (2003). *A Primer in Density Functional Theory*. Springer Science & Business Media.
- Fischer, M., Handt, J., and Schmidt, R. (2014). Nonadiabatic quantum molecular dynamics with hopping. III. photoinduced excitation and relaxation of organic molecules. *Phys. Rev. A*, 90(1):012527.
- Földi, P., Benedict, M. G., and Yakovlev, V. S. (2013). The effect of dynamical Bloch oscillations on optical-field-induced current in a wide-gap dielectric. *New J. Phys.*, 15(6):063019.
- Foldi, P., Marton, I., Nemet, N., and Dombi, P. (2014). Nanoscale optical waveform control of strong-field photoemission. *arXiv:1405.5372*.
- Fowler, R. H. and Nordheim, L. (1928). Electron emission in intense electric fields. *Proc. R. Soc. Lond. A*, 119(781):173.
- Franco, I., Shapiro, M., and Brumer, P. (2007). Robust ultrafast currents in molecular wires through Stark shifts. *Phys. Rev. Lett.*, 99:126802.
- Fridkin, V. M. (2001). Bulk photovoltaic effect in noncentrosymmetric crystals. *Crystallogr. Rep.*, 46(4):654.
- Fuks, J. I., Elliott, P., Rubio, A., and Maitra, N. T. (2013). Dynamics of charge-transfer processes with time-dependent density functional theory. *J. Phys. Chem. Lett.*, 4(5):735.
- Gaiduk, A. P., Mizzi, D., and Staroverov, V. N. (2012). Self-interaction correction scheme for approximate Kohn-Sham potentials. *Phys. Rev. A*, 86(5):052518.
- Ganeev, R. A., Bom, L. B. E., Hadi, J. A., Wong, M. C. H., Brichta, J. P., Bhardwaj, V. R., and Ozaki, T. (2009). Higher-order harmonic generation from fullerene by means of the plasma harmonic method. *Phys. Rev. Lett.*, 102(1):013903.
- Gavnholt, J., Rubio, A., Olsen, T., Thygesen, K. S., and Schiøtz, J. (2009). Hot-electron-assisted femtochemistry at surfaces: A time-dependent density functional theory approach. *Phys. Rev. B*, 79(19):195405.
- Gérard, D., Wenger, J., Devilez, A., Gachet, D., Stout, B., Bonod, N., Popov, E., and Rigneault, H. (2008). Strong electromagnetic confinement near dielectric microspheres to enhance single-molecule fluorescence. *Opt. Express*, 16(19):15297.
- Gertszvolf, M., Jean-Ruel, H., Rajeev, P., Klug, D., Rayner, D., and Corkum, P. (2008). Orientation-dependent multiphoton ionization in wide band gap crystals. *Phys. Rev. Lett.*, 101(24).
- Gertszvolf, M., Spanner, M., Rayner, D. M., and Corkum, P. B. (2010). Demonstration of attosecond ionization dynamics inside transparent solids. *J. Phys. B*, 43(13):131002.
- Geuzaine, C. and Remacle, J.-F. (2009). Gmsh: A 3-d finite element mesh generator with built-in pre- and post-processing facilities. *Int. J. Numer. Meth. Engng.*, 79(11):1309.
- Ghimire, S., DiChiara, A. D., Sistrunk, E., Agostini, P., DiMauro, L. F., and Reis, D. A. (2011a). Observation of high-order harmonic generation in a bulk crystal. *Nat. Phys.*, 7(2):138.
- Ghimire, S., DiChiara, A. D., Sistrunk, E., Ndabashimiye, G., Szafruga, U. B., Mohammad, A., Agostini, P., DiMauro, L. F., and Reis, D. A. (2012). Generation and propagation of high-order harmonics in crystals. *Phys. Rev. A*, 85(4):043836.
- Ghimire, S., DiChiara, A. D., Sistrunk, E., Szafruga, U. B., Agostini, P., DiMauro, L. F., and Reis, D. A. (2011b). Redshift in the optical absorption

- of ZnO single crystals in the presence of an intense midinfrared laser field. *Phys. Rev. Lett.*, 107(16):167407.
- Gisbergen, S. J. A. v., Osinga, V. P., Gritsenko, O. V., Leeuwen, R. v., Snijders, J. G., and Baerends, E. J. (1996). Improved density functional theory results for frequency-dependent polarizabilities, by the use of an exchange-correlation potential with correct asymptotic behavior. *J. Chem. Phys.*, 105(8):3142.
- Giugni, A., Torre, B., Toma, A., Francardi, M., Malerba, M., Alabastri, A., Zaccaria, R. P., Stockman, M. I., and Fabrizio, E. D. (2013). Hot-electron nanoscopy using adiabatic compression of surface plasmons. *Nat. Nanotechnol.*, 8(11):845.
- Giuliani, G. and Vignale, G. (2005). *Quantum Theory of the Electron Liquid*. Cambridge University Press. Published: Hardcover.
- Giustino, F. and Pasquarello, A. (2005). Theory of atomic-scale dielectric permittivity at insulator interfaces. *Phys. Rev. B*, 71(14).
- Giustino, F., Umari, P., and Pasquarello, A. (2003). Dielectric discontinuity at interfaces in the atomic-scale limit: Permittivity of ultrathin oxide films on silicon. *Phys. Rev. Lett.*, 91(26).
- Glass, A. M., Linde, D. v. d., and Negran, T. J. (1974). High-voltage bulk photovoltaic effect and the photorefractive process in LiNbO₃. *Appl. Phys. Lett.*, 25(4):233.
- Gnani, E., Reggiani, S., and Rudan, M. (2002). Density of states and group velocity of electrons in SiO₂ calculated from a full band structure. *Phys. Rev. B*, 66(19):195205.
- Goncharenko, A., Wang, J.-K., and Chang, Y.-C. (2006). Electric near-field enhancement of a sharp semi-infinite conical probe: Material and cone angle dependence. *Phys. Rev. B*, 74(23).
- Gonze, X., Ghosez, P., and Godby, R. (1995). Density-polarization functional theory of the response of a periodic insulating solid to an electric field. *Phys. Rev. Lett.*, 74(20):4035.
- Goodman, A. (1967). Electron hall effect in silicon dioxide. *Phys. Rev.*, 164(3):1145.
- Gould, R. G. (1959). The LASER, light amplification by stimulated emission of radiation. In *Franken, P.A. and Sands, R.H. (Eds.): The Ann Arbor conference on optical pumping: the University of Michigan, June 15 through June 18, 1959.*, Ann Arbor.
- Goulielmakis, E., Loh, Z.-H., Wirth, A., Santra, R., Rohringer, N., Yakovlev, V. S., Zherebtsov, S., Pfeifer, T., Azzeer, A. M., Kling, M. F., Leone, S. R., and Krausz, F. (2010). Real-time observation of valence electron motion. *Nature*, 466(7307):739.
- Goulielmakis, E., Uiberacker, M., Kienberger, R., Baltuska, A., Yakovlev, V., Scrinzi, A., Westerwalbesloh, T., Kleineberg, U., Heinzmann, U., Drescher, M., and Krausz, F. (2004). Direct measurement of light waves. *Science*, 305(5688):1267.
- Graf, U., Fieß, M., Schultze, M., Kienberger, R., Krausz, F., and Goulielmakis, E. (2008). Intense few-cycle light pulses in the deep ultraviolet. *Opt. Express*, 16(23):18956.
- Gray, S. K. (2012). Theory and modeling of plasmonic structures. *J. Phys. Chem. C*, 117(5):1983.
- Grzela, G., Paniagua-Domínguez, R., Barten, T., Fontana, Y., Sánchez-Gil, J. A., and Gómez Rivas, J. (2012). Nanowire antenna emission. *Nano Lett.*, 12(11):5481.
- Grzela, G., Paniagua-Domínguez, R., Barten, T., van Dam, D., Sánchez-Gil, J. A., and Rivas, J. G. (2014). Nanowire antenna absorption probed with time-reversed fourier microscopy. *Nano Lett.*, 14(6):3227.
- Gubler, U. and Bosshard, C. (2000). Optical third-harmonic generation of fused silica in gas atmosphere: Absolute value of the third-order nonlinear optical susceptibility $\chi^{(3)}$. *Phys. Rev. B*, 61:10702.
- Gulde, M., Schweda, S., Storeck, G., Maiti, M., Yu, H. K., Wodtke, A. M., Schäfer, S., and Ropers, C. (2014). Ultrafast low-energy electron diffraction in transmission resolves polymer/graphene superstructure dynamics. *Science*, 345(6193):200.
- Gullans, M., Tiecke, T. G., Chang, D. E., Feist, J., Thompson, J. D., Cirac, J. I., Zoller, P., and Lukin, M. D. (2012). Nanoplasmonic lattices for ultracold atoms. *Phys. Rev. Lett.*, 109(23):235309.
- Gunnarsson, O., Handschuh, H., Bechtold, P. S., Kessler, B., Ganteför, G., and Eberhardt, W. (1995). Photoemission spectra of C₆₀⁻: Electron-phonon coupling, Jahn-Teller effect, and superconductivity in the fullerides. *Phys. Rev. Lett.*, 74(10):1875.
- Haddon, R. C., Brus, L. E., and Raghavachari, K. (1986). Electronic structure and bonding in icosahedral C₆₀. *Chem. Phys. Lett.*, 125(5-6):459.
- Haessler, S., Caillat, J., and Salières, P. (2011). Self-probing of molecules with high harmonic generation. *J. Phys. B*, 44(20):203001.
- Han, S., Lee, M. H., and Ihm, J. (2002). Dynamical simulation of field emission in nanostructures. *Phys. Rev. B*, 65:085405.
- Hands, I. D., Dunn, J. L., Bates, C. A., Hope, M. J., Meech, S. R., and Andrews, D. L. (2008). Vibronic interactions in the visible and near-infrared spectra of C₆₀⁻ anions. *Phys. Rev. B*, 77(11):115445.
- Harris, M. (2012). The academic pyramid. *Phys. World*, 25(10):54.
- Hartschuh, A. (2008). Tip-enhanced near-field optical microscopy. *Angew. Chem. Int. Ed.*, 47(43):8178.
- Hassan, M. T., Wirth, A., Grguraš, I., Moulet, A., Luu, T. T., Gagnon, J., Pervak, V., and Goulielmakis, E. (2012). Invited article: Attosecond photonics: Synthesis and control of light transients. *Rev. Sci. Instrum.*, 83(11):11301.
- Hawkins, P. G. and Ivanov, M. Y. (2013). Role of sub-cycle transition dynamics in high-order-harmonic generation in periodic structures. *Phys. Rev. A*, 87(6).
- Heath, J. R., Curl, R. F., and Smalley, R. E. (1987). The UV absorption spectrum of C₆₀ (buckminsterfullerene): A narrow band at 3860 Å. *J. Chem. Phys.*, 87(7):4236.

- Heath, J. R., O'Brien, S. C., Zhang, Q., Liu, Y., Curl, R. F., Tittel, F. K., and Smalley, R. E. (1985). Lanthanum complexes of spheroidal carbon shells. *J. Am. Chem. Soc.*, 107(25):7779.
- Herink, G., Solli, D. R., Gulde, M., and Ropers, C. (2012). Field-driven photoemission from nanostructures quenches the quiver motion. *Nature*, 483(7388):190.
- Hoffrogge, J., Stein, J. P., Krüger, M., Förster, M., Hammer, J., Ehberger, D., Baum, P., and Hommelhoff, P. (2014). Tip-based source of femtosecond electron pulses at 30 keV. *J. Appl. Phys.*, 115(9):094506.
- Hohenberg, P. and Kohn, W. (1964). Inhomogeneous electron gas. *Phys. Rev.*, 136(3B):B864–B871.
- Hohenester, U. and Trügler, A. (2011). MNPBEM – a matlab toolbox for the simulation of plasmonic nanoparticles. *Comput. Phys. Commun.*, 10.1016/j.cpc.2011.09.009.
- Hommelhoff, P., Kealhofer, C., and Kasevich, M. A. (2006a). Ultrafast electron pulses from a tungsten tip triggered by low-power femtosecond laser pulses. *Phys. Rev. Lett.*, 97(24):247402.
- Hommelhoff, P., Sortais, Y., Talesh, A. A., and Kasevich, M. A. (2006b). Field emission tip as a nanometer source of free electron femtosecond pulses. *Phys. Rev. Lett.*, 96(7):077401.
- Hörl, A., Trügler, A., and Hohenester, U. (2013). Tomography of particle plasmon fields from electron energy loss spectroscopy. *Phys. Rev. Lett.*, 111(7).
- Huang, C., Libisch, F., Peng, Q., and Carter, E. A. (2014). Time-dependent potential-functional embedding theory. *J. Chem. Phys.*, 140(12):124113.
- Hughes, R. (1973). Charge-carrier transport phenomena in amorphous SiO₂: Direct measurement of the drift mobility and lifetime. *Phys. Rev. Lett.*, 30(26):1333.
- Huisman, Y., Rouzée, A., Gijsbertsen, A., Jungmann, J. H., Smolkowska, A. S., Logman, P. S. W. M., Lépine, F., Cauchy, C., Zamith, S., Marchenko, T., Bakker, J. M., Berden, G., Redlich, B., Meer, A. F. G. v. d., Muller, H. G., Vermin, W., Schafer, K. J., Spanner, M., Ivanov, M. Y., Smirnova, O., Bauer, D., Popruzhenko, S. V., and Vrakking, M. J. J. (2011). Time-resolved holography with photoelectrons. *Science*, 331(6013):61.
- Husser, H., van Heys, J., and Pehlke, E. (2011). Non-perturbative approach to photoemission by direct simulation of photocurrents. *Phys. Rev. B*, 84(23).
- Issa, N. A. and Guckenberger, R. (2007). Optical nanofocusing on tapered metallic waveguides. *Plasmonics*, 2(1):31.
- Itatani, J., Levesque, J., Zeidler, D., Niikura, H., Pepin, H., Kieffer, J. C., Corkum, P. B., and Villeneuve, D. M. (2004). Corkum graphic imaging of molecular orbitals. *Nature*, 432(7019):867.
- Iwahara, N., Sato, T., Tanaka, K., and Chibotaru, L. F. (2010). Vibronic coupling in C₆₀ anion revisited: Derivations from photoelectron spectra and DFT calculations. *Phys. Rev. B*, 82(24):245409.
- Iwasa, T. and Nobusada, K. (2009). Nonuniform light-matter interaction theory for near-field-induced electron dynamics. *Phys. Rev. A*, 80:043409.
- Iwasa, T. and Nobusada, K. (2010). Near-field-induced optical force on a metal particle and C₆₀: Real-time and real-space electron dynamics simulation. *Phys. Rev. A*, 82:043411.
- Jackson, J. D. (1998). *Classical Electrodynamics*. Wiley.
- Jennings, P. J., Jones, R. O., and Weinert, M. (1988). Surface barrier for electrons in metals. *Phys. Rev. B*, 37(11):6113.
- Jensen, L. and Van Duijnen, P. T. (2005). Refractive index and third-order nonlinear susceptibility of C₆₀ in the condensed phase calculated with the discrete solvent reaction field model. *Int. J. Quantum Chem.*, 102(5):612.
- Joannopoulos, J. D., Johnson, S. G., Winn, J. N., and Meade, R. D. (2011). *Photonic Crystals: Molding the Flow of Light (Second Edition)*. Princeton University Press.
- K. Yabana, Y. Shinohara, T. Otake, Jun-Ichi Iwata, and George F. Bertsch (2013). Chapter 6: First-principles calculations for laser induced electron dynamics in solids. In *Advances in Multi-Photon Processes and Spectroscopy*, volume Volume 21 of *Advances in Multi-Photon Processes and Spectroscopy*, p. 209. World Scientific.
- Kastler, A. (1967). Optical methods for studying hertzian resonances. *Science*, 158(3798):214.
- Kauranen, M. and Zayats, A. V. (2012). Nonlinear plasmonics. *Nat. Phot.*, 6(11):737.
- Kawano, H. (2008). Effective work functions for ionic and electronic emissions from mono- and polycrystalline surfaces. *Prog. Surf. Sci.*, 83(1-2):1.
- Kawashita, Y., Yabana, K., Noda, M., Nobusada, K., and Nakatsukasa, T. (2009). Oscillator strength distribution of in the time-dependent density functional theory. *J. Mol. Struct. THEOCHEM*, 914(1-3):130.
- Kawata, S., Inouye, Y., and Verma, P. (2009). Plasmonics for near-field nano-imaging and superlensing. *Nat. Phot.*, 3(7):388.
- Keldysh, L. V. (1965). Ionization in the field of a strong electromagnetic wave. *Soviet Physics JETP*, 20:1307.
- Kemper, A. F., Moritz, B., Freericks, J. K., and Devereaux, T. P. (2013). Theoretical description of high-order harmonic generation in solids. *New J. Phys.*, 15(2):023003.
- Kim, S., Jin, J., Kim, Y.-J., Park, I.-Y., Kim, Y., and Kim, S.-W. (2008). High-harmonic generation by resonant plasmon field enhancement. *Nature*, 453(7196):757.
- Klamroth, T. and Nest, M. (2009). Ultrafast electronic excitations of small sodium clusters and the onset of electron thermalization. *Phys. Chem. Chem. Phys.*, 11(2):349.
- Klotz, D., Sacuto, S., Paladini, C., Hron, J., and Wachter, G. (2012). Geometrical model fitting for interferometric data: GEM-FIND. In *Proc. SPIE 8445, Optical and Infrared Interferometry III*, volume 8445, p. 84451A.

- Kohler, M. C., Ott, C., Raith, P., Heck, R., Schlegel, I., Keitel, C. H., and Pfeifer, T. (2010). High harmonic generation via continuum wave-packet interference. *Phys. Rev. Lett.*, 105(20):203902.
- Kohn, W. and Sham, L. J. (1965). Self-consistent equations including exchange and correlation effects. *Phys. Rev.*, 140(4A):A1133.
- Koller, D., Tran, F., and Blaha, P. (2011). Merits and limits of the modified Becke-Johnson exchange potential. *Phys. Rev. B*, 83:195134.
- Koller, D., Tran, F., and Blaha, P. (2012). Improving the modified Becke-Johnson exchange potential. *Phys. Rev. B*, 85:155109.
- Kootstra, F., de Boeij, P. L., and Srijders, J. G. (2000). Efficient real-space approach to time-dependent density functional theory for the dielectric response of nonmetallic crystals. *J. Chem. Phys.*, 112(15):6517.
- Korbman, M., Kruchinin, S. Y., and Yakovlev, V. S. (2013). Quantum beats in the polarization response of a dielectric to intense few-cycle laser pulses. *New J. Phys.*, 15(1):013006.
- Koval, N. E., Sánchez-Portal, D., Borisov, A. G., and Muiño, R. D. (2012a). Dynamic screening of a localized hole during photoemission from a metal cluster. *Nanoscale Res. Lett.*, 7(1):447.
- Koval, N. E., Sánchez-Portal, D., Borisov, A. G., and Muiño, R. D. (2012b). Dynamic screening of a localized hole during photoemission from a metal cluster. [arxiv:1203.4944](https://arxiv.org/abs/1203.4944).
- Krätschmer, W., Lamb, L. D., Fostiropoulos, K., and Huffman, D. R. (1990). Solid C₆₀: a new form of carbon. *Nature*, 347(6291):354.
- Krausz, F. and Ivanov, M. (2009). Attosecond physics. *Rev. Mod. Phys.*, 81(1):163.
- Krausz, F. and Stockman, M. I. (2014). Attosecond metrology: from electron capture to future signal processing. *Nat. Phot.*, 8(3):205.
- Kreibich, T. and Gross, E. K. U. (2001). Multicomponent density-functional theory for electrons and nuclei. *Phys. Rev. Lett.*, 86(14):2984.
- Kreibich, T., van Leeuwen, R., and Gross, E. K. U. (2004). Time-dependent variational approach to molecules in strong laser fields. *Chem. Phys.*, 304(1–2):183.
- Kreibich, T., van Leeuwen, R., and Gross, E. K. U. (2008). Multicomponent density-functional theory for electrons and nuclei. *Phys. Rev. A*, 78(2):022501.
- Kroto, H. W., Heath, J. R., O'Brien, S. C., Curl, R. F., and Smalley, R. E. (1985). C₆₀ buckminsterfullerene. *Nature*, 318(6042):162.
- Kruchinin, Korbman, M., and Yakovlev, V. S. (2013). Theory of strong-field injection and control of photocurrent in dielectrics and wide band gap semiconductors. *Phys. Rev. B*, 87(11):115201.
- Krüger, M., Schenk, M., and Hommelhoff, P. (2011). Attosecond control of electrons emitted from a nanoscale metal tip. *Nature*, 475(7354):78.
- Krüger, M., Schenk, M., Hommelhoff, P., Wächter, G., Lemell, C., and Burgdörfer, J. (2012). Interaction of ultrashort laser pulses with metal nanotips: a model system for strong-field phenomena. *New J. Phys.*, 14(8):085019.
- Kuleff, A. I., Lünemann, S., and Cederbaum, L. S. (2013). Electron-correlation-driven charge migration in oligopeptides. *Chem. Phys.*, 414:100.
- Kunz, K. S. and Luebbers, R. J. (1993). *The Finite Difference Time Domain Method for Electromagnetics*. CRC Press. Published: Hardcover.
- Kuo, H.-S., Hwang, I.-S., Fu, T.-Y., Wu, J.-Y., Chang, C.-C., and Tsong, T. T. (2004). Preparation and characterization of single-atom tips. *Nano Lett.*, 4(12):2379.
- Lackner, F. (2014). Dynamics of correlated many-body systems: propagating reduced two-particle density matrices without wave functions. (Master thesis, TU Wien).
- Lang, N. D. and Kohn, W. (1970). Theory of metal surfaces: Charge density and surface energy. *Phys. Rev. B*, 1:4555.
- Le, A. T., Lucchese, R. R., Tonzani, S., Morishita, T., and Lin, C. D. (2009). Quantitative rescattering theory for high-order harmonic generation from molecules. *Phys. Rev. A*, 80(1):013401.
- Le, A. T., Morishita, T., Lucchese, R. R., and Lin, C. D. (2012). Theory of high harmonic generation for probing time-resolved large-amplitude molecular vibrations with ultrashort intense lasers. *Phys. Rev. Lett.*, 109:203004.
- Lee, K.-M., Kim, C. M., Sato, S. A., Otobe, T., Shinohara, Y., Yabana, K., and Jeong, T. M. (2014). First-principles simulation of the optical response of bulk and thin-film α -quartz irradiated with an ultrashort intense laser pulse. *J. Appl. Phys.*, 115(5):053519.
- Lein, M. and Kümmel, S. (2005). Exact time-dependent exchange-correlation potentials for strong-field electron dynamics. *Phys. Rev. Lett.*, 94(14):143003.
- Lemell, C., Burgdörfer, J., Gräfe, S., Dimitriou, K. I., Arbó, D. G., and Tong, X.-M. (2013). Classical-quantum correspondence in atomic ionization by midinfrared pulses: Multiple peak and interference structures. *Phys. Rev. A*, 87(1):013421.
- Lemell, C., Solleder, B., Tökési, K., and Burgdörfer, J. (2009). Simulation of attosecond streaking of electrons emitted from a tungsten surface. *Phys. Rev. A*, 79(6):062901.
- Lemell, C., Tong, X.-M., Krausz, F., and Burgdörfer, J. (2003). Electron emission from metal surfaces by ultrashort pulses: Determination of the carrier-envelope phase. *Phys. Rev. Lett.*, 90(7):076403.
- Lewenstein, M., Balcou, P., Ivanov, M. Y., L'Huillier, A., and Corkum, P. B. (1994). Theory of high-harmonic generation by low-frequency laser fields. *Phys. Rev. A*, 49(3):2117.
- Lewenstein, M., Kulander, K. C., Schafer, K. J., and Bucksbaum, P. H. (1995). Rings in above-threshold ionization: A quasiclassical analysis. *Phys. Rev. A*, 51(2):1495.
- Li, H., Mignolet, B., Wächter, G., Skruszewicz, S., Zherebtsov, S., Süßmann, F., Kessel, A., Trushin, S. A., Kling, N. G., Kübel, M., Ahn, B., Kim, D.,

- Ben-Iltzhak, I., Cocke, C. L., Fennel, T., Tiggesbäumker, J., Meiwes-Broer, K.-H., Lemell, C., Burgdörfer, J., Levine, R. D., Remacle, F., and Kling, M. F. (2014). Coherent electronic wave packet motion in C_{60} controlled by the waveform and polarization of few-cycle laser fields. *subm. to Phys. Rev.*
- Libisch, F., Huang, C., and Carter, E. A. (2014). Embedded correlated wavefunction schemes: Theory and applications. *Acc. Chem. Res.* doi:10.1021/ar500086h.
- Liebsch, A. (1997). *Electronic excitations at metal surfaces*. Plenum, New York.
- Liebsch, T., Plotzke, O., Heiser, F., Hergenhanh, U., Hemmers, O., Wehlitz, R., Viefhaus, J., Langer, B., Whitfield, S. B., and Becker, U. (1995). Angle-resolved photoelectron spectroscopy of C_{60} . *Phys. Rev. A*, 52(1):457.
- Lin, C. D., Le, A.-T., Chen, Z., Morishita, T., and Lucchese, R. (2010). Strong-field rescattering physics—self-imaging of a molecule by its own electrons. *J. Phys. B*, 43(12):122001.
- Liu, Y. and Zhang, X. (2011). Metamaterials: a new frontier of science and technology. *Chem. Soc. Rev.*, 40(5):2494.
- Lock, R. M., Ramakrishna, S., Zhou, X., Kapteyn, H. C., Murnane, M. M., and Seideman, T. (2012). Extracting continuum electron dynamics from high harmonic emission from molecules. *Phys. Rev. Lett.*, 108:133901.
- Luan, S., Hippler, R., Schwier, H., and Lutz, H. O. (1989). Electron emission from polycrystalline copper surfaces by multi-photon absorption. *Europhys. Lett.*, 9(5):489.
- Lupetti, M., Kling, M. F., and Scrinzi, A. (2013). Plasmon-enhanced attosecond-extreme ultraviolet source. *Phys. Rev. Lett.*, 110:223903.
- Madlener, T. (2014). Strong field photoemission from a nano-tip by two-color laser fields. (Project thesis, TU Wien).
- Maier, S. A. and Atwater, H. A. (2005). Plasmonics: Localization and guiding of electromagnetic energy in metal/dielectric structures. *J. Appl. Phys.*, 98(1):011101.
- Maiman, T. H. (1960). Stimulated optical radiation in ruby. *Nature*, 187(4736):493.
- Maitra, N. T., Burke, K., Appel, H., Gross, E. K. U., and van Leeuwen, R. (2002). Ten topical questions in time dependent density functional theory. In Sen, K. D., editor, *A celebration of the contributions of Robert Parr*, p. 1186. World Scientific, Singapore.
- Maksymov, I. S., Staude, I., Miroshnichenko, A. E., and Kivshar, Y. S. (2012). Optical Yagi-Uda nanoantennas. arxiv:1204.0330.
- Marini, A., Del Sole, R., and Rubio, A. (2003). Bound excitons in time-dependent density-functional theory: Optical and energy-loss spectra. *Phys. Rev. Lett.*, 91:256402.
- Marques, M. (2003). octopus: a first-principles tool for excited electron-ion dynamics. *Comput. Phys. Commun.*, 151(1):60.
- Marques, M. A. L. and Gross, E. K. U. (2004). Time-dependent density functional theory. *Ann. Rev. Phys. Chem.*, 55(1):427.
- Marques, M. A. L., Maitra, N. T., Nogueira, F. M. S., Gross, E. K. U., and Rubio, A., editors (2012). *Fundamentals of Time-Dependent Density Functional Theory*, volume 837 of *Lecture Notes in Physics*. Springer.
- Marques, M. A. L., Ullrich, C. A., Nogueira, F., Rubio, A., Burke, K., and Gross, E. K. U. (2006). *Time-Dependent Density Functional Theory*. Springer, Berlin, 2006 edition edition.
- Martin, Y. C., Hamann, H. F., and Wickramasinghe, H. K. (2001). Strength of the electric field in apertureless near-field optical microscopy. *J. Appl. Phys.*, 89(10):5774.
- Maurer, F., Dangwal, A., Lysenkov, D., Müller, G., Toimil-Molares, M. E., Trautmann, C., Brötz, J., and Fuess, H. (2006). Field emission of copper nanowires grown in polymer ion-track membranes. *Nucl. Instrum. Methods Phys. Res., Sect. B Beam Interactions with Materials and Atoms*, 245(1):337.
- Meckel, M., Comtois, D., Zeidler, D., Staudte, A., Pavičić, D., Bandulet, H. C., Pépin, H., Kieffer, J. C., Dörner, R., Villeneuve, D. M., and Corkum, P. B. (2008). Laser-induced electron tunneling and diffraction. *Science*, 320(5882):1478.
- Mendes, M. J., Tobias, I., Martí, A., and Luque, A. (2011). Light concentration in the near-field of dielectric spheroidal particles with mesoscopic sizes. *Opt. Express*, 19(17):16207.
- Mertens, H., Koenderink, A. F., and Polman, A. (2007). Plasmon-enhanced luminescence near noble-metal nanospheres: Comparison of exact theory and an improved Gersten and Nitzan model. *Phys. Rev. B*, 76(11):115123.
- Meyer, H.-D. (2012). Studying molecular quantum dynamics with the multiconfiguration time-dependent hartree method. *WIREs Comput. Mol. Sci.*, 2(2):351.
- Midorikawa, K. (2011). High-order harmonic generation and attosecond science. *Jpn. J. Appl. Phys.*, 50(9R):090001.
- Mignolet, B., Levine, R. D., and Remacle, F. (2014). Control of electronic dynamics visualized by angularly resolved photoelectron spectra: A dynamical simulation with an IR pump and XUV attosecond-pulse-train probe. *Phys. Rev. A*, 89(2):021403.
- Milosevic, D. B. (2006). Theoretical analysis of high-order harmonic generation from a coherent superposition of states. *J. Opt. Soc. Am. B*, 23(2):308.
- Milošević, D. B., Paulus, G. G., Bauer, D., and Becker, W. (2006). Above-threshold ionization by few-cycle pulses. *J. Phys. B*, 39(14):R203–R262.
- Mitrofanov, A. V., Verhoef, A. J., Serebryannikov, E. E., Lumeau, J., Glebov, L., Zheltikov, A. M., and Baltuška, A. (2011). Optical detection of attosecond ionization induced by a few-cycle laser field in a transparent dielectric material. *Phys. Rev. Lett.*, 106(14):147401.
- Mohan, S., Lange, J., Graener, H., and Seifert, G. (2012). Surface plasmon assisted optical nonlin-

- earities of uniformly oriented metal nano-ellipsoids in glass. *Opt. Express*, 20(27):28655.
- Morishita, T., Le, A. T., Chen, Z., and Lin, C. D. (2008). Accurate retrieval of structural information from laser-induced photoelectron and high-order harmonic spectra by few-cycle laser pulses. *Phys. Rev. Lett.*, 100(1):013903.
- Mortensen, J. J., Hansen, L. B., and Jacobsen, K. W. (2005). Real-space grid implementation of the projector augmented wave method. *Phys. Rev. B*, 71(3):035109.
- Mossotti, O. F. (1850). *Azioni e deformazioni nei dielettrici*, volume 49 of *Memorie die Matematica e di Fisica della Società Italiana delle Scienze Residente in Modena*.
- Moulton, P. F. (1986). Spectroscopic and laser characteristics of TiAl_2O_3 . *J. Opt. Soc. Am. B*, 3(1):125.
- Muñoz, R. D., Sánchez-Portal, D., Silkin, V. M., Chulkov, E. V., and Echenique, P. M. (2011). Time-dependent electron phenomena at surfaces. *Proc. Natl. Acad. Sci. U.S.A.*, 108(3):971.
- Mukherjee, S., Libisch, F., Large, N., Neumann, O., Brown, L. V., Cheng, J., Lassiter, J. B., Carter, E. A., Nordlander, P., and Halas, N. J. (2013). Hot electrons do the impossible: Plasmon-induced dissociation of H_2 on Au. *Nano Lett.*, 13(1):240.
- Mulser, P. and Bauer, D. (2010). Intense laser-atom interaction high power laser-matter interaction. volume 238 of *Springer Tracts in Modern Physics*, p. 267. Springer Berlin / Heidelberg, Berlin, Heidelberg.
- Münzer, H.-J., Mosbacher, M., Bertsch, M., Zimmermann, J., Leiderer, P., and Boneberg, J. (2001). Local field enhancement effects for nanostructuring of surfaces. *J. Microsc.*, 202(1):129.
- Nastos, F. and Sipe, J. E. (2006). Optical rectification and shift currents in GaAs and GaP response: Below and above the band gap. *Phys. Rev. B*, 74(3):035201.
- Nastos, F. and Sipe, J. E. (2010). Optical rectification and current injection in unbiased semiconductors. *Phys. Rev. B*, 82(23):235204.
- Nazarov, V., Pitarke, J., Takada, Y., Vignale, G., and Chang, Y. C. (2007). Including nonlocality in the exchange-correlation kernel from time-dependent current density functional theory: Application to the stopping power of electron liquids. *Phys. Rev. B*, 76(20):205103.
- Nazarov, V. U. and Vignale, G. (2011). Optics of semiconductors from meta-generalized-gradient-approximation-based time-dependent density-functional theory. *Phys. Rev. Lett.*, 107(21):216402.
- Neacsu, C. C., Reider, G. A., and Raschke, M. B. (2005). Second-harmonic generation from nanoscopic metal tips: Symmetry selection rules for single asymmetric nanostructures. *Phys. Rev. B*, 71(20):201402.
- Neidel, C., Klei, J., Yang, C.-H., Rouzée, A., Vrakking, M. J. J., Klünder, K., Miranda, M., Arnold, C. L., Fordell, T., L'Huillier, A., Gisselbrecht, M., Johnsson, P., Dinh, M. P., Suraud, E., Reinhard, P.-G., Despré, V., Marques, M. A. L., and Lépine, F. (2013). Probing time-dependent molecular dipoles on the attosecond time scale. *Phys. Rev. Lett.*, 111(3):033001.
- Neppel, S. et al. (2014). Direct observation of electron propagation and dielectric screening on the atomic length scale. *subm. to Nature*.
- Nest, M. (2010). Origin of dissipative dynamics in correlated few electron systems. *Chem. Phys.*, 370(1–3):119.
- Neuhauser, D. and Lopata, K. (2008). Quantum drude friction for time-dependent density functional theory. *J. Chem. Phys.*, 129(13):134106.
- Novotny, L. and van Hulst, N. (2011). Antennas for light. *Nat. Phot.*, 5(2):83.
- Olmon, R. L., Slovick, B., Johnson, T. W., Shelton, D., Oh, S.-H., Boreman, G. D., and Raschke, M. B. (2012). Optical dielectric function of gold. *Phys. Rev. B*, 86(23).
- Onida, G., Reining, L., and Rubio, A. (2002). Electronic excitations: density-functional versus many-body green's-function approaches. *Rev. Mod. Phys.*, 74(2):601.
- Osawa, E. and Yoshida, Z. (1971). *Aromaticity*, volume 22 of *Chemical Monograph Series*. Kagaku-dojin: Kyoto, Japan.
- Oskooi, A. F., Roundy, D., Ibanescu, M., Bermel, P., Joannopoulos, J. D., and Johnson, S. G. (2010). Meep: A flexible free-software package for electromagnetic simulations by the FDTD method. *Comput. Phys. Commun.*, 181(3):687.
- Otobe, T. (2012). First-principle description for the high-harmonic generation in a diamond by intense short laser pulse. *J. Appl. Phys.*, 111(9):093112.
- Otobe, T., Yabana, K., and Iwata, J. I. (2009). First-principles calculation of the electron dynamics in crystalline SiO_2 . *J. Phys. Condens. Matter*, 21(6):064224.
- Otobe, T., Yamagiwa, M., Iwata, J. I., Yabana, K., Nakatsukasa, T., and Bertsch, G. F. (2008). First-principles electron dynamics simulation for optical breakdown of dielectrics under an intense laser field. *Phys. Rev. B*, 77:165104.
- Paasch-Colberg, T., Schiffrin, A., Karpowicz, N., Kruchinin, S., Saqlam, Ö., Keiber, S., Razskazovskaya, O., Mühlbrandt, S., Alnaser, A., Kübel, M., Apalkov, V., Gerster, D., Reichert, J., Wittmann, T., Barth, J. V., Stockman, M. I., Ernstorf, R., Yakovlev, V. S., Kienberger, R., and Krausz, F. (2014). Solid-state light-phase detector. *Nat. Phot.*, 8(3):214.
- Palik, E. D. (1991). *Handbook of optical constants of solids II*. Academic Press.
- Park, D. J., Piglosiewicz, B., Schmidt, S., Kollmann, H., Mascheck, M., and Lienau, C. (2012). Strong field acceleration and steering of ultrafast electron pulses from a sharp metallic nanotip. *Phys. Rev. Lett.*, 109:244803.
- Parr, R. G. (1994). *Density-Functional Theory of Atoms and Molecules*. Oxford University Press, New York; Oxford England.
- Parr, R. G. and Sen, K. D. (2002). *Reviews of Modern Quantum Chemistry: A Celebration of the Contri-*

- butions of Robert G. Parr. Volumes I & II.* World Scientific Pub Co Inc, River Edge, NJ.
- Paulus, G. G., Becker, W., Nicklich, W., and Walther, H. (1994). Rescattering effects in above-threshold ionization: a classical model. *J. Phys. B*, 27(21):L703–L708.
- Paulus, G. G., Grasbon, F., Walther, H., Kopold, R., and Becker, W. (2002). Identification and application of quantum trajectories in above-threshold ionization. *Laser Phys.*, 12:262.
- Paulus, G. G., Lindner, F., Walther, H., Baltuška, A., Goulielmakis, E., Lezius, M., and Krausz, F. (2003). Measurement of the phase of few-cycle laser pulses. *Phys. Rev. Lett.*, 91(25):253004.
- Pazourek, R., Feist, J., Nagele, S., and Burgdörfer, J. (2012). Attosecond streaking of correlated two-electron transitions in helium. *Phys. Rev. Lett.*, 108:163001.
- Pazourek, R., Nagele, S., and Burgdörfer, J. (2014). Attosecond chronoscopy in photoemission. *Rev. Mod. Phys.* (subm.).
- Perdew, J. P. and Zunger, A. (1981). Self-interaction correction to density-functional approximations for many-electron systems. *Phys. Rev. B*, 23(10):5048.
- Pfeifer, T., Abel, M. J., Nagel, P. M., Jullien, A., Loh, Z.-H., Justine Bell, M., Neumark, D. M., and Leone, S. R. (2008). Time-resolved spectroscopy of attosecond quantum dynamics. *Chem. Phys. Lett.*, 463(1-3):11.
- Pfeiffer, A. N., Cirelli, C., Smolarski, M., Dimitrovski, D., Abu-samha, M., Madsen, L. B., and Keller, U. (2012). Attoclock reveals natural coordinates of the laser-induced tunnelling current flow in atoms. *Nat. Phys.*, 8(1):76.
- Pfullmann, N., Waltermann, C., Noack, M., Rausch, S., Nagy, T., Reinhardt, C., Kovačev, M., Knittel, V., Bratschitsch, R., Akemeier, D., Hütten, A., Leitenstorfer, A., and Morgner, U. (2013). Bow-tie nanoantenna assisted generation of extreme ultraviolet radiation. *New J. Phys.*, 15(9):093027.
- Philipp, H. R. (1966). Optical transitions in crystalline and fused quartz. *Solid State Commun.*, 4(1):73.
- Piglosiewicz, B., Schmidt, S., Park, D. J., Vogelsang, J., Groß, P., Manzoni, C., Farinello, P., Cerullo, G., and Lienau, C. (2014). Carrier-envelope phase effects on the strong-field photoemission of electrons from metallic nanostructures. *Nat. Phot.*, 8(1):37.
- Pitarke, J. M. and Eguiluz, A. G. (2001). Jellium surface energy beyond the local-density approximation: Self-consistent-field calculations. *Phys. Rev. B*, 63(4):045116.
- Pohl, A., Reinhard, P. G., and Suraud, E. (2000). Towards single-particle spectroscopy of small metal clusters. *Phys. Rev. Lett.*, 84(22):5090.
- Pohl, A., Reinhard, P. G., and Suraud, E. (2001). Influence of intermediate states on photoelectron spectra. *J. Phys. B*, 34(24):4969.
- Pohl, A., Reinhard, P. G., and Suraud, E. (2003). Photoelectron spectra from K and Na clusters. *Phys. Rev. A*, 68(5):053202.
- Pohl, A., Reinhard, P. G., and Suraud, E. (2004). Angular distribution of electrons emitted from Na clusters. *Phys. Rev. A*, 70(2):023202.
- Popmintchev, T., Chen, M.-C., Popmintchev, D., Arpin, P., Brown, S., Ališauskas, S., Andriukaitis, G., Balčiūnas, T., Mücke, O. D., Pugzlys, A., Baltuška, A., Shim, B., Schrauth, S. E., Gaeta, A., Hernández-García, C., Plaja, L., Becker, A., Jaron-Becker, A., Murnane, M. M., and Kapteyn, H. C. (2012). Bright coherent ultrahigh harmonics in the keV x-ray regime from mid-infrared femtosecond lasers. *Science*, 336(6086):1287.
- Popov, V. (1999). Energy and angular distributions of photoelectrons in multiphoton ionization. *JETP Letters*, 70(8):502.
- Purcell, E. M. and Morin, D. J. (2013). *Electricity and Magnetism*. Cambridge University Press.
- Quong, A. A. and Pederson, M. R. (1992). Density-functional-based linear and nonlinear polarizabilities of fullerene and benzene molecules. *Phys. Rev. B*, 46(19):12906.
- Ramsden, J. D. and Godby, R. W. (2012). Exact density-functional potentials for time-dependent quasiparticles. *Phys. Rev. Lett.*, 109:036402.
- Reid, M. T. H. and Johnson, S. G. (2013). Efficient computation of power, force, and torque in BEM scattering calculations. arxiv:1307.2966.
- Reid, M. T. H., White, J., and Johnson, S. G. (2013). Fluctuating surface currents: An algorithm for efficient prediction of casimir interactions among arbitrary materials in arbitrary geometries. *Phys. Rev. A*, 88(2).
- Reiter, F., Graf, U., Schultze, M., Schweinberger, W., Schröder, H., Karpowicz, N., Azzeer, A. M., Kienberger, R., Krausz, F., and Goulielmakis, E. (2010). Generation of sub-3 fs pulses in the deep ultraviolet. *Opt. Lett.*, 35(13):2248.
- Resta, R. and Vanderbilt, D. (2007). Theory of polarization: A modern approach. In *Physics of Ferroelectrics*, number 105 in Topics in Applied Physics, p. 31. Springer Berlin Heidelberg.
- Rioux, F. (1994). Quantum mechanics, group theory, and C_{60} . *J. Chem. Educ.*, 71(6):464.
- Ropers, C., Solli, D. R., Schulz, C. P., Lienau, C., and Elsaesser, T. (2007). Localized multiphoton emission of femtosecond electron pulses from metal nanotips. *Phys. Rev. Lett.*, 98(4):043907.
- Rozzi, C. A., Falke, S. M., Spallanzani, N., Rubio, A., Molinari, E., Brida, D., Maiuri, M., Cerullo, G., Schramm, H., Christoffers, J., and Lienau, C. (2013). Quantum coherence controls the charge separation in a prototypical artificial light-harvesting system. *Nat Commun*, 4:1602.
- Rubio, A., Alonso, J. A., López, J. M., and Stott, M. J. (1994). Collective electronic excitations in metal-coated C_{60} . *Phys. Rev. B*, 49(24):17397.
- Ruggenthaler, M., Popruzhenko, S. V., and Bauer, D. (2008). Recollision-induced plasmon excitation in strong laser fields. *Phys. Rev. A*, 78:033413.
- Runge, E. and Gross, E. K. U. (1984). Density-functional theory for time-dependent systems. *Phys. Rev. Lett.*, 52(12):997.

- Saito, Y. and Uemura, S. (2000). Field emission from carbon nanotubes and its application to electron sources. *Carbon*, 38(2):169.
- Salvat, F., Jablonski, A., and Powell, C. J. (2005). elsepa—Dirac partial-wave calculation of elastic scattering of electrons and positrons by atoms, positive ions and molecules. *Comput. Phys. Commun.*, 165(2):157.
- Sarid, D. and Challener, W. (2010). *Modern Introduction to Surface Plasmons: Theory, Mathematica Modeling, and Applications*. Cambridge University Press.
- Sato, S. A. and Yabana, K. (2014). Efficient basis expansion for describing linear and non-linear electron dynamics in crystalline solids. *arXiv:1404.5118*.
- Sato, S. A., Yabana, K., Shinohara, Y., Otobe, T., and Bertsch, G. F. (2014). Numerical pump-probe experiments of laser-excited silicon in nonequilibrium phase. *Phys. Rev. B*, 89(6):064304.
- Savage, K. J., Hawkeye, M. M., Esteban, R., Borisov, A. G., Aizpurua, J., and Baumberg, J. J. (2012). Revealing the quantum regime in tunnelling plasmonics. *Nature*, 491(7425):574.
- Schafer, K. J., Yang, B., DiMauro, L. F., and Kulan-der, K. C. (1993). Above threshold ionization beyond the high harmonic cutoff. *Phys. Rev. Lett.*, 70(11):1599.
- Schenk, M., Krüger, M., and Hommelhoff, P. (2010). Strong-field above-threshold photoemission from sharp metal tips. *Phys. Rev. Lett.*, 105(25):257601.
- Schiffrin, A., Paasch-Colberg, T., Karpowicz, N., Apalkov, V., Gerster, D., Muhlbrandt, S., Korbman, M., Reichert, J., Schultze, M., Holzner, S., Barth, J. V., Kienberger, R., Ernstorfer, R., Yakovlev, V. S., Stockman, M. I., and Krausz, F. (2013). Optical-field-induced current in dielectrics. *Nature*, 493(7430):70.
- Schiffrin, A., Paasch-Colberg, T., Karpowicz, N., Apalkov, V., Gerster, D., Muhlbrandt, S., Korbman, M., Reichert, J., Schultze, M., Holzner, S., Barth, J. V., Kienberger, R., Ernstorfer, R., Yakovlev, V. S., Stockman, M. I., and Krausz, F. (2014). Addendum: Optical-field-induced current in dielectrics. *Nature*, 507(7492):386.
- Schlegel, V. (1883). *Theorie der homogen zusammengesetzten Raumgebilde*. Nova acta Academiae Caesareae Leopoldino-Carolinae Germanicae Naturae Curiosorum Kaiserlich-Leopoldinisch-Carolinische Deutsche Akademie der Naturforscher 1757.
- Schlipper, R., Kusche, R., von Issendorff, B., and Haberland, H. (1998). Multiple excitation and lifetime of the sodium cluster plasmon resonance. *Phys. Rev. Lett.*, 80(6):1194.
- Schubert, O., Hohenleutner, M., Langer, F., Urbanek, B., Lange, C., Huttner, U., Golde, D., Meier, T., Kira, M., Koch, S. W., and Huber, R. (2014). Sub-cycle control of terahertz high-harmonic generation by dynamical Bloch oscillations. *Nat. Phot.*, 8(2):119.
- Schultze, M., Bothschafter, E. M., Sommer, A., Holzner, S., Schweinberger, W., Fiess, M., Hofstetter, M., Kienberger, R., Apalkov, V., Yakovlev, V. S., Stockman, M. I., and Krausz, F. (2013). Controlling dielectrics with the electric field of light. *Nature*, 493(7430):75.
- Schultze, M., Fieß, M., Karpowicz, N., Gagnon, J., Korbman, M., Hofstetter, M., Neppl, S., Cavalieri, A. L., Komninos, Y., Mercouris, T., Nicolaides, C. A., Pazourek, R., Nagele, S., Feist, J., Burgdörfer, J., Azzeer, A. M., Ernstorfer, R., Kienberger, R., Kleineberg, U., Goulielmakis, E., Krausz, F., and Yakovlev, V. S. (2010). Delay in photoemission. *Science*, 328(5986):1658.
- Serena, P. A., Soler, J. M., and García, N. (1988). Work function and image-plane position of metal surfaces. *Phys. Rev. B*, 37(15):8701.
- Shafir, D., Soifer, H., Bruner, B. D., Dagan, M., Mairesse, Y., Patchkovskii, S., Ivanov, M. Y., Smirnova, O., and Dudovich, N. (2012). Resolving the time when an electron exits a tunnelling barrier. *Nature*, 485(7398):343.
- Sheikholeslami, S., Jun, Y.-w., Jain, P. K., and Alivisatos, A. P. (2010). Coupling of optical resonances in a compositionally asymmetric plasmonic nanoparticle dimer. *Nano Lett.*, 10(7):2655.
- Shi, N. and Ramprasad, R. (2005). Dielectric properties of ultrathin SiO₂ slabs. *Appl. Phys. Lett.*, 87(26):262102.
- Shi, N. and Ramprasad, R. (2006). Atomic-scale dielectric permittivity profiles in slabs and multilayers. *Phys. Rev. B*, 74(4):045318.
- Shih, T., Winkler, M. T., Voss, T., and Mazur, E. (2009). Dielectric function dynamics during femtosecond laser excitation of bulk ZnO. *Appl. Phys. A*, 96(2):363.
- Shiner, A. D., Schmidt, B. E., Trallero-Herrero, C., Worner, H. J., Patchkovskii, S., Corkum, P. B., Kieffer, J. C., Legare, F., and Villeneuve, D. M. (2011). Probing collective multi-electron dynamics in xenon with high-harmonic spectroscopy. *Nat. Phys.*, 7(6):464.
- Shinohara, Y., Sato, S. A., Yabana, K., Iwata, J. I., Otobe, T., and Bertsch, G. F. (2012a). Nonadiabatic generation of coherent phonons.
- Shinohara, Y., Sato, S. A., Yabana, K., Iwata, J.-I., Otobe, T., and Bertsch, G. F. (2012b). Nonadiabatic generation of coherent phonons. *J. Chem. Phys.*, 137(22):22A527.
- Shinohara, Y., Yabana, K., Kawashita, Y., Iwata, J.-I., Otobe, T., and Bertsch, G. F. (2010). Coherent phonon generation in time-dependent density functional theory. *Phys. Rev. B*, 82(15):155110.
- Sipe, J. E. and Shkrebtii, A. I. (2000). Second-order optical response in semiconductors. *Phys. Rev. B*, 61(8):5337.
- Sirotti, F., Beaulieu, N., Bendounan, A., Sully, M. G., Chauvet, C., Malinowski, G., Fratesi, G., Véniard, V., and Onida, G. (2014). Multiphoton k-resolved photoemission from gold surface states with 800-nm femtosecond laser pulses. *Phys. Rev. B*, 90(3):035401.

- Sivis, M., Duwe, M., Abel, B., and Ropers, C. (2012). Nanostructure-enhanced atomic line emission. *Nature*, 485(7397):E1–E3.
- Skopalová, E., Lei, D. Y., Witting, T., Arrell, C., Frank, F., Sonnefraud, Y., Maier, S. A., Tisch, J. W. G., and Marangos, J. P. (2011). Numerical simulation of attosecond nanoplasmonic streaking. *New J. Phys.*, 13(8):083003.
- Smith, F. T. (1960). Lifetime matrix in collision theory. *Phys. Rev.*, 118(1):349.
- Sonntag, M. D., Pozzi, E. A., Jiang, N., Hersam, M. C., and Van Duyne, R. P. (2014). Recent advances in tip-enhanced raman spectroscopy. *J. Phys. Chem. Lett.*, 5(18):3125.
- Soukoulis, C. M. (2002). The history and a review of the modelling and fabrication of photonic crystals. *Nanotechnology*, 13(3):420.
- Sparks, M., Mills, D. L., Warren, R., Holstein, T., Maradudin, A. A., Sham, L. J., Loh, E., and King, D. F. (1981). Theory of electron-avalanche breakdown in solids. *Phys. Rev. B*, 24(6):3519.
- Stella, L., Zhang, P., García-Vidal, F. J., Rubio, A., and García-González, P. (2013). Performance of nonlocal optics when applied to plasmonic nanostructures. *J. Phys. Chem. C*, 117(17):8941.
- Stockman, M. I. (2004). Nanofocusing of optical energy in tapered plasmonic waveguides. *Phys. Rev. Lett.*, 93(13):137404.
- Stockman, M. I. and Hewageegana, P. (2007). Absolute phase effect in ultrafast optical responses of metal nanostructures. *Appl. Phys. A*, 89(2):247.
- Stockman, M. I., Kling, M. F., Kleineberg, U., and Krausz, F. (2007). Attosecond nanoplasmonic-field microscope. *Nat. Phot.*, 1(9):539.
- Stolow, A., Bragg, A. E., and Neumark, D. M. (2004). Femtosecond time-resolved photoelectron spectroscopy. *Chem. Rev.*, 104(4):1719.
- Sturman, P. J. (1992). *Photovoltaic and Photo-refractive Effects in Noncentrosymmetric Materials*. CRC Press.
- Süssmann, F. and Kling, M. F. (2011). Attosecond nanoplasmonic streaking of localized fields near metal nanospheres. *Phys. Rev. B*, 84:121406.
- Swanwick, M. E., Keathley, P. D., Fallahi, A., Krogen, P. R., Laurent, G., Moses, J., Kärtner, F. X., and Velásquez-García, L. F. (2014). Nanostructured ultrafast silicon-tip optical field-emitter arrays. *Nano Lett.*, 14(9):5035.
- Szipöcs, R., Spielmann, C., Krausz, F., and Ferencz, K. (1994). Chirped multilayer coatings for broadband dispersion control in femtosecond lasers. *Opt. Lett.*, 19(3):201.
- Taflove, A. and Hagness, S. C. (2005). *Computational Electrodynamics: The Finite-Difference Time-Domain Method, Third Edition*. Artech House, 3 edition. Published: Hardcover.
- Tang, Z. and Wei, A. (2012). Fabrication of anisotropic metal nanostructures using innovations in template-assisted lithography. *ACS Nano*, 6(2):998.
- Thiele, M. and Kümmel, S. (2014). Frequency dependence of the exact exchange-correlation kernel of time-dependent density-functional theory. *Phys. Rev. Lett.*, 112:083001.
- Thomas, S., Krüger, M., Förster, M., Schenk, M., and Hommelhoff, P. (2013). Probing of optical near-fields by electron rescattering on the 1 nm scale. *Nano Lett.* doi:10.1021/nl402407r.
- Tran, F. and Blaha, P. (2009). Accurate band gaps of semiconductors and insulators with a semilocal exchange-correlation potential. *Phys. Rev. Lett.*, 102:226401.
- Troullier, N. and Martins, J. L. (1991). Efficient pseudopotentials for plane-wave calculations. *Phys. Rev. B*, 43(3):1993.
- Uda, S. (1927). High angle radiation of short electric waves. *Proceedings of the Institute of Radio Engineers*, 15(5):377.
- Uiberacker, M., Uphues, T., Schultze, M., Verhoef, A. J., Yakovlev, V., Kling, M. F., Rauschenberger, J., Kabachnik, N. M., Schröder, H., Lezius, M., Kompa, K. L., Müller, H.-G., Vrakking, M. J. J., Hendel, S., Kleineberg, U., Heinzmann, U., Drescher, M., and Krausz, F. (2007). Attosecond real-time observation of electron tunnelling in atoms. *Nature*, 446(7136):627.
- Ullrich, C. A. (2011). *Time-Dependent Density-Functional Theory: Concepts and Applications*. Oxford Graduate Texts.
- Ullrich, C. A. and Tokatly, I. V. (2006). Nonadiabatic electron dynamics in time-dependent density-functional theory. *Phys. Rev. B*, 73:235102.
- Ullrich, C. A. and Vignale, G. (2002). Time-dependent current-density-functional theory for the linear response of weakly disordered systems. *Phys. Rev. B*, 65(24):245102.
- Vampa, G., McDonald, C. R., Orlando, G., Klug, D. D., Corkum, P. B., and Brabec, T. (2014). Theoretical analysis of high-harmonic generation in solids. *Phys. Rev. Lett.*, 113(7):073901.
- van Leeuwen, R. (1999). Mapping from densities to potentials in time-dependent density-functional theory. *Phys. Rev. Lett.*, 82(19):3863.
- van Leeuwen, R. (2004). First-principles approach to the electron-phonon interaction. *Phys. Rev. B*, 69(11):115110.
- Verhoef, A. J., Mitrofanov, A. V., Serebryannikov, E. E., Kartashov, D. V., Zheltikov, A. M., and Baltuška, A. (2010). Optical detection of tunneling ionization. *Phys. Rev. Lett.*, 104(16):163904.
- Vignale, G. (2004). Mapping from current densities to vector potentials in time-dependent current density functional theory. *Phys. Rev. B*, 70(20):201102.
- Vignale, G. and Kohn, W. (1996). Current-dependent exchange-correlation potential for dynamical linear response theory. *Phys. Rev. Lett.*, 77(10):2037.
- Vignale, G., Ullrich, C. A., and Conti, S. (1997). Time-dependent density functional theory beyond the adiabatic local density approximation. *Phys. Rev. Lett.*, 79:4878.
- Vincent, R., Juaristi, J. I., and Apell, P. (2011). *Geometry and Surface Plasmon energy*.

- Volkov, D. M. (1935). Über eine Klasse von Lösungen der Diracschen Gleichung. *Z. Physik*, 94(3-4):250.
- von Freymann, G., Kitaev, V., Lotsch, B. V., and Ozin, G. A. (2013). Bottom-up assembly of photonic crystals. *Chem. Soc. Rev.* 42(7):2528.
- Vozzi, C., Negro, M., Calegari, F., Sansone, G., Nisoli, M., De Silvestri, S., and Stagira, S. (2011). Generalized molecular orbital tomography. *Nat. Phys.*, 7(10):822.
- Wachter, G., Lemell, C., and Burgdoerfer, J. (2013). Electron rescattering at metal nanotips induced by ultrashort laser pulses. arxiv:1308.1225 / *J. Phys.: Conf. Ser.* 488 012005 (2014), DOI: 10.1088/1742-6596/488/1/012005.
- Wachter, G., Lemell, C., and Burgdörfer, J. (2012). Electron emission from a metal nano-tip by ultrashort laser pulses. *J. Phys. Conf. Ser.*, 399(1):012010.
- Wachter, G., Lemell, C., and Burgdörfer, J. (2014a). Electron rescattering at metal nanotips induced by ultrashort laser pulses. *J. Phys.: Conf. Ser.*, 488(1):012005.
- Wachter, G., Lemell, C., Burgdörfer, J., Sato, S. A., Tong, X.-M., and Yabana, K. (2014b). Ab initio simulation of electrical currents induced by ultrafast laser excitation of dielectric materials. *Phys. Rev. Lett.*, 113(8):087401.
- Wais, M. (2014). Time-resolved photoemission from endohedral fullerenes using attosecond streaking. (Project thesis, TU Wien).
- Wakui, S., Nakamura, J., and Natori, A. (2008). Atomic scale dielectric constant near the SiO₂/Si(001) interface. *J. Vac. Sci. Technol., B*, 26(4):1579.
- Walter, M., Häkkinen, H., Lehtovaara, L., Puska, M., Enkovaara, J., Rostgaard, C., and Mortensen, J. J. (2008). Time-dependent density-functional theory in the projector augmented-wave method. *J. Chem. Phys.*, 128(24):244101.
- Wang, R., Hou, D., and Zheng, X. (2013). Time-dependent density-functional theory for real-time electronic dynamics on material surfaces. *Phys. Rev. B*, 88(20):205126.
- Wang, Y. and Cheng, L. T. (1992). Nonlinear optical properties of fullerenes and charge-transfer complexes of fullerenes. *J. Phys. Chem.*, 96(4):1530.
- Wiener, A., Fernández-Domínguez, A. I., Horsfield, A. P., Pendry, J. B., and Maier, S. A. (2012). Non-local effects in the nanofocusing performance of plasmonic tips. *Nano Lett.*, 12(6):3308.
- Wigner, E. P. (1955). Lower limit for the energy derivative of the scattering phase shift. *Phys. Rev.*, 98(1):145.
- Wijewardane, H. O. and Ullrich, C. A. (2005). Time-dependent Kohn-Sham theory with memory. *Phys. Rev. Lett.*, 95:086401.
- Williams, R. (1965). Photoemission of electrons from silicon into silicon dioxide. *Phys. Rev.*, 140(2A):A569.
- Wimmer, L., Herink, G., Solli, D. R., Yalunin, S. V., Echterkamp, K. E., and Ropers, C. (2014). Terahertz control of nanotip photoemission. *Nat. Phys.*, 10(6):432.
- Windt, D. L., Cash, W. C., Scott, M., Arendt, P., Newnam, B., Fisher, R. F., and Swartzlander, A. B. (1988). Optical constants for thin films of Ti, Zr, Nb, Mo, Ru, Rh, Pd, Ag, Hf, Ta, W, Re, Ir, Os, Pt, and Au from 24 Å to 1216 Å. *Appl. Opt.*, 27(2):246.
- Wirth, A., Th, Grguraš, I., Gagnon, J., Moulet, A., Luu, T. T., Pabst, S., Santra, R., Alahmed, Z. A., Azzeer, A. M., Yakovlev, V. S., Pervak, V., Krausz, F., and Goulielmakis, E. (2011). Synthesized light transients. *Science*, 334(6053):195.
- Wittmann, T., Horvath, B., Helml, W., Schatzel, M. G., Gu, X., Cavalieri, A. L., Paulus, G. G., and Kienberger, R. (2009). Single-shot carrier-envelope phase measurement of few-cycle laser pulses. *Nat. Phys.*, 5(5):357.
- Xie, X., Roither, S., Kartashov, D., Persson, E., Arbó, D. G., Zhang, L., Gräfe, S., Schöffler, M. S., Burgdörfer, J., Baltuška, A., and Kitzler, M. (2012). Attosecond probe of valence-electron wave packets by subcycle sculpted laser fields. *Phys. Rev. Lett.*, 108:193004.
- Yabana, K. and Bertsch, G. F. (1993). Electronic structure of C₆₀ in a spherical basis. *Phys. Scr.*, 48(5):633.
- Yabana, K. and Bertsch, G. F. (1996). Time-dependent local-density approximation in real time. *Phys. Rev. B*, 54(7):4484.
- Yabana, K., Nakatsukasa, T., lwata, J.-I., and Bertsch, G. F. (2006). Real-time, real-space implementation of the linear response time-dependent density-functional theory. *Phys. Status. Solidi B*, 243(5):1121.
- Yabana, K., Sugiyama, T., Shinohara, Y., Ootobe, T., and Bertsch, G. F. (2012). Time-dependent density functional theory for strong electromagnetic fields in crystalline solids. *Phys. Rev. B*, 85(4):045134.
- Yamamoto, S., Saitou, N., and Fukuhara, S. (1978). Field emission current instability induced by migrating atoms on W(310) surface. *Surf. Sci.*, 71(1):191.
- Yasumatsu, H., Kondow, T., Kitagawa, H., Tabayashi, K., and Shobatake, K. (1996). Absorption spectrum of C₆₀ in the gas phase: Autoionization via core-excited rydberg states. *J. Chem. Phys.*, 104(3):899.
- Young, S. M., Zheng, F., and Rappe, A. M. (2012). First-principles calculation of the bulk photovoltaic effect in bismuth ferrite. *Phys. Rev. Lett.*, 109(23):236601.
- Yudin, G. L. and Ivanov, M. Y. (2001). Nonadiabatic tunnel ionization: Looking inside a laser cycle. *Phys. Rev. A*, 64(1):013409.
- Zaks, B., Liu, R. B., and Sherwin, M. S. (2012). Experimental observation of electron-hole recollisions. *Nature*, 483(7391):580.
- Zanghellini, J., Jungreuthmayer, C., and Brabec, T. (2006). Plasmon signatures in high harmonic generation. *J. Phys. B*, 39(3):709.
- Zhang, P., Feist, J., Rubio, A., Garcia-Gonzalez, P., and Garcia-Vidal, F. J. (2014). Ab-initio nanoplasmonics: atoms matter. arXiv:1403.8016 .

- Zhang, W., Cui, X., and Martin, O. J. F. (2009). Local field enhancement of an infinite conical metal tip illuminated by a focused beam. *J. Raman Spectrosc.*, 40(10):1338.
- Zhao, J., Frank, B., Neubrech, F., Zhang, C., Braun, P. V., and Giessen, H. (2014). Hole-mask colloidal nanolithography combined with tilted-angle-rotation evaporation: A versatile method for fabrication of low-cost and large-area complex plasmonic nanostructures and metamaterials. *Beilstein J. Nanotechnol.*, 5:577.
- Zheng, X., Chen, G., Li, Z., Deng, S., and Xu, N. (2004). Quantum-mechanical investigation of field-emission mechanism of a micrometer-long single-walled carbon nanotube. *Phys. Rev. Lett.*, 92(10):106803.
- Zherebtsov, S., Fennel, T., Plenge, J., Antonsson, E., Znakovskaya, I., Wirth, A., Herrwerth, O., Suszmann, F., Peltz, C., Ahmad, I., Trushin, S. A., Pervak, V., Karsch, S., Vrakking, M. J. J., Langer, B., Graf, C., Stockman, M. I., Krausz, F., Rühl, E., and Kling, M. F. (2011). Controlled near-field enhanced electron acceleration from dielectric nanospheres with intense few-cycle laser fields. *Nat. Phys.*, 7(8):656.
- Zherebtsov, S., Süßmann, F., Peltz, C., Plenge, J., Betsch, K. J., Znakovskaya, I., Alnaser, A. S., Johnson, N. G., Kübel, M., Horn, A., Mondes, V., Graf, C., Trushin, S. A., Azzeer, A., Vrakking, M. J. J., Paulus, G. G., Krausz, F., Rühl, E., Fennel, T., and Kling, M. F. (2012). Carrier-envelope phase-tagged imaging of the controlled electron acceleration from SiO₂ nanospheres in intense few-cycle laser fields. *New J. Phys.*, 14(7):075010.
- Zope, R. R., Baruah, T., Pederson, M. R., and Dunlap, B. I. (2008). Static dielectric response of icosahedral fullerenes from C₆₀ to C₂₁₆₀ characterized by an all-electron density functional theory. *Phys. Rev. B*, 77:115452.
- Zuloaga, J., Prodan, E., and Nordlander, P. (2009). Quantum description of the plasmon resonances of a nanoparticle dimer. *Nano Lett.*, 9(2):887.
- Zuloaga, J., Prodan, E., and Nordlander, P. (2010). Quantum plasmonics: Optical properties and tunability of metallic nanorods. *ACS Nano*, 4(9):5269.

Acknowledgments

During my PhD I had the pleasure to learn from many people contributing to the success of this work. I hope to cover the most important ones in the following non-exhaustive list. Complementarily, a statistical overview of the scientist population I encountered is given in appendix B.

The most important person enabling success of the thesis was my advisor *Joachim Burgdörfer*. Perhaps first among the many things I am indebted to him for is that he agreed to give me money to pursue research on “something with lasers” (the working topic of my thesis for about a year) so that I could make a living from doing science for a while. He made sure I had ample opportunity to interact with people and learn new things by encouraging me to apply to the Max Planck research school, sending me to conferences including three invited talks, and he found ways and means to initiate collaborations with people we became interested in. He upheld scientific standards, which in contrast to the current fashion lead not to publication “pressure” but to publication “suction”, in the end producing high quality work that I am proud of. I have learned a tremendous amount from his deep understanding of presentation and language, from giving talks and lectures to writing papers, and I admire his cut-and-paste technique and work ethic. I most thank him for taking time to sit down and think when it was necessary, and for letting me do what I wanted otherwise.

It was a pleasure to work in *Joachim’s group*. The administrative staff (*Heike Höller*, *Elfriede Mössmer*, and *Sylvia Riedler*) made sure everything went smoothly. The inspiring scientists provided a very productive environment. I thank everyone for the open atmosphere, the countless interchanges and talks, much technical assistance, and the formidable lunch breaks with coffee and chocolate.

I especially would like to thank *Christoph Lemell* who first attracted me to the group – mainly by his personality – and advised me during my master thesis. To my knowledge, he does physic faster than anyone who does it better, and better than anyone who does it faster. I know he will appreciate the compliment. He was very supportive and first acquainted me with TD-DFT. I am continually amazed by his gut feeling for orders of magnitude. He is the main investigator of surface streaking (section 3.7).

I thank *Paul Tiwald* for great companionship in the offices we inhabited, and for leading our musical pastimes as well as in the “team-building” events organized with *Larisa Chizhova* that included barbecue. Paul, Larisa, and *Katharina Doblhoff-Dier* were wonderful colleagues and I had great fun at our lectures at *Kinderuni* building motors with children. I enjoyed working with *Renate Pazourek*, *Stefan Nagele*, and *Iva Březinová* pursuing adventures in atomic physics, and Stefan originally got me interested in C_{60} and streaking. All of them were also great travel partners on the occasional field trip to a Bavarian castle or to Beijing.

I learned a lot from *Steffi Gräfe*, who became a professor in Jena in 2012 and is missed dearly in our group. With her unparalleled knowledge of the literature and the community, she was my guide to the world of attosecond physics.

A warm thank you goes to the bachelor and project students whom I had the pleasure to advise or co-advise. *Michael Wais* worked on C_{60} (chapter 5), *Julian Huber* on non-sequential double ionization, *Hao Yin* on laser-cluster interaction, and *Thomas Madlener* found interesting physics in electron emission from tips by two-color pulses [Madlener, 2014]. I thank them for their enthusiasm and willingness to join our work group instead of taking the path of least resistance, hopefully to our mutual benefit.

Turning to people outside Joachim's group, I thank the *International Max Planck Research School for Advanced Photon Science (IMPRS-APS)*, who awarded me a stipend to pursue science. The IMPRS was vital to the success of my thesis allowing me to meet inspiring peers and establish a scientific network and collaborations. I especially thank the main organizing force, *Ms. Monika Wild*, for the countless meetings and visits, and also coordinators *Peter Hommelhoff*, *Vlad Yakovlev*, *Nick Karpowics*, and *Matthias Kling*. Mostly Frau Wild though.

I had the pleasure to collaborate with and learn from leading experts from external institutions. First, I would like to thank *Kazuhiro Yabana*, *Xiao-Min Tong* and *Shunsuke A. Sato* from Tsukuba who were great hosts during my visits to Japan. From them I learned most of the things I know about TD-DFT in theory and in practice. Chapters 4 and 5 would have been impossible without their expertise and help.

A special thanks goes to *Peter Hommelhoff* and his group at MPQ and now in Erlangen including *Michael Krüger*, *Markus Schenk*, *Michael Förster*, *Sebastian Thomas*, and *Lothar Maisenbacher*. Peter introduced us to nano-tips (chapters 2 and 3) and we closely collaborated throughout my PhD to publish papers, discuss fresh results, and explore new ideas. Peter's unshakable enthusiasm and positive can-do attitude made a lasting impression on me. I also thank his group for providing the experimental data in chapter 3.

Further thanks go to *Ferenc Krausz*, *Mark Stockman*, and *Vlad Yakovlev* from MPQ Garching and Georgia State in Atlanta for their ideas and suggestions on nonlinear interaction of laser pulses with dielectrics (chapter 4) as well as the experimentalists who provided insight into ongoing projects: *Nick Karpowics*, *Annkatrin Sommer*, *Sabine Keiber*, and *Elisabeth Bothschafter*.

I had the pleasure to work with *Fritz Aumayr* and his group at TU Wien on ion-surface interactions. Fritz was immensely supportive from the beginning – he took me along to my first conference, an ITS-LEIF meeting in Spain – and was my guide to the ion beam community. Work begun during my master thesis lead to joint publications and even an invited talk at his favorite conference, the IISC, which was a great pleasure.

I would like to thank *Károly Tökési* from Atomki Debrecen for being a great host during my visits to Hungary including an enthusiastic tennis match, and for countless entertaining discussions in Debrecen and during his frequent visits to Vienna.

Special thanks go to *Dominique Vernhet* and her group at INSP Paris for the experimental perspective on laser-cluster interaction continuing the work of *Cornelia Deiss*. I especially thank Cornelia who despite her crowded schedule at McKinsey made time to help with technical issues in reviving her particle-in-cell code. Despite being out of the game for years she was very insightful and remembered details in astonishing clarity.

I would like to thank *Matthias Kling* and *Hui Li* from Kansas and now Munich for our collaboration on C_{60} and other things initiated by Matthias' visit to Vienna in 2012. Pending finalization, and containing yet unpublished experimental data, our work on CEP-resolved electron emission from C_{60} by ultrashort laser pulses will be available soon.

Many thanks go to *MT Homer Reid* for providing the code of his Maxwell solver *scuff-EM* prior to its official release and for helping me use it effectively. Chapter 2 would have been impossible without his work.

I would also like to thank the *support team of the Vienna Scientific Cluster* for answering countless questions and great advice on how to make the best use of the supercomputer.

Finally, I would like to thank the group of *Josef Hron* and the principal investigator *Daniela Klotz* from the department for Astrophysics of the University of Vienna for consulting me about Monte-Carlo simulations for, well, interferometric measurements of asymptotic giant branch stars. Daniela was a great co-author and is still a great partner, and I fondly remember our "science meetings" with extended breakfasts on our balcony. The outcome was a great paper to which I however contributed only marginally [Klotz et al., 2012]. I also thank them for all the nice barbecues at the Institute of Astronomy.

Daniela Klotz also provided the L^AT_EX template for this manuscript and her experience as an editor saved me countless hours producing this monograph. I gratefully acknowledge proofreading and suggestions from her, *Christoph Lemell*, *Xiao-Min Tong*, *Shunsuke A. Sato*, *Michael Krüger*, *Peter Hommelhoff* and especially *Joachim Burgdörfer*.

Finally and most importantly, I would like to thank *Daniela, my friends and my family* for their guidance, continuous support, and all the fun we had. It's easy to enjoy life with you around.

Georg Wachter

I gratefully acknowledge a stipend from the International Max Planck Research School of Advanced Photon Science. Furthermore, this work was financially supported by the FWF (Austria) in SFB-041 ViCoM, SFB-049 Next Lite, and P21141-N16. Calculations were performed on the Vienna Scientific cluster, the T2K computer (Tsukuba), the supercomputer at the Institute of Solid State Physics of the University of Tokyo, and K Computer (Kobe).

Curriculum vitae

Contact

Georg Wachter
Institute for theoretical physics, TU Wien
Wiedner Hauptstr. 8-10 / 136, A-1040 Wien, Austria, EU
+43-(0)1-58801-13630, georg.wachter@tuwien.ac.at, georgwachter.com

Personal data

born on 09.08.1984 in Innsbruck
Austrian citizenship

Education

- 2010–2014 PhD study Theoretical Physics, Vienna University of Technology and International Max Planck Research School for Advanced Photon Science (IMPRS-APS)
- 2003–2009 Master study Technische Physik, Vienna University of Technology. Diploma with distinction
- 1994–2002 High school, BRG Adolf-Pichler-Platz, Innsbruck. Diploma with distinction

Work experience

- 2010–2014 Project assistant, TU Wien
- 2006–2009 Teaching assistant, Inst. for theoretical physics, TU Wien
- 2002–2003 Civilian service, Elisabethinum Axams. Handicapped children and youths care

Languages

- German native
- English fluent
- French intermediate
- Spanish intermediate

Awards

- 2010 – 2014 Dissertation scholarship of the Max-Planck-Society
- 2009 Achievement scholarship TU Wien

Publications

Journal articles

- G Wachter, C Lemell, J Burgdörfer, SA Sato, XM Tong, K Yabana
Ab initio simulation of electrical currents induced by ultrafast laser excitation of dielectric materials
Physical Review Letters 113, 087401 (2014)
- H Li, B Mignolet, G Wachter, S Skruszewicz, S Zhrebtsov, F Süßmann, A Kessel, S A Trushin, Nora G Kling, M Kübel, B Ahn, D Kim, I Ben-Itzhak, C L Cocke, T Fennel, J Tiggesbäumker, K-H Meiwes-Broer, C Lemell, J Burgdörfer, R D Levine, F Remacle, M F Kling
Coherent electronic wave packet motion in C_{60} controlled by the waveform and polarization of few-cycle laser fields
submitted to Physical Review (2014)
- S Nepll, R Ernstorfer, A L Cavalieri, C Lemell, G Wachter, E Magerl, E Bothschafter, M Hofstetter, J V Barth, D Menzel, J Burgdörfer, P Feulner, F Krausz, R Kienberger
Real-time observation of electron propagation and dielectric screening on the atomic length scale
submitted to Nature publishing group (2014)
- A S El-Said, R A Wilhelm, R Heller, S Facsko, C Lemell, G Wachter, J Burgdörfer, R Ritter, F Aumayr
Phase diagram for nanostructuring CaF_2 surfaces by slow highly charged ions
Physical Review Letters 109, 117602 (2012)
- M Krüger, M Schenk, P Hommelhoff, G Wachter, C Lemell, J Burgdörfer
Interaction of ultrashort laser pulses with metal nanotips: a model system for strong-field phenomena
New Journal of Physics, 14, 085019 (2012)
- G Wachter, C Lemell, J Burgdörfer, M Schenk, M Krüger, P Hommelhoff
Electron rescattering at metal nanotips induced by ultrashort laser pulses
Physical Review B, 86, 035402 (2012)
- E Persson, M Pichler, G Wachter, T Hisch, W Jakubetz, J Burgdörfer, S Gräfe
Quantum control of electron wave packets in bound molecules by trains of half-cycle pulses
Physical Review A, 84, 043421 (2011)
- A Golczewski, K Dobes, G Wachter, M Schmid, F Aumayr
A quartz-crystal-microbalance technique to investigate ion-induced erosion of fusion relevant surfaces
Nuclear Instruments and Methods in Physics Research B, 267, 695 (2009)

Conference proceeding articles

- G Wachter, C Lemell, J Burgdörfer
Electron rescattering at metal nanotips induced by ultrashort laser pulses
J. Phys.: Conf. Ser., 488, 012005 (2014)
- S Nagele, R Pazourek, M Wais, G Wachter, J Burgdörfer
Time-resolved photoemission using attosecond streaking
J. Phys.: Conf. Ser., 488, 012004 (2014)
- A S El-Said, R A Wilhelm, R Heller, R Ritter, G Wachter, S Facsko, C Lemell, J Burgdörfer, F Aumayr
Nanostructuring CaF_2 surfaces with slow highly charged ions
J. Phys.: Conf. Ser., 488, 012002 (2014)
- M Krüger, S Thomas, M Förster, L Maisenbacher, G Wachter, C Lemell, J Burgdörfer, P Hommelhoff
Attosecond physics at a nanoscale metal tip: strong field physics meets near-field optics
SPIE OPTO, 862313-862313-6 (2013)

- G Wachter, K Tökési, G Betz, C Lemell, J Burgdörfer
Modelling surface restructuring by slow highly charged ions
Nucl. Instrum. Methods Phys. Res. Sect. B, 317, 149 (2013)
- G Wachter, C Lemell, J Burgdörfer
Electron emission from a metal nano-tip by ultrashort laser pulses
J. Phys.: Conf. Ser., 399, 012010 (2012)
- G Wachter, E Persson, M Pichler, T Hisch, J Burgdörfer, S Gräfe
Quantum Control of Electron Wavepacket Dynamics in Molecules by Trains of Half-Cycle Pulses
J. Phys.: Conf. Ser., 388, 132018 (2012)
- D Klotz, S Sacuto, C Paladini, J Hron, G Wachter
Geometrical model fitting for interferometric data: GEM-FIND
SPIE Astronomical Telescopes and Instrumentation, SPIE Conference Series 8445, 84451A (2012)
- P Tiwald, C Lemell, G Wachter, J Burgdörfer
Theory of below-threshold kinetic electron emission
J. Phys.: Conf. Ser., 257, 012012 (2010)

Invited talks at international conferences

- G Wachter,
Electron rescattering at metal nanotips induced by ultrashort laser pulses
XXVIII International Conference on Photonic, Electronic and Atomic Collisions (IC-PEAC), Lanzhou, China (7/2013)
- G Wachter, K Tökési, G Betz, C Lemell, J Burgdörfer
A microscopic model for track formation by swift heavy ions
19th International Workshop on Inelastic Ion-Surface Collisions (IISC-19), Frauenchiemsee, Germany (9/2012)
- G Wachter, C Lemell, J Burgdörfer
Electron emission from a metal nano-tip by ultrashort laser pulses
26th Summer School and International Symposium on the Physics of Ionized Gases (SPIG26), Zrenjanin, Serbia (8/2012)

Talks at conferences and workshops

- G Wachter
Interaction of ultrashort laser pulses with metal nanotips
ViCoM Young Researchers Meeting, Vienna (4/2014)
- G Wachter
Interaction of ultrashort laser pulses with metal nanotips and dielectrics
Joint Symposium SFB IR-ON and SFB Next-Lite, Vienna (3/2014)
- G Wachter
Electron photoemission from metal nanotips induced by ultrashort laser pulses
International Max Planck Research School for Advanced Photon Science (IMPRS-APS) Annual Meeting, Ringberg Castle, Tegernsee (12/2013)
- G Wachter, C Lemell, J Burgdörfer
Electron rescattering at metal nanotips induced by ultrashort laser pulses
Quantum Dynamics and Photon-Matter Interaction Joint IMPRS workshop, Max Planck Institute for the Physics of Complex Systems, Dresden (5/2013)
- G Wachter, C Lemell, J Burgdörfer
Theoretical aspects of laser-nanotip interaction
International Max Planck Research School for Advanced Photon Science (IMPRS-APS) Annual Meeting, Ringberg Castle, Tegernsee (7/2012)

- G Wachter, C Lemell, J Burgdörfer
Modelling of laser-tip interaction
International Max Planck Research School for Advanced Photon Science (IMPRS-APS)
Annual Meeting, Ringberg Castle, Tegernsee (7/2011)
- G Wachter, C Lemell, J Burgdörfer
Theoretical aspects of laser-tip interactions
International Max Planck Research School for Advanced Photon Science (IMPRS-APS)
Annual Meeting, München (12/2010)

Posters

- H Yin, G Wachter, C Deiss, C Lemell, J Burgdörfer, E Lamour, C Prigent, C Ramond, JP Rozet, S Steydli, M Trassinelli, D Vernhet
keV electron heating in laser-cluster interaction probed by X-ray and electron spectroscopy
28th Intern. Conf. on Photonic, Electronic and Atomic Collisions (XXVIII ICPEAC), Lanzhou (7/2013)
- G Wachter, K Tőkési, G Betz, C Lemell, J Burgdörfer, AS El-Said, RA Wilhelm, R Heller, S Facsko, R Ritter, F Aumayr
Nano-structuring of CaF₂ surfaces by slow highly charged ions: simulation and experiment
28th Intern. Conf. on Photonic, Electronic and Atomic Collisions (XXVIII ICPEAC), Lanzhou (7/2013)
- G Wachter, G Betz, C Lemell, J Burgdörfer
Modifications of crystal structures induced by slow highly charged ion and swift heavy ion impact
Conference on Ion-Surface Interactions 2011 (ISI-2011), Zvenigorod (8/2011)
- G Wachter, C Lemell, J Burgdörfer
Electron emission in laser-nanotip interaction
27th Intern. Conf. on Photonic, Electronic and Atomic Collisions (XXVII ICPEAC), Belfast (7/2011)
- G Wachter, K Tőkési, G Betz, C Lemell, J Burgdörfer
Nanomelting and track formation in insulators by swift heavy ions
27th Intern. Conf. on Photonic, Electronic and Atomic Collisions (XXVII ICPEAC), Belfast (7/2011)
- G Wachter, C Lemell, J Burgdörfer
Electron emission in laser-nanotip interaction
International Max Planck Research School - Munich Centre for Advanced Photonics (IMPRS-MAP) summer school, Wildbad Kreuth (8/2010)
- G Wachter, K Tőkési, G Betz, C Lemell, J Burgdörfer
Track formation in fast atom-insulator interactions
24th International Conference on Atomic Collisions in Solids (ICACS24), Kraków (7/2010)
- G Wachter, C Lemell, G Betz, K Tőkési, J Burgdörfer
Track formation in ion-insulator interactions
4th Annual Meeting of the EU network ITS-LEIF, Platja d'Aro, Girona/Spain (5/2009)
- G Wachter, S Lederer, HP Winter, H Winter, C Lemell, J Burgdörfer
Subthreshold kinetic electron emission
25th Intern. Conf. on Photonic, Electronic and Atomic Collisions (XXV ICPEAC), Freiburg, Germany (7/2007)

Academic texts (author or supervisor)

- T Madlener
Project thesis: *Strong field photoemission from a nano-tip by two-color laser fields*
Supervisors: G Wachter, J Burgdörfer, C Lemell
TU Wien / Institut für Theoretische Physik (2014)
- J Huber
Bachelor thesis: *Non-sequential double ionization of atoms in ultra-short strong laser fields*
Supervisors: J Burgdörfer, S Nagele, R Pazourek, G Wachter
TU Wien / Institut für Theoretische Physik (2014)
- M Wais
Bachelor thesis: *Time-resolved photoemission from endohedral fullerenes using attosecond streaking*
Supervisors: J Burgdörfer, S Nagele, R Pazourek, G Wachter
TU Wien / Institut für Theoretische Physik (2014)
- H Yin
Project thesis: *Simulation of the dynamics of laser-cluster interaction*
Supervisors: G Wachter, C Lemell, J Burgdörfer
TU Wien / Institut für Theoretische Physik (2012)
- G Wachter
Diploma thesis: *Crystal restructuring by nano-scale melting*
Supervisors: C Lemell, J Burgdörfer
TU Wien / Institut für Theoretische Physik (2009)